Diss. ETH No. 16864

EFFECTS OF STRONG CORRELATIONS ON LOW-DIMENSIONAL AND MULTI-ORBITAL ELECTRONIC SYSTEMS

A dissertation submitted to the

SWISS FEDERAL INSTITUTE OF TECHNOLOGY ZURICH
(ETH ZÜRICH)

for the degree of
Doctor of Natural Sciences

presented by

MARTIN INDERGAND

Dipl. Phys. ETH
born February 21, 1975
Swiss citizen

accepted on the recommendation of
Prof. Dr. M. Sigrist, examiner
Prof. Dr. C. Honerkamp, co-examiner
Dr. A. Läuchli, co-examiner

2006

Seite Leer /
Blank leaf

Seite Leer /
Blank leaf

Seite Leer /
Blank leaf

Abstract

In this thesis the effects of strong correlations on several low-dimensional fermionic lattice models is explored by different theoretical approaches. The focus lies on the appearance of low-temperature phases with spontaneous broken symmetry. We study the properties of general models for strongly correlated electron systems, like the Hubbard model or the t-J model, on different frustrated and/or low-dimensional lattices and derive a new model for a novel material with unusual properties.

After a general introduction to the field and to the methods in Chapter 1 we derive in Chapter 2 a multi-orbital model for the recently synthesized, layered transition metal compound Na_xCoO_2. We focus on a single CoO_2 layer and describe the kinetic energy for the degenerate t_{2g} orbitals of the Co ions by indirect hopping over the oxygen p orbitals. This leads naturally to the concept of four inter-penetrating kagomé lattices. The local multi-orbital Coulomb interaction couples the four kagomé lattices and we can write an effective Hamiltonian for the interaction in the top band in terms of fermionic operators with four different flavors. The effective interaction reduces the SU(4) symmetry of the quadratic part of the Hamiltonian to a discrete but still large symmetry group. Taking this symmetry into account we can calculate all coupling constants for charge and spin density wave instabilities within this model. We find a big variety of attractive (negative coupling constant) metallic states with spontaneously broken symmetry, where the system shows an ordering pattern with a modulation of the charge, orbital, spin or orbital angular momentum degrees of freedom. We also discuss the strong superstructure formation at $x = 0.5$ within this model.

In Chapter 3 we explore both analytically and numerically the properties of doped t-J models on a class of highly frustrated lattices, such as the kagomé and the pyrochlore lattice. Focusing on a particular sign of the hopping integral and on antiferromagnetic exchange, we find a generic symmetry breaking instability

towards a twofold degenerate ground state at a rational fractional filling below half-filling. These states show modulated bond strengths and only break lattice symmetries. They can be regarded as a generalization of the well-known valence bond solid states to fractional filling.

In Chapter 4 we study the t-J model on inhomogeneously doped two-leg ladder and bilayer systems. The inhomogeneous doping is achieved by assuming different chemical potentials on the legs or on the layers, respectively. We find that a chemical potential difference between the legs of the two-leg ladder is harmful for Cooper pairing and we analyze this instability of superconductivity on the ladder by comparing results of various analytical and numerical methods. Exact diagonalization of finite systems shows that hole binding is unstable beyond a finite, critical chemical potential difference. The spinon-holon mean-field theory for the t-J model shows a clear reduction of the BCS gaps upon increasing the chemical potential difference leading to a breakdown of superconductivity on the two-leg ladder. We also determine the doping dependent phase diagram with different chemical potentials for the weakly interacting Hubbard model on the two-leg ladder. On the bilayer we apply the spinon-holon mean-field theory and find that an initial s-wave pairing state evolves into a d-wave pairing upon increasing the chemical potential difference. The symmetry change occurs via two second order phase transitions that comprise a time-reversal symmetry breaking mixed state of the form $s \pm \mathrm{i}d$.

In the last chapter we give a rigorous proof for the existence of long range antiferromagnetic order in the ground state of several two-dimensional spin-1/2 Heisenberg systems. We consider three types of systems: The first type consists of an even number N of coupled square lattices with antiferromagnetic nearest-neighbor Heisenberg interactions. Here, we can prove long range order (LRO) in the ground state for an inter-plane to inplane coupling ratio r between $0.16 \leq r \leq 2.1$ if $N \geq 4$. Further we can prove that the antiferromagnetic bilayer with ferromagnetic next-nearest-neighbor (nnn) inter-plane couplings has LRO in the ground state for $0.21 \leq r < 1/4$, where r is the absolute value of the ratio between the ferromagnetic and the antiferromagnetic coupling. The final example is constructed from two antiferromagnetic spin-1/2 square lattices that are coupled via an antiferromagnetic nnn inter-plane coupling r. For $r = 1$ the system is effectively a spin-1 square lattice. We show that in the region $0.85 \leq r \leq 1$ LRO exists.

Zusammenfassung

In dieser Doktorarbeit werden die Effekte von starken Korrelationen in verschiedenen elektronischen Gittermodellen mit Hilfe von mehreren theoretischen Methoden erforscht. Der Schwerpunkt wird dabei auf die Beschreibung von Phasen mit spontaner Symmetriebrechung bei tiefen Temperaturen gelegt. Wir untersuchen die Eigenschaften von allgemeinen Modellen für stark korrelierte Elektronensysteme, wie das Hubbard Modell oder das t-J Modell, in verschiedenen frustrierten und niedrig-dimensionalen Gittermodellen. Zudem leiten wir ein neues Modell für ein neuartiges Material mit ungewöhnlichen Eigenschaften her.

Nach einer allgemeinen Einleitung in das Gebiet und in die Methoden in Kapitel 1 leiten wir in Kapitel 2 ein multi-orbitales Modell für das neulich synthetisierte Übergangsmetall-Oxid Na_xCoO_2 her. Wir fokussieren uns dabei auf eine einzige CoO_2 Schicht und beschreiben die kinetische Energie für die entarteten t_{2g} Orbitale der Kobalt-Ionen durch indirekte Hüpfprozesse über die Sauerstoff p Orbitale. Dies führt auf natürliche Weise zu dem Konzept von vier sich gegenseitig durchdringenden Kagomé Gittern. Die lokale Coulomb Abstossung koppelt die vier Kagomé Gitter und wir können eine effektive Theorie für die Wechselwirkung im obersten Band herleiten. Die SU(4) Symmetrie des nicht wechselwirkenden Systems wird durch die Wechselwirkung auf eine diskrete aber immer noch grosse Symmetriegruppe reduziert. Unter Berücksichtigung dieser Symmetriegruppe können wir alle Kopplungskonstanten für Ladungs- und Spin-Dichtewellen innerhalb von diesem Modell berechnen. Wir finden eine grosse Vielfalt von von attraktiven (negative Kopplungskonstanten), metallischen Zuständen mit spontaner Symmetriebrechung, in welchen die Ladungs-, die Spin- und die Orbital-Freiheitsgrade periodische Muster bilden. Wir diskutieren auch die Superstrukturbildung, welche beim Natriumgehalt $x = 0.5$ auftritt, innerhalb von diesem Modell.

Im Kapitel 3 untersuchen wir mit analytischen und numerischen Methoden die Eigenschaften des dotierten t-J Modells in einer Klasse von stark frustrierten Gittern, wie zum Beispiel das Kagomé oder das Pyrochlor Gitter. Für positives t und antiferromagnetisches J und bei einer kommensurablen partiellen Füllung unterhalb von halber Füllung entdecken wir eine generische Instabilität, welche zu einem zweifach entarteten Grundzustand führt. Diese Zustände stellen eine Verallgemeinerung der bekannten *Valence Bond Solid* Zustände bei halber Füllung dar.

Im Kapitel 4 untersuchen wir das t-J Modell auf inhomogen dotierten Doppelketten und Doppelschichten. Die inhomogene Dotierung wird durch unterschiedliche chemische Potentiale auf den beiden Ketten oder Schichten erreicht. Für die Doppelkette schliessen wir auf Grund von Resultaten aus exakter Diagonalisierung von endlichen Systemen und aus speziellen Molekularfeldrechnungen für das t-J Modell, dass die BCS Energielücke durch die unterschiedlichen chemischen Potentiale klar reduziert wird und dass der supraleitende Zustand schliesslich zusammenbricht. Für die Doppelschicht erhalten wir durch Molekularfeldrechnungen das Resultat, dass ein supraleitender Zustand mit s-Wellen Paarungssymmetrie durch die unterschiedlichen Potentiale auf den Schichten in einen Zustand mit d-Wellen Symmetrie übergeht. Dieser Symmetriewechsel erfolgt über zwei Phasenübergänge zweiter Ordnung mit einer dazwischenliegend Phase, welche die Zeitumkehrsymmetrie bricht.

Im letzten Kapitel geben wir einen rigorosen Beweis für die Existenz von langreichweitiger antiferromagnetischer Ordnung im Grundzustand von verschiedenen zweidimensionalen Spin-1/2 Heisenberg Modellen. Wir betrachten ein System bestehend aus einer geraden Anzahl N von gekoppelten Quadratgittern mit antiferromagnetischer Wechselwirkung zwischen den nächsten Nachbarn, und wir können für $N \geq 4$ die Existenz von langreichweitiger Ordnung im Grundzustand beweisen. Auch für $N = 2$ mit diagonalen ferromagnetischen Kopplungen zwischen den Quadratgittern können wir die Existenz von antiferromagnetischer Ordnung im Grundzustand rigoros beweisen.

Contents

1 Introduction **1**

1.1 A General Outline 1

1.2 From a multi-band Hubbard model to a single-band model . . . 6

1.3 From the single-band model to the mean-field model 9

2 Effective Interaction between the Inter-Penetrating Kagomé Lattices in Na_xCoO_2 **17**

2.1 Introduction 17

2.2 Tight-binding model 22

2.3 Coulomb interaction 27

2.4 SU(4) generators 30

2.5 Reduction of the symmetry 31

2.6 Ordering patterns 36

2.7 Possible instabilities 49

2.7.1 Coupling constants 49

2.7.2 Effect of the trigonal distortion 50

2.8 Na-superstructures 52

2.9 Wannier functions 57

2.10 Superconductivity 59

2.11 Discussion and conclusion 61

3 Bond Order Wave Instabilities in Doped Frustrated Antiferromagnets **65**

3.1 Introduction 65

3.2 Model and lattices 67

3.3 The limit of decoupled simplices 69

3.3.1 Approaching the uniform lattices 70

3.4 Doped quantum dimer model 72

3.5 Mean-field discussion 74
3.5.1 "Supersolid" 80
3.6 Weak-coupling discussion 82
3.6.1 Kagomé strip 83
3.6.2 Checkerboard lattice 85
3.6.3 Kagomé lattice 90
3.7 Numerical results 91
3.7.1 Kagomé lattice 91
3.7.2 Checkerboard lattice 92
3.7.3 Kagomé strip 94
3.8 The Dirac points of the kagomé lattice 97
3.9 Discussion and conclusion 105

4 Inhomogeneously Doped t-J Ladder and Bilayer Systems 109
4.1 Introduction 109
4.2 Strong rung coupling limit 111
4.3 Exact diagonalization 114
4.4 Renormalization group 117
4.5 Mean-field analysis for the t-J ladder 124
4.5.1 Spinon-holon decomposition 124
4.5.2 Mean-field results for the t-J ladder 127
4.6 Mean-field analysis for the bilayer 131
4.6.1 The symmetric bilayer 133
4.6.2 The inhomogeneously doped bilayer 134
4.7 Discussion and conclusion 137

5 Existence of Long Range Magnetic Order in the Ground State of Two-Dimensional Spin-1/2 Heisenberg Antiferromagnets 139
5.1 Introduction 139
5.2 N layers with nearest-neighbor couplings 141
5.3 Bilayer with ferromagnetic next-nearest-neighbor coupling . . . 144
5.4 Diagonal bilayer 150
5.5 Discussion and conclusion 153

A Appendix to Chapter 2 155
A.1 Definitions of the pocket operators 155
A.2 Derivation of the effective Hamiltonian 155
A.3 The symmetry group G 157

B Appendix to Chapter 3 **159**
B.1 RG analysis 159
B.1.1 Kagomé strip 159
B.1.2 Checkerboard lattice 161
B.1.3 Weak-coupling on the honeycomb lattice 162

C Appendix to Chapter 5 **167**
C.1 Anderson bound for the energy 167
C.2 Proof of Gaussian domination 168

Bibliography **169**

Acknowledgments **179**

Curriculum Vitae **181**

Chapter 1

Introduction

1.1 A General Outline

Strong correlations in low-dimensional electronic systems are responsible for an almost inexhaustibly rich variety of phenomena. High-temperature superconductivity and the fractional quantum Hall effect are probably the most prominent examples, but also magnetism in solids originates from the Coulomb repulsion between the electrons. Ordering processes can be observed at low temperatures that lead to phases with spontaneously broken symmetry but also disordered and highly fluctuating liquid ground states like spin liquids or Luttinger liquids might describe the low energy physics of a material.

For a theoretical understanding of these different order and disorder phenomena the effective dimension of the system plays a crucial role. All solids are three-dimensional (3D) but often the quantum mechanical models used to describe the low-energy behavior are one-dimensional (1D) or two-dimensional (2D).

Due to the progress in materiel research many bulk materials containing 1D structures have been synthesized. Famous examples are the organic superconductors, carbon nanotubes, spin-chain and ladder compounds [1]. In this thesis we study in Chapter 4 the superconducting phases in inhomogeneously doped ladder and bilayer systems. Note, that these superconducting phases in 1D systems that we describe by a mean-field analysis can only be realized in materials owing to the actual three-dimensionality of the solids and due to inevitable weak interconnections between the 1D structures. In a pure 1D electron system no continuous symmetry breaking can occur even in the ground state due to the disordering effects of the quantum fluctuations. A discrete symmetry can

be broken but as in this case no Goldstone mode appears the system usually acquires a gap. Ungapped 1D systems of interacting particles have peculiar properties: One particle can not move independently of the other particles and therefore the fundamental excitations of the system are collective excitations rather than single-particle excitations. This insight led to the development of the Bosonization technique, which is only one of several powerful theoretical tools available in 1D.[a] It turns out that at low energies these ungapped 1D systems form so-called Luttinger liquids, which can be described by a universal Hamiltonian with only two free parameters. The Luttinger liquids form the 1D analogue to the 3D Fermi liquid, in the sense that also the Fermi liquid theory provides a universal low-energy theory for a 3D interacting Fermi system without broken symmetry.[b] In 2D such a universal low-energy theory is still missing and for this reason the 2D and quasi-2D materials provide the most exciting, but probably also the most puzzling and controversial condensed matter systems. Graphene is a recently found 2D semi-metallic allotrope of carbon that is currently being intensively studied due to its possible technical applications [2]. Its chiral fermionic excitations with linear dispersion reminding of the massless Dirac spectrum have very recently been suggested to be a solid state implementation of quantum electrodynamics in (2+1) dimension and, e.g., to allow for an experimental test of the Klein paradox [3]. In Sec. 3.8 we analyze the properties of the Dirac cones in the kagomé lattice and show how theoretical results for the honeycomb lattice can be translated to the kagomé lattice [4, 5].

Another very interesting 2D material is the layered transition metal oxide Na_xCoO_2. The attention of the strongly correlated electrons community was especially focused on this material after the discovery of superconductivity in the hydrated samples with $x \approx 0.35$ [6], which came as big surprise after the intense search for superconductivity in layered transition metal oxides. The nature and the origin of the superconducting state are still not clarified, but it was realized quickly that already the normal state of Na_xCoO_2 is very unusual: At $x = 0.5$ a magnetic transition at 88 K is followed by a metal-insulator transition at 53 K [7], and for larger values of x metallic behavior is coexisting with local moments and Curie-Weiss susceptibility. At even higher Na concentrations ($x > 0.75$) a spin-density wave instability occurs at 22 K [8]. One

[a] This technique is also applied in this thesis for two different 1D models in Sec. 3.6.1 and in Sec. 4.4.

[b] In contrast to the Luttinger liquid, the elementary excitations in a Fermi liquid are single-particle excitations.

problem in the theoretical analysis of this model is posed by the Na ions that provide a disordered charge background or impose superstructures with rather large unit cells. A further complication arises due to the multi-orbital character of the CoO_2 plane consisting of three almost degenerate t_{2g} orbitals on a Co site. The first chapter of this thesis is devoted to this material. It contains a derivation of an effective model for the orbital and spin degrees of freedom of a single CoO_2 plane taking into account the multi-orbital aspect and the Coulomb interaction.

Another important property of Na_xCoO_2 is the fact that it is build up of triangular lattices. The triangular lattice or any other lattice that contains triangles is frustrated in the sense that no antiferromagnetic spin arrangement with an opposite alignment of all neighboring spins is possible. Antiferromagnetic spin systems on highly frustrated lattices are a relatively new and fascinating research field [9]. In our work on Na_xCoO_2 we are confronted with doped frustrated lattices and also in Chapter 3 we study doped highly frustrated lattices like the kagomé or the pyrochlore lattice. In our study it turns out that due to presence of charge degrees of freedom the frustration can be avoided and an unfrustrated ground state can be obtained.

Many of these exotic phases and ordering phenomena described above only exist at low temperatures. In fact the energy scale associated with their critical temperatures are often several orders of magnitude lower than the energy scale of the parameters in the microscopic models, like the Coulomb repulsion U and the hopping integral t in the Hubbard model for example.

The derivation of an effective Hamiltonian that allows for a description of the low-energy physics from the original microscopic Hamiltonian is one of the most important and most challenging problems in theoretical solid state physics. In the following we will present several alternatives for deriving such effective low-energy theories and and point out where and in which context these different methods where applied within this thesis:

The most direct method for such a derivation are based on the renormalization group (RG) ideas. Usually, the implementation of these methods uses a functional integral representation that allows to integrate out successively high-energy degrees of freedom by renormalizing at the same time the interaction between the low-energy degrees of freedom. The energy scale can be reduced in discrete steps or in a continuous way and in the latter case it is possible to obtain a set of differential equations that generate a flow of the action towards the effective low-energy action. The RG schemes are most easily

derived for 1D systems where the Fermi surface (FS) consists only of a discrete set of points [10]. An alternative way to explore the low-energy correlations of an interacting 1D Fermi system is provided by the density matrix renormalization group (DMRG) method which is a very modern numerical RG method for 1D systems [11]. In higher dimensions it is in special cases also possible to restrict the RG analysis to the vicinities of a few selected points of the FS [12, 13] but in general it is necessary to derive an RG scheme not only for a set of coupling constants but for continuous coupling functions (functional RG) [14, 15]. In this thesis we apply the RG equations for the two-leg ladder [16] to a doped frustrated 1D system (Sec. 3.6.1) and find good agreement with numerical DMRG results (Sec. 3.7.3). We also compare our mean-field calculations for the inhomogeneously doped t-J ladder with a weak-coupling RG analysis in Sec. 4.4. Furthermore, we use a simple RG scheme for the square lattice to analyze the doped checkerboard lattice which is a 2D analog of the 3D pyrochlore lattice (Sec. 3.6.2).

For strong interactions and increasing dimensionality the RG schemes might become intractable. An alternative way to derive an effective low-energy model in any dimension is given for large Coulomb repulsion where we have the small parameter $\lambda = t/U$ [17]. In this method, the Hilbert space is constrained to the subspace $\mathcal{M}$ of lowest energy eigenstates of the interaction, which is usually well separated from the higher-energy subspaces. The effective Hamiltonian is then found by a canonical transformation, $\tilde{H} = \mathrm{e}^{-\mathrm{i}S} H \mathrm{e}^{\mathrm{i}S}$, such that $\tilde{H}$ is block diagonal with respect to the subspace $\mathcal{M}$ and by a restriction of $\tilde{H}$ to $\mathcal{M}$. In first order of λ the effective Hamiltonian consists just of the kinetic energy hopping processes within the subspace $\mathcal{M}$. In second order it contains also the "virtual processes" of hopping out of and back into the subspace $\mathcal{M}$. In this way a new effective interaction at an intermediate energy scale $J \propto t^2/U$ can be obtained. The disadvantage of such a reduced Hilbertspace are the awkward commutation relations of the so-called Hubbard operators that must be introduced to enforce the constraint. An elegant reformulation of the problem can be achieved if the Hubbard operators are replaced by products of a fermionic and a bosonic particle [18].[c] These additional "slave" particles allow however to study the system with a mean-field theory that takes the constraint at least approximatively into account. In Chapter 4 we perform such a mean-field anal-

[c] Note, that these particles are also not free fermions or bosons. The still have to fulfill a local constraint.

ysis for the t-J model[d] on inhomogeneously doped two-leg ladder and bilayer systems. Furthermore, in Sec. 3.5 we study a different strong-coupling model, the somewhat more general t-J-V model, on the kagomé and on the pyrochlore lattice, accounting for the constraint by the statistical Gutzwiller mean-field method. Note, that the mean-field analysis of the effective interaction goes much further than a mean-field analysis of the original interaction, as due to the canonical transformation new and longer range interaction terms appear which lead to new types of mean-fields and to a bigger variety of possible instabilities.

The fact that the dimensionality of the Hilbertspace is drastically reduced in the effective strong coupling models like the t-J model can be directly exploited in 1D and 2D. The exact diagonalization (ED) method allows to calculate the ground state energy and correlation functions in the ground state exactly for reasonably large systems (about 20 sites for the t-J model). We compare our analytical or mean-field results against ED data for the t-J model in Sec. 3.7.1-3.7.2 and in Sec. 4.3. This mutual comparison of complementary approaches allows us to assure that the we describe intrinsic properties of the system and not an artifact of the approximation or the finite size.

At fractional filling, i.e., if the number of electrons per unit cell is a simple fraction, there exists often a unique charge distribution (up to translations) that minimizes the interaction energy. In this case all charge excitations are gapped and there are no terms of first order in $\lambda = t/U$ in the low-energy subspace. The strong-coupling model describes then the effective second order interaction between the remaining spin and orbital degrees of freedom. These models loose their fermionic character as the interaction can be expressed through operators that are quadratic in the original fermionic operators. The most prominent example of such a model is the antiferromagnetic Heisenberg model obtained for the half-filled large U Hubbard model. The redundancy of the description of such a model with fermionic operators shows up in the local SU(2) gauge symmetry of the interaction, which transforms the creation operators with down spin into the annihilation operators with up spin but leaves the local spin operators invariant [20]. The presence of this local gauge symmetry plays a role close to half-filling [21], but exactly at half-filling the system reduces to a pure spin model. The antiferromagnetic spin-1/2 Heisenberg models in 2D is

[d]The t-J model was derived by Zhang and Rice [19] as an effective single-band model for the high-T_c superconductors. It is similar but not identical to the strong coupling Hubbard model.

the topic of Chapter 5 which is the last chapter of this thesis. We address the question, whether there exists antiferromagnetic long range order in the ground state or whether the ground state is disordered due to quantum fluctuations. For models on the hypercubic lattice this question can be rigorously answered in any dimension except for 2D.[e] We do not manage to provide a rigorous proof for the square lattice, but we give examples of spin-1/2 models on the bilayer where long-range antiferromagnetic order can in fact be proven.

1.2 From a multi-band Hubbard model to a single-band model

In the previous section we discussed the derivation of an effective interaction for a strong-coupling model. In this section, we describe a straightforward procedure to reduce a weak-coupling multi-band or multi-orbital Hubbard model to a single band model. This procedure can be useful to describe correlated metals and was applied in Chapter 2 to the multi-orbital system Na_xCoO_2. A further application of this method is given in Chapter 3, where the weak-coupling Hubbard model on bisimplex lattices was studied. We consider the Hamiltonian

$$H = H_0 + H_{\text{Int}}. \tag{1.1}$$

The quadratic part, H_0, of the Hamiltonian for a general multi-band or multi-orbital tight-binding model without spin-orbit coupling is of the form

$$H_0 = \sum_{\mathbf{r}\mathbf{r}'} \sum_{ij} \sum_{\sigma} \left(t^{ij}_{\mathbf{r}-\mathbf{r}'} - \delta_{\mathbf{r}\mathbf{r}'}\delta_{ij}\mu \right) c^{\dagger}_{\mathbf{r}i\sigma} c_{\mathbf{r}'j\sigma} = \sum_{\mathbf{k}\nu\sigma} \xi^{\nu}_{\mathbf{k}} \gamma^{\dagger}_{\mathbf{k}\nu\sigma} \gamma_{\mathbf{k}\nu\sigma}, \tag{1.2}$$

where $t^{ij}_{\mathbf{r}-\mathbf{r}'}$ is the transfer integral between the orbitals (atoms) i and j in the unit cells at $\mathbf{r}$ and $\mathbf{r}'$ and $\xi^{\nu}_{\mathbf{k}}$ is the dispersion of the band ν. Furthermore, H_0 includes a chemical potential term proportional to μ. The operators $\gamma_{\mathbf{k}\nu\sigma}$ are obtained by the orthogonal transformation $\gamma_{\mathbf{k}\nu\sigma} = \sum_j O^{\nu j}_{\mathbf{k}} c_{\mathbf{k}j\sigma}$ where $c_{\mathbf{k}j\sigma}$ are the Fourier transformed operators of $c_{\mathbf{r}i\sigma}$. The Hamiltonian H_0 contains the atomic energy of the orbitals the kinetic energy gain due to delocalization and the potential of crystalline lattice.

[e] There is of course good numerical evidence that also the 2D ground state is ordered, but a rigorous proof is still missing.

The interaction part, H_{Int}, of the Hamiltonian is given by

$$H_{\text{Int}} = \frac{1}{2} \sum_{\mathbf{r}} \sum_{ij} \sum_{i'j'} \sum_{\sigma\sigma'} V^{iji'j'} c^{\dagger}_{\mathbf{r}i\sigma} c^{\dagger}_{\mathbf{r}j\sigma'} c_{\mathbf{r}i'\sigma'} c_{\mathbf{r}j'\sigma}. \tag{1.3}$$

It describes the screened Coulomb interaction between the electrons. Note, that we restrict us here for simplicity to on-site interactions. In general also nearest-neighbor or even longer range interactions can be treated in similar way, as we will show for the extended Hubbard model on the checkerboard lattice in Sec. 3.6.2. The single-orbital Hubbard model in a system with several sites in a unit cell is obtained by the choice $V^{iji'j'} = U\delta_{ij}\delta_{ii'}\delta_{ij'}$. If a system has only one atomic site per unit cell with several symmetry related orbitals, e.g., the three t_{2g} orbitals, the interaction (1.3) contains in addition to the intra-orbital Coulomb repulsion, U, also an inter-orbital Coulomb repulsion, $U'\delta_{ij'}\delta_{ji'}$, a Hund's coupling term, $J_{\text{H}}\delta_{ii'}\delta_{jj'}$, and a pair hopping term, $J'\delta_{ij}\delta_{i'j'}$.[f] As the interaction is local it leads to a momentum independent interaction in reciprocal space. In the basis of the single-particle states $c_{\mathbf{k}i\sigma}$ the interaction Hamiltonian, H_{Int}, simply reads as

$$H_{\text{Int}} = \frac{1}{2N} {\sum_{\mathbf{k}_1 \ldots \mathbf{k}_4}}' \sum_{ij} \sum_{i'j'} \sum_{\sigma\sigma'} V^{iji'j'} c^{\dagger}_{\mathbf{k}_1 i\sigma} c^{\dagger}_{\mathbf{k}_2 j\sigma'} c_{\mathbf{k}_3 i'\sigma'} c_{\mathbf{k}_4 j'\sigma}. \tag{1.4}$$

Due to the translational symmetry of the interaction the sum over the momenta is restricted, i.e., the vector $\mathbf{k}_1 + \mathbf{k}_2 - \mathbf{k}_3 - \mathbf{k}_4$ must be a reciprocal lattice vector, which is indicated by the prime over the sum. We assume that the typical interaction energies of H_{Int} are much smaller than a typical bandwidth of the quadratic Hamiltonian, H_0. It is therefore convenient to express the interaction Hamiltonian, H_{Int}, in terms of the operators $\gamma_{\mathbf{k}\mu\sigma}$ that describe the eigenstates of H_0. This transformation leads to a momentum dependence of the interaction Hamiltonian.

$$H_{\text{Int}} = \frac{1}{2N} {\sum_{\mathbf{k}_1 \ldots \mathbf{k}_4}}' \sum_{\mu\nu} \sum_{\mu'\nu'} \sum_{\sigma\sigma'} V^{\mu\nu\mu'\nu'}_{\mathbf{k}_1 \ldots \mathbf{k}_4} \gamma^{\dagger}_{\mathbf{k}_1\mu\sigma} \gamma^{\dagger}_{\mathbf{k}_2\nu\sigma'} \gamma_{\mathbf{k}_3\mu'\sigma'} \gamma_{\mathbf{k}_4\nu'\sigma} \tag{1.5}$$

$$V^{\mu\nu\mu'\nu'}_{\mathbf{k}_1 \ldots \mathbf{k}_4} = \sum_{ij} \sum_{i'j'} O^{\mu i}_{\mathbf{k}_1} O^{\nu j}_{\mathbf{k}_2} O^{\mu' i'}_{\mathbf{k}_3} O^{\nu' j'}_{\mathbf{k}_4} V^{iji'j'} \tag{1.6}$$

Such a multi-orbital Hubbard model is generally far too complicated for a fully-fledged analytical treatment. A first substantial simplification can be achieved

[f] It is of course also possible to describe the general situation with several atomic sites per unit cell and several different orbitals on each site within this formalism.

by restricting the system to a single band model. In general several bands $\xi^{\mu}_{\mathbf{k}}$ will cross the Fermi energy and it will not be possible to choose one single band, μ. However, it is possible to assign to every point $\mathbf{k}$ of the Brillouin zone a band index $\nu_{\mathbf{k}}$ by the implicit definition

$$\xi^{\nu_{\mathbf{k}}}_{\mathbf{k}} = \min_{\nu} |\xi^{\nu}_{\mathbf{k}}|. \tag{1.7}$$

If the different sheets (or lines) of the Fermi surface are well separated and if we assume that the interaction is weak we can restrict our attention to the Hilbert space spanned by the operators $\gamma^{\dagger}_{\mathbf{k}\nu_{\mathbf{k}}\sigma}$ and still correctly describe the low-energy physics of the system. We can now introduce the single-band notation as follows

$$\xi_{\mathbf{k}} = \xi^{\nu_{\mathbf{k}}}_{\mathbf{k}}, \quad \gamma_{\mathbf{k}\sigma} = \gamma_{\mathbf{k}\nu_{\mathbf{k}}\sigma}, \quad \text{and} \quad V_{\mathbf{k}_1\ldots\mathbf{k}_4} = V^{\nu_{\mathbf{k}_1}\ldots\nu_{\mathbf{k}_4}}_{\mathbf{k}_1\ldots\mathbf{k}_4} \tag{1.8}$$

and write down a single-band Hamiltonian

$$H_{\mathrm{sb}} = \sum_{\mathbf{k}\sigma} \xi_{\mathbf{k}}\, \gamma^{\dagger}_{\mathbf{k}\sigma}\gamma_{\mathbf{k}\sigma} + \frac{1}{2N} {\sum_{\mathbf{k}_1\ldots\mathbf{k}_4}}' \sum_{\sigma\sigma'} V_{\mathbf{k}_1\ldots\mathbf{k}_4}\, \gamma^{\dagger}_{\mathbf{k}_1\sigma}\gamma^{\dagger}_{\mathbf{k}_2\sigma'}\gamma_{\mathbf{k}_3\sigma'}\gamma_{\mathbf{k}_4\sigma}. \tag{1.9}$$

Provided that the interactions are weak enough this single-band Hamiltonian, H_{sb}, reproduces the low-energy physics of the original system accurately. We showed that in weak coupling a single band description of a multi-band model is possible. The momentum independent local interaction of the original Hamiltonian will however acquire a momentum dependence in the single-band Hamiltonian.

In certain cases, it is however possible to describe the momentum dependent interaction approximately by a few constants. In a 1D system for example the Fermi surface consists of a discrete set of points. For each of the four vectors $\mathbf{k}_l$ in Eq. (1.6) we can associate the closest Fermi point and denote it with $\mathbf{k}_{\mathrm{F}l}$. For weak coupling the Eq. (1.6) can be approximated by

$$V^{\mu\nu\mu'\nu'}_{\mathbf{k}_1\ldots\mathbf{k}_4} = \sum_{ij}\sum_{i'j'} O^{\mu i}_{\mathbf{k}_{\mathrm{F}1}} O^{\nu j}_{\mathbf{k}_{\mathrm{F}2}} O^{\mu' i'}_{\mathbf{k}_{\mathrm{F}3}} O^{\nu' j'}_{\mathbf{k}_{\mathrm{F}4}} V^{iji'j'}. \tag{1.10}$$

This procedure was carried out for the 1D kagomé strip in Sec. 3.6.1. In higher dimensions a similar simplification is sometimes possible. For example if the Fermi surface consists of individual hole or electron pockets, we can again associate to each vector $\mathbf{k}_l$ the closest pocket center $\mathbf{k}_{\mathrm{F}l}$ and find again through Eq. 1.10 an effective interaction that does only depend on a few constants. In Chapter 2 we show an application of this method to the 2D multi-orbital system of a CoO_2 plane.

In the special case where two bands $\xi^{\mu}_{\mathbf{k}}$ and $\xi^{\nu}_{\mathbf{k}}$ are symmetric about the Fermi energy, i.e., if $\xi^{\mu}_{\mathbf{k}} = \pm\xi^{\nu}_{\mathbf{k}}$, the association of a single band index to every vector in the Brillouin zone as described in Eq. 1.7 is not possible. This situation occurs for example in the 2D kagomé lattice at 1/3-filling. The derivation of a single-band model is not possible in this case, but we show in Sec. 3.6.3 how an effective two-band model can be derived from the original three-band model.

The single-band Hamiltonian derived in this way possesses still the full symmetry of the system[g] and does therefore not allow to detect the occurrence of a spontaneous symmetry breaking. The mean-field approximation provides a simple and widely applicable method for the detection and the description of phases with spontaneously broken symmetry. As this thesis contains several different mean-field approaches we provide in the following section an outline of the standard mean-field analysis for a general single-band electronic lattice model.

1.3 From the single-band model to the mean-field model

The theoretical analysis of the single-band model, although much simpler than the multi-band model, is still a formidable challenge. An often used and rather drastic simplification of the problem can be achieved by the mean-field approximation. The mean-field theory is well suited to detect phases with spontaneously broken symmetry where operators, whose expectation values are identically zero for finite systems due to symmetry, acquire a finite expectation value in the thermodynamic limit. The symmetry group of the system is spontaneously reduced to a subgroup and the different subgroups characterize the various possible phases. According to the presence or absence of the global U(1) symmetry that guarantees the particle number conservation of the Hamiltonian (1.1)[h] one distinguishes between particle-hole and particle-particle instabilities, respectively. The basic idea of the mean-field theory is the assumption that the ground state can be reasonably well described by a Slater determinant, i.e., that the ground state of the interacting system can be approximated by the

[g] As the energy of the non-interacting state is the only selection criterion for the low-energy subspace, this subspace and the restriction of the Hamiltonian to this subspace are invariant under all symmetry operations of the system.

[h] H_0 and H_{Int} are invariant under the global gauge transformation $c_{\mathbf{r}i\sigma} \to \mathrm{e}^{\mathrm{i}\varphi} c_{\mathbf{r}i\sigma}$.

ground state, $|\psi\rangle$, of a non-interacting (quadratic) Hamiltonian. In the ground state $|\psi\rangle$ the expectation value of an operator can be evaluated by applying the Wick theorem, e.g., the expectation value of the interaction term in the single-band model of Eq. (1.9) model is given by

$$V_0 = \frac{1}{2N} {\sum_{\mathbf{k}_1 \ldots \mathbf{k}_4}}' \sum_{\sigma\sigma'} V_{\mathbf{k}_1 \ldots \mathbf{k}_4} \Big(\underbrace{\gamma^\dagger_{\mathbf{k}_1\sigma} \gamma^\dagger_{\mathbf{k}_2\sigma'} \gamma_{\mathbf{k}_3\sigma'} \gamma_{\mathbf{k}_4\sigma}} - \underbrace{\gamma^\dagger_{\mathbf{k}_1\sigma} \gamma_{\mathbf{k}_3\sigma'} \gamma^\dagger_{\mathbf{k}_2\sigma'} \gamma_{\mathbf{k}_4\sigma}} + + \underbrace{\gamma^\dagger_{\mathbf{k}_1\sigma} \gamma_{\mathbf{k}_4\sigma} \gamma^\dagger_{\mathbf{k}_2\sigma'} \gamma_{\mathbf{k}_3\sigma'}} \Big), \tag{1.11}$$

where the operators that are connected by a brace stand for the ground-state expectation values of these operators, e.g., $\underbrace{\gamma^\dagger_{\mathbf{k}_1\sigma} \gamma^\dagger_{\mathbf{k}_2\sigma'}} = \langle\psi|\gamma^\dagger_{\mathbf{k}_1\sigma} \gamma^\dagger_{\mathbf{k}_2\sigma'}|\psi\rangle$. The mean-field Hamiltonian

$$H_{\mathrm{MF}} = \sum_{\mathbf{k}\sigma} \xi_{\mathbf{k}} \gamma^\dagger_{\mathbf{k}\sigma} \gamma_{\mathbf{k}\sigma} + \frac{1}{2N} {\sum_{\mathbf{k}_1 \ldots \mathbf{k}_4}}' \sum_{\sigma\sigma'} V_{\mathbf{k}_1 \ldots \mathbf{k}_4} O^{\mathbf{k}_1 \ldots \mathbf{k}_4}_{\sigma\sigma'} - V_0 \tag{1.12}$$

$$O^{\mathbf{k}_1 \ldots \mathbf{k}_4}_{\sigma\sigma'} = \Big(\underbrace{\gamma^\dagger_{\mathbf{k}_1\sigma} \gamma^\dagger_{\mathbf{k}_2\sigma'} \gamma_{\mathbf{k}_3\sigma'} \gamma_{\mathbf{k}_4\sigma}} - \underbrace{\gamma^\dagger_{\mathbf{k}_1\sigma} \gamma_{\mathbf{k}_3\sigma'} \gamma^\dagger_{\mathbf{k}_2\sigma'} \gamma_{\mathbf{k}_4\sigma}} + \underbrace{\gamma^\dagger_{\mathbf{k}_1\sigma} \gamma_{\mathbf{k}_4\sigma} \gamma^\dagger_{\mathbf{k}_2\sigma'} \gamma_{\mathbf{k}_3\sigma'}} + \mathrm{h.c.} \Big)$$

has by construction the same expectation value in the ground state $|\psi\rangle$ as the original Hamiltonian (1.9).[i] The Hamiltonian H_{MF} is quadratic and if we replace the braced operators by a given set of complex numbers, we can diagonalize H_{MF} by a Bogoliubov transformation, calculate the expectation values of the braced operators in this ground state and use these values as a new set of complex numbers or mean-fields. This procedure can be iterated until a self-consistent set of mean-fields is found. The ground-state energy of the Hamiltonian H_{MF} is extremal with respect to all mean-fields for a self-consistent set of mean-fields. This follows directly from (1.12) and from the Feynman-Hellman theorem. If several self-consistent solutions exist the one with the lowest energy is chosen. If the ground-state does not break any of the symmetries of the system, i.e., if it is invariant (up to a phase) under all symmetry transformations, most of the mean-fields are identically zero. The non-vanishing mean-fields only renormalize $\xi_{\mathbf{k}}$ in the Hamiltonian (1.9) and will not produce any spectacular effect. In weak-coupling, these mean-fields can even be neglected. In the following we will focus on the different types of symmetry breaking mean-fields. Three different categories of symmetry breaking mean-fields can be distinguished:

[i] We used the properties $V_{\mathbf{k}_1\mathbf{k}_2\mathbf{k}_3\mathbf{k}_4} = V_{\mathbf{k}_2\mathbf{k}_1\mathbf{k}_4\mathbf{k}_3} = V_{\mathbf{k}_4\mathbf{k}_3\mathbf{k}_2\mathbf{k}_1}$ that follow from the commutation relations and from Hermicity.

- *Superconducting mean-fields* are finite expectation values of $\gamma_{\mathbf{k}+\mathbf{q},\sigma'}\gamma_{-\mathbf{k}\sigma}$ for a fixed value of $\mathbf{q}$. They break (at least) the $U(1)$ gauge symmetry. In the so-called Cooper channel the total momentum of the particle pair, $\mathbf{q}$, vanishes. The rather special case of finite $\mathbf{q}$ is called Fulde-Ferrell-Larkin-Ovchinnikov pairing state and might be present in systems with broken time-reversal symmetry. For the case where only superconducting symmetry breaking mean-fields with momentum $\mathbf{q}$ are finite it is possible to write down a reduced Hamiltonian that produces the same mean-field behavior. This Hamiltonian only keeps a single channel of the interaction in the original Hamiltonian (1.9) and is given by

$$H_{\mathrm{SC}} = \sum_{\mathbf{k}\sigma} \xi_{\mathbf{k}}\, \gamma^{\dagger}_{\mathbf{k}\sigma}\gamma_{\mathbf{k}\sigma} + \frac{1}{2N}\sum_{\mathbf{k}\mathbf{k}'}\sum_{\sigma\sigma'} V^{\mathrm{SC}}_{\mathbf{k}\mathbf{k}'}\, \gamma^{\dagger}_{-\mathbf{k}\sigma}\gamma^{\dagger}_{\mathbf{k}+\mathbf{q},\sigma'}\gamma_{\mathbf{k}'+\mathbf{q},\sigma'}\gamma_{-\mathbf{k}'\sigma}, \quad (1.13)$$

with $V^{\mathrm{SC}}_{\mathbf{k}\mathbf{k}'} = V_{-\mathbf{k},\mathbf{k}+\mathbf{q},\mathbf{k}'+\mathbf{q},-\mathbf{k}'}$. In comparison to the original interaction the sum over three independent momenta has been reduced to a sum over two independent momenta, i.e., only an infinitesimal part of the terms in the original interaction Hamiltonian is kept in the mean-field analysis, but this infinitesimal fraction of terms can still provide an extensive contribution to the ground-state energy.

In the following discussion we set $\mathbf{q} = 0$ as this is by far the most important case and because in this case the Hamiltonian (1.13) is invariant under all symmetry transformations of the original Hamiltonian (1.9). $V^{\mathrm{SC}}_{\mathbf{k}\mathbf{k}'}$ is invariant under the exchange of $\mathbf{k}$ and $\mathbf{k}'$ and under a simultaneous sign change of $\mathbf{k}$ and $\mathbf{k}'$ but, in general, $V^{\mathrm{SC}}_{\mathbf{k}\mathbf{k}'}$ is not invariant under a sign change of a single vector. This invites to the decomposition $V^{\mathrm{SC}}_{\mathbf{k}\mathbf{k}'} = V^{\mathrm{SC,s}}_{\mathbf{k}\mathbf{k}'} + V^{\mathrm{SC,t}}_{\mathbf{k}\mathbf{k}'}$.[j] The even part, $V^{\mathrm{SC,s}}_{\mathbf{k}\mathbf{k}'}$, leads to singlet pairing and the odd part, $V^{\mathrm{SC,t}}_{\mathbf{k}\mathbf{k}'}$, to triplet pairing. For $\mathbf{q} = 0$ we have $V^{\mathrm{SC}}_{\mathcal{R}(\mathbf{k})\mathcal{R}(\mathbf{k}')} = V^{\mathrm{SC}}_{\mathbf{k}\mathbf{k}'}$ for all point group symmetry operations $\mathcal{R}$. From this invariance follows that $V^{\mathrm{SC}}_{\mathbf{k}\mathbf{k}'}$ must be a linear combination of the invariants associated with each point group representation and that it can be written as

$$V^{\mathrm{SC}}_{\mathbf{k}\mathbf{k}'} = \sum_{j}\sum_{\alpha} V^{j\alpha}_{\mathbf{k}\mathbf{k}'} \quad \text{with} \quad V^{j\alpha}_{\mathbf{k}\mathbf{k}'} = \sum_{s} \lambda^{j\alpha} f^{j\alpha}_{s}(\mathbf{k}) \bar{f}^{j\alpha}_{s}(\mathbf{k}'). \quad (1.14)$$

where the index j runs over all irreducible point group representations and $f^{j\alpha}_{s}(\mathbf{k})$ is a set of basis functions for the representation j. The index

[j] $V^{\mathrm{SC,s}}_{\mathbf{k}\mathbf{k}'} = (V^{\mathrm{SC}}_{\mathbf{k}\mathbf{k}'} + V^{\mathrm{SC}}_{-\mathbf{k}\mathbf{k}'})/2$ and $V^{\mathrm{SC,t}}_{\mathbf{k}\mathbf{k}'} = (V^{\mathrm{SC}}_{\mathbf{k}\mathbf{k}'} - V^{\mathrm{SC}}_{-\mathbf{k}\mathbf{k}'})/2$.

s runs from 1 to the dimension of the representation j. As there might be different basis functions for a given representation we need the additional index α that runs over the different realizations of the representation j. This is similar to atomic physics where there are also different types of s orbitals. On the hypercubic lattice, e.g., we have the functions $f(\mathbf{k}) = 1$ and $f(\mathbf{k}) = \sum_i \cos k_i$ as different functions for the trivial representation. The former is called s-wave and describes local pairing and the latter is usually called extended s-wave and describes nearest-neighbor pairing. The coefficients $\lambda^{j\alpha}$ are called coupling constants. If the point group contains the inversion symmetry the decomposition (1.14) is compatible with the singlet triplet decomposition. A spontaneous symmetry breaking can only occur in the channels where the coupling constant $\lambda^{j\alpha}$ is attractive, i.e., $\lambda^{j\alpha} < 0$.[k] The self-consistency requirement of the mean-field calculation can be translated into a gap equation. The linearized version of the gap equation allows to determine the critical temperature given by $T_c = \max_j T_c^j$. T_c^j is defined as the lowest temperature where the equation $g(\mathbf{k}) = -\sum_{\alpha s} \lambda^{j\alpha} f_s^{j\alpha}(\mathbf{k}) \langle f_s^{j\alpha}, g \rangle_T$ has a non-trivial solution, g. For $\xi_{\mathbf{k}} = \xi_{-\mathbf{k}}$ the temperature dependent scalar product is defined as

$$\langle f, g \rangle_T = \frac{1}{N} \sum_{\mathbf{k}} \bar{f}(\mathbf{k}) g(\mathbf{k}) \frac{\tanh(\xi_{\mathbf{k}}/2T)}{2\xi_{\mathbf{k}}}, \tag{1.15}$$

which diverges logarithmically at low temperatures (Cooper instability). If only one type of representation, j, exists in $V_{\mathbf{k}\mathbf{k}'}^{\mathrm{SC}}$ the definition of the T_c^j reduces to $1 = -\lambda^j \langle f_s^j, f_s^j \rangle_{T_c^j}$ which is independent of s.

It is possible that superconducting mean-fields corresponding to two different point group representations, e.g., s-wave and d-wave, are simultaneously finite in the ground state. These systems do however not only break the U(1) gauge symmetry, but the symmetry group of the system will be reduced such that the combination of the different representations is again a representation of the reduced symmetry group. Therefore, such a ground-state is separated from the high-temperature phase with full symmetry by two phase transitions.

For a single-band model derived from a multi-band model as described in the previous section a spontaneous superconducting instability in such

[k] Note that the interaction is a sum over terms of the form $\lambda^{j\alpha} A_{j\alpha}^\dagger A_{j\alpha}$ and the expectation value of such a term has the same sign as $\lambda^{j\alpha}$.

a mean-field analysis is generally not expected. As the original Coulomb interaction is repulsive the electrons do not easily form bound states, i.e., most of the superconducting channels described above will be repulsive. It can not be excluded that an attractive channel exists, e.g., a large Hund's coupling term could produce a spontaneous superconducting instability with triplet pairing, but in most cases the bare Coulomb interaction will not be sufficient for the mean-field description of the superconductor. In the spin-fluctuation theory for the high-T_c superconductors the bare Coulomb interaction is replaced by an effective interaction, and $V^{\mathrm{SC}}_{\mathbf{k}\mathbf{k}'}$ contains a term which is roughly proportional to the spin correlation function $\chi(\mathbf{k}-\mathbf{k}')$. This term that has a pronounced maximum at $\mathbf{k}-\mathbf{k}'=(\pi,\pi)$ allows for a d-wave mean-field instability.

- *Charge density wave (CDW) mean-fields* are finite expectation values of $\sum_\sigma \gamma^\dagger_{\mathbf{k}+\mathbf{q},\sigma}\gamma_{\mathbf{k}\sigma}$ for a fixed value of $\mathbf{q}$. They can be viewed as pairing amplitudes in the particle-hole channel whereas superconductivity is produced by pairing in the particle-particle channel. As in the superconducting case it is possible to write down a reduced Hamiltonian for the CDW instabilities that produces the same mean-field behavior. It is given by

$$H_{\mathrm{CDW}} = \sum_{\mathbf{k}\sigma} \xi_{\mathbf{k}}\, \gamma^\dagger_{\mathbf{k}\sigma}\gamma_{\mathbf{k}\sigma} + \frac{1}{4N}\sum_{\mathbf{k}\mathbf{k}'}\sum_{\sigma\sigma'} V^{\mathrm{CD}}_{\mathbf{k}\mathbf{k}'}\, \gamma^\dagger_{\mathbf{k}\sigma}\gamma_{\mathbf{k}+\mathbf{q},\sigma}\gamma^\dagger_{\mathbf{k}'+\mathbf{q},\sigma'}\gamma_{\mathbf{k}'\sigma'} \quad (1.16)$$

with $V^{\mathrm{CD}}_{\mathbf{k}\mathbf{k}'} = 2V_{\mathbf{k},\mathbf{k}'+\mathbf{q},\mathbf{k}',\mathbf{k}+\mathbf{q}} - V_{\mathbf{k},\mathbf{k}'+\mathbf{q},\mathbf{k}+\mathbf{q},\mathbf{k}'}$. The CDW instability breaks translational symmetry. If the vector $\mathbf{q}$ is not a high-symmetry point of the Brillouin zone that is invariant under all point group symmetries (like the point (π,π) for the square lattice), the point group of (1.16) is smaller than the original point group. With respect to this reduced point group a symmetry decomposition of $V^{\mathrm{CD}}_{\mathbf{k}\mathbf{k}'}$ can be done as in Eq. (1.14). Note, that CDW phases with even and with odd form factors $f^{j\alpha}_s(\mathbf{k})$ are possible.

  The critical temperature of the CDW instability can be calculated in the same way as for the superconducting instability. Only the temperature dependent scalar product has to be redefined as

$$\langle f,g\rangle_T = \frac{1}{N}\sum_{\mathbf{k}} \bar{f}(\mathbf{k})g(\mathbf{k})\frac{f^{\mathrm{F}}_{\mathbf{k}+\mathbf{q}} - f^{\mathrm{F}}_{\mathbf{k}}}{\xi_{\mathbf{k}} - \xi_{\mathbf{k}+\mathbf{q}}}, \quad (1.17)$$

  where $f^{\mathrm{F}}_{\mathbf{k}} = (\mathrm{e}^{\xi_{\mathbf{k}}/T}+1)^{-1}$ is the Fermi function. Note, that for constant functions (f=g=1) the scalar product is given by the susceptibility

$\chi^0_{\mathbf{q}}$ and the critical temperature is determined by the Stoner criterion $1 = -\lambda^j \chi^0_{\mathbf{q}}$. The susceptibility $\chi^0_{\mathbf{q}}$ is generally not diverging at low temperatures. However, if the nesting condition $\xi_{\mathbf{k}+\mathbf{q}} = -\xi_{\mathbf{k}}$ is satisfied the scalar product (1.17) reduces to the logarithmically diverging scalar product of Eq. (1.15).

The variety of CDW order parameters is very rich, especially if the form factor is non-trivial: Staggered flux phases (e.g., *d*-density waves) as well as bond order waves can be understood within this formalism as CDW phases. Starting from the repulsive Coulomb interaction we do not expect to generate spontaneously a charge modulation and in fact we generally obtain repulsive interaction in the mean-field Hamiltonians. If the original interaction contains not only on-site but also nearest-neighbor repulsion the CDW instabilities can occur spontaneously. In Sec. 3.6.2 we show applying the procedure described above that for the checkerboard lattice a CDW (or bond order wave) instability occurs.

But also from purely on-site Coulomb interactions it is possible to obtain attractive CDW coupling constants as we show in Chapter 2 for the multi-orbital model of Na_xCoO_2. However, the CDW coupling constants are not as attractive as the coupling constants of the spin density waves that we discuss now.

- *Spin density wave (SDW) mean-fields* are finite expectation values of $(\gamma^\dagger_{\mathbf{k}+\mathbf{q},\uparrow}\gamma_{\mathbf{k}\uparrow} - \gamma^\dagger_{\mathbf{k}+\mathbf{q},\downarrow}\gamma_{\mathbf{k}\downarrow})$ for a fixed value of $\mathbf{q}$.[1] The SDW Hamiltonian can be written as

$$H_{\mathrm{SDW}} = \sum_{\mathbf{k}\sigma} \xi_{\mathbf{k}}\, \gamma^\dagger_{\mathbf{k}\sigma}\gamma_{\mathbf{k}\sigma} + \frac{1}{4N} \sum_{\mathbf{k}\mathbf{k}'} \sum_{\sigma\sigma'} V^{\mathrm{SD}}_{\mathbf{k}\mathbf{k}'}\, \sigma\sigma' \gamma^\dagger_{\mathbf{k}\sigma}\gamma_{\mathbf{k}+\mathbf{q},\sigma}\gamma^\dagger_{\mathbf{k}'+\mathbf{q},\sigma'}\gamma_{\mathbf{k}'\sigma'} \quad (1.18)$$

with $V^{\mathrm{SD}}_{\mathbf{k}\mathbf{k}'} = -V_{\mathbf{k},\mathbf{k}'+\mathbf{q},\mathbf{k}+\mathbf{q},\mathbf{k}'}$. As we selected one of the three equivalent SDW order parameters the Hamiltonian (1.18) is not invariant under SU(2) transformations. The potential $V^{\mathrm{SD}}_{\mathbf{k}\mathbf{k}'}$ can be decomposed as in (1.14) according to the representations of the point group of the Hamiltonian (1.18) which might be reduced for a finite vector $\mathbf{q}$ and the critical temperature can be determined in the same way as for the CDW instabilities. The variety of the SDW phases is again very rich and ranges

[1] Due to the SU(2) invariance of our system we could equivalently choose $(\gamma^\dagger_{\mathbf{k}+\mathbf{q},\uparrow}\gamma_{\mathbf{k}\downarrow} + \gamma^\dagger_{\mathbf{k}+\mathbf{q},\downarrow}\gamma_{\mathbf{k}\uparrow})$ or $\mathrm{i}(\gamma^\dagger_{\mathbf{k}+\mathbf{q},\uparrow}\gamma_{\mathbf{k}\downarrow} - \gamma^\dagger_{\mathbf{k}+\mathbf{q},\downarrow}\gamma_{\mathbf{k}\uparrow})$ for a discussion of the SDW states.

from a normal ferromagnet ($\mathbf{q} = 0$) over antiferromagnetic phases to the exotic phases containing staggered spin currents. Apart from the SU(2) symmetry these phases usually break also time-reversal symmetry except for the spin-current phases where time-reversal symmetry is broken in the corresponding CDW phase. Due to the global minus sign in the definition of $V^{\mathrm{SD}}_{\mathbf{k}\mathbf{k}'}$ the SDW coupling constants are usually attractive. In Chapter 2 a discussion of several SDW states for Na_xCoO_2 with attractive coupling constants is presented

The method described in this and in the previous section is a valuable approach for a system with several electronic degrees of freedom in a single unit cell. If the quadratic Hamiltonian, H_0, is simple enough it is possible to derive the single-band model analytically and to present it in a closed and explicit form. In this way, the complexity of the problem can be reduced substantially and the single band model can either be analyzed by the standard mean-field treatment described above or can be studied by more sophisticated numerical or analytical techniques. In any case, the mean-field analysis of the direct (zeroth-order) interaction provides important information about the dominant fluctuations in the system. It is however important to remember, that these fluctuations lead to effective interactions that might trigger also instabilities that are not detectable directly in mean-field, e.g., a mean-field analysis of the Hubbard can directly detect the antiferromagnetic fluctuations, but only after including antiferromagnetic interactions in the Hamiltonian, superconductivity can be obtained from the mean-field calculation.

Seite Leer /
Blank leaf

Chapter 2

Effective Interaction between the Inter-Penetrating Kagomé Lattices in Na_xCoO_2

2.1 Introduction

The layered Na_xCoO_2 has been initially studied for its extraordinary thermoelectric properties and for its interesting dimensional crossover [22–25]. But recently wider attention has been triggered by the discovery of superconductivity in hydrated $Na_{0.35}CoO_2$ and the discovery of an insulating phase in $Na_{0.5}CoO_2$ [6, 26–28]. Since then, various types of charge ordering phenomena in Na_xCoO_2 have been reported [29–43], but also strong spin-fluctuations and spin density wave transitions have been observed [7, 8, 44–56].

The structure of the material of Na_xCoO_2 is shown in Fig. 2.1. It consists of CoO_2-layers where Co-ions are enclosed in edge-sharing O-octahedra. These layers alternate with the Na-ion layers with Na entering as Na^{1+} and donating one electron each to the CoO_2-layer. Due to the crystal field splitting produced by the O-octahedra, the Co $3d$ orbitals are split into the lower t_{2g} orbitals and the higher e_g orbitals. Local density approximation (LDA) calculations show that the t_{2g} bands are clearly separated from the higher e_g bands and from the lower oxygen p bands. The total bandwidth of the t_{2g} band is 1.6 eV [57], and the Fermi energy lies close to the top of the t_{2g} bands. Note, that the formal valence of the Co-ions is $(4-x)+$, and that a Co^{3+} ion has a completely filled t_{2g} shell, such that $x = 1$ and $x = 0$ correspond to a band-insulating and

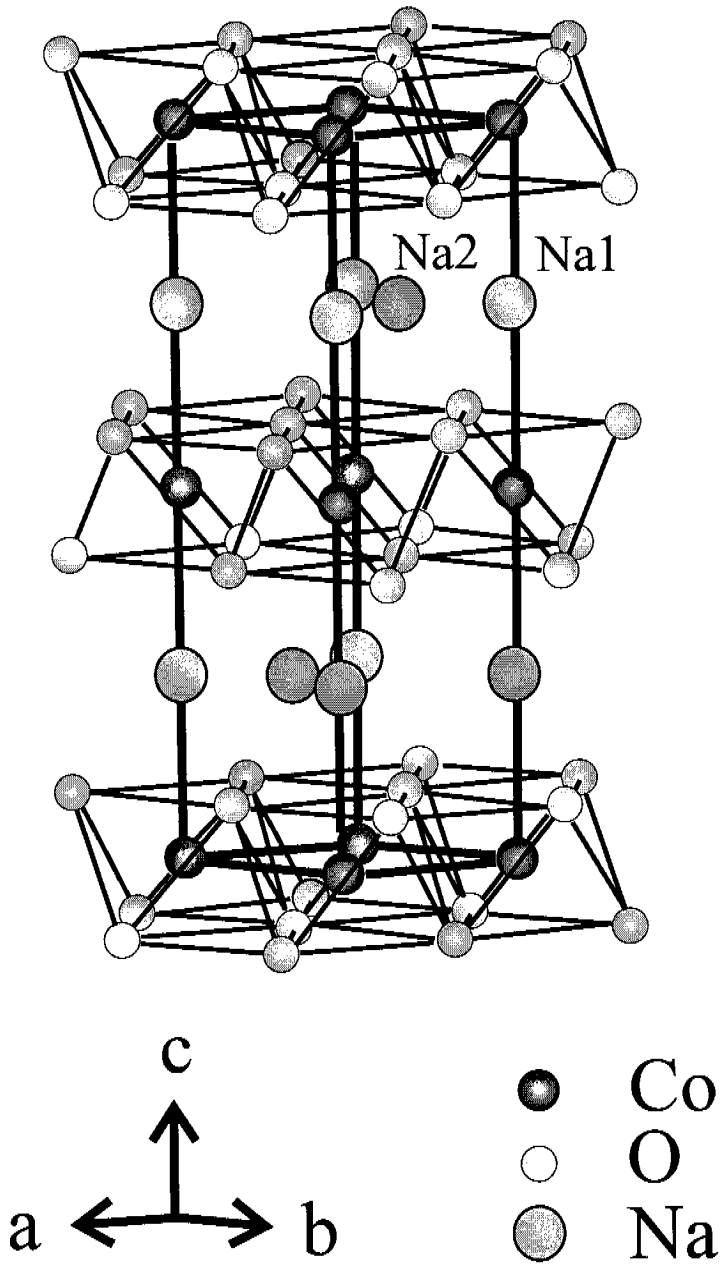

Figure 2.1: The structure of Na_xCoO_2 can be viewed as close-packed stacking of triangular layers. The stacking within a unit cell is given by $A_O{-}B_{Co}{-}C_O{-}(A,B)_{Na}{-}C_O{-}B_{Co}{-}A_O{-}(B,C)_{Na}$, where the letters A, B, and C denote the three different types of triangular layers. The Na positions are only partially occupied and neighboring Na1 and Na2 sites can not be simultaneously occupied. The Co-ions are coordinated by edge-sharing oxygen octahedra.

a Mott-insulating filling, respectively. The electronic properties are therefore dominated by the $3d$-t_{2g} electrons of the Co-ions which form a two-dimensional triangular lattice. However, the spatial arrangement of the Na^{1+}-ions plays a crucial role too for the physics of this material. There are two basic positions for the Na-ions, one directly above or below a Co-site and another in a center position of a triangle spanned by the Co-lattice (cf. Fig. 2.1). The metallic properties are unusual and vary with the Na-concentration and arrangement.

A brief overview of the present knowledge of the phase diagram of Na_xCoO_2 shown in Fig. 2.2 leads to following still rough picture. The most salient and robust feature, at first sight is the charge ordered phase for $x = 0.5$ separating the Na-poor from the Na-rich system. At this particular filling the Na-ions arrange along zig-zag chains already at 100 K, reducing the crystal symmetry from hexagonal to orthorhombic [29]. This Na pattern might induce also the magnetic transition at $T_X = 88$ K and the metal-insulator transition at $T_{MI} = 53$ K, which could be clearly identified by magnetic resonance, transport and susceptibility measurements [7]. Neutron scattering measurements propose that the magnetic instability leads to an antiferromagnetic structure with rows of ordered and non-ordered Co-ions where the ordered ions have staggered inplane magnetic moments [58, 59].

On the Na-poor side ($x < 0.5$) the compound behaves like a paramagnetic metal. When it is intercalated with H_2O superconductivity appears at about 5 K between $x \approx 0.25$ and $x \approx 0.35$. The symmetry of the superconducting order parameter is not yet clarified, but it is probably unconventional and maybe even spin triplet superconductivity [60].

On the Na-rich side one finds a so-called Curie-Weiss metal. Here the magnetic susceptibility displays a pronounced Curie-Weiss-like behavior after subtracting an underlying temperature independent part: $\chi = C/(T-\Theta)$ where Θ ranges roughly between -50 K and -200 K depending on x, and the Curie constant is consistent with a magnetic moment in the range of (1- 1.7) μ_B per formula unit. Deviations from the Curie-Weiss behavior have been observed at low temperatures [61], and evidence for strong low-energy spin fluctuations that can be suppressed by a magnetic field have been reported [37]. A transition at high temperature $\sim$ 250 - 340 K has been observed and interpreted as charge ordering [35, 38, 48].

For even higher Na concentrations, $x > 0.75$, a magnetic transition occurs at 22 K, which is most likely a commensurate spin density wave [47–50]. Neutron scattering experiments find ferromagnetic correlations in the layers and

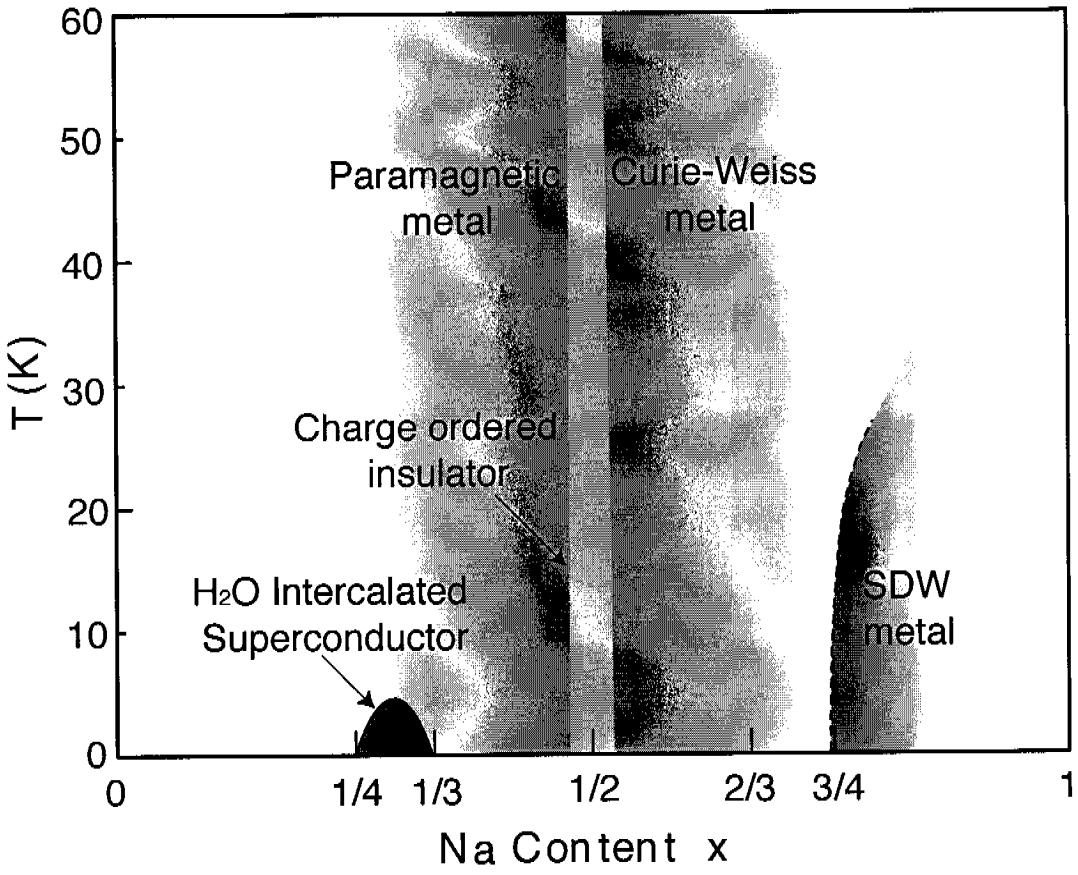

Figure 2.2: The phase diagram for Na_xCoO_2 from Ref. [27].

antiferromagnetic correlations perpendicular to the layers which is consistent with an A-type antiferromagnetic ordering. Furthermore they show that the magnetic fluctuations are highly three dimensional [45]. Interestingly, this magnetic phase is metallic and has even a higher mobility than the non-magnetic phase.

The arrangement of the Na-ions between the layers depends on the Na doping x and several superstructures have been found [29, 30]. The clearest evidence for the superstructure formation is at $x = 0.5$ where the Na-ordering leads to the metal-insulator transition at low temperatures [27, 28, 32]. But also away from $x = 0.5$, nuclear magnetic resonance (NMR) experiments indicate the existence of non equivalent cobalt sites and of nanoscopic phase separation [34, 36].

The complex interplay between Na-arrangement and the electronic prop-

erties poses an interesting problem. Various theoretical studies have mainly focused on single-band models on the frustrated triangular lattice, in particular in connection with the superconducting phase ignoring Na-potentials [62–68]. There is also work done on multi-orbital models [60, 69, 70] and density functional calculations have been performed [57, 71–77]. According to the LDA calculations the Fermi surface, which lies close to the top of the $3d$-t_{2g}-bands, forms a large hole-like Fermi surface of predominantly a_{1g} character. This result is in agreement with angle-resolved photoemission spectroscopy (ARPES) experiments [78–82]. In addition the LDA calculations suggest, that smaller hole pockets with mixed a_{1g} and e'_g character exist on the Γ-K direction on the Na-poor side, however, so far the existence of these pockets has not been confirmed with ARPES.

At the Γ point the states with a_{1g} and e'_g symmetry are clearly split, but on average over the entire Brillouin zone the mixing between a_{1g} and e'_g is substantial. Koshibae and Maekawa argued that the splitting at the Γ point originates from the cobalt-oxygen hybridization rather than from a crystal field effect due to the distortion of the oxygen octahedra, because the crystal field effect in a simple ionic picture would lead to the opposite splitting of the a_{1g} and e'_g states [69]. There is also spectral evidence, that the low-energy excitations of Na_xCoO_2 have significant O-$2p$ character [83]. Reproducing the LDA Fermi surface with a tight-binding fit for the cobalt t_{2g} orbitals, it turns out that the direct overlap integral between the cobalt orbitals is much smaller than the indirect hopping integral over the oxygen $2p$ orbitals [70]. Therefore, it is reasonable to start with a three band tight-binding model of degenerate t_{2g} orbitals, where the only hopping processes are indirect hopping processes over intermediate oxygen orbitals. This approximation provides an interesting system of four independent and inter-penetrating kagomé lattices as it was already pointed out by Koshibae and Maekawa [69].

Our study is based on this tight-binding model band structure which has a high symmetry. Within this model we examine various forms of order that could be possible from onsite Coulomb interaction. This chapter is organized as follows: In Sec. 2.2, the tight-binding model and the concepts of kagomé operators and pocket operators are introduced. In section 2.3 an effective Hamiltonian for the local Coulomb interaction is derived and in Sec. 2.4 this effective interaction is written in a diagonal form, by choosing an appropriate basis of SU(4) generators. Sec. 2.5 deals with the effects of small deviations from our simplified tight-binding model and in Sec. 2.6, all possible charge and

spin ordering patterns of our model and the corresponding phase transitions are shortly described. Sec. 2.7 contains a discussion of the relevance of the above described collective degrees of freedom to Na_xCoO_2 comparing the different coupling constants and by taking into account symmetry lowering effects and in Sec. 2.8 we apply our model to the Na-ordering observed at $x = 0.5$. Sec. 2.9 is dedicated to the local degrees of freedom (Wannier functions) in our model and Sec. 2.10 discusses the decoupling of the effective interaction into the possible superconducting channels. We summarize and conclude in Sec. 2.11. The major part of the results in this chapter are published in Ref. [84] and Ref. [85].

2.2 Tight-binding model

We base our model on the assumption that the $3d$-t_{2g} orbitals on the Co-ions are degenerate. Their electrons disperse only via π-hybridization with the intermediate oxygens occupying the surrounding octahedra (Fig. 2.3). As noticed by Koshibae and Maekawa the resulting electronic structure corresponds to a system of four decoupled equivalent electron systems of electrons hopping on a kagomé lattice [69]. The different sites of a kagomé lattice, however, are represented by different orbitals. Each of the three orbitals $\{d_{yz}, d_{zx}, d_{xy}\}$ on a given site participates in one kagomé lattice, and the fourth kagomé lattice has a void on this site. A schematic representation of how the t_{2g} orbitals on a triangular lattice are grouped into four kagomé lattices is shown in Fig. 2.4.

The corresponding tight-binding model has the following form,

$$H_{\mathrm{tb}} = \sum_{\mathbf{k}\sigma} \sum_{mm'} \epsilon_{\mathbf{k}}^{mm'} c_{\mathbf{k}m\sigma}^{\dagger} c_{\mathbf{k}m'\sigma}, \tag{2.1}$$

where $c_{\mathbf{k}m\sigma}^{\dagger} = \frac{1}{\sqrt{N}} \sum_{\mathbf{r}} \mathrm{e}^{\mathrm{i}\mathbf{k}\cdot\mathbf{r}} c_{\mathbf{r}m}^{\dagger}$ are the operators in momentum space of $c_{\mathbf{r}m\sigma}^{\dagger}$ which creates a t_{2g} orbital (d_{yz}, d_{zx}, d_{xy}) with index $m = 1, 2, 3$ and spin $\sigma = \uparrow, \downarrow$ on the cobalt-site $\mathbf{r}$. N is the number of Co-sites in the lattice. The matrix $\epsilon_{\mathbf{k}}^{mm'}$ is given by

$$\hat{\epsilon}_{\mathbf{k}} = \begin{pmatrix} -\mu & 2t\cos k_3 & 2t\cos k_2 \\ 2t\cos k_3 & -\mu & 2t\cos k_1 \\ 2t\cos k_2 & 2t\cos k_1 & -\mu \end{pmatrix}, \tag{2.2}$$

with $k_i = \mathbf{k} \cdot \mathbf{a}_i$, cf. Fig. 2.3. The hopping parameter $t = t_{pd}^2/\Delta > 0$, where t_{pd} is the hopping integral between the p_y and the d_{xy} or d_{yz} orbital shown in

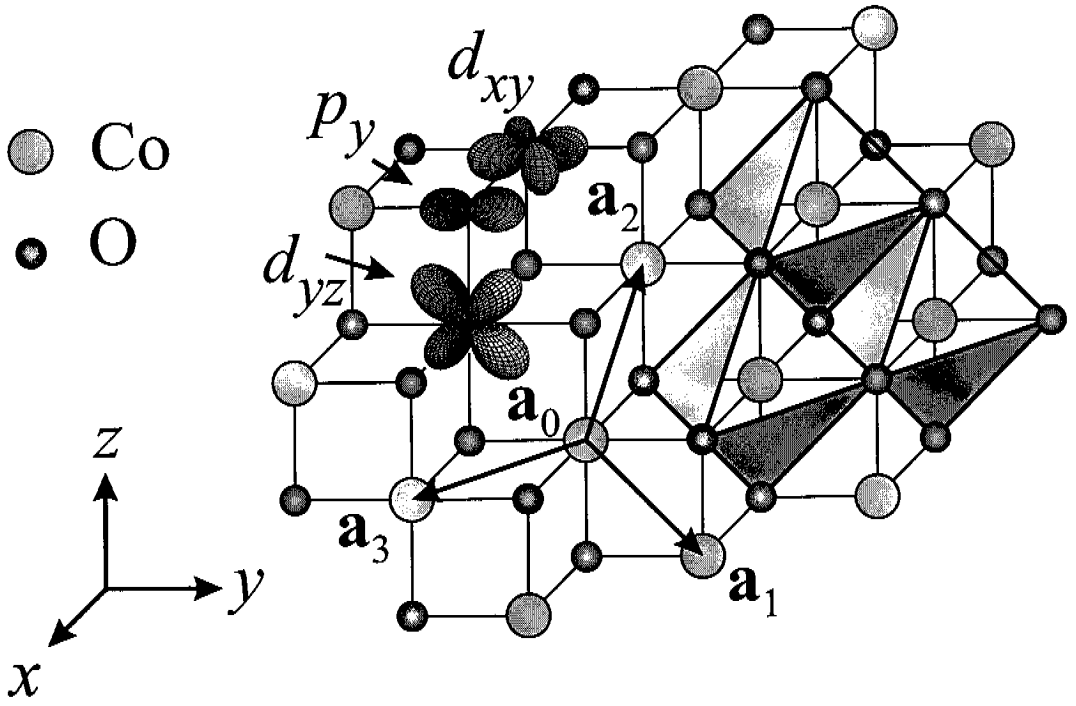

Figure 2.3: Schematic figure of a CoO_2 plane drawn with cubic unit cells. The edge-sharing of the oxygen octahedra around the Co-ions is visualized. The edges of the cubes are oriented along the coordinate system (x, y, z). The triangular lattice of the cobalt is spanned by the vectors $\mathbf{a}_1, \mathbf{a}_2, \mathbf{a}_3$. $(\mathbf{a}_1 + \mathbf{a}_2 = -\mathbf{a}_3)$. $a = |\mathbf{a}_i|$ is the lattice spacing. An oxygen $2p$ orbital and the cobalt t_{2g} orbitals hybridizing with it by π-hybridization are shown.

Fig. 2.3. Δ is the energy difference between the oxygen p and the Co-t_{2g} levels. The diagonalization of the matrix $\hat{\epsilon}_{\mathbf{k}}$ by a rotation matrix $\hat{O}_{\mathbf{k}} \in \mathrm{SO}(3)$

$$\sum_{mm'} O^{im}_{\mathbf{k}} \epsilon^{mm'}_{\mathbf{k}} O^{jm'}_{\mathbf{k}} = \delta_{ij} E^{i}_{\mathbf{k}} \tag{2.3}$$

results in the three energy bands

$$\begin{aligned} E^1_{\mathbf{k}} &= t + t\sqrt{1 + 8\cos k_1 \cos k_2 \cos k_3} - \mu \\ E^2_{\mathbf{k}} &= t - t\sqrt{1 + 8\cos k_1 \cos k_2 \cos k_3} - \mu \\ E^3_{\mathbf{k}} &= -2t - \mu. \end{aligned} \tag{2.4}$$

These bands have the periodicity $E^l_{\mathbf{k}+\mathbf{B}_j} = E^l_{\mathbf{k}}$, where the vectors $\mathbf{B}_j$ are defined

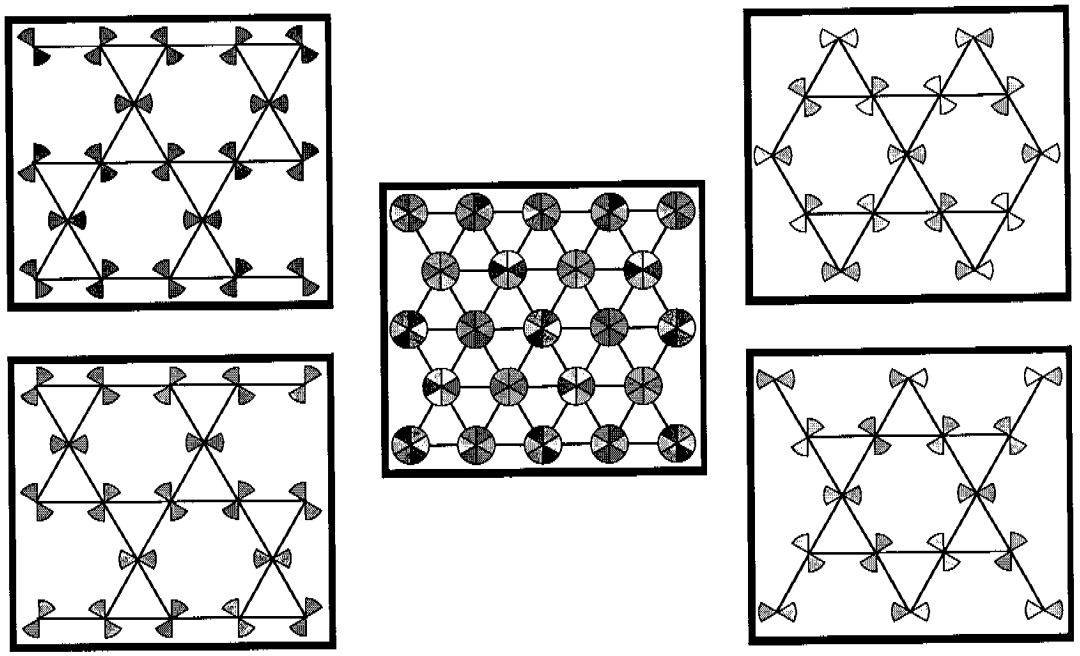

Figure 2.4: Schematic picture of the triangular lattice with three t_{2g} orbitals (middle). It can be decomposed into four inter-penetrating kagomé lattices. Only the inplane lobes of the t_{2g} orbitals are drawn. Note, that each orbital can hop only along two directions of the triangular lattice, furthermore, the hopping is always off-diagonal, i.e., between different orbitals.

by

$$\mathbf{a}_i \cdot \mathbf{B}_j = \frac{2\pi}{\sqrt{3}} \sin(\theta_i - \theta_j) \quad i,j = 1,\ldots,3 \tag{2.5}$$

with $\theta_j = 2\pi j/3$. These three vectors $\mathbf{B}_j$ connect the Γ point with the three M points in the Brillouin zone (BZ), and the vectors $2\,\mathbf{B}_j$ are primitive reciprocal lattice vectors. The bands of this tight-binding model have therefore a higher periodicity than the bands of a more general model. This leads to the appearance of special symmetry lines (thin lines) and symmetry points (M' and K') in the Brillouin zone, shown in Fig. 2.5, where the bands are plotted along the line Γ'-K'-M'-Γ'. Within a reduced BZ, these bands correspond to the bands of a nearest-neighbor tight-binding model on a kagomé lattice [69]. The density of states per spin and per reduced BZ is also shown in Fig. 2.5. It has a logarithmic singularity at $E = 2\,t$ and jumps from $\sqrt{3}/(2\pi t)$ to 0 at $E = 4\,t$.

Since the CoO_2-plane consists of four independent and inter-penetrating kagomé lattices [69], it is convenient to label the states belonging to the same

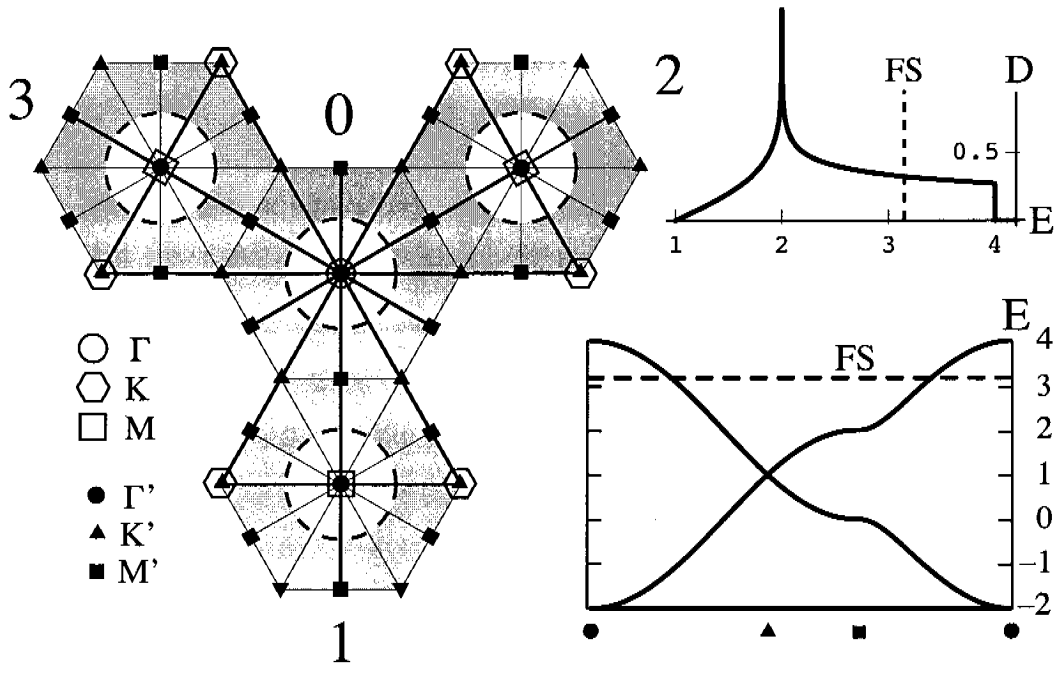

Figure 2.5: The original Brillouin zone (BZ) of the triangular lattice consists of four reduced BZs around of the Γ point (0) and the three M points (1,2,3). The symmetry points of the reduced BZs, M', K' and Γ' are symmetry points for the tight-binding model in Eq. (2.1) due to the higher periodicity of the bands. It is therefore sufficient to draw the bands along the lines Γ'-K'-M'-Γ'. The Fermi surface (FS) for $x = 0.5$ lies at $E^1_{\mathbf{k}} \approx 3.16\,t$. The density of states per spin and per reduced Brillouin zone D is given in units of $1/t$. It has a logarithmic singularity at $E = 2\,t$.

kagomé lattice with an index $l = 0, \ldots, 3$. This can be done with the vectors $\mathbf{a}_l$ of Fig. 2.3 as

$$a^{\dagger l}_{\mathbf{R}m\sigma} = c^{\dagger}_{\mathbf{R}+\mathbf{a}_l+\mathbf{a}_m\, m\sigma}. \tag{2.6}$$

In this way, the operators $a^{\dagger l}_{\mathbf{R}m}$ with fixed l create all the states off a kagomé lattice. In the following, these operators will be called *kagomé operators*. Their Fourier transform is given by

$$a^{\dagger l}_{\mathbf{K}m\sigma} = \frac{2}{\sqrt{N}} \sum_{\mathbf{R}} \mathrm{e}^{\mathrm{i}\mathbf{K}\cdot(\mathbf{R}+\mathbf{a}_l+\mathbf{a}_m)}\, a^{\dagger l}_{\mathbf{R}m\sigma}, \tag{2.7}$$

where the vector $\mathbf{K}$ belongs to the reduced BZ labeled 0 in Fig. 2.5 and $\mathbf{R}$ runs over the lattice spanned by the vectors $2\mathbf{a}_i$.

The BZ consists of four reduced BZs shown in Fig. 2.5. An alternative labeling of the states is obtained therefore by defining the operators

$$b^{\dagger j}_{\mathbf{K}m\sigma} = \mathrm{e}^{-\mathrm{i}\mathbf{B}_j\cdot\mathbf{a}_m}\, c^{\dagger}_{\mathbf{K}+\mathbf{B}_j m\sigma}, \tag{2.8}$$

where the vectors $\mathbf{B}_j$ are defined in Eq. (2.5) and in addition we set $\mathbf{B}_0 = 0$. As shown in Eq. (A.1) in App. A, the transformation between the kagomé operators $a^{\dagger l}_{\mathbf{K}}$ and the *pocket operators* $b^{\dagger j}_{\mathbf{K}}$ corresponds to a discrete Fourier transformation of a 2×2 lattice, and is given by

$$b^{\dagger j}_{\mathbf{K}m\sigma} = \frac{1}{2}\sum_l \mathrm{e}^{\mathrm{i}\mathbf{B}_j\cdot\mathbf{a}_l} a^{\dagger l}_{\mathbf{K}m\sigma} = \sum_l \mathcal{F}_{jl} a^{\dagger l}_{\mathbf{K}m\sigma}, \tag{2.9}$$

where we have defined the symmetric and orthogonal 4×4 matrix

$$\mathcal{F}_{jl} = \mathcal{F}_{lj} = \mathcal{F}^{*}_{jl} = \mathcal{F}^{-1}_{jl} = \frac{1}{2}\mathrm{e}^{\mathrm{i}\mathbf{B}_j\cdot\mathbf{a}_l}. \tag{2.10}$$

Note that the matrix elements of $\mathcal{F}$ are $\pm 1/2$, as the scalar products $\mathbf{B}_j \cdot \mathbf{a}_l$ of Eq. (2.5) equal 0 or $\pm\pi$.

The tight-binding Hamiltonian (2.1) is diagonal in the pocket indices j (cf. Appendix A Eq. (A.2)),

$$H_{\mathrm{tb}} = \sum_{l\mathbf{K}\sigma}\sum_{mm'} \epsilon^{mm'}_{\mathbf{K}} b^{\dagger l}_{\mathbf{K}m\sigma} b^{l}_{\mathbf{K}m'\sigma}. \tag{2.11}$$

From this expression it is apparent, that the tight-binding Hamiltonian is invariant under any U(4) transformation of the of the form

$$b^{\dagger j}_{\mathbf{K}m\sigma} \rightarrow \tilde{b}^{\dagger j}_{\mathbf{K}m\sigma} = \sum_{j'} U_{jj'} b^{\dagger j'}_{\mathbf{K}m\sigma}. \tag{2.12}$$

Eq. (2.9) is just a special case of Eq. (2.12). This shows that H_{tb} is also diagonal in the kagomé indices.

It is important to notice that the transformations in Eq. (2.12) involves symmetries that are not present in a more general tight-binding model. For example a finite hopping integral t_{dd} due to the σ-hybridization between neighboring t_{2g} orbitals would break this symmetry. We will discuss this aspect below in more detail and remain for the time being in this high-symmetry situation.

In Na_xCoO_2 the lower two bands are completely filled and will be quite inert. For this reason in the following sections we will only deal with the operators of the top band $E^1_{\mathbf{k}}$ whose operators are denoted as

$$a^{\dagger l}_{\mathbf{K}\sigma} = \sum_m O^{1m}_{\mathbf{K}} a^{\dagger l}_{\mathbf{K}m\sigma} \quad \text{and} \quad b^{\dagger j}_{\mathbf{K}\sigma} = \sum_m O^{1m}_{\mathbf{K}} b^{j}_{\mathbf{K}m\sigma}, \tag{2.13}$$

respectively, where $O^{1m}_{\mathbf{K}}$ are matrix elements of the rotation matrix $\hat{O}_{\mathbf{K}}$ of Eq. (2.3).

The top band gives rise to four identical Fermi surface pockets in the BZ, one in the Γ point and three at the M points. A translation in the reciprocal space by the vectors $\mathbf{B}_j$ maps the pocket around the Γ point onto a pocket around the M point. However, this fact does not lead to nesting singularities in the susceptibility because a hole pocket is mapped onto a hole pocket by the vector $\mathbf{B}_j$. The susceptibility of the top band is given by

$$\chi^0_{\mathbf{q}} = \frac{1}{N}\sum_{\mathbf{k}} \frac{f_{\mathbf{k}+\mathbf{q}} - f_{\mathbf{k}}}{E^1_{\mathbf{k}} - E^1_{\mathbf{k}+\mathbf{q}}} = \frac{4}{N}\sum_{\mathbf{K}} \frac{f_{\mathbf{K}+\mathbf{Q}} - f_{\mathbf{K}}}{E^1_{\mathbf{K}} - E^1_{\mathbf{K}+\mathbf{Q}}}, \tag{2.14}$$

where $f_{\mathbf{k}} = f[\beta(E^1_{\mathbf{k}} - \mu)]$ and f is the Fermi function. In the last expression of Eq. (2.14) the sum over $\mathbf{K}$ is restricted to the reduced BZ. The momentum $\mathbf{Q}$ also lies in the reduced BZ and is given by $\mathbf{Q} = q + \mathbf{B}_j$. The susceptibility $\chi^0_{\mathbf{q}} = \chi^0_{\mathbf{Q}}$ is periodic with respect to the reduced BZ and is just four times the susceptibility of a single kagomé lattice. As we have almost circular hole pockets with quadratic dispersion around the Γ and the M points, the susceptibility is therefore approximately given by the susceptibility of the free electron gas in two dimensions within each reduced BZ, with circular plateaus of radius $2\mathbf{K}_{\mathrm{F}}$ around the Γ and the three M points.

2.3 Coulomb interaction

In this section we introduce the Coulomb interaction between the electrons. As we have spin and orbital degrees of freedom, the on-site Coulomb interaction consists of intra-orbital repulsion U, inter-orbital repulsion U', Hund's coupling J_{H} and a pair hopping term J'. These parameters are related by $U \approx U' + 2J_{\mathrm{H}}$ and $J_{\mathrm{H}} = J'$, where the first relation is exact for spherical symmetry. We can write the onsite Coulomb interaction as

$$\begin{aligned} H^{\mathrm{C}}_{\mathbf{r}} &= U\sum_{m} n_{\mathbf{r}m\uparrow} n_{\mathbf{r}m\downarrow} + \frac{U'}{2}\sum_{m\neq m'}\sum_{\sigma\sigma'} n_{\mathbf{r}m\sigma} n_{\mathbf{r}m'\sigma'} \\ &+ \frac{J_{\mathrm{H}}}{2}\sum_{m\neq m'}\sum_{\sigma\sigma'} c^\dagger_{\mathbf{r}m\sigma} c^\dagger_{\mathbf{r}m'\sigma'} c_{\mathbf{r}m\sigma'} c_{\mathbf{r}m'\sigma} \\ &+ \frac{J'}{2}\sum_{m\neq m'}\sum_{\sigma\neq\sigma'} c^\dagger_{\mathbf{r}m\sigma} c^\dagger_{\mathbf{r}m\sigma'} c_{\mathbf{r}m'\sigma'} c_{\mathbf{r}m'\sigma}, \end{aligned} \tag{2.15}$$

where $n_{\mathbf{r}m\sigma} = c^\dagger_{\mathbf{r}m\sigma} c_{\mathbf{r}m\sigma}$. We obtain an effective Hamiltonian for the Coulomb interaction by rewriting the Hamiltonian in terms of the pocket operators of the top band $b^{\dagger l}_{\mathbf{K}\sigma}$ defined in Eq. (2.13). For small $\kappa = |\mathbf{K}|a$ we can expand Eq. (2.13) in powers of κ^2 and obtain up to terms of the order κ^2

$$b^{\dagger j}_{\mathbf{K}\sigma} = \frac{1}{\sqrt{3}} \sum_m \left(1 + \frac{\kappa^2}{12} \cos\left[2(\theta - \theta_m)\right]\right) b^j_{\mathbf{K}m\sigma}, \tag{2.16}$$

where $\theta_m = 2\pi m/3$. Expanding the energy of the top band around the point Γ', we obtain

$$\epsilon^1_{\mathbf{K}} = t\left[4 - \kappa^2 + \frac{\kappa^4}{12} - \frac{\kappa^6}{360}\cos(6\theta) + \mathcal{O}(\kappa^8)\right]. \tag{2.17}$$

This shows that the pockets around the points Γ' are almost perfectly circular. The radius κ_F/a of these pockets depends on the Na doping x. Note that x corresponds to the density of carriers with $x = 1$ giving a completely filled top band. We have $\kappa_F^2 = \pi(1-x)/\sqrt{3}$. For the interaction in weak coupling and at low temperatures, the states near the Fermi surface are important. For these states and for not too small Na doping x we can neglect the second term in the parenthesis of Eq. (2.16) compared to 1. Note, that this condition on x is not very restrictive. Even for $x = 0.35$ the second term together with all higher order terms is on the average one order of magnitude smaller than 1. Dropping the second term in Eq. (2.16) spreads the a_{1g} symmetry of the states $b^{\dagger j}_{\mathbf{K}\sigma}$, which is exact only for $\mathbf{K} = 0$, to all relevant states in the top band. The interaction (2.15) can now be rewritten in terms of the a_{1g} symmetric operators $b^{\dagger j}_{\mathbf{K}\sigma}$. Processes involving states of the filled lower bands are dropped. The dropping of the second term in the parenthesis of Eq. (2.16) is a considerable simplification because it removes all $\mathbf{K}$-dependence of the potential.

At this point it is convenient to introduce density and spin density operators for the pocket operators of the top band:

$$\begin{aligned} \hat{n}^{ij}_{\mathbf{Q}} &= \frac{4}{N} \sum_{\mathbf{K}\sigma} b^{\dagger i}_{\mathbf{K}+\mathbf{Q}\,\sigma}\, b^j_{\mathbf{K}\sigma}, \\ \hat{\mathbf{S}}^{ij}_{\mathbf{Q}} &= \frac{2}{N} \sum_{\mathbf{K}\sigma\sigma'} b^{\dagger i}_{\mathbf{K}+\mathbf{Q}\,\sigma}\, \boldsymbol{\sigma}_{\sigma\sigma'}\, b^j_{\mathbf{K}\sigma}, \end{aligned} \tag{2.18}$$

where $\boldsymbol{\sigma}$ is a vector consisting of the three Pauli matrices. The resulting effective interaction can be expressed with these operators in the following way

$$H_{\text{eff}} = \frac{N}{32} \sum_{\mathbf{Q}} \sum_{ijkl} \left(B^{\text{s}}_{ijkl}\, \hat{\mathbf{S}}^{ij}_{\mathbf{Q}} \cdot \hat{\mathbf{S}}^{lk}_{-\mathbf{Q}} + \frac{1}{4} B^{\text{c}}_{ijkl}\, \hat{n}^{ij}_{\mathbf{Q}}\, \hat{n}^{lk}_{-\mathbf{Q}} \right). \tag{2.19}$$

Table 2.1: The coefficients of Eq. (2.20).

$9C = -3U + 2J' + 2J_{\rm H} + 2U'$	$9D = +3U + 6J' - 2J_{\rm H} - 2U'$
$9E^{\rm c} = +3U - 2J' - 10J_{\rm H} + 14U'$	$9E^{\rm s} = -3U + 2J' - 6J_{\rm H} + 2U'$
$9F^{\rm c} = +3U - 2J' + 14J_{\rm H} - 10U'$	$9F^{\rm s} = -3U + 2J' + 2J_{\rm H} - 6U'$

The symbols $B^{\rm c/s}$ depend on the Coulomb integrals and are given by

$$B^{\rm c/s}_{ijkl} = \pm C(2\delta_{ijkl} - \epsilon^2_{ijkl}) \pm D\delta_{il}\delta_{jk} + E^{\rm c/s}\delta_{ij}\delta_{kl} + F^{\rm c/s}\delta_{ik}\delta_{jl}, \tag{2.20}$$

where the δ (ϵ^2) symbol equals 1, if all the indices are equal (different) and 0 otherwise. The coefficients C, D, $E^{\rm c/s}$, and $F^{\rm c/s}$ are listed in Table 2.1. Note, that for small pockets, the momenta $\mathbf{K}$ of the pocket operators $b^j_{\mathbf{K}}$ in the four fermion terms of Eq. (2.19) can not add up to a half a reciprocal lattice vector $\mathbf{B}_i$. In order to conserve momentum they must therefore add up to zero. Due to the position of the pockets in the BZ, Umklapp processes with low energy transfer are however possible for arbitrary small pockets. In fact, the processes proportional to ϵ^2_{ijkl} and $\delta_{il}\delta_{jk}(1-\delta_{ij})$ are Umklapp processes, as $\mathbf{B}_i - \mathbf{B}_j + \mathbf{B}_l - \mathbf{B}_k$ is a non-vanishing reciprocal lattice vector for $\epsilon_{ijkl} \neq 0$ and for $\delta_{il}\delta_{jk}(1-\delta_{ij}) \neq 0$, and from Eq. (2.8) the momentum created by the operator $b^{\dagger j}_{\mathbf{K}}$ is $\mathbf{K} + \mathbf{B}_j$.

Some details about the derivation of Eq. (2.19) are provided in App. A.2. There are different ways of writing this interaction in terms of the operators in (2.18). Our formulation treats charge and spin degrees of freedom on an equal footing. It corresponds to the decomposition of a Hubbard interaction $n_\uparrow n_\downarrow$ into $\frac{1}{2}(\frac{1}{4}n^2 - \mathbf{S}\cdot\mathbf{S})$.

In order to express the effective interaction Hamiltonian of Eq. (2.19) in terms of the kagomé operators, $a^l_{\mathbf{K}\sigma}$, we define spin and charge density operators from the kagomé operators $a^l_{\mathbf{K}\sigma}$ as in Eq. (2.18).

$$\begin{aligned} n^{ij}_{\mathbf{Q}} &= \frac{4}{N}\sum_{\mathbf{K}\sigma} a^{\dagger i}_{\mathbf{K}+\mathbf{Q}\,\sigma}\, a^j_{\mathbf{K}\sigma}, \\ \mathbf{S}^{ij}_{\mathbf{Q}} &= \frac{2}{N}\sum_{\mathbf{K}\sigma\sigma'} a^{\dagger i}_{\mathbf{K}+\mathbf{Q}\,\sigma}\, \boldsymbol{\sigma}_{\sigma\sigma'}\, a^j_{\mathbf{K}\sigma}. \end{aligned} \tag{2.21}$$

Note, that the density operators, which are defined from the pocket operators $b^j_{\mathbf{K}\sigma}$ are marked by a hat. The effective Hamiltonian, $H_{\rm eff}$, of Eq. (2.19) can be

rewritten as

$$H_{\text{eff}} = \frac{N}{32} \sum_{\mathbf{Q}} \sum_{ijkl} \left(A^{\text{s}}_{ijkl}\, \mathbf{S}^{ij}_{\mathbf{Q}} \cdot \mathbf{S}^{lk}_{-\mathbf{Q}} + \frac{1}{4} A^{\text{c}}_{ijkl}\, n^{ij}_{\mathbf{Q}}\, n^{lk}_{-\mathbf{Q}} \right). \tag{2.22}$$

From Eq. (2.9) and (2.10) follows that

$$A^{\text{c/s}}_{ijkl} = \sum_{mnop} \mathcal{F}_{im} \mathcal{F}_{jn} \mathcal{F}_{ko} \mathcal{F}_{lp} B^{c/s}_{mnop}. \tag{2.23}$$

The symbols $A^{\text{c/s}}$ turn out to have a simpler structure, given by

$$\begin{aligned} A^{\text{c}}_{ijkl} &= \frac{8}{9} \Big[-\frac{C}{2} \delta_{ijkl} + J' \delta_{il} \delta_{jk} + (2U' - J_{\text{H}}) \delta_{ij} \delta_{kl} + \\ &\qquad + (2J_{\text{H}} - U') \delta_{ik} \delta_{jl} \Big], \\ A^{\text{s}}_{ijkl} &= \frac{8}{9} \Big[+\frac{C}{2} \delta_{ijkl} - J' \delta_{il} \delta_{jk} - J_{\text{H}} \delta_{ij} \delta_{kl} - U' \delta_{ik} \delta_{jl} \Big]. \end{aligned} \tag{2.24}$$

2.4 SU(4) generators

The tight-binding Hamiltonian described in Sec. 2.2 has a U(4) symmetry, reflecting the fact that it consists of 4 independent and equivalent kagomé lattices. The correlations introduced by the on-site Coulomb repulsion in Eq. (2.15) breaks this symmetry and leads to interaction between orbitals belonging to different kagomé lattices, as the three t_{2g} orbitals on a given Co-site belong to three different kagomé lattices. The effective Hamiltonian in Eq. (2.19) is not invariant under general U(4) transformations, but is still invariant under a finite subgroup of U(4). The symbols $A^{\text{c/s}}_{ijkl}$ defined in Eq. (2.24) are invariant under permutation of the indices, i.e.,

$$A^{\text{s/c}}_{ijkl} = A^{\text{s/c}}_{\mathcal{P}(i)\mathcal{P}(j)\mathcal{P}(k)\mathcal{P}(l)}, \qquad \mathcal{P} \in \mathcal{S}_4. \tag{2.25}$$

From this follows that even including Coulomb interactions the symmetric group $\mathcal{S}_4$ is a subgroup of the symmetry group of our system, G. Multiplying all operators $a^{l}_{\mathbf{K},\sigma}$ with the same kagomé index l by -1 also leaves the Hamiltonian, H_{eff}, invariant, because the symbols $A^{\text{c/s}}_{ijkl}$ are nonzero only if the four indices $ijkl$ are pairwise equal. These two different symmetry operations generate a group with 384 elements. This group G is isomorphic to the symmetry group of the four-dimensional hypercube. In App. A.3 the structure of the group G is discussed and the character table is shown in Table A.1.

To proceed, let Q^r with $r = 0, \ldots, 15$ be a basis in the 16 dimensional real vector space, V, of Hermitian 4×4 matrices fulfilling the usual orthonormality and completeness relations:

$$\sum_{ij} Q^r_{ij} Q^l_{ji} = \frac{1}{2}\delta_{rl} \quad \text{and} \quad \sum_{r=0}^{15} Q^r_{ij} Q^r_{kl} = \frac{1}{2}\delta_{il}\delta_{jk}. \tag{2.26}$$

This basis can be chosen such, that Q^0 is proportional to the unit matrix, Q^{1-3} are diagonal, Q^{4-9} are real, and Q^{10-15} are imaginary. It is convenient to define also the *dual* matrices

$$K^r_{ij} = \sum_{mn} \mathcal{F}_{im}\mathcal{F}_{jn} Q^r_{mn}. \tag{2.27}$$

In Table 2.2 a choice of a basis Q^r which is particularly suitable for our purposes is provided. Table 2.3 shows the dual basis consisting of the matrices K^r. A representation ρ of the group G on V is given by $\rho(g)Q^r = N_g^\top Q^r N_g$ for $g \in G$, where N_g is the natural four-dimensional representation of G (cf. App. A.3). The representation ρ is reducible and V is the direct sum of the four irreducible subspaces V^0, V^{1-3}, V^{4-9} and V^{10-15} spanned by matrices Q^0, Q^{1-3}, Q^{4-9} and Q^{10-15}, respectively. Therefore, the chosen basis is appropriate for the symmetry group G. Defining charge and spin density operators as

$$\begin{aligned} n^r_{\mathbf{Q}} &= \sum_{ij} Q^r_{ij} n^{ij}_{\mathbf{Q}} = \sum_{ij} K^r_{ij} \hat{n}^{ij}_{\mathbf{Q}}, \\ \mathbf{S}^r_{\mathbf{Q}} &= \sum_{ij} Q^r_{ij} \mathbf{S}^{ij}_{\mathbf{Q}} = \sum_{ij} K^r_{ij} \hat{\mathbf{S}}^{ij}_{\mathbf{Q}}, \end{aligned} \tag{2.28}$$

the interaction Hamiltonian can be written in a diagonal form as

$$H_{\text{eff}} = \frac{N}{8} \sum_{r=0}^{15} \sum_{\mathbf{Q}} \left(\Lambda^{\text{s}}_r \, \mathbf{S}^r_{\mathbf{Q}} \cdot \mathbf{S}^r_{-\mathbf{Q}} + \frac{1}{4} \Lambda^{\text{c}}_r \, n^r_{\mathbf{Q}} \, n^r_{-\mathbf{Q}} \right). \tag{2.29}$$

The coupling constants $\Lambda^{\text{c/s}}_r$ are equal for all Q^r belonging to the same irreducible subspace in V. They are given in Table 2.4.

2.5 Reduction of the symmetry

The tight-binding Hamiltonian in Eq. (2.11) has a U(4) symmetry and even after introducing Coulomb interaction, the effective Hamiltonian (2.29) is invariant under the symmetry group G. In a real CoO_2-plane this symmetry is

Table 2.2: The matrices Q^{1-15} are a choice of an orthonormal complete basis of the 15 dimensional real vector space of traceless hermitian matrices, so-called generators of SU(4), that is adequate to the symmetry of the CoO_2-layer. The matrices K^r can be obtained from Q^r using Eq. (2.27). Note that $\bar{1} = -1$ and $\bar{\mathrm{i}} = -\mathrm{i}$. $2\sqrt{2}Q^0 = 2\sqrt{2}K^0$ is the 4×4 unit matrix.

$$Q^1\ (\Gamma_5^a)\quad \frac{1}{2\sqrt{2}}\begin{pmatrix} 1 & 0 & 0 & 0 \\ 0 & 1 & 0 & 0 \\ 0 & 0 & \bar{1} & 0 \\ 0 & 0 & 0 & \bar{1} \end{pmatrix}$$

$$Q^2\ (\Gamma_5^a)\quad \frac{1}{2\sqrt{2}}\begin{pmatrix} 1 & 0 & 0 & 0 \\ 0 & \bar{1} & 0 & 0 \\ 0 & 0 & 1 & 0 \\ 0 & 0 & 0 & \bar{1} \end{pmatrix}$$

$$Q^3\ (\Gamma_5^a)\quad \frac{1}{2\sqrt{2}}\begin{pmatrix} 1 & 0 & 0 & 0 \\ 0 & \bar{1} & 0 & 0 \\ 0 & 0 & \bar{1} & 0 \\ 0 & 0 & 0 & 1 \end{pmatrix}$$

$$Q^4\ (\Gamma_1^b)\quad \frac{1}{2\sqrt{6}}\begin{pmatrix} 0 & 1 & 1 & 1 \\ 1 & 0 & 1 & 1 \\ 1 & 1 & 0 & 1 \\ 1 & 1 & 1 & 0 \end{pmatrix}$$

$$Q^5\ (\Gamma_3)\quad \frac{1}{4}\begin{pmatrix} 0 & 1 & \bar{1} & 0 \\ 1 & 0 & 0 & \bar{1} \\ \bar{1} & 0 & 0 & 1 \\ 0 & \bar{1} & 1 & 0 \end{pmatrix}$$

$$Q^6\ (\Gamma_3)\quad \frac{1}{4\sqrt{3}}\begin{pmatrix} 0 & 1 & 1 & \bar{2} \\ 1 & 0 & \bar{2} & 1 \\ 1 & \bar{2} & 0 & 1 \\ \bar{2} & 1 & 1 & 0 \end{pmatrix}$$

$$Q^7\ (\Gamma_5^b)\quad \frac{1}{2\sqrt{2}}\begin{pmatrix} 0 & 1 & 0 & 0 \\ 1 & 0 & 0 & 0 \\ 0 & 0 & 0 & \bar{1} \\ 0 & 0 & \bar{1} & 0 \end{pmatrix}$$

$$Q^8\ (\Gamma_5^b)\quad \frac{1}{2\sqrt{2}}\begin{pmatrix} 0 & 0 & 1 & 0 \\ 0 & 0 & 0 & \bar{1} \\ 1 & 0 & 0 & 0 \\ 0 & \bar{1} & 0 & 0 \end{pmatrix}$$

$$Q^9\ (\Gamma_5^b)\quad \frac{1}{2\sqrt{2}}\begin{pmatrix} 0 & 0 & 0 & 1 \\ 0 & 0 & \bar{1} & 0 \\ 0 & \bar{1} & 0 & 0 \\ 1 & 0 & 0 & 0 \end{pmatrix}$$

$$Q^{10}\ (\Gamma_4)\quad \frac{1}{4}\begin{pmatrix} 0 & 0 & \bar{\mathrm{i}} & \mathrm{i} \\ 0 & 0 & \mathrm{i} & \bar{\mathrm{i}} \\ \mathrm{i} & \bar{\mathrm{i}} & 0 & 0 \\ \bar{\mathrm{i}} & \mathrm{i} & 0 & 0 \end{pmatrix}$$

$$Q^{11}\ (\Gamma_4)\quad \frac{1}{4}\begin{pmatrix} 0 & \mathrm{i} & 0 & \bar{\mathrm{i}} \\ \bar{\mathrm{i}} & 0 & \mathrm{i} & 0 \\ 0 & \bar{\mathrm{i}} & 0 & \mathrm{i} \\ \mathrm{i} & 0 & \bar{\mathrm{i}} & 0 \end{pmatrix}$$

$$Q^{12}\ (\Gamma_4)\quad \frac{1}{4}\begin{pmatrix} 0 & \bar{\mathrm{i}} & \mathrm{i} & 0 \\ \mathrm{i} & 0 & 0 & \bar{\mathrm{i}} \\ \bar{\mathrm{i}} & 0 & 0 & \mathrm{i} \\ 0 & \mathrm{i} & \bar{\mathrm{i}} & 0 \end{pmatrix}$$

$$Q^{13}\ (\Gamma_5^c)\quad \frac{1}{4}\begin{pmatrix} 0 & 0 & \bar{\mathrm{i}} & \bar{\mathrm{i}} \\ 0 & 0 & \bar{\mathrm{i}} & \bar{\mathrm{i}} \\ \mathrm{i} & \mathrm{i} & 0 & 0 \\ \mathrm{i} & \mathrm{i} & 0 & 0 \end{pmatrix}$$

$$Q^{14}\ (\Gamma_5^c)\quad \frac{1}{4}\begin{pmatrix} 0 & \bar{\mathrm{i}} & 0 & \bar{\mathrm{i}} \\ \mathrm{i} & 0 & \mathrm{i} & 0 \\ 0 & \bar{\mathrm{i}} & 0 & \bar{\mathrm{i}} \\ \mathrm{i} & 0 & \mathrm{i} & 0 \end{pmatrix}$$

$$Q^{15}\ (\Gamma_5^c)\quad \frac{1}{4}\begin{pmatrix} 0 & \bar{\mathrm{i}} & \bar{\mathrm{i}} & 0 \\ \mathrm{i} & 0 & 0 & \mathrm{i} \\ \mathrm{i} & 0 & 0 & \mathrm{i} \\ 0 & \bar{\mathrm{i}} & \bar{\mathrm{i}} & 0 \end{pmatrix}$$

Table 2.3: The matrices K^{1-15} are a choice of an orthonormal complete basis of the 15 dimensional real vector space of traceless hermitian matrices, so-called generators of SU(4), that is adequate to the symmetry of the CoO_2-layer. The matrices Q^r can be obtained from K^r using Eq. (2.27). Note that $\bar{1} = -1$ and $\bar{\mathrm{i}} = -\mathrm{i}$. $2\sqrt{2}Q^0 = 2\sqrt{2}K^0$ is the 4×4 unit matrix.

$$K^1\ (\Gamma_5^a) \quad \frac{1}{2\sqrt{2}} \begin{pmatrix} 0 & 1 & 0 & 0 \\ 1 & 0 & 0 & 0 \\ 0 & 0 & 0 & 1 \\ 0 & 0 & 1 & 0 \end{pmatrix}$$

$$K^2\ (\Gamma_5^a) \quad \frac{1}{2\sqrt{2}} \begin{pmatrix} 0 & 0 & 1 & 0 \\ 0 & 0 & 0 & 1 \\ 1 & 0 & 0 & 0 \\ 0 & 1 & 0 & 0 \end{pmatrix}$$

$$K^3\ (\Gamma_5^a) \quad \frac{1}{2\sqrt{2}} \begin{pmatrix} 0 & 0 & 0 & 1 \\ 0 & 0 & 1 & 0 \\ 0 & 1 & 0 & 0 \\ 1 & 0 & 0 & 0 \end{pmatrix}$$

$$K^4\ (\Gamma_1^b) \quad \frac{1}{2\sqrt{6}} \begin{pmatrix} 3 & 0 & 0 & 0 \\ 0 & \bar{1} & 0 & 0 \\ 0 & 0 & \bar{1} & 0 \\ 0 & 0 & 0 & \bar{1} \end{pmatrix}$$

$$K^5\ (\Gamma_3) \quad \frac{1}{2} \begin{pmatrix} 0 & 0 & 0 & 0 \\ 0 & 1 & 0 & 0 \\ 0 & 0 & \bar{1} & 0 \\ 0 & 0 & 0 & 0 \end{pmatrix}$$

$$K^6\ (\Gamma_3) \quad \frac{1}{2\sqrt{3}} \begin{pmatrix} 0 & 0 & 0 & 0 \\ 0 & 1 & 0 & 0 \\ 0 & 0 & 1 & 0 \\ 0 & 0 & 0 & \bar{2} \end{pmatrix}$$

$$K^7\ (\Gamma_5^b) \quad \frac{1}{2\sqrt{2}} \begin{pmatrix} 0 & 1 & 0 & 0 \\ 1 & 0 & 0 & 0 \\ 0 & 0 & 0 & \bar{1} \\ 0 & 0 & \bar{1} & 0 \end{pmatrix}$$

$$K^8\ (\Gamma_5^b) \quad \frac{1}{2\sqrt{2}} \begin{pmatrix} 0 & 0 & 1 & 0 \\ 0 & 0 & 0 & \bar{1} \\ 1 & 0 & 0 & 0 \\ 0 & \bar{1} & 0 & 0 \end{pmatrix}$$

$$K^9\ (\Gamma_5^b) \quad \frac{1}{2\sqrt{2}} \begin{pmatrix} 0 & 0 & 0 & 1 \\ 0 & 0 & \bar{1} & 0 \\ 0 & \bar{1} & 0 & 0 \\ 1 & 0 & 0 & 0 \end{pmatrix}$$

$$K^{10}\ (\Gamma_4) \quad \frac{1}{2} \begin{pmatrix} 0 & 0 & 0 & 0 \\ 0 & 0 & 0 & 0 \\ 0 & 0 & 0 & \mathrm{i} \\ 0 & 0 & \bar{\mathrm{i}} & 0 \end{pmatrix}$$

$$K^{11}\ (\Gamma_4) \quad \frac{1}{2} \begin{pmatrix} 0 & 0 & 0 & 0 \\ 0 & 0 & 0 & \bar{\mathrm{i}} \\ 0 & 0 & 0 & 0 \\ 0 & \mathrm{i} & 0 & 0 \end{pmatrix}$$

$$K^{12}\ (\Gamma_4) \quad \frac{1}{2} \begin{pmatrix} 0 & 0 & 0 & 0 \\ 0 & 0 & \mathrm{i} & 0 \\ 0 & \bar{\mathrm{i}} & 0 & 0 \\ 0 & 0 & 0 & 0 \end{pmatrix}$$

$$K^{13}\ (\Gamma_5^c) \quad \frac{1}{2} \begin{pmatrix} 0 & \mathrm{i} & 0 & 0 \\ \bar{\mathrm{i}} & 0 & 0 & 0 \\ 0 & 0 & 0 & 0 \\ 0 & 0 & 0 & 0 \end{pmatrix}$$

$$K^{14}\ (\Gamma_5^c) \quad \frac{1}{2} \begin{pmatrix} 0 & 0 & \mathrm{i} & 0 \\ 0 & 0 & 0 & 0 \\ \bar{\mathrm{i}} & 0 & 0 & 0 \\ 0 & 0 & 0 & 0 \end{pmatrix}$$

$$K^{15}\ (\Gamma_5^c) \quad \frac{1}{2} \begin{pmatrix} 0 & 0 & 0 & \mathrm{i} \\ 0 & 0 & 0 & 0 \\ 0 & 0 & 0 & 0 \\ \bar{\mathrm{i}} & 0 & 0 & 0 \end{pmatrix}$$

Table 2.4: The coefficients $\Lambda_r^{s/c}$.

r	Λ_r^c	Λ_r^s
0	$\frac{2}{9}(+3U+12U'-6J_H)$	$-\frac{2}{9}(3U+6J_H)$
1–3	$\frac{2}{9}(+3U-4U'+2J_H)$	$-\frac{2}{9}(3U-2J_H)$
4–9	$\frac{2}{9}(-2U'+4J_H-2J')$	$-\frac{2}{9}(2U'-2J')$
10–15	$\frac{2}{9}(-2U'+4J_H+2J')$	$-\frac{2}{9}(2U'+2J')$

reduced even in the paramagnetic state. There are terms in the Hamiltonian of the real system that restrict the symmetry operations of G to the subgroup, which describes real crystallographic space-group symmetries.

A trigonal distortion of the oxygen octahedra by approaching the two O-layers to the Co-layer, is for example compatible with the point group symmetry D_{3d} of the CoO_2-layer. However, it lifts the degeneracy of the t_{2g} orbitals, leading to a term

$$\begin{aligned} H_{\rm tr} &= D_{\rm tr}\sum_{\mathbf{k}\sigma}\sum_{m\neq m'} c^\dagger_{\mathbf{k}m\sigma}c_{\mathbf{k}m'\sigma} \\ &= D_{\rm tr}\sum_{l\mathbf{K}\sigma}\sum_{m\neq m'} b^{\dagger l}_{\mathbf{K}m\sigma}b^{l}_{\mathbf{K}m'\sigma}e^{i\mathbf{B}_l\cdot(\mathbf{a}_m-\mathbf{a}_{m'})}, \end{aligned} \tag{2.30}$$

in the Hamiltonian, where $3D_{\rm tr}$ is the splitting induced by the trigonal distortion. [a] We used Eq. (2.8) to obtain the second line. For the top band we obtain with Eq. (2.16) and (A.6)

$$\begin{aligned} H_{\rm tr} &= \sqrt{2/3}\, D_{\rm tr}\, 4\sum_{l\mathbf{K}\sigma}\left[K^4_{ll}+\mathcal{O}(\kappa^2)\right]\, b^{\dagger l}_{\mathbf{K}\sigma}b^{l}_{\mathbf{K}\sigma} \\ &\approx \sqrt{2/3}\, D_{\rm tr}Nn_0^4, \end{aligned} \tag{2.31}$$

where the matrix K^4 is given in Table 2.3, and $\kappa = |\mathbf{K}|a$ is small for the relevant states near the Fermi pockets if the pockets are small enough. Similarly, a finite

[a] The energy of the orbital $(d_x+d_y+d_z)/\sqrt{3}$ goes up by $2D_{\rm tr}$ whereas the energy of the orthogonal two orbitals goes down by $D_{\rm tr}$.

direct hopping integral t_{dd} leads to the term

$$\begin{aligned} H_{dd} &= t_{dd} \sum_{km\sigma} 2\cos k_m c^\dagger_{km\sigma} c_{km\sigma} \\ &= 4\sqrt{6}\, t_{dd} \sum_{l\mathbf{K}\sigma} \left[K^4_{ll} + \mathcal{O}(\kappa^2)\right] b^{\dagger l}_{\mathbf{K}\sigma} b^l_{\mathbf{K}\sigma} \\ &\approx \sqrt{6} t_{dd} N n_0^4, \end{aligned} \tag{2.32}$$

where we again dropped the terms involving the lower bands in the second line. In fact, any other additional hopping term or any quadratic perturbation compatible with the space group is proportional to the field n_0^4 in the limit of small pockets, if the perturbation is diagonal in the spin indices. As the trigonal distortion of the octahedra is nonzero and additional hopping terms are present in the CoO_2-layer, a term proportional to n_0^4 exists in the Hamiltonian acting like a symmetry breaking field. For simplicity, we will refer to a term proportional to n_0^4 in the Hamiltonian as the *trigonal distortion*, even though this term is rather an effective trigonal distortion that also includes the effects of additional hopping terms.

From the matrix K^4 can be seen, that the presence of a finite field, n_0^4, in the Hamiltonian leads to a distinction between the Γ and the M points in the BZ and the four hole pockets are no longer equivalent. In real space, the four kagomé lattices are still equivalent, as they transform under space group symmetries among themselves. In fact, the matrix Q^4 is still invariant under permutations of rows and columns, i.e., $N_g^{\mathrm{T}} Q^4 N_g = Q^4$ for all $g \in \mathcal{S}_4$, but Q^4 is not invariant under changing the sign of all operators with the same kagomé index. These sign changes, however, are not space-group symmetries, but gauge symmetries, originating from the fact that the charge on the kagomé lattices is conserved by H_{tb} (2.1) and also by the Coulomb interaction except for the pair-hopping term proportional to J' in Eq. (2.15). This term however can only change the number of electrons by two, leading to these gauge symmetries, that are broken, as soon as single electron hopping processes between the kagomé lattices are introduced.

To classify the states according to the real symmetry group of the CoO_2-layer without gauge symmetries, it is therefore sufficient, to consider the presence of a small field n_0^4, that restricts the symmetry group G to a subgroup, consisting of space group symmetries of the CoO_2-layer. This subgroup of G is isomorphic to $\mathcal{S}_4 \simeq T_d \simeq O$. [b] Intuitively it is understandable that the

[b] The symbol $\mathcal{S}_4$ denotes the symmetric group 4, i.e., all permutations of 4 elements, T_d

symmetry of the four dimensional cube reduces to the symmetry of a three dimensional cube, if one of the four hole pockets is not equivalent to the other three.

Form Table 2.2 can be seen, that the matrices Q^0, Q^{1-3}, Q^4, Q^{5-6}, Q^{7-9}, Q^{10-12} and Q^{13-15} transform irreducibly under $\mathcal{S}_4$ with the representations Γ_1^a, Γ_5^a, Γ_1^b, Γ_3, Γ_5^b, Γ_4 and Γ_5^c, respectively, where the upper-script letter distinguishes between different subspaces transforming with the same representation.

The appearance of three dimensional irreducible representations in the classification of the order parameters can be understood as follows. The point group P of a single CoO_2-layer is D_{3d}, and the degree of its irreducible representations is less or equal 2. The point group is the factor group S/T where S is the space group of the CoO_2-layer and T is the subgroup of all pure translations. For our system it is convenient to consider the factor group $P' = S/2T$, where $2T$ is the subgroup of T that is generated by translations of $2\mathbf{a}_i$. P' is isomorphic to the cubic group O_h and has irreducible representations of degree 3. The operators $n_{\mathbf{Q}}^r$ and $\mathbf{S}_{\mathbf{Q}}^r$ transforms irreducibly under the translations in $2T$ for every r. The symmetry operations of P' however mix operators $n_{\mathbf{Q}}^r$ (or $\mathbf{S}_{\mathbf{Q}}^r$) with different r and the irreducible representations as given above or shown in Table 2.2 are obtained. Strictly speaking, the basis of SU(4) generators shown in Table 2.2 is the correct eigenbasis only for an infinitesimal small trigonal distortion. For a finite distortion, the representations Γ_1^a and Γ_1^b as well as Γ_5^a and Γ_5^b can hybridize as they transform with the same irreducible representation. Note, that Γ_5^c transforms differently under the time reversal symmetry. The situation here is similar to atomic physics, where a crossover from the Zeeman effect to the Paschen-Back effect with increasing magnetic field occurs, because states with the same J_z can hybridize.

2.6 Ordering patterns

In this section the different types of symmetry breaking phase transitions are discussed in a mean-field picture. The symmetry breaking is due to existence of a finite order parameter, that is in our case given by the expectation value $\langle n_{\mathbf{Q}}^r \rangle$ or $\langle \mathbf{S}_{\mathbf{Q}}^r \rangle$. Note, that a finite expectation value $\langle n_0^0 \rangle$ or $\langle n_0^4 \rangle$ does not break any symmetry of the CoO_2-layer.

is the symmetry group of the tetrahedron and O is the pure rotational subgroup of the full cubic symmetry group. $|\mathcal{S}_4| = |T_d| = |O| = 4!$.

In our tight-binding model as it was discussed in Sec. 2.2, the susceptibility, χ^0 is given by 4 identical plateaux around the Γ and the M points. In the presence of a trigonal distortion, the susceptibility still keeps a plateaux like structure but the diameter of the plateaux decreases, such that the susceptibility appears sharply enhanced around the M and the Γ points. Therefore we restrict the discussion to the case where $\mathbf{Q}$ equals zero and write n^r and $\mathbf{S}^r$ instead of n_0^r and $\mathbf{S}_0^r$ from now on. Note, that in our formalism the states with $\mathbf{Q} = 0$ describe periodic states with the enlarged unit cell of the kagomé lattice. But the internal degrees of freedom within this enlarged unit cell still allows for rather complicated charge- and spin-patterns. States with a small but finite $\mathbf{Q}$ describe modulations of these local states on long wavelengths. It is therefore important to understand first the local states the are described by $\mathbf{Q} = 0$ instabilities. Furthermore, only $\mathbf{Q} = 0$ states couple to the periodic potential produced by a Na-superstructure at $x = 0.5$.

The $\mathbf{Q} = 0$ instabilities lead to a chemical potential difference for states belonging to different hole pockets. In general, the BZ is folded and states of different hole pockets combine to new quasi-particles. In this case, translational and/or rotational symmetry is broken. Complex ordering patterns can be realized without opening of gaps, i.e., the system stays metallic.

We consider first the orderings given by a finite expectation value of the charge density operators n^r. This expectation value is given by

$$\langle n^r \rangle = \frac{4}{N} \sum_{\mathbf{K}l\sigma} \lambda_l^r \langle v_{\mathbf{K}\sigma}^{\dagger l} v_{\mathbf{K}\sigma}^l \rangle, \tag{2.33}$$

where λ_l^r are the eigenvalues of the matrix Q^r ($U_{ki}^r Q_{ij}^r \bar{U}_{lj}^r = \lambda_l^r \delta_{kl}$) and $v_{\mathbf{K}\sigma}^l = U_{ln}^r a_{\mathbf{K}\sigma}^n$ are the annihilation operators of the quasi-particles. If only one $\langle n^r \rangle \neq 0$, the effective interaction Hamiltonian in the mean-field approximation reduces to

$$\frac{\Lambda_r^c \langle n^r \rangle}{4} \sum_{\mathbf{K}l\sigma} \lambda_l^r v_{\mathbf{K}\sigma}^{\dagger l} v_{\mathbf{K}\sigma}^l. \tag{2.34}$$

If the coupling constant Λ_r^c is negative, the interaction energy of the system can be lowered by introducing an imbalance between the occupation numbers $n_l = \sum_{\mathbf{K}\sigma} \langle v_{\mathbf{K}\sigma}^{\dagger l} v_{\mathbf{K}\sigma}^l \rangle$. The operator $v_{\mathbf{K}\sigma}^\dagger$ creates a Bloch state with momentum $\mathbf{K}$ in the reduced BZ. The amplitudes of the three t_{2g} orbitals on a given Co site with these Bloch states can be obtained from Eq. (2.6) and (2.7) and the relation $a_{\mathbf{K}}^{\dagger l} \approx 1/\sqrt{3} \sum_m a_{\mathbf{K}m}^{\dagger l}$ which follows from Eq. (2.9) and (2.16).

For the matrices Q^{0-4} these Bloch states are given by a single t_{2g} orbital on each Co site. For the non-diagonal matrices Q^{4-9} these Bloch states are on each Co site proportional to a linear combination of t_{2g} orbitals of the form

$$\frac{1}{\sqrt{3}}(s_x d_x + s_y d_y + s_z d_z) \quad \text{with} \quad s_x, s_y, s_z = \pm 1. \tag{2.35}$$

This linear combination is the atomic d orbital $\varphi_0 \equiv \mathcal{Y}_{20}$ [c] parallel to the body-diagonal $[s_x, s_y, s_z]$ of the cubic environment around a Co atom (cf. Fig. 2.3).

The eigenvectors of the matrices Q^{10-15} are complex. A complex linear combination of t_{2g} orbitals has in general a non-vanishing expectation value of the orbital angular momentum operator $\mathbf{L}$. In Table 2.5 the angular momentum expectation values, which are relevant for our discussion are shown. The quasi-

Table 2.5: The expectation values the angular momentum operator $\mathbf{L}$ for several complex linear combinations of t_{2g} orbitals. $\omega = e^{2\pi i/3}$.

$(id_x + d_y + d_z)/\sqrt{3}$	$\langle \mathbf{L} \rangle = \hbar(0, -1, 1)2/3$	(cyclic)
$(id_x + d_y - d_z)/\sqrt{3}$	$\langle \mathbf{L} \rangle = \hbar(0, 1, 1)2/3$	(cyclic)
$(d_x + \omega^2 d_y + \omega d_z)/\sqrt{3}$	$\langle \mathbf{L} \rangle = \hbar(1, 1, 1)/\sqrt{3}$	
$(\omega^2 d_y + \omega d_z)/\sqrt{2}$	$\langle \mathbf{L} \rangle = \hbar(1, 0, 0)\sqrt{3}/2$	(cyclic)

particles $v^l_{\mathbf{K}\sigma}$ are expressed in terms of pocket operators by $v^l_{\mathbf{K}\sigma} = \hat{U}^r_{lm} b^m_{\mathbf{K}\sigma}$, where the unitary matrix $\hat{U}^r_{lm} = U^r_{ln}\mathcal{F}_{nm}$ diagonalizes K^r. From this follows that if K^r is already diagonal, no folding of the BZ occurs and translational symmetry is not broken. Otherwise, the BZ is folded and states of different pockets recombine to form the new quasi-particles.

Now we consider finite expectation values of the spin-density operators $\mathbf{S}^r$. Due to the absence of spin-orbit coupling, our model has an SU(2) rotational symmetry in spin space. Therefore the discussion can be restricted to the order parameters $\langle S^r_z \rangle = \langle \mathbf{e}_z \cdot \mathbf{S}^r \rangle$, given by

$$\langle S^r_z \rangle = \frac{2}{N} \sum_{\mathbf{K}l\sigma} \lambda^r_l \sigma \langle v^{\dagger l}_{\mathbf{K}\sigma} v^l_{\mathbf{K}\sigma} \rangle, \tag{2.36}$$

[c] The orbital $\varphi_0 \equiv \mathcal{Y}_{20}$ is real and is given by a radial function multiplied by the spherical harmonic Y_{20}. The axes around which φ_0 is invariant can be specified.

where σ in formula takes the values 1 (-1) for $\sigma = \uparrow$ $(\sigma = \downarrow)$. If only one $\langle S_z^r \rangle \neq 0$, the effective interaction Hamiltonian reduces to

$$\frac{\Lambda_r^s \langle S_z^r \rangle}{2} \sum_{\mathbf{K}l\sigma} \lambda_l^r \sigma \, v_{\mathbf{K}\sigma}^{\dagger l} v_{\mathbf{K}\sigma}^l. \tag{2.37}$$

The mean-field Hamiltonian (2.37) is given by the same quasi-particles and the same eigenvalues λ_l^r as the Hamiltonian in (2.34). The only difference is that the sign of the splitting of the quasi-particle bands depends on the spin. In the following, all ordering transitions with order parameters $\langle n^r \rangle$ and $\langle S_z^r \rangle$ for $r = 0, \ldots, 15$ are shortly discussed.

$r = 0$

- *Charge:* The expectation valued $\langle n^0 \rangle$ is the total charge of the system, which is fixed and non-zero, even in the paramagnetic phase.

- *Spin:* A finite value of $\langle S_z^0 \rangle$ describes a Stoner ferromagnetic instability. The coupling constant Λ_0^s given in Table 2.4 is the most negative coupling constant. In the unperturbed system without trigonal distortion, the critical temperature of all continuous transitions discussed here, only depends on the density of states and on the coupling constant in the mean-field picture. In this case, ferromagnetism is the leading instability for the unperturbed system. In the real CoO_2-plane, this must not necessarily occur, but strong ferromagnetic fluctuations will be present in any case.

$r = 1, 2, 3$

- *Charge:* A finite expectation value $\langle n^r \rangle$ for $r = 1, 2, 3$ corresponds to a difference in the charge density on the four kagomé lattices, because the matrices Q^{1-3} of Table 2.2 are diagonal and the quasi-particles $v_{\mathbf{K}\sigma}^{\dagger l}$ are just the kagomé states $a_{\mathbf{K}\sigma}^{\dagger l}$. From the view point of Fermi surface pockets given by K^{1-3} which are non-diagonal, this order yields a folding of the BZ, because the quasi-particles $v_{\mathbf{K}\sigma}^{\dagger l}$ are linear combinations of states belonging to different hole pockets. This means that the translational symmetry is broken. In the matrix Q^{1-3} we find two positive and two negative diagonal elements. Consequently, a finite expectation value $\langle n^{1-3} \rangle$ leads to a charge enhancement on two kagomé lattices and to a

charge reduction on the other two. As specifying two kagomé lattices specifies a direction on the triangular lattice, rotational symmetry is broken and crystal symmetry is reduced from hexagonal to orthorhombic. The phases described by the matrices Q^{1-3} have the same coupling constant Λ_1^c because they transform irreducibly into each other under crystal symmetries with the representation Γ_5^a. In order to examine which linear combinations of the three order parameters $\langle n^1 \rangle$, $\langle n^2 \rangle$ and $\langle n^3 \rangle$ could be stable below the critical temperature, we consider the Landau expansion of the free energy $\Delta F = F - F_0$

$$\begin{aligned} \Delta F &= \frac{\alpha}{2}(\eta_1^2 + \eta_2^2 + \eta_3^2) + \beta\,\eta_1\,\eta_2\,\eta_3 + \frac{\gamma_1}{4}(\eta_1^2 + \eta_2^2 + \eta_3^2)^2 \\ &\quad + \frac{\gamma_2}{4}(\eta_1^2\,\eta_2^2 + \eta_2^2\,\eta_3^2 + \eta_3^2\,\eta_1^2), \end{aligned} \tag{2.38}$$

with $\eta_1 = \langle n^1 \rangle$, $\eta_2 = \langle n^2 \rangle$, $\eta_3 = \langle n^3 \rangle$. The real parameters are α, β, γ_1, and γ_2 are the phenomenological Landau parameters. For $\gamma_1 > \max\{0, -\gamma_2\}$, the free energy is globally stable. For $\gamma_2 < 0$, Eq. (2.38) has a minimum of the form $\eta_1 = \eta_2 = \eta_3$, if $\beta^2 - 4\alpha(3\gamma_1 + \gamma_2) > 0$. This phase is described by the symmetric combination $\tilde{Q}^1 = (Q^1 + Q^2 + Q^3)/\sqrt{3}$ which does not break the rotational symmetry. In Fig. 2.6, the folding of BZ and the splitting of the bands (the dotted line is triply degenerate) and the orbital pattern of the quasi-particles $v_{\mathbf{K}\sigma}^{\dagger l} = a_{\mathbf{K}\sigma}^{\dagger l}$ are shown. Note that $\tilde{Q}^1$ has one positive and three negative diagonal elements. The charge is enhanced or reduced on a single kagomé lattice depending on the sign of the coefficient β in Eq. (2.38). The third-order term in the free energy expansion is allowed by symmetry, because there is no inversion-like symmetry that would switch $(\eta_1, \eta_2, \eta_3) \rightarrow (-\eta_1, -\eta_2, -\eta_3)$. Therefore the transition can be first order. On the other hand, for $\gamma_2 > 0$, there is a competition between the terms proportional to γ_2 and β in Eq. (2.38). The minimum has not a simple form. For $|\beta| \ll \gamma_2$, however, the transition yields states approximately described by the matrix Q^1, Q^2 or Q^3. In any case this phase does break the rotational symmetry.

- *Spin:* The spin density mean-fields $\langle S_z^i \rangle$ $i = 1, 2, 3$ transform under space group symmetries like Γ_5^a and time reversal symmetry gives $\langle S_z^i \rangle$ to $-\langle S_z^i \rangle$. Due to the latter the third order term in Eq. (2.38) is forbidden, so that the transition is continuous. For $\gamma_2 < 0$, Eq. (2.38) has again a minimum of the form $\eta_1 = \eta_2 = \eta_3$, whereas for $\gamma_2 > 0$ the minimum is realized for $\eta_1 \neq 0$ and $\eta_2 = \eta_3 = 0$ (and permutations), if $\alpha < 0$. The folding of the

BZ, the quasi-particles and the breaking of space-group symmetries is the same as for the charge density operators n^i. However, the splitting of the bands depends now on the spin and time reversal symmetry is broken.

These states are spin density waves, spatial modulations of the spin density with a vanishing total magnetization. The two different types of spin density modulations for $\gamma_2 > 0$ or $\gamma_2 < 0$ are shown in Fig. 2.7. For $\gamma_2 > 0$ rotational and translational symmetry is broken yielding a collinear spin orientation along one spatial direction and alternation perpendicular. In contrast $\gamma_2 < 0$ yields a rotationally symmetric spin density wave with a doubled unit cell. This special type of spin density wave gives a subset of lattice points, forming a triangular lattice, of large spin density and another subset with opposite spin density of a third in size, forming a kagomé lattice. Both states are metallic, because no gaps are opened at the FS. This spin density wave is not a result of Fermi surface nesting, but due to the complex orbital structure. The coupling constant for this transition, Λ_1^s is the second strongest coupling in the model Hamiltonian after the ferromagnetic coupling constant, Λ_0^s, as it is best seen in Fig. 2.10 which will be discussed in the next section.

$r = 4$

- *Charge:* As discussed in Sec. 2.5, a finite expectation value of n^4 does not break any space group symmetry. The matrix K^4 is diagonal with one positive and three negative elements. This leads to a change of the band energy of the band at the Γ point relative to those at the M points (Fig. 2.8 (a)). This results in an orbital order, a pattern as shown in Fig. 2.8 (a), because the number of holes associated with the hole pocket around the Γ point is different from that of the other pockets. The net charge onsite vanishes, but the charge distribution has the quadrupolar form, which results from

$$\begin{aligned} \rho(r) \;\propto\; & \frac{1}{4}\Big(3|\psi_{yz}+\psi_{zx}+\psi_{xy}|^2 - |\psi_{yz}-\psi_{zx}+\psi_{xy}|^2 \\ & - |\psi_{yz}+\psi_{zx}-\psi_{xy}|^2 - |\psi_{yz}-\psi_{zx}-\psi_{xy}|^2\Big) \qquad (2.39) \\ =\; & \left(\psi_{yz}^*\psi_{zx}+\psi_{zx}^*\psi_{xy}+\psi_{xy}^*\psi_{yz}+\text{c.c.}\right). \end{aligned}$$

The corresponding tensor operator belongs to the representation Γ_1 of the subgroup D_3 of the cubic group with the three-fold rotation axis

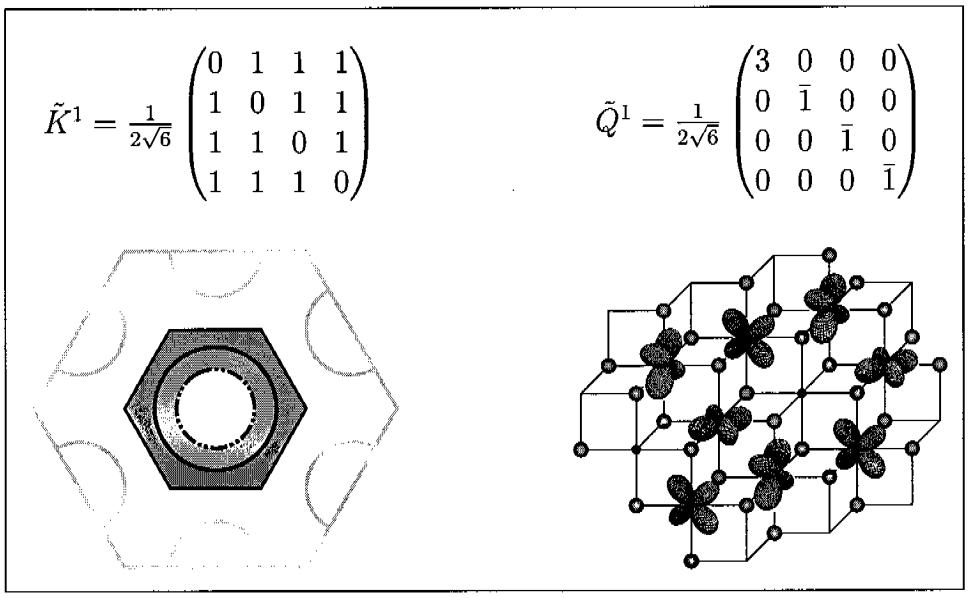

Figure 2.6: Charge ordering instability with finite expectation value $\langle \tilde{n}_0^1 \rangle = \langle n_0^1 + n_0^2 + n_0^3 \rangle / \sqrt{3}$ leading to a charge enhancement or reduction on one kagomé lattice. The folding of the BZ and the splitting of the pockets is shown (The double dotted line in the BZ indicates a triply degenerate pocket). On the right a quasi-particle state that is in this case just a kagomé lattice state is drawn.

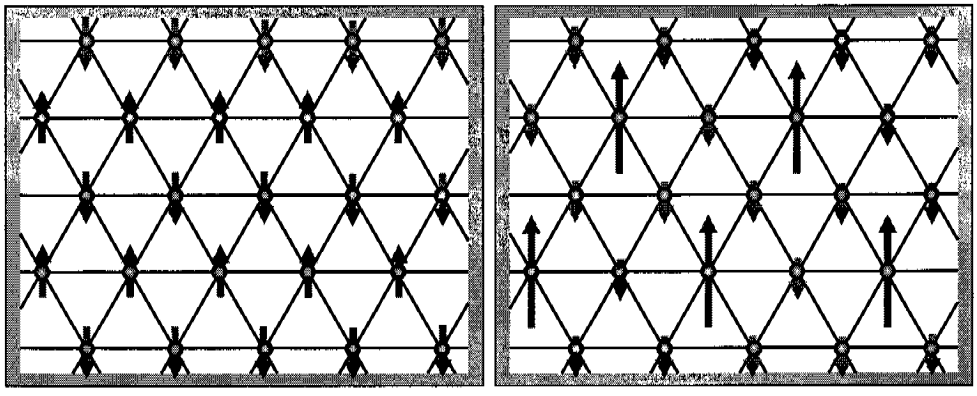

Figure 2.7: The spin density wave patterns corresponding to a finite expectation value $\langle S_z^1 \rangle$ is shown on the left. This pattern is stabilized if $\gamma_2 > 0$ in Eq. (2.38). The pattern on the right corresponds to a finite order parameter $\langle S_z^1 + S_z^2 + S_z^3 \rangle$, which is stabilized for $\gamma_2 < 0$.

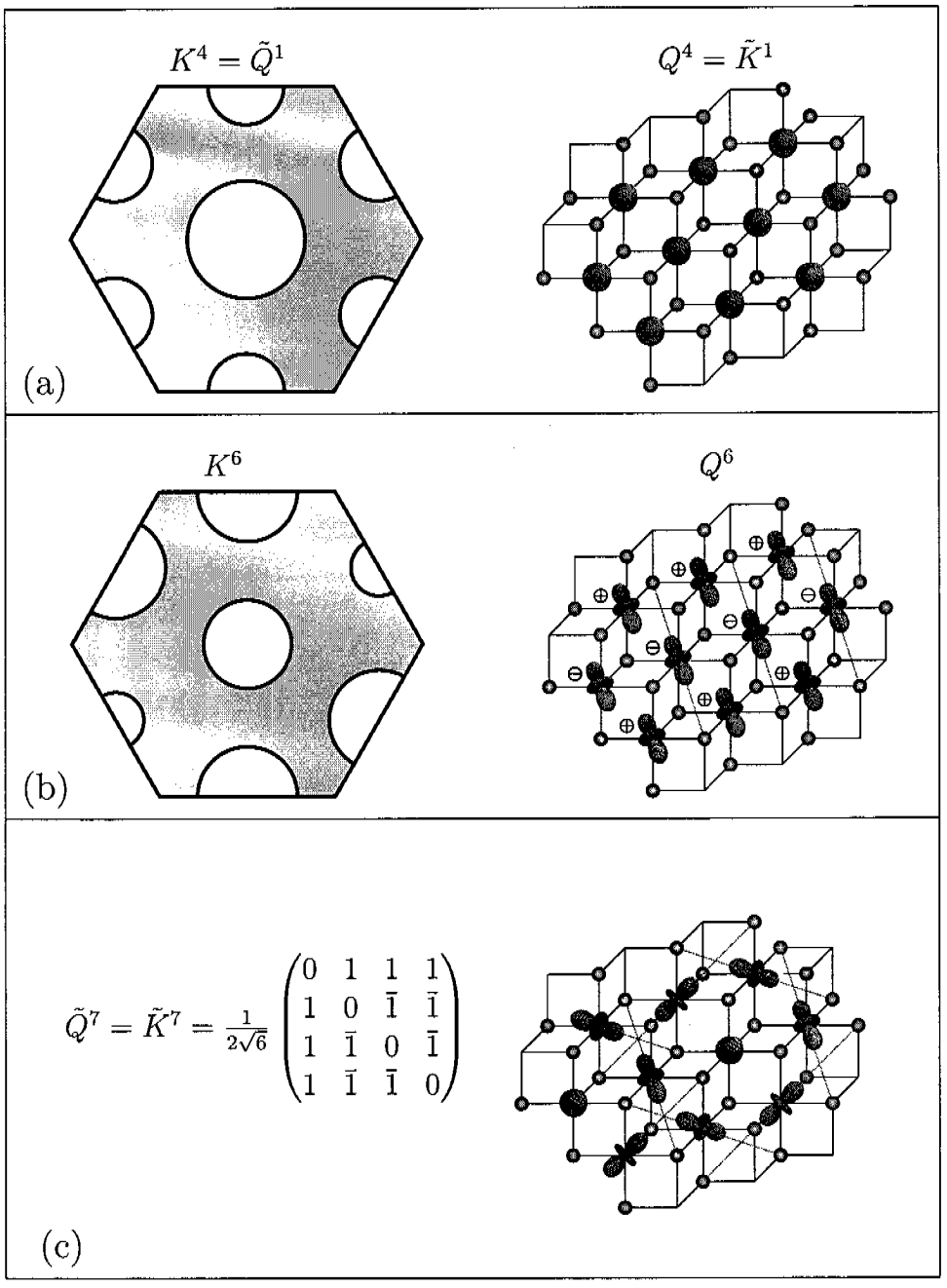

Figure 2.8: Ordering instabilities, described by real off-diagonal SU(4) generators Q^{4-9}. (a) Q^4 breaks neither translational nor rotational symmetry. (b) shows the ordering corresponding to Q^6. The ordering shown in (c) is described in real space and in reciprocal space by the same matrix $\tilde{Q}^7 = \tilde{K}^7$ and breaks translational symmetry. The corresponding BZ is shown in Fig. 2.6.

parallel to [111], i.e., along the c-axis perpendicular to the layer. This quadrupolar field would be driven by the symmetry reduction discussed above, through trigonal distortion and direct dd-hopping among the t_{2g} orbitals.

- *Spin:* While the corresponding order parameter $\langle S_z^4 \rangle$ breaks time reversal symmetry, space group symmetry is conserved. This order is spatially uniform analogous to a ferromagnet without, however, having a net magnetic moment. Because the magnetic moment associated with the Fermi surface pocket at the Γ point is opposite and three times larger than the moment at the three M pockets. While the net dipole moment vanishes on every site, this configuration has a finite quadrupolar spin density corresponding to the onsite spin density distribution of the same form as the charge distribution in Eq. (2.39), which also belongs to Γ_1 representation of D_3. It is also important to note that no third order terms are allowed due to broken time reversal symmetry, such that the transition to this order would be continuous.

$r = 5, 6$

- *Charge:* The order parameters $\langle n^5 \rangle = \eta_5$ and $\langle n^6 \rangle = \eta_6$ transform according to the irreducible representation Γ_3 of the cubic point group. The Landau expansion of the free energy is given by

$$\Delta F = \frac{\alpha}{2}(\eta_5^2 + \eta_6^2) + \frac{\beta}{3}\eta_6(3\eta_5^2 - \eta_6^2) + \frac{\gamma}{4}(\eta_5^2 + \eta_6^2)^2, \tag{2.40}$$

whose global stability requires $\gamma > 0$. The third order term, allowed here, induces a first order transition and simultaneously introduce an anisotropy which is not present in the second- and fourth-order terms. We can write $(\eta_5, \eta_6) = \eta(\cos\varphi, \sin\varphi)$ and obtain

$$\Delta F = \frac{\alpha}{2}\eta^2 + \frac{\beta}{3}\eta^3 \sin 3\varphi + \frac{\gamma}{4}\eta^4. \tag{2.41}$$

Depending on the sign of β the stable angles will be $\varphi = \mathrm{sign}(\beta)\pi/2 + 2\pi n/3$. This yields three degenerate states of uniform orbital order whose charge distribution has the quadrupolar form:

$$\begin{aligned} \rho(r) \quad \propto \quad & e^{i\varphi}\Big[(\psi_{zx}^*\psi_{xy} + \psi_{xy}^*\psi_{zx}) + \omega(\psi_{yz}^*\psi_{zx} + \psi_{zx}^*\psi_{yz}) \\ & + \omega^2(\psi_{xy}^*\psi_{yz} + \psi_{yz}^*\psi_{xy})\Big] + \text{c.c.} \end{aligned} \tag{2.42}$$

with a tensor operator belonging to Γ_3 of D_3. Each state is connected with the choice of one M pocket which has a different filling compared to the other two (Fig. 2.8 (b). The main axis of each state points locally along one of the three cubic body-diagonals, $[\bar{1},1,1]$, $[1,\bar{1},1]$, $[1,1,\bar{1}]$, and the sign of the local orbital wave function is staggered along the corresponding direction on the triangular lattice, $[\bar{2},1,1]$, $[1,\bar{2},1]$, $[1,1,\bar{2}]$. In this way the rotational symmetry is broken but the translational symmetry is conserved. The matrices Q^5 and Q^6 commute with Q^4 such that the external symmetry reduction has only a small effect on this type of order.

- *Spin:* The spin densities $\langle S_z^5 \rangle$ and $\langle S_z^6 \rangle$ also belong to the two-dimensional representation Γ_3 of the cubic point group. Here time reversal symmetry ensures that the Landau expansion only allows even orders of the order parameter $(\eta_5, \eta_6) = \eta(\cos\varphi, \sin\varphi)$ (i.e., $\beta = 0$ in Eq. (2.40)). The continuous degeneracy in φ is only lifted by the sixth order term, given by

$$\frac{\delta_1}{6}(\eta_5^2+\eta_6^2)^3 + \frac{\delta_2}{6}\eta_6^2(3\eta_5^2-\eta_6^2)^2 = \frac{\delta_1}{6}\eta^6 + \frac{\delta_2}{6}\eta^6\sin^2 3\varphi \qquad (2.43)$$

  Stability requires $\delta_1 > \max\{0, -\delta_2\}$. The anisotropy is lifted by the δ_2-term which give rise to two possible sets of three-fold degenerate states. Depending on the sign of δ_2 we have a minimum of the free energy for $\varphi = (1 - \operatorname{sign}\delta_2)\pi/4 + \pi n$. The corresponding spin densities have no net dipole on every site, but again a quadrupolar form of the same symmetry as for the charge, given by Eq. (2.42).

$r = 7, 8, 9$

- *Charge:* The order parameters $\langle n^i \rangle$ for $i = 7, 8, 9$ transform irreducibly under space group symmetries with the representation Γ_5^b. The expansion (2.38) of the free energy holds also for these order parameters. The third order term makes the transition first order and favors the symmetric rotationally invariant combination of the order parameters, described by the matrix $\tilde{Q}^7 = (Q^7 + Q^8 + Q^9)/\sqrt{3} = \tilde{K}^7$ shown in Fig. 2.8 (c). The folding of the BZ and the splitting of the bands is the same as in Fig. 2.6. The orbital pattern of the non-degenerate quasi-particle band is also shown in Fig. 2.8 (c). It consists of atomic φ^0 orbitals pointing along

all four cubic space diagonals. Translational but not rotational symmetry is broken.

- *Spin:* The discussion for the spin density operators is analogous to the discussion in the section $r = 1, 2, 3$.

$r = 10, 11, 12$

- *Charge:* The order parameters $\langle n^i \rangle$ for $i = 10, 11, 12$ transform irreducibly under space group symmetries with the representation Γ_4. For the Γ_4 representation of T_d, there is no third order invariant. All other terms in Eq. (2.38) are however also invariants for Γ_4. The absence of the third order term leads to continuous transition. The stabilized state for $\alpha < 0$ depends on the sign of γ_2 in Eq. (2.38).

  For $\gamma_2 > 0$ a nontrivial minimum with $\langle n^{11} \rangle = \langle n^{12} \rangle = 0$ exists, which is described by the hermitian, imaginary matrix Q^{10}. If λ is an eigenvalue of Q^{10}, then $-\lambda$ is also an eigenvalue of Q^{10} and the corresponding quasi-particles are connected by time reversal symmetry. Therefore the non-vanishing eigenvalues of Q^{10} belong to quasi-particle states, which are not invariant under time reversal symmetry. They are given by complex linear combinations of t_{2g} orbitals. For complex linear combinations of t_{2g} orbitals, the expectation value of the orbital angular momentum operator $\langle \mathbf{L} \rangle$ does not vanish in general, as can be seen from Table 2.5. In Fig. 2.9 (a), the pattern of the angular momentum expectation values $\langle \mathbf{L} \rangle$ for a quasi-particle of Q^{10} is shown. It is invariant under translations along $\mathbf{a}_1$ and staggered under translations along $\mathbf{a}_2$ and $\mathbf{a}_3$. The expectation values of $\mathbf{L}$ are parallel to [011]. The folding of the BZ and the splitting of the bands is shown in Fig. 2.9 (c). Rotational, translational and time reversal symmetry is broken and the state has the magnetic point-group $\underline{2}/\underline{m}$.

  For $\gamma_2 < 0$ the symmetric combination $\tilde{Q}^{10} = (Q^{10}+Q^{11}+Q^{12})/\sqrt{3} = \tilde{K}^{10}$ is stabilized. The angular momentum pattern for a quasi-particle with non-vanishing eigenvalue is shown in Fig. 2.9 (a). Depending on the site, the expectation value points along [100], [010], [001] or $[\bar{1}\bar{1}\bar{1}]$ and the magnitudes are such, that the pattern is rotationally invariant and the expectation value of the total angular momentum perpendicular to the

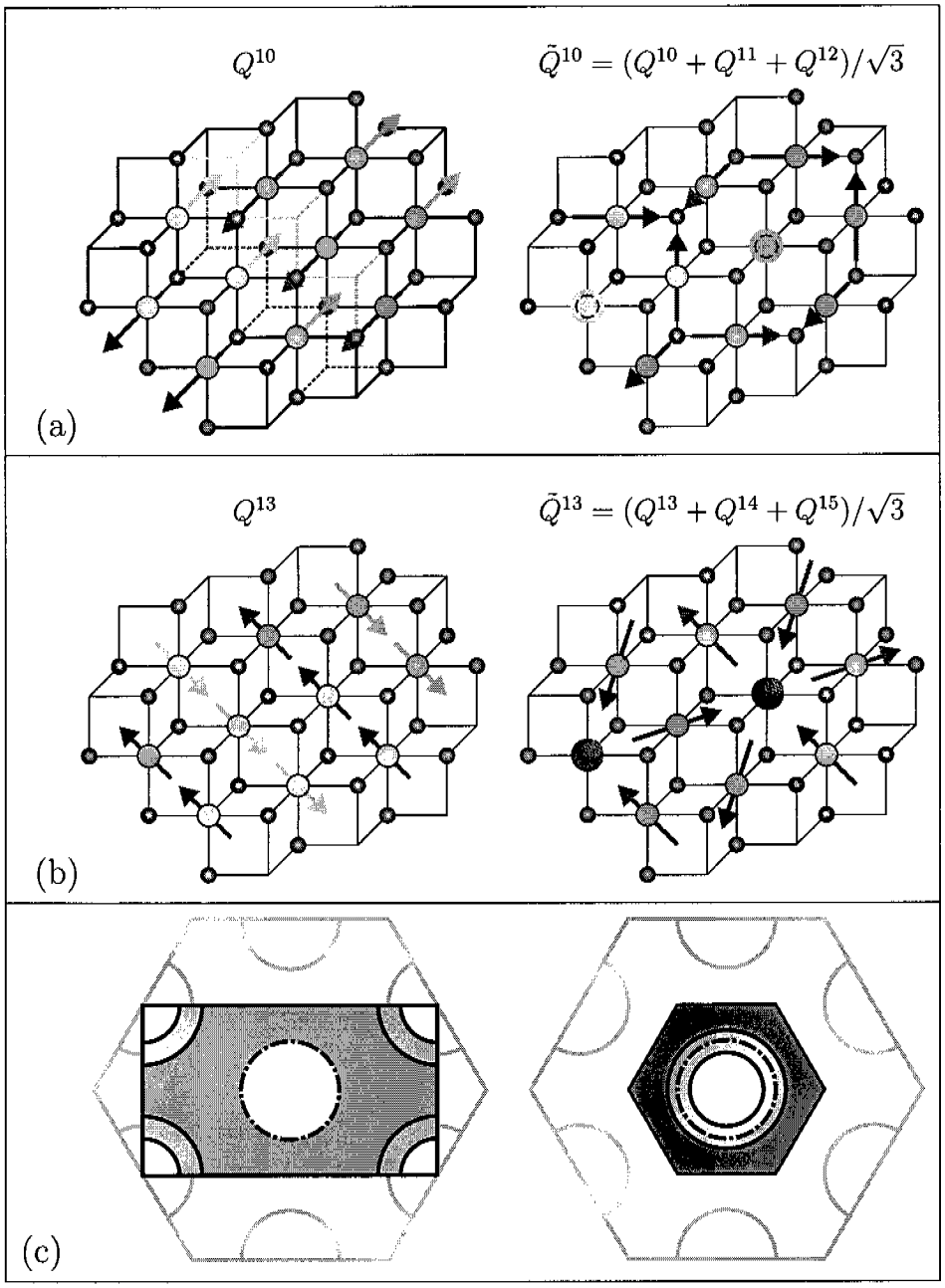

Figure 2.9: Transitions to time reversal symmetry breaking states, where the expectation value of the orbital angular momentum $\langle \mathbf{L} \rangle$ on the Co-sites is finite. (a) States where the angular momentum does not lie in the plane. $\tilde{K}^{10} = \tilde{Q}^{10}$. (b) States with the angular momentum in the plane. $\tilde{K}^{13} = -\tilde{Q}^{13}$. (c) The folding of the BZ and the hybridization of the bands for (a). Dotted lines indicate double degenerate bands.

plane vanishes. The folding of the BZ and the splitting of the pockets is shown in Fig. 2.9 (c). This state has the magnetic point group $\underline{\bar{3}m}$. Note, that these states can also be considered as a kind of staggered flux states. The matrices Q^{10-12} commute with Q^4 and therefore the transitions are only little affected by a trigonal distortion.

- *Spin:* The spin density order parameters $\langle S_z^i \rangle$ for $i = 10, 11, 12$ also transform under space group symmetries like Γ_4 and except for the spin dependent quasi-particle energy, the discussion is the same as for the charge density operators. Note, however, that these spin density operators do not change sign under time reversal symmetry, because both the orbital angular momentum and the spin is reversed. This, however does not lead to a third order term in the Landau expansion, as there is no third order invariant for the Γ_4 representation anyway.

$r = 13, 14, 15$

- *Charge:* The order parameters $\langle n^i \rangle$ for $i = 13, 14, 15$ transform irreducibly under space group symmetries with the representation Γ_5^c. The matrices Q^{13-15} are also imaginary and time reversal symmetry changes the sign of the order parameters. The Landau expansion of the free energy is given as above by Eq. (2.38) with $\beta = 0$.

  For $\gamma_2 > 0$ and $\alpha < 0$ a minimum of the free energy is given by the order parameter $\langle n^{13} \rangle$. The angular momentum pattern of the quasi-particles is shown in Fig. 2.9 (b). The expectation values of $\mathbf{L}$ lie in the CoO_2-plane and are parallel to the $\mathbf{a}_1$ direction. Their sign is staggered along the $\mathbf{a}_2$ and $\mathbf{a}_3$ direction. The quasi-particles consist of states belonging to the Γ and the M pocket. The folding of the BZ is given in Fig. 2.9 (c), but with the single dotted line in the center being a doubly degenerate M pocket. Rotational, translational and time reversal symmetry is broken.

  For $\gamma_2 < 0$ the symmetric combination $\tilde{Q}^{13} = (Q^{13} + Q^{14} + Q^{15})/\sqrt{3} = -\tilde{K}^{13}$ is stabilized. The pattern of the quasi-particles corresponding to $\tilde{Q}^{13}$ is shown in Fig. 2.9 (b). It consists of non-magnetic sites with a φ_0 orbital perpendicular to the plane and of sites with angular momentum expectation values along $\mathbf{a}_i$. Rotational symmetry is not broken in this case. The folding of the BZ and the splitting of the bands is shown in Fig. 2.9 (c). All angular momentum expectation values for these two

states lie in the CoO_2-plane. Therefore, it is not possible to interpret these states as staggered flux states.

- *Spin:* The spin density order parameters $\langle S_z^i \rangle$ for $i = 13, 14, 15$ are invariant under time reversal symmetry. Therefore, the third order term in Eq. (2.38) is allowed and the transition is a first order transition.

An overview over the different symmetry breaking states is provided in Table 2.6.

2.7 Possible instabilities

2.7.1 Coupling constants

As can be seen from Table 2.4, the coupling constants for the spin density wave (SDW) transitions Λ^s are rather negative whereas the charge coupling constants Λ^c tend to be positive. This is not surprising as only local repulsive interaction is considered here, that tends to spread out the charge as much as possible.

The coupling constants $\Lambda_r^{c/s}$ with $r = 0, \ldots, 3$ depend on the intra-orbital Coulomb repulsion U. As U is the largest Coulomb integral, the absolute value of these coupling constants is biggest. The remaining coupling constants $\Lambda_r^{c/s}$ do not depend on U. For $J' = 0$ they are also independent of r. For finite J' the degeneracy between the real (4-9) and imaginary (10-15) SU(4) generators is lifted. In order to compare the different coupling constants, we reduce the number of parameters and we use the relations $U = U' + 2J_H$ and $J_H = J'$, that hold exactly in a spherically symmetric system, but can be assumed to hold approximately for our system. The ratio $\alpha = U'/U$ is positive and usually larger than 1/2 and smaller than 1. These assumptions allow to order the dimensionless coupling constants $\tilde{\Lambda}^{c/s} = 9\Lambda^{c/s}/(2U)$ according to their strength. In Fig. 2.10 the dimensionless coupling constants $\tilde{\Lambda}_r^{c/s}$ are shown as functions of α. The most negative coupling constant is the ferromagnetic one with $\tilde{\Lambda}_0^s = -6 + 3\alpha$. For α close to 1, the coupling constant for spin density order $\tilde{\Lambda}_1^s = -(2 + \alpha)$ is comparable. Smaller but still clearly negative are also the coupling constants for the spin density angular momentum states $\tilde{\Lambda}_{10}^s = -(1 + \alpha)$. The coupling constants $\tilde{\Lambda}_4^c = \tilde{\Lambda}_4^s = 1 - 3\alpha$ are also negative. Finally, the coupling constant for time reversal symmetry breaking angular momentum states $\tilde{\Lambda}_{10}^c = 3 - 5\alpha$ and for the charge density order $\tilde{\Lambda}_1^c = 4 - 5\alpha$

Table 2.6: The possible symmetry breaking states for the spin density and charge density operators. The first column gives the irreducible representations of $\mathcal{S}_4$. An x marks the presence of a symmetry. Θ stands for time reversal symmetry. The minimal number of primitive translations along the three lattice directions is given below T ($\underline{1}$: translation followed by Θ) and finally the (magnetic) point group is given.

		spin					charge				
r		Θ	C_3	C_x	T		Θ	C_3	C_x	T	
0	Γ_1		x	x	(111)	$\bar{3}m$					
1–3	Γ_5		x	x	(222)	$\bar{3}m$	x	x	x	(222)	$\bar{3}m$
				x	(122)	$2/m$	x		x	(122)	$2/m$
4–9	Γ_1		x	x	(111)	$\bar{3}m$	x	x	x	(111)	$\bar{3}m$
	Γ_3			x	(111)	$2/m$	x		x	(111)	$2/m$
					(111)	$\bar{1}$					
	Γ_5		x	x	(222)	$\bar{3}m$	x	x	x	(222)	$\bar{3}m$
				x	(122)	$2/m$	x		x	(122)	$2/m$
10-15	Γ_4	x	x	x	(222)	$\bar{3}m$		x		(222)	$\bar{3}\underline{m}$
		x		x	(122)	$2/m$				(1$\underline{1}$1)	$\underline{2}/\underline{m}$
	Γ_5	x	x	x	(222)	$\bar{3}m$		x	x	(222)	$\bar{3}m$
		x		x	(122)	$2/m$			x	(1$\underline{1}$1)	$2/m$

are rather positive, but can in principle also be negative if α is close enough to one. In fact it is quite remarkable that for $\alpha > 0.8$ all coupling constants constants (except Λ_0^c) are negative. For $\alpha = 1$ additional degeneracies among the coupling constants appear, as can be seen in Fig. 2.10. This indicates the existence of a higher symmetry at this point. In fact, the local Coulomb interaction $H_{\mathbf{r}}^{\mathrm{C}}$ of Eq. (2.15) depends only on the total charge $n_{\mathbf{r}} = \sum_{m\sigma} n_{\mathbf{r}m\sigma}$ on the site $\mathbf{r}$ and is given by $Un_{\mathbf{r}}(n_{\mathbf{r}} - 1)/2$ for $\alpha = 1$.

2.7.2 Effect of the trigonal distortion

In the mean-field description, an instability occurs if the Stoner-type criterion is satisfied. At zero temperature in the system with full symmetry, this criterion

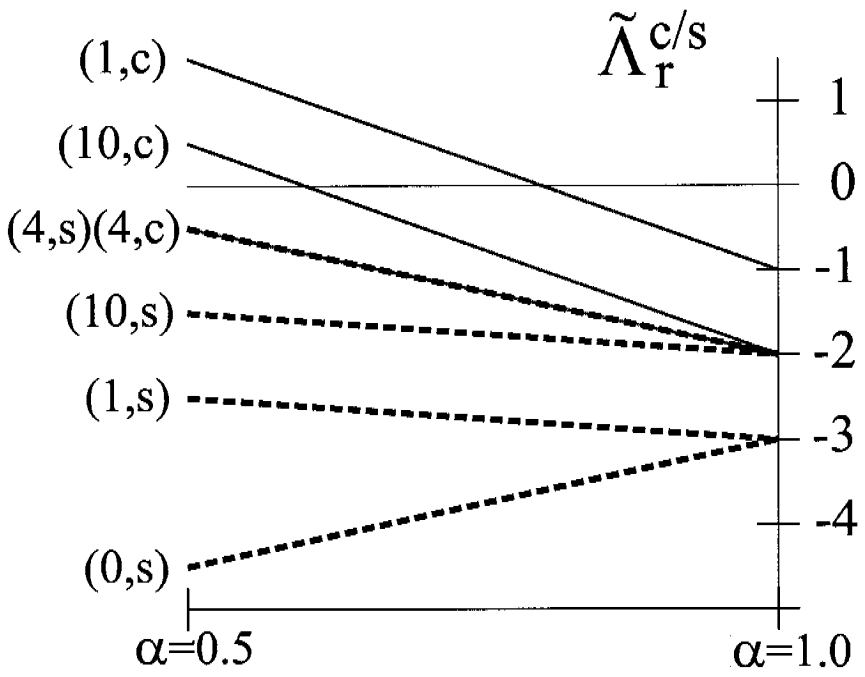

Figure 2.10: The dimensionless coupling constants $\tilde{\Lambda}_r^{c/s} = 9\Lambda^{c/s}{}_r/(2U)$ as functions of $\alpha = U'/U$. The relations $U = U' + 2J_H$ and $J' = J_H$ are assumed to hold. The solid (dashed) lines denote the charge (spin) coupling constants.

reads in our notation as

$$\frac{-\Lambda_r^{c/s}}{4} D(E_F) = 1, \tag{2.44}$$

where $D(E_F)$ is the density of states per spin and per hole pocket. For rather small pockets $D(E_F)$ is given by $\sqrt{3}/(2\pi t) \approx 0.28/t$ in our tight-binding model, increases however with decreasing E_F (cf. Fig. 2.5). From Eq. (2.44) we can estimate that the critical U must be larger than $10\,t$ for having a ferromagnetic instability. With the introduction of the trigonal distortion, as it was discussed in Sec. 2.5, the Stoner criteria of Eq. (2.44) are modified.

For the order parameters described by the matrices K^0, K^4, K^{5-6}, and K^{10-12}, that commute with the trigonal distortion, K^4, the change of the Stoner criterion is only due to the changing of the density of states at the M and the Γ pockets by the trigonal distortion, and the Stoner criterion is only slightly modified as long as all four pockets exist. On the other hand, the instabilities towards states, where the order parameters with the matrices K^{13-15} are finite,

would be strongly affected by the trigonal distortion, as the pocket states that hybridize in such a transition are no longer degenerate.

Finally, as mentioned above, the order parameters described by the matrices K^{1-3} and K^{7-9} transform with the same representation and are mixed by the trigonal distortion. For strong distortions the mixing tends to odd-even combinations and only the odd combinations, $K^1 - K^7$, $K^2 - K^8$, $K^3 - K^9$ commute with the symmetry breaking field, K^4, and connects the still degenerate states of the M pockets. If the trigonal distortion is so strong, that the pockets states at the M points lie below the FS, only a spontaneous ferromagnetic instability can still occur according to the Stoner criterion. First order transitions, however, are still possible.

The ferromagnetism is the leading instability in the symmetric model and is least affected by the trigonal distortion. Therefore, in real Na_xCoO_2 systems where a rather strong trigonal distortion is unavoidably present, ferromagnetism would be most robust and is in fact the only type of all the described, exotic symmetry breaking states, that would have a chance to occur spontaneously.

However, even if the coupling constants of the more exotic states are not negative enough, to produce a spontaneous instability, their corresponding susceptibilities can be large enough to give rise to an important response of the electrons in CoO_2-plane to external perturbations. In the next section, we describe how the Na-ions can be viewed as an external field for the charge degrees of freedom.

2.8 Na-superstructures

In Na_xCoO_2 the Na-ions separate the CoO_2-planes. There are two different Na-positions which are both in prismatic coordination with the nearest O-ions. The Na2 position is also in prismatic coordination with the nearest Co-ions, while the Na1 position lies along the c-axis between two Co-ions below and above as shown in Fig. 2.11 This leads to significant Na–Co repulsion, suggesting that the Na1 position is higher in energy. In fact, the Na2 position is the preferred site for $Na_{0.75}CoO_2$, where the ratio of occupied Na1-sites to occupied Na2-sites is about 1:2 [32]. Deintercalation of Na does however not lead to a further depletion of the Na1-sites. On the contrary, the occupancy ratio goes to 1 for x going to 0.5. Further there is a clear experimental evidence, that at $x = 0.5$ the Na-ions form a commensurable orthorhombic superstructure already at room

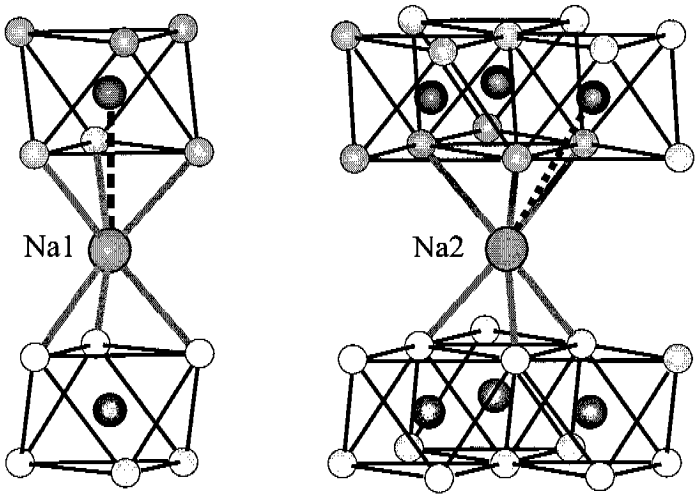

Figure 2.11: The two different Na-positions in Na_xCoO_2. Note, that the Na1 position is located between two Co-ions along the c-axis.

temperature [28]. For several other values of x also superstructure formation has been reported, but $x = 0.5$ shows the strongest signals and has the simplest superstructure [29, 30]. In addition for $x = 0.5$ samples a sharp increase of the resistivity at 50 K respectively at 30K was reported [27, 31, 41].

This experimental situation is rather surprising. Naively, one expects commensurability effects to be strongest at $x = 1/3$ or at $x = 2/3$ on a triangular lattice but not at $x = 0.5$. Therefore, it was concluded that structural and electronic degrees of freedom are coupled in a subtle manner in Na_xCoO_2 [32].

In this section we show how the different ordering patterns can couple to the observed Na-superstructure at $x = 0.5$. Before going into the details, we note that due to our starting point of inter-penetrating kagomé lattices, commensurability effects will be strongest for samples where the Na-ions can form a simple periodic superstructures that double or quadruple the area of the unit cell, since specifying a single kagomé lattice also quadruples the unit cell. For $x = 0.5$ such simple superstructures exist as shown in Fig. 2.12. A sodium superstructure couples to the charge but not to the spin degrees of freedom in the CoO_2-layer. In our model, there are 15 collective charge degrees of freedom. From Fig. 2.10 can be seen that Λ_r^c is most negative for $r = 4, \ldots, 9$. Hence, these modes are the "softest" charge modes generating the strongest response to a Na-pattern. As shown in Fig. 2.8, the charge order corresponding to $r = 4, 5, 6$ does not enlarge the unit cell and does therefore not optimally couple to the Na-

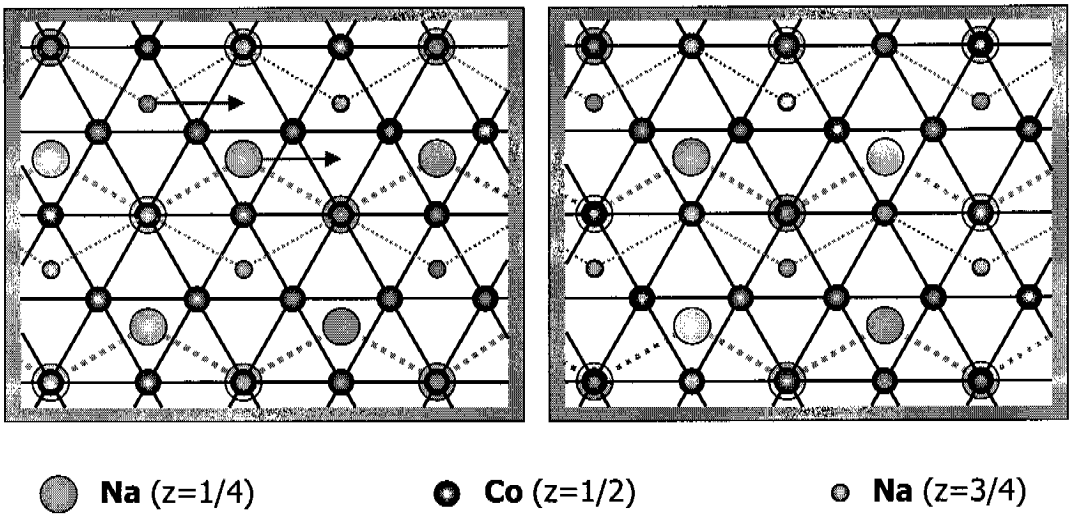

Figure 2.12: Two different Na-superstructures in $Na_{1/2}CoO_2$. The left one does not break rotational symmetry and would drive a charge ordering as shown in Fig. 2.8 (c). The right one is in fact realized in $Na_{1/2}CoO_2$, it is obtained from the right one by shifting the Na-chains along the arrows. This shift is due to the Coulomb repulsion of the Na-ions. z denotes the position along the c-axis.

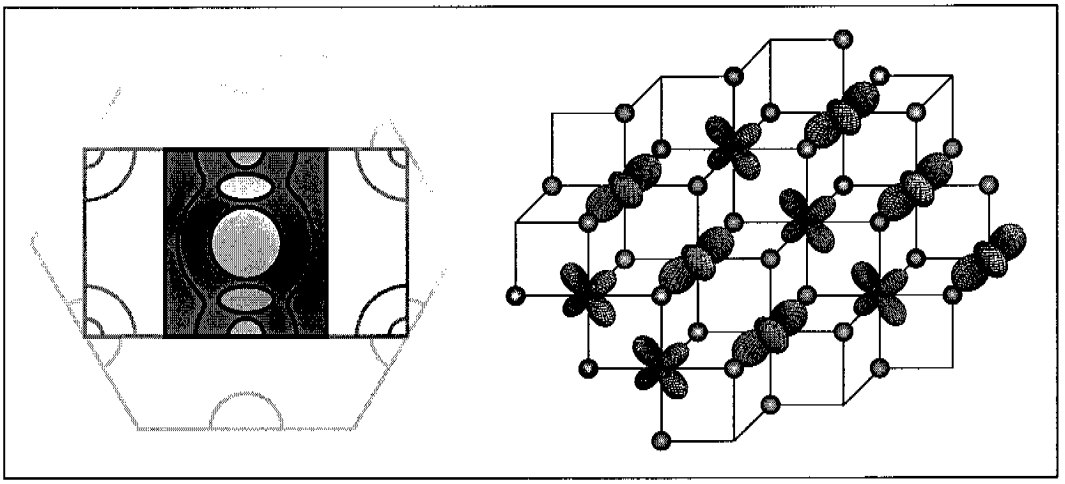

Figure 2.13: The right hand side shows the charge ordering pattern corresponding to the matrix $K^1 - K^7$, which consists of alternating rows of d_x and $d_y - d_z$ orbitals. On the left hand side the original BZ, the orthorhombic BZ due to the charge ordering and the experimentally observed reduced orthorhombic BZ (dark) are shown.

patterns that can be formed with $x = 0.5$. However the orbital pattern shown in Fig. 2.8 (c) has lobes of electron density pointing towards selected Na1 and Na2 positions. For $x = 0.5$ it is possible to occupy all these and only these positions. This leads to the left Na-superstructure of Fig. 2.12. In other words, this Na-superstructure couples in an optimal way to this rotationally symmetric charge pattern. Further, the Landau expansion shows that the rotationally symmetric combination is favored by the third-order term. Therefore, it is clear that the electronic degrees of freedom would favor this Na-superstructure. This pattern however does not maximize the Na-ions distances. It is apparent that the average distances between the Na-ions can be increased, if every second of the one-dimensional sodium chains is shifted by one lattice constant as shown in Fig. 2.12. In this way an orthorhombic Na-superstructure is obtained, which is the one observed in experiments [29]. This orthorhombic pattern does not drive the rotationally symmetric charge pattern shown in Fig. 2.8 (c), which is described by the matrix $\tilde{K}^7 = (K^7 + K^8 + K^9)/\sqrt{3}$. It might however drive the orthorhombic charge pattern described by the matrix K^7 or rather the orthorhombic charge pattern described by $K^1 - K^7$, as in the presence of trigonal distortion the K^1 and K^7 mix and the odd combination will have the most negative coupling constant. This charge pattern is shown in Fig. 2.13. It consists of lines of d_x orbitals alternating with lines of the linear combination $d_y - d_z$ orbitals. Note, that this charge pattern corresponds to the mixed $K^1 - K^7$ matrix, the charge is not uniformly distributed on the Co-atoms. In this charge pattern, the Na1-sites above the $(d_y - d_z)$ Co-sites will be lower in energy than the Na1-sites above the d_x Co-sites and similarly the Na2-positions are separated into nonequivalent rows.

In reciprocal space, such a charge ordering leads to a folding of the BZ such that the two M pockets hybridize. The ordering of the Na-ions along the chains leads to a further folding of the BZ and to a hybridization of the bands, as it is shown in Fig. 2.13. The schematic FS in Fig. 2.13 is drawn to illustrate the hybridization occurring due to the translational symmetry breaking. Li *et al.* performed density-functional calculations in order to determine the band-structure of $Na_{0.5}CoO_2$ in the presence of the orthorhombic superstructure from first-principles [74]. Quite generally one can assume that this superstructure, which specifies a direction on the triangular lattice, can lead to quasi-onedimensional bands in the reduced BZ. For such one-dimensional bands, nesting features are likely to occur and would lead to a SDW-like instability, as it was observed at 53 K by Huang *et al.* [28, 55]. Such a transition

could open a gap at least on parts of the FS and in this way lead to the drastic increase of the resistivity observed at 53 K [27]. At higher temperature, the resistivity is comparable in magnitude to the metallic samples and increases only slightly with lowering temperature. This weakly insulating behavior could be another effect of Na-ion ordering. Since the rotational symmetry is broken, domains can be formed. The existence of domain walls would be an obstacle for transport where thermally activated tunneling processes play a role. It would be interesting to test this idea by removing the domains and see whether metallic temperature dependence of the resistivity would result. A bias on the domains can be given by in-plane uniaxial distortion.

To finish this section, we will discuss a further mechanism, that could lead to a non-magnetic low-temperature instability in $Na_{0.5}CoO_2$. In Sec. 2.6 we saw that the third order term in the Landau expansion, Eq. (2.38), favors always a rotationally symmetric charge ordering where all three order parameters η_1, η_2, and η_3 have the same magnitude. But as argued above, the Na-ion repulsion leads nevertheless to an orthorhombic charge ordering, where only one order parameter η_1 is finite. From Eq. (2.38), we obtain a Landau expansion for the remaining two order parameters η_2 and η_3 containing only second and forth order terms. The second order term is given by

$$\frac{\tilde{\alpha}}{2}(\eta_2^2 + \eta_3^2) + \tilde{\beta}\,\eta_2\,\eta_3, \tag{2.45}$$

where

$$\tilde{\alpha} = \alpha + \left(\gamma_1 + \frac{\gamma_2}{2}\right)\eta_1^2 \quad \text{and} \quad \tilde{\beta} = \beta\eta_1. \tag{2.46}$$

The condition for a second order phase transition, that leads to finite values of η_2 and η_3 is $\tilde{\alpha} < |\tilde{\beta}|$. As we have $\alpha > 0$ and linear growth of $|\tilde{\beta}|$ and quadratic growth of $\tilde{\alpha} - \alpha$ with η_1, the condition is fulfilled neither for large nor for small values of η_1. But for intermediate values of η_1 it can be fulfilled. This tendency back towards the original hexagonal symmetry in this or a similar form could be responsible for the appearance of additional Bragg peaks at the intermediate temperature of 80-100 K in $Na_{0.5}CoO_2$ [28]. Note however, that it was speculated that these Bragg peaks only exist over a narrow range of temperature.

2.9 Wannier functions

It would be desirable to have an understanding of the localized degrees of freedom in our model. This is usually achieved in a single-band model by calculating the Wannier orbitals. However before calculating the Wannier orbitals, let us introduce first a different set of local states that have a certain relation to the four kagomé lattices by

$$a^{\dagger l}_{\mathbf{R}\sigma} := \frac{2}{\sqrt{N}} \sum_{\mathbf{K}} \mathrm{e}^{-\mathrm{i}\mathbf{K}\cdot\mathbf{R}} a^{\dagger l}_{\mathbf{K}\sigma}. \tag{2.47}$$

From Eq. (2.7) follows together with a little algebra that these states are given by

$$a^{\dagger l}_{\mathbf{R}\sigma} = \frac{1}{\sqrt{3}} \sum_{\mathbf{R}'} \sum_{m} I_{\mathbf{R}'-\mathbf{R}+\mathbf{a}_l+\mathbf{a}_m}\, a^{\dagger l}_{\mathbf{R}'m\sigma}, \tag{2.48}$$

with

$$I_{\mathbf{R}+\mathbf{a}_l} = \frac{4}{N} \sum_{\mathbf{K}} \mathrm{e}^{\mathrm{i}\mathbf{K}\cdot(\mathbf{R}+\mathbf{a}_l)} = \begin{cases} \delta_{\mathbf{R},0} & \text{if } l = 0, \\ I_{\mathbf{R},m} & \text{if } l = m = 1,2,3, \end{cases} \tag{2.49}$$

$$I_{\mathbf{R},m} = \frac{6}{(2\pi)^2} \frac{\cos\left[\frac{4\pi}{3}(r+s+\frac{1}{2})\right] - \cos\left[\frac{2\pi}{3}(r+s+\frac{1}{2})\right]}{(r-2s+\frac{1}{2})(2r-s-\frac{1}{2})}, \tag{2.50}$$

where we have written $\mathbf{R}$ in the form $\mathbf{R} = 2(r\mathbf{a}_{m+1} + s\mathbf{a}_{m-1})$.[d] Further, we have the Parseval relation $\sum_{\mathbf{R}} |I_{\mathbf{R},m}|^2 = 1$ for the amplitudes. The amplitudes $I_{\mathbf{R}+\mathbf{a}_l}$ decay fast but not exponentially fast. The moduli squared of these local wave functions slightly above and below the CoO_2-plane are shown in Fig. 2.14. The white lines correspond to Co sites. The thick white line marks the central Co site. The Na positions are above (below) the triangles with smaller amplitudes (cf. Fig. 2.3). Note, that the kagomé lattice with $l = 0$ has the origin in the center of a hexagon and therefore the corresponding local orbital is symmetric with respect to $2\pi/3$ rotations around the c-axis.

Now, we go back to the definition of the Wannier orbitals. Our first guess would be

$$w^{\dagger}_{\mathbf{r}\sigma} = w^{\dagger}_{\mathbf{R}+\mathbf{a}_l,\sigma} = \frac{1}{\sqrt{N}} \sum_{\mathbf{K}j} \mathrm{e}^{-\mathrm{i}(\mathbf{K}+\mathbf{B}_j)\cdot(\mathbf{R}+\mathbf{a}_l)} b^{\dagger j}_{\mathbf{K}\sigma} = \frac{2}{\sqrt{N}} \sum_{\mathbf{K}} \mathrm{e}^{-\mathrm{i}\mathbf{K}\cdot(\mathbf{R}+\mathbf{a}_l)} a^{\dagger l}_{\mathbf{K}\sigma}. \tag{2.51}$$

[d] The index $l = 0,1,2,3$ takes four values. The index $m = 1,2,3$ takes only three values and is cyclic, e.g., $m - 1 = 3$ for $m = 1$.

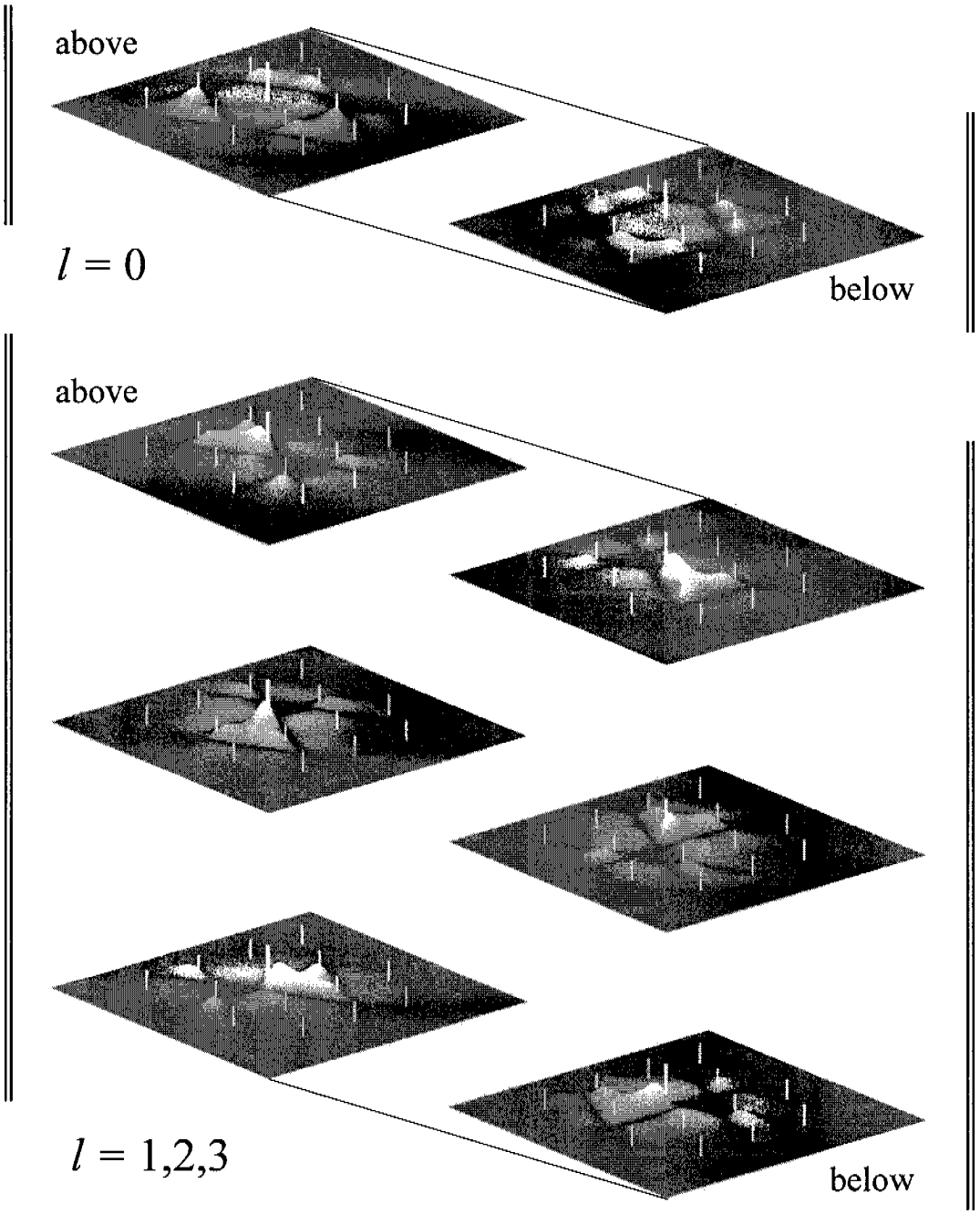

Figure 2.14: The modulus square of the local wave functions $a^{\dagger l}_{\mathbf{R}\sigma}$ for $l = 0, 1, 2, 3$ above (left) and below (right) of the CoO_2-plane. The white lines correspond to Co sites. The thick white line marks the central Co site.

For $l = 0$ we find exactly the orbital $a^{\dagger 0}_{\mathbf{R}\sigma}$ shown in the first row of Fig. 2.14. For $l = 1, 2, 3$ we find the same orbital shifted by the vector $\mathbf{a}_l$. The operators $w^{\dagger}_{\mathbf{r}\sigma}$ defined in (2.51) generate in fact states that are localized at the site $\mathbf{r}$ and have the full point group symmetry. But are the operators $w^{\dagger}_{\mathbf{r}\sigma}$ the only operators with these two properties?

In fact it turns out that we have to be careful. In the definition (2.51) we could also have used different phases for the different Bloch states. As in our approximation the periodic function of the Bloch states does not depend on $\mathbf{K}$, we can assume that also the phase of the Bloch states entering into the definition of the Wannier orbitals does not depend on $\mathbf{K}$. On the other hand the phase could well depend on the pocket index j. If we would for example shift the phase of all Bloch states with $j = 0$ in (2.51) by π, we would obtain different Wannier orbitals. The Wannier orbitals on the kagomé lattice with $l = 0$ lattice for example would be given by $(a^{\dagger 0}_{\mathbf{R}\sigma} - a^{\dagger 1}_{\mathbf{R}\sigma} - a^{\dagger 2}_{\mathbf{R}\sigma} - a^{\dagger 3}_{\mathbf{R}\sigma})/2$ instead of $a^{\dagger 0}_{\mathbf{R}\sigma}$. There is no argument that would allow us to discard one of these Wannier orbitals as both of them are invariant under rotations and both do not decay exponentially. In fact we can see that it is not possible to present a unique local wave function for a given lattice site that decays exponentially, but, we can provide four orthogonal local states per enlarged unit cell that decay algebraically. For the site $\mathbf{R}$ these are exactly the states $a^{\dagger l}_{\mathbf{R}\sigma}$ shown in Fig. 2.14. Which linear combinations of these states has to be used in solving a local physical problem can not be answered in a general way.

2.10 Superconductivity

So far, the focus in this chapter was on the possible charge and spin density wave instabilities in Na_xCoO_2. The effective interaction (2.29) is written in a form that allows to read off directly the coupling constants for the charge and spin density wave instabilities. Furthermore, this interaction was derived for values of x close to one, where no superconductivity can be observed in experiments.

It is, however, instructive to decouple the interaction (2.22) into the different superconducting channels. To this end, let us define the order parameters

$$\Delta^{r}_{\sigma\sigma'} = \frac{1}{N} \sum_{\mathbf{K}} \sum_{ij} Q^{r}_{ij} \langle a^{i}_{\mathbf{K}\sigma} a^{j}_{-\mathbf{K}\sigma'} \rangle. \tag{2.52}$$

As the effective interaction does not depend on $\mathbf{K}$, we must have singlet pairing

Table 2.7: The coefficients Γ_r^{s} (singlet) and Γ_r^{t} (triplet).

r	Γ_r^{s}	Γ_r^{t}
0	$\frac{8}{81}(3U + 16U' + 16J_{\mathrm{H}} + 70J')$	0
1–3	$\frac{8}{81}(3U + 16U' + 16J_{\mathrm{H}} - 2J')$	0
4–9	$\frac{16}{9}(J_{\mathrm{H}} + U')$	0
10–15	0	$-\frac{16}{9}(J_{\mathrm{H}} - U')$

for $r = 0, \ldots, 9$ and triplet pairing for $r = 10, \ldots, 15$ because the corresponding matrices Q_{ij}^r are even respectively odd under the exchange of the indices i and j. The coupling constants for these superconducting instabilities are given by

$$\Gamma_r^{\mathrm{s}} = \sum_{ijkl} (A_{ijkl}^{\mathrm{c}} - 3A_{ijkl}^{\mathrm{s}})\, Q_{li}^r\, Q_{jk}^r \tag{2.53}$$

$$\Gamma_r^{\mathrm{t}} = \sum_{ijkl} (A_{ijkl}^{\mathrm{c}} + A_{ijkl}^{\mathrm{s}})\, Q_{li}^r\, Q_{jk}^r \tag{2.54}$$

and tabulated in Table 2.7. Note, that all coupling constants for singlet pairing are clearly repulsive. The coupling constants for the triplet instability is only attractive for $J_{\mathrm{H}} > U$ which is usually not the case. Note that only the instabilities with $r = 0$ and with $r = 4, \ldots, 6$ occur in the usual Cooper channel. The remaining instabilities are given by Cooper pairs with a finite momentum, similar to a Fulde-Ferrell-Larkin-Ovchinnikov state. These states also break translational symmetries and depending on their combination also rotational symmetries. Note, that the degeneracies of the pairing partners for the usual type of Cooper pairing is guaranteed by inversion symmetry, whereas for the Fulde-Ferrell type of instabilities, the degeneracy of the states that have to be paired up is a property of our tight-binding model, that will be at least partially broken by additional hopping terms or by trigonal distortion. However, as long as the pockets around the M points are spherical, the degeneracy of the pairing states for the triplet states with $r = 10, \ldots, 12$, that only pairs states belonging to these M pockets, is still guaranteed. In this subsection we do not attempt to provide a complete discussion of the superconducting instabilities in our model or even in the hydrated Na_xCoO_2. For such a discussion it would be necessary to include charge, spin, and orbital fluctuations in the interactions.

This could be done using RPA or the FLEX method [e] We refer to Ref. [70] for a FLEX discussion of superconductivity in Na_xCoO_2. In this work, spin triplet superconductivity is found, that exists due to the presence of small hole pockets. However, this triplet superconductor is neither a Fulde-Ferrell state, nor are the pockets around the M points.

2.11 Discussion and conclusion

In this chapter the properties of a high-symmetry multi-orbital model for the CoO_2-layer in combination with local Coulomb interaction are discussed. The tight-binding model is a zeroth order approximation to the kinetic energy, as it only includes the most relevant hopping processes using Co-O π-hybridization. Nevertheless it produces the hole pocket with predominantly a_{1g} character around the Γ point, in agreement with both LDA calculations and ARPES experiments. Furthermore, the three further pockets around the M points, although not seen in ARPES experiments, suggest that additional degrees of freedom that can not be captured in a single-band picture could be relevant. The existence of identical hole, pockets in the BZ does however not produce pronounced nesting features.

The local Coulomb repulsion of the t_{2g} orbitals can be taken into account by an effective interaction of fermions with four different flavors, associated with the four hole pockets or the four inter-penetrating kagomé lattices. This effective interaction has a large discrete symmetry group, that allows to classify the spin- and charge-density operators, and to the determine for every mode the corresponding coupling constant.

It turns out that with an effective trigonal distortion, that splits the degeneracy between the Γ and the M points, general corrections to the quadratic part of the Hamiltonian, such as trigonal distortion or additional hopping terms, can be taken into account, provided they are small. This effective trigonal distortion reduces the symmetry of the Hamiltonian down to the space-group symmetries of the CoO_2-plane, by breaking the gauge symmetries of the effective interaction.

Most coupling constants are negative for reasonable assumptions on the Coulomb integrals U, U', J', and J_H, but the ferromagnetic coupling constant is most negative and constitutes the dominant correlation. The charge and

[e] RPA=Random Phase Approximation, FLEX=FLuctuation-EXchange approximation.

spin density wave instabilities without trigonal distortion are easily described in a mean-field picture. In reciprocal space the degenerate bands split, and if bands belonging to different pockets hybridize, the BZ is folded. In real space different types of orderings are possible. The occupancy of the different t_{2g} orbitals on different sites can be nonuniform, resulting in a charge ordering with nonuniform charge distribution on the Co-sites. Further, certain real or complex linear combinations of t_{2g} orbitals can be preferably occupied on certain sites. In this case, the charge is uniformly distributed on the sites, but depending on the linear combinations of the orbitals, certain space group symmetries are broken. The complex linear combinations of t_{2g} orbitals have in general a non-vanishing expectation value of the orbital angular momentum.

The tendency to these rather exotic states turns out to be smaller than the ferromagnetic tendency, and this dominance of the ferromagnetic state is even more enhanced by the trigonal distortion. This is in good agreement with experiments, where ferromagnetic inplane fluctuations have been observed by neutron scattering measurements in $Na_{0.75}CoO_2$ [44, 45]. There are also several reports of a phase transition in $Na_{0.75}CoO_2$ at 22 K to a static magnetic order, which is probably ferromagnetic inplane but antiferromagnetic along the c-axis [47, 49, 50].

In $Na_{0.5}CoO_2$, a periodic Na-superstructure couples directly to a charge pattern in our model and crystallizes already at room temperature, whereas simple $\sqrt{3} \times \sqrt{3}$-superstructures, that would correspond $x = 1/3$ or $x = 2/3$ do not couple.

For general values of x the disordered Na-ions provide a random potential that couples to the charge degrees of freedom. Due to the incommensurability, this does not lead to long range order, but the short range correlations will also be influenced by the charge degrees of freedom in the CoO_2-layers. This interaction between the Na-correlations and the charge degrees of freedom could be the origin of the charge ordering phenomena at room temperature and the observation of inequivalent Co-sites in NMR experiments [34, 35].

The overall agreement of our model with the experimental situation is good. Ferromagnetic fluctuations are dominant in our model and in experiments. Furthermore, our model is based on a metallic state and allows for charge ordering and spin density ordering transitions without changing the metallic character of the state. Finally, the clear Na-superstructures, that were found at $x = 0.5$, can be understood quite naturally in this model.

On the other hand there are still many open questions for the cobaltates.

Mainly the origin and the symmetry of the superconducting state of $Na_xCoO_2 \cdot yH_2O$ is still under debate. Unfortunately the Na content $x = 0.35$ is beyond the validity of the approximations made in the derivation of our model. But also the samples with $x \geq 0.5$ have still many intriguing properties like the strongly anisotropic magnetic susceptibility, which shows the unusual Curie-Weiss temperature dependence. A possible description of the anisotropy of the magnetic susceptibility could be achieved by introducing a spin-orbit term into the kinetic energy.

Seite Leer /
Blank leaf

Chapter 3

Bond Order Wave Instabilities in Doped Frustrated Antiferromagnets: Valence Bond Solids at Fractional Filling

3.1 Introduction

Highly frustrated quantum magnets are fascinating and complex systems where the macroscopic ground-state degeneracy at the classical level leads to many intriguing phenomena at the quantum level. The ground-state properties of spin $S = 1/2$ Heisenberg antiferromagnets on the kagomé and the pyrochlore lattice remain still puzzling and controversial in many aspects. While the magnetic properties of the Heisenberg and extended models have indeed been studied for quite some time, the investigation of highly frustrated magnets upon doping with mobile charge carriers has started recently [86–90]. Such interest has been motivated for example by the observation that in some strongly correlated materials, such as the spinel compound LiV_2O_4, itinerant charge carriers and frustrated magnetic fluctuations interact strongly [91, 92]. Furthermore, the possibility of creating optical kagomé lattices in the context of cold atomic gases has been pointed out [93], making it possible to "simulate" interacting fermionic or bosonic models in an artificial setting [94].

At this point we should stress that the behavior in a simple single-band model at weak and at strong correlations are not expected to be related in a

trivial way. The weak-coupling limit allows us to discuss the electronic properties within the picture of itinerant electrons in momentum space based on the notions of a Fermi surface and Fermi surface instabilities (see, e.g., Refs. [86] and [89]). Considering for example the Fermi surfaces of a triangular or a kagomé lattice at half-filling we do not find any obvious signature of the magnetic frustration present at large U. Although at weak coupling these systems do not seem to be particularly special, at intermediate to strong coupling the high density of low-energy fluctuations of the highly frustrated systems displays characteristic features from which the physics of the frustrated system of localized degrees of freedom will emerge [87, 88].

In the following we study a class of highly frustrated lattices, the so-called bisimplex lattices [95], which are composed of corner-sharing simplices residing on a bipartite underlying lattice. We restrict ourselves to the triangle and the tetrahedron as the basic building blocks in the following. This class hosts lattices such as the kagomé or the pyrochlore lattice and their lower-dimensional analogues, the kagomé strip and the checkerboard lattice (cf. Fig. 3.1).

Our main result is the spontaneous symmetry breaking taking place at a the electron density of one electron per simplex ($n = 2/3$ for the kagomé lattice and the kagomé strip, $n = 1/2$ for the pyrochlore and the checkerboard lattice) for a wide range of interactions. This instability is driven by a cooperative effect of the kinetic energy and the nearest-neighbor (nn) interaction, which can be an antiferromagnetic exchange interaction and/or nearest-neighbor Coulomb repulsion. In the resulting low-symmetry phase only lattice symmetries are broken,[a] resulting in different bond strengths, e.g., different expectation values of the kinetic energy on equivalent lattice bonds. Therefore, we will refer to this instability in the following as a bond order wave (BOW) instability. An alternative name would be Peierls or spin Peierls instability, however, these terms could be misleading as contrary to the original Peierls transition the elasticity of the lattice is not relevant in our model, i.e., the BOW instability can also occur in an infinitely rigid lattice and, in contrast to the spin Peierls transition, the kinetic energy and the charge degrees of freedom play a crucial role for the BOW instability described in the chapter.

The outline of this chapter is as follows. In a first section we introduce the lattices and the model. The limit of decoupled simplices, which we study in Sec. 3.3 by the analysis of the spectrum of isolated or weakly coupled simplices,

[a] In the kagomé and in the pyrochlore lattice the inversion symmetry is broken, whereas in the lower-dimensional analogues a doubling of the elementary unit cell occurs.

provides an illuminating starting point. An additional intuitive and somewhat complementary picture of the spontaneous symmetry breaking can be obtained from a simple doped quantum dimer model, that we discuss in Sec. 3.4. For the isotropic t-J model on kagomé and on the pyrochlore lattice we show in Sec. 3.5, that within the Gutzwiller mean-field formalism the BOW instability is clearly dominant at the considered filling. Without interactions, the bisimplex lattices with one electron per simplex have half-filled particle-hole symmetric bands, with empty flat bands on top of them. The half-filled bands are exactly the bands of the underlying bipartite lattices and the empty bands can be ignored in the weak-coupling limit. Based on these facts we derive in Sec. 3.6 effective models for the underlying bipartite lattices in weak-coupling. These models we analyze with renormalization group (RG) and/or within mean-field methods. Also in weak-coupling we can establish the presence of the BOW phases for the kagomé strip and the checkerboard lattice. In Sec. 3.7 we compare the results of the previous sections to extensive numerical data that corroborate the theoretical picture. Before we summarize and conclude in Sec. 3.9 we focus in Sec. 3.8 on the Dirac points that form the Fermi surface for the kagomé lattice at the considered filling. An analysis of the wave function of the non-interacting (tight-binding) states close to these points helps to understand the observed symmetry breaking. We also discuss some additional peculiarities of these states and compare to the analogous phenomena for the honeycomb lattice. The major part of the results presented in this chapter is published in the references [96] and [97]. The numerical calculations (Sec. 3.3.1 and Sec. 3.7) were performed by Andreas Läuchli and Sylvain Capponi in the framework of a collaboration on Ref. [96]. The reference [97] contains additional numerical results for the checkerboard lattice that are not presented in this thesis.

3.2 Model and lattices

We study in this chapter the Hamiltonian $H = H_0 + H_{\text{int}}$ on the bisimplex lattices shown in Fig. 3.1 at the filling of two electrons per simplex. The kinetic part is given by

$$H_0 = -t \sum_{\langle ij \rangle} \sum_{\sigma=\uparrow\downarrow} \left(c^\dagger_{i\sigma} c_{j\sigma} + \text{h.c.} \right) \tag{3.1}$$

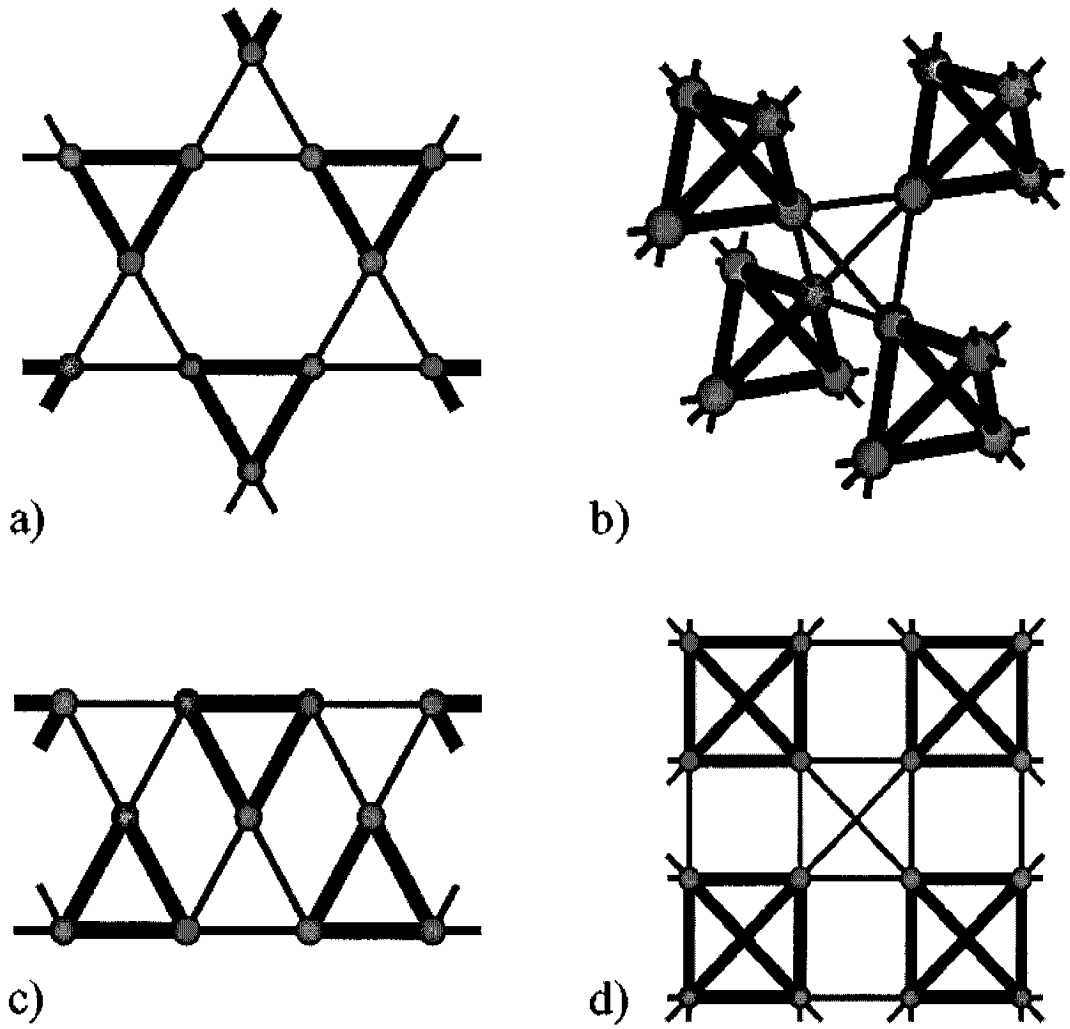

Figure 3.1: The kagomé lattice (a) and the pyrochlore lattice (b) together with their lower dimensional analogues, the kagomé strip (c) and the checkerboard lattice (d). The two types of corner sharing units (up vs. down) are distinguished by the line width. They correspond to the bond order wave symmetry breaking pattern occurring at $n = 2/3$ on the triangle based lattices and at $n = 1/2$ on the tetrahedron based lattices.

with the hopping matrix element t. The sum $\sum_{\langle ij \rangle}$ runs over all bonds of the bisimplex lattices. The interaction part of the Hamiltonian is given by

$$H_{\text{int}} = U \sum_i n_{i\uparrow} n_{i\downarrow} + J \sum_{\langle ij \rangle} \mathbf{S}_i \cdot \mathbf{S}_j + V \sum_{\langle ij \rangle} n_i n_j \tag{3.2}$$

with onsite repulsion U, n.n. repulsion V, and n.n. spin exchange J. For $U = \infty$ we obtain the strong coupling Hamiltonian

$$H_{t\text{-}J\text{-}V} = \mathcal{P} H_0 \mathcal{P} + J \sum_{\langle ij \rangle} \mathbf{S}_i \cdot \mathbf{S}_j + V \sum_{\langle ij \rangle} n_i n_j, \tag{3.3}$$

$$= H_{t\text{-}J} + V' \sum_{\langle ij \rangle} n_i n_j, \tag{3.4}$$

where $\mathcal{P}$ is the projection operator that enforces the single occupancy constraint and $V' = V + J/4$. For $V' = 0$ the strong coupling Hamiltonian reduces to the usual t-J model. The sign of the hopping amplitude t is relevant on these highly frustrated lattices and in the following discussion it will always be positive. A negative sign of t will most likely induce ferromagnetic tendencies at the fillings we are considering [98].

The kagomé lattice and the pyrochlore lattice consist of corner-sharing triangles and tetrahedra, respectively. They are shown in Fig. 3.1 together with their lower dimensional analogues, the kagomé strip and the checkerboard lattice. The centers of the triangles in the kagomé lattice form a honeycomb lattice, whereas the centers of the tetrahedra in the pyrochlore lattice reside on a diamond lattice. These two underlying lattices and also the underlying lattices of the kagomé strip and the checkerboard lattice are bipartite and we can separate the triangles and the tetrahedra into two different classes, which is visualized in Fig. 3.1 by a different line-style (light and bold bonds). To refer to triangles (tetrahedra) of a given class we call them up- and down-triangles (tetrahedra), and the same for the bonds. The considered lattices all have inversion centers, that map the up-bonds onto down-bonds and vice versa.

3.3 The limit of decoupled simplices

To get a basic understanding of the effect of doping in highly frustrated lattices we first consider the limit of decoupled units by turning the couplings within the down-subunits off. Eventually we will connect this limit with the uniformly

connected lattice. For this purpose we use the parameter α ($0 \leq \alpha \leq 1$) to tune the coupling strength of the down-bonds as $(\alpha t, \alpha J)$, while the up-bonds are constant (t, J) in our Hamiltonian. In this way the inversion symmetry is explicitly broken. The eigenvalues of $H_{t\text{-}J}$ and their degeneracies are listed in Table 3.1 for a single triangle and a single tetrahedron. For $t > 0$ and $J \geq 0$, there is a single state with two electrons, $N_e = 2$, that has the lowest energy of all states and, furthermore, is separated from the remaining spectrum by a finite gap. This state has at the same time the lowest kinetic energy ($-2t$ or $-4t$, respectively) of all states and gains the maximal exchange energy ($-J$) for two spins. This state is not frustrated anymore because it minimizes the kinetic and the exchange energy at the same time.

After having revealed this particularly stable state with two electrons on a single unit, we are naturally led to the question whether the homogeneous lattices could spontaneously exhibit strong and weak units at the filling $n = 2/3$ for the triangle based lattices and at $n = 1/2$ for the tetrahedron based ones. Such an instability has the character of a bond order wave – modulated expectation values of the bond energies – and yields an insulating fully gapped ground state. One way to address this question is to track the evolution of the excitation gaps to all forms of excitations as a function of α. If the gaps do not close before reaching $\alpha = 1$ this would suggest an instability towards spontaneous symmetry breaking.

3.3.1 Approaching the uniform lattices

We now determine these gaps for the kagomé lattice numerically as a function of the parameter α, which is proportional to the inter-triangle couplings. Our results are obtained from exact diagonalization (ED) and the contractor renormalization (CORE) algorithm [99–102]. This latter method extends the range of tractable sizes of finite clusters, based on a careful selection of relevant low-energy degrees of freedom. In order to apply this algorithm, the lattice has to be divided into blocks; here, we naturally choose the up-triangles. A reduced Hilbert space is defined by retaining a certain number of low-lying states on each block. The choice of the states to keep depends also on the quantities to be obtained. While for a ground-state calculation fewer states already provide good results, one has to retain usually more states to calculate the excited states. Here we choose to keep the 4 lowest states in the 3-electrons sector, the 7 lowest states with 2 electrons and the 2 lowest states in the 1-electron sector.

Table 3.1: Classification of the eigenstates of the t-J model (3.4) on a triangle and on a tetrahedron. The degeneracy is given in the form $r \times (2S+1)$, where r is the dimension of the irreducible representation of $\mathcal{S}_3$, respectively $\mathcal{S}_4$, and S is the total spin of the state. The asterisk denotes the states retained in the CORE calculations for the kagomé system, see text.

	Triangle			Tetrahedron	
N_e	Energy	Degen.		Energy	Degen.
0	0	1×1		0	1×1
1	$-2t$	1×2	*	$-3t$	1×2
	t	2×2		t	3×2
2	$-2t-J$	1×1	*	$-4t-J$	1×1
	$t-J$	2×1		$-J$	3×1
	$-t$	2×3	*	$2t-J$	2×1
	$2t$	1×3		$-2t$	3×3
				$2t$	3×3
3	$-3J/2$	2×2	*	$-2t-3J/2$	3×2
	0	1×4		$-3J/2$	2×2
				$2t-3J/2$	3×2
				$-t$	3×4
				$3t$	1×4
4				$-3J$	2×1
				$-2J$	3×3
				0	1×5

These states are denoted with an asterisk in Table 3.1. This choice leads to a reduction of the local triangle basis from 27 down to 13 states, thus allowing indeed to perform simulations on larger lattices than would be possible by conventional ED.

Then, by computing the exact low-lying eigenstates of two coupled triangles, we calculate the effective interactions at interaction range two for each value of α and we neglect longer range terms. Comparison to ED data on the smaller clusters shows that this approach gives very good results.

The basic excitation gaps of interest in the present problem are the spin gap, the single particle gap and the two particle gap. These are defined as follows:

$$\Delta_{S=1} = E(N_e, 1) - E(N_e, 0), \tag{3.5}$$

$$\Delta_{1p} = \frac{1}{2}\left(E(N_e + 1, 1/2) + E(N_e - 1, 1/2)\right) - E(N_e, 0), \tag{3.6}$$

$$\Delta_{2p} = \frac{1}{2}\left(E(N_e + 2, 0) + E(N_e - 2, 0)\right) - E(N_e, 0), \tag{3.7}$$

where $E(N_e, S^z)$ denotes the ground-state energy in the sector with N_e electrons and spin polarization S^z.

We have determined these gaps on kagomé finite size samples at $n = 2/3$ and $J/t = 1$ containing 18 to 27 sites. Two different versions of samples with 18 and 24 sites have been treated (v1 and v2). The results are displayed in Fig. 3.2. There are two main observations: (1) the gaps do not close for any $\alpha \in [0, 1]$, giving first evidence for the proposed symmetry breaking; (2) there is a strong dependence of the gap curves on the specific sample. Note that there is no discrepancy between ED and CORE results. The second phenomenon can be understood from the discretization of the finite size Brillouin zones: indeed, the measured gaps directly depend on the distance between the closest point in the Brillouin zone to the corner of the zone, the K-point. The 18,v2 and the 27 sites samples both contain this specific point and differ only slightly in the values of the gap. Thus supporting the claim of a finite gap for all $\alpha \in [0, 1]$. The strong dependence is at the same time also a hint towards a sizable dispersion of the excitations in this system.

3.4 Doped quantum dimer model

In the previous sections we discussed mostly the case $\alpha < 1$, where the Hamiltonian itself is not invariant under inversion symmetry. In this case it is natural to apply a method which is based on the existence of strong subunits (triangles or tetrahedra) that are only weakly coupled. If the system has in fact the tendency to develop such strong subunits, the results of this method can be quantitatively good even for the uniform case. However, in order to get some insight into the mechanism of spontaneous symmetry breaking, it is desirable to treat up- and down-triangles (tetrahedra) on an equal footing. In the following, we present a simple but illustrative picture of the mechanism that leads to the spontaneous breaking of the inversion symmetry.

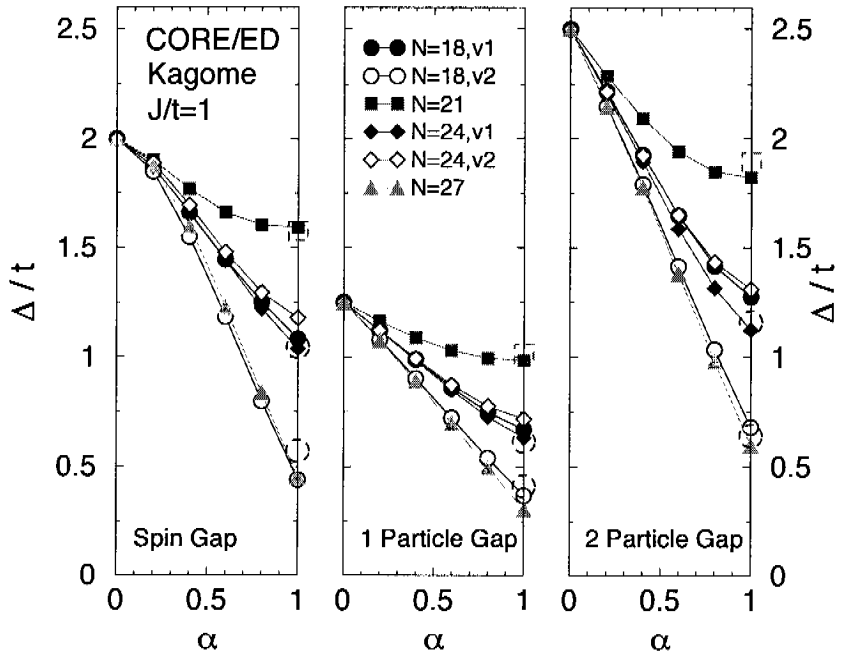

Figure 3.2: Excitation gaps of the t-J model on the kagomé lattice at $J/t = 1$ as a function of the parameter α, which denotes the ratio of the inter-triangle to the intra-triangle couplings. The gaps are obtained by the CORE method for different sample sizes (and geometries). On selected samples ED data is shown for comparison at $\alpha = 1$.

A close inspection of the wave function of the lowest energy eigenstate of two electrons on either a triangle or a tetrahedron reveals that it consists of the equal amplitude superposition of all possible positions of the singlet formed by the two electrons:

$$|\psi_{\mathrm{GS}}\rangle = \frac{1}{\mathcal{N}} \sum_{i<j} (c^\dagger_{i\uparrow} c^\dagger_{j\downarrow} - c^\dagger_{i\downarrow} c^\dagger_{j\uparrow})|0\rangle, \tag{3.8}$$

where the normalization $\mathcal{N} = \sqrt{3}$ for the triangle and $\mathcal{N} = \sqrt{6}$ for the tetrahedron. This wave function motivates us to design a simple quantum dimer model which on each triangle prefers the exact wave function described above. Such a Hamiltonian reads for example for the kagomé lattice:

$$\begin{aligned} H_{\mathrm{QDM}} &= -t \sum_{\triangle} \left[|\triangle\rangle\langle\triangle| + |\triangle\rangle\langle\triangle| + |\triangle\rangle\langle\triangle| + \mathrm{h.c.} \right] \\ &\quad -t \sum_{\triangledown} \left[|\triangledown\rangle\langle\triangledown| + |\triangledown\rangle\langle\triangledown| + |\triangledown\rangle\langle\triangledown| + \mathrm{h.c.} \right] \end{aligned} \tag{3.9}$$

where the Hilbert space consists of all coverings of the kagomé lattice with N_c nearest-neighbor dimers and N_c monomers, N_c counting the number of unit cells. This corresponds to the situation at $n = 2/3$ in the t-J model. The interpretation is simple: the antiferromagnetic exchange term tends all the electrons to pair up into singlets, while the kinetic energy term tends to delocalize the singlets as much as possible on a triangle. The quantum dimer model for the tetrahedron based lattices are defined by letting a single singlet resonate on a tetrahedron. This simple model allows us to find the exact ground state on these lattices. The ground state is twofold degenerate and each state is the direct product of equal amplitude resonances on the same type of triangles/tetrahedra, either all up or all down. In such a situation each resonating dimer can independently fully optimize its kinetic energy. The argument has much in common with the reasoning for the close packed dimer model on the pyrochlore lattice discussed in Ref. [103].

Although this model is only a cartoon version of the real electronic system, it illustrates nicely how the tendency of the electrons to form nearest-neighbor singlets obstructs the motion of the singlets between corner-sharing simplices, but within a given simplex an individual singlet can hop without obstacles and optimize its kinetic energy. The bipartite nature of the underlying lattice allows for the localization of the singlets on simplices without interference and triggers in this way the spontaneous symmetry breaking.

3.5 Mean-field discussion

In this section we present a mean-field calculation for the kagomé lattice and the pyrochlore lattice. The mean-field discussion is particularly valuable for the pyrochlore lattice, as due to its higher dimension it is less affected by fluctuations and not treatable with numerical methods. We can show that in the mean-field analysis the spontaneous inversion symmetry breaking, discussed in the previous sections, is also the natural and leading instability.

We start with discussing the properties of the nearest-neighbor tight-binding model on the kagomé and the pyrochlore lattice, given by

$$H_0 = -\mu\hat{N} - t\sum_{\mathbf{r}\sigma}\sum_{m\neq n}\sum_{\nu=\pm 1} c^{\dagger}_{\mathbf{r}+\nu\mathbf{a}_m,\sigma}c_{\mathbf{r}+\nu\mathbf{a}_n,\sigma}, \tag{3.10}$$

where $\sigma = \uparrow, \downarrow$ is the spin index and the indices m, n run from zero to the dimension of the lattice, d. Further, $\mathbf{r}$ is an elementary lattice vector connecting

unit cells and the vectors $\mathbf{a}_0, \ldots, \mathbf{a}_d$ point to the vertices of an elementary triangle (tetrahedron) in the kagomé (pyrochlore) lattice, $\mathbf{a}_0 = 0$. Note, that in (3.10) we introduced a chemical potential term, where $\hat{N}$ is the total electron number operator and μ is the chemical potential. In the following we will use units where $t = 1$ and we will always choose $\mu = -1$ for the kagomé and $\mu = -2$ for the pyrochlore lattice, which corresponds to two electrons per unit cell. H_0 can be diagonalized in reciprocal space and can be written as

$$H_0 = \sum_{\mathbf{k}m\sigma} \xi_{\mathbf{k}m} \gamma^\dagger_{\mathbf{k}m\sigma} \gamma_{\mathbf{k}m\sigma}, \tag{3.11}$$

with

$$-\xi_{\mathbf{k}0} = \xi_{\mathbf{k}1} \equiv \xi_{\mathbf{k}}, \quad \xi_{\mathbf{k}m} = d + 1 \text{ for } m > 1. \tag{3.12}$$

For the kagomé lattice we have

$$\xi_{\mathbf{k}} = \sqrt{1 + 8\cos(k_1/2)\cos(k_2/2)\cos([k_1 - k_2]/2)} \tag{3.13}$$

with $k_m = \mathbf{k} \cdot \mathbf{a}_m$. The three bands of the kagomé lattice consist of one flat band and two dispersing bands. The dispersing bands are identical to the bands of a honeycomb lattice. They are shown together with the density of states per unit cell and spin in Fig. 3.3. Note, that around the points K and $-$K the

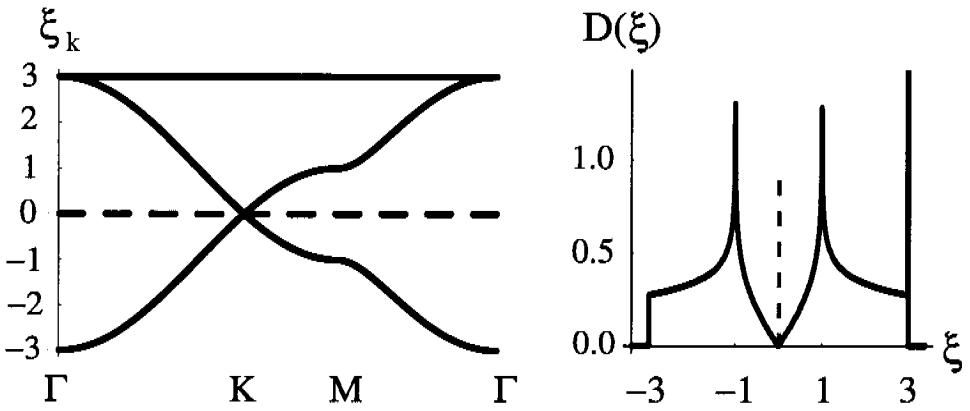

Figure 3.3: The kagomé bands and the density of states per unit cell and spin. The energy is measured in units of t.

dispersion shows a Dirac spectrum, i.e., the bands $\xi_{\mathbf{k}0}$ and $\xi_{\mathbf{k}1}$ touch each other at these points with linear dispersion. For the given chemical potential the

Fermi surface reduces to points at K and $-$K and the density of states vanishes linearly with ξ, i.e., we have $D(\xi) \propto |\xi|$ for small ξ.

For the pyrochlore lattice we have

$$\xi_{\mathbf{k}} = \sqrt{2 \sum_m (\cos k_m + \cos k_m^{\perp})}. \tag{3.14}$$

with $k_m^{\perp} = \sum_n (\mathbf{k} \wedge \mathbf{a}_m) \cdot \mathbf{a}_n$. The four bands of the pyrochlore lattice consist of two flat bands and two dispersing bands. The dispersing bands are identical to the bands of a diamond lattice. They are shown together with the density of states per unit cell and spin in Fig. 3.4. Note, that $\xi_{\mathbf{k}}$ vanishes along the lines

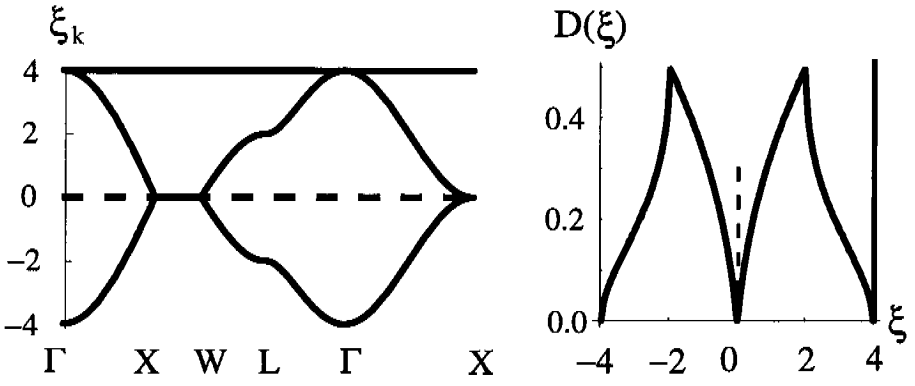

Figure 3.4: The pyrochlore bands and the density of states per unit cell and spin. The energy is measured in units of t.

connecting X and W. The density of states also vanishes linearly at zero up to logarithmic corrections, i.e., we have $D(\xi) \propto |\xi| \log |\xi|$ for small ξ.

Systems with this form of the density of states at the Fermi level are neither band-insulators nor normal metals, therefore, they are sometimes called semimetals or zero-gap semiconductors. Although they have an even number of electrons per unit cell and no fractionally filled bands, they have no energy gap at the Fermi surface. Fermi surface instabilities are suppressed in this situation. There is no Cooper instability that leads to an obvious breakdown of perturbation theory for arbitrarily small attractive interactions, as the particle-particle polarization function involves the convergent integral $\int \mathrm{d}\xi D(\xi)/2|\xi|$ at zero temperature. For the half-filled honeycomb lattice it has been shown that the Coulomb interactions lead to non-Fermi liquid behavior and that strong enough Coulomb interactions lead to antiferromagnetic order and to the opening of a

charge gap [13, 104–106]. The situation in the kagomé and the pyrochlore lattice at the filling considered here is different. Because the lattices are not at half-filling, it is not obvious that even arbitrarily large U would enforce a charge gap (Mott insulator) and an antiferromagnetic order would be hampered by the frustrated topology of the lattice. However, if we consider the triangles (tetrahedra) as the fundamental units of our lattice we obtain the honeycomb (diamond) lattice and the properties of this underlying bipartite lattice will be reflected in the ground state and provide a way to circumvent the frustration effects.

We study the electron-electron interactions described by the $H_{t\text{-}J\text{-}V}$ Hamiltonian (3.3) and we will show that both the exchange and the repulsion term favor the bond order wave instability. As the projection operator, $\mathcal{P}$, is difficult to handle in analytic calculations, the projection is often approximated by a purely statistical renormalization of the Hamiltonian with Gutzwiller factors [107]. We obtain a renormalized Hamiltonian without constraints given by

$$H_{\mathrm{r}} = g_t H_0 + J g_J \sum_{\langle ij \rangle} \mathbf{S}_i \cdot \mathbf{S}_j + V \sum_{\langle ij \rangle} n_i n_j. \tag{3.15}$$

The renormalization is given by the Gutzwiller factors $g_t = 2\delta/(1+\delta)$ and $g_J = 4/(1+\delta)^2$ and δ is the hole doping measured from half-filling. Note, that the nearest-neighbor repulsion is not renormalized by a statistical factor.

In the following we will determine the critical J and V for spontaneous symmetry breaking in this model within mean-field theory. Superconductivity is a possible way of spontaneous symmetry breaking. As it is an instability in the particle-particle channel, the relation $\xi_{\mathbf{k}} = \xi_{-\mathbf{k}}$, which is ensured by inversion and time reversal symmetry, plays an essential role. Concerning the symmetry of the order parameter, we can restrict ourselves to singlet pairing in the spin sector because the nearest-neighbor interaction is antiferromagnetic, and to s-wave pairing in the orbital sector because in this way we obtain a nodeless, even gap-function.

Another possibility of spontaneous symmetry breaking is an instability in the particle-hole channel. Such instabilities tend to occur if a nesting condition of the form $\xi_{\mathbf{k}} = -\xi_{\mathbf{k}+\mathbf{q}}$ is fulfilled. In general, this condition is not ensured by basic symmetries and therefore instabilities in the particle-hole channel are much more special than superconducting instabilities. In our case, the relation $\xi_{\mathbf{k}0} = -\xi_{\mathbf{k}1}$ can be considered as perfect nesting with $\mathbf{q} = 0$. Therefore, the relevant question is which one of the two considered instabilities is dominant in

our system. In order to answer this question we consider the following single-particle Hamiltonian,

$$H_{\text{trial}} = H_0 + \Delta_{\text{ph}} H_{\text{ph}} + \Delta_{\text{pp}} H_{\text{pp}} \tag{3.16}$$

where we have introduced the two quadratic Hamiltonians

$$H_{\text{ph}} = \sum_{\mathbf{r}\sigma} \sum_{m\neq n} \sum_{\nu=\pm 1} \nu\, c^{\dagger}_{\mathbf{r}+\nu\mathbf{a}_m,\sigma} c_{\mathbf{r}+\nu\mathbf{a}_n,\sigma}, \tag{3.17}$$

$$H_{\text{pp}} = \sum_{\mathbf{r}} \sum_{m\neq n} \sum_{\nu=\pm 1} (c_{\mathbf{r}+\nu\mathbf{a}_m,\downarrow} c_{\mathbf{r}+\nu\mathbf{a}_n,\uparrow} + \text{h.c.}). \tag{3.18}$$

The idea is to calculate the expectation value of H_{r} (3.15) for the ground state of H_{trial} (3.16) and to choose the variational parameters Δ_{pp} and Δ_{ph} such that this expectation value is minimized. In terms of the operators that diagonalize H_0 we can express the pairing operators as

$$H_{\text{ph}} = \sum_{\mathbf{k}\sigma} \mathrm{i} x_{\mathbf{k}} \gamma^{\dagger}_{\mathbf{k}0\sigma} \gamma_{\mathbf{k}1\sigma} + \text{h.c.}, \tag{3.19}$$

$$H_{\text{pp}} = \sum_{\mathbf{k}m} \epsilon_{\mathbf{k}m} \gamma_{-\mathbf{k}m\uparrow} \gamma_{\mathbf{k}m\downarrow} + \text{h.c.}, \tag{3.20}$$

with the relations

$$\xi_{\mathbf{k}m} = \epsilon_{\mathbf{k}m} - \mu, \qquad x^2_{\mathbf{k}} = \xi^2_0 - \xi^2_{\mathbf{k}}. \tag{3.21}$$

For small values of Δ_{ph} and Δ_{pp} we can expand the ground-state expectation value of H_{r} in terms of Δ^2_{pp} and Δ^2_{ph}. Using the Wick theorem, we obtain up to higher order terms

$$\begin{aligned} \frac{\Delta E}{bN} &= \Delta^2_{\text{ph}} I_{\text{ph}} \left(\tilde{t} - \frac{3\tilde{J}}{8}(I_{\text{ph}} - \chi) - \frac{V}{2}(I_{\text{ph}} - \chi) \right) \\ &+ \Delta^2_{\text{pp}} I_{\text{pp}} \left(\tilde{t} - \frac{3\tilde{J}}{8}(I_{\text{pp}} - \chi) + \frac{V}{2}(I_{\text{pp}} + \chi) \right), \end{aligned} \tag{3.22}$$

where ΔE is the deviation from the ground-state expectation value with $\Delta_{\text{ph}} = \Delta_{\text{pp}} = 0$. N is the number of unit cells, $\tilde{t} = t g_t$, $\tilde{J} = J g_J$, b is the number of bonds in the unit cell, and

$$\chi = \frac{1}{b} \int_{\xi<0} \mathrm{d}\xi (-\xi - \mu) D(\xi), \tag{3.23}$$

$$I_{\text{ph}} = \frac{1}{b} \int_{\xi<0} \mathrm{d}\xi \frac{\xi^2_0 - \xi^2}{|\xi|} D(\xi), \tag{3.24}$$

$$I_{\text{pp}} = \frac{1}{b} \int \mathrm{d}\xi \frac{(\xi + \mu)^2}{2|\xi|} D(\xi). \tag{3.25}$$

Note that only the density of states enters these formulas because we are restricting ourselves to $\mathbf{q} = 0$ instabilities. The system spontaneously breaks inversion (U(1)) symmetry, if the coefficient of $\Delta_{\rm ph}^2$ ($\Delta_{\rm pp}^2$) in Eq. (3.22) changes sign. If we assume that only one of the parameters V and J is nonzero, we obtain the following expressions for the critical values:

$$J_{\rm c}^{\rm ph} = \frac{8g_t\, t}{3g_J(I_{\rm ph} - \chi)}, \qquad V_{\rm c}^{\rm ph} = \frac{2g_t\, t}{(I_{\rm ph} - \chi)}, \tag{3.26}$$

$$J_{\rm c}^{\rm pp} = \frac{8g_t\, t}{3g_J(I_{\rm pp} - \chi)}, \qquad V_{\rm c}^{\rm pp} = \frac{-2g_t\, t}{(I_{\rm pp} + \chi)}. \tag{3.27}$$

The numerical values for $J_{\rm c}$ and $V_{\rm c}$ are given in Table 3.2. One can see, that the

Table 3.2: The parameters for the kagomé (K) and the pyrochlore (P) lattice. The critical values are given in units of t. The coefficient of $\Delta_{\rm ph}$ (bond order wave) in Eq. (3.22) is negative for $J > J_{\rm c}^{\rm ph}$ ($V = 0$) or for *repulsive* $V > V_{\rm c}^{\rm ph}$ ($J = 0$). The coefficient of $\Delta_{\rm pp}$ (superconductivity) is negative for $J > J_{\rm c}^{\rm pp}$ ($V = 0$) or for *attractive* $V < V_{\rm c}^{\rm pp}$ ($J = 0$).

	d	μ	b	ξ_0	δ	g_t	g_J
K	2	-1	6	3	1/3	1/2	9/4
P	3	-2	12	4	1/2	2/3	16/9
	χ	$I_{\rm ph}$	$I_{\rm pp}$	$J_{\rm c}^{\rm ph}$	$J_{\rm c}^{\rm pp}$	$V_{\rm c}^{\rm ph}$	$V_{\rm c}^{\rm pp}$
K	0.43	1.08	0.59	0.91	3.58	1.53	-0.98
P	0.32	1.05	0.62	1.36	3.33	1.81	-1.43

tendency for inversion symmetry breaking is much stronger than the tendency for superconductivity in both lattices and that both the antiferromagnetic J and the repulsive V support the inversion symmetry breaking. The integral $I_{\rm ph}$ is large because the factor $\xi_0^2 - \xi^2$ takes its maximum at $\xi = 0$ whereas the factor $(\xi + \mu)^2$ in the integral $I_{\rm pp}$ is much smaller for small values of ξ. In other words, superconductivity has the handicap that the potential is proportional to the dispersion $\epsilon_{\mathbf{k}}$, therefore it is small at the Fermi surface and is only finite due to the finite value of μ. The nearest-neighbor repulsion is harmful for Cooper (particle-particle) pairing, as can be seen from Table 3.2. In the particle-hole instability, however, two particles tend to form a singlet on every second triangle (tetrahedron) on the kagomé (pyrochlore) lattice. In this way

the singlet is still mobile and keeps $-dt$ of its kinetic energy and at the same time reduces the nearest-neighbor repulsion energy from $4V/3$ ($3V/2$) to V on every second triangle (tetrahedron). On the triangles (tetrahedra) without a singlet, the expectation value of the nearest-neighbor repulsion is however still $4V/3$ ($3V/2$). In the limit where the kinetic energy is negligible ($t \ll V, J$) also other phases may appear. It is therefore important to emphasize that a finite kinetic energy is necessary to stabilize the bond order wave, because this phase arises due to the interplay between the kinetic and interaction energy.

The limit of large V was recently discussed in the context of LiV_2O_4 by Yushankhai *et al.* in Ref. [108] for the pyrochlore lattice with $n = 1/2$. The possibility of inversion symmetry breaking was not considered in that study. But if V is of the order of t, the optimization of the kinetic and the repulsion energy can lead to a compromise which breaks the inversion symmetry.

In the bond order wave phase that we found in this section for the kagomé and the pyrochlore lattice, the up-triangles (tetrahedra) have a higher expectation value of the kinetic energy than the down-triangles (tetrahedra). Furthermore a gap proportional to Δ_{ph} opens at the Fermi surface. Therefore, the system made a transition from a semi-metal to an insulator. This transition is similar to the Peierls metal-insulator transition, where a half-filled system lowers spontaneously its crystal symmetry in order to open a gap at the Fermi surface. Phonons or the elasticity of the crystal play a crucial role in the Peierls transition. In our case, as we showed, the transition can be driven by a purely electronic mechanism in an infinitely rigid lattice. In reality, the crystal structure will always relax and in this way additionally enhance the transition.

3.5.1 "Supersolid"

So far we have restricted our attention to the commensurate filling with 2 electrons per unit cell. Here, we will qualitatively discuss the possible effects of doping such a system. As we have shown above, a gap can form at the Fermi surface at this fractional filling due to the spontaneous inversion symmetry breaking.[b] Lets assume that the nearest-neighbor interactions V and J are such that a small gap $2m = 6\Delta_{\mathrm{ph}}$ exists between the mass hyperboloids at the K points. The original density of states $D(\xi)$ changes to the gapped density of states $D_m(\xi)$, given by $\theta(|\xi| - m)D(\xi)$ for ξ close to the gap, as shown in Fig. 3.5.

[b]For concreteness we focus on the kagomé lattice.

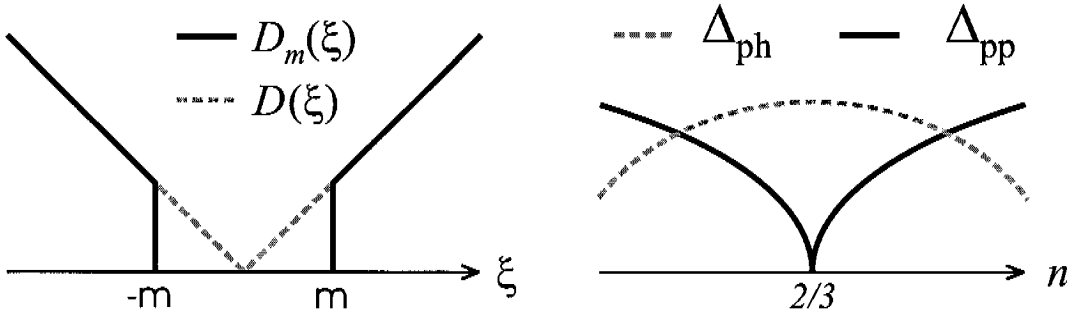

Figure 3.5: (left) The density of states with and without gap for small ξ. (right) A possible scenario for the order parameters Δ_{pp} and Δ_{ph} close to the filling $n = 2/3$.

Due to this gap the grand-canonical free energy is linear in the chemical potential. This linearity is mapped onto a kink in the free energy by the Legendre transform. While the chemical potential lies within the gap, the system is incompressible, i.e., the particle number is not changed by a variation of the gap. If the chemical potential however lies below or above the gap, the system is doped with additional holes or particles, respectively. The thermodynamic ground state of the doped system is not known so far and different scenarios are possible: The system could phase separate into a doped region and into an undoped region. The undoped regions would still profit from the BOW mechanism and the doped region could become superconducting as the Cooper instability is not limited to a specific filling. Due to the Coulomb repulsion between the electrons, which in our model is given by the on-site repulsion U and the nearest-neighbor repulsion V, it might be favorable for the system to form domains of a given size rather than only two macroscopic regions. An alternative scenario could be the formation 1D domains similar to the stripes observed in certain cuprate-superconductors.

If the system stays homogeneous, we can assume that the BOW state is destroyed for large enough doping, leading to a superconducting ground state. The transition from the BOW to the superconducting state could be a first order or transition. It is, however, possible that for a finite doping range both order parameters coexist and that the superconducting order parameter disappears and reappears continuously at the point $n = 2/3$ as it is sketched on the right hand side of Fig. 3.5. In the coexistence region the system would break spontaneously lattice symmetries and the U(1) gauge symmetry and could therefore be called a "supersolid". We have not investigated the doped

system away from the fractional filling in detail but we believe that the study of the ground state and the excitations of such a system is a difficult but very interesting task.

3.6 Weak-coupling discussion

The underlying lattices of the four bisimplex lattices considered here are bipartite lattices. The tight-binding bands of the bisimplex lattice follow the tight-binding dispersion of the underlying bipartite lattice with additional flat bands on top of them. At the particular filling of one electron per simplex the dispersing bands of the underlying bipartite lattice are exactly half-filled. For the two-leg ladder, the square lattice, and the honeycomb lattice, which are the underlying lattices of the kagomé strip, the checkerboard, and the kagomé lattice, respectively, weak-coupling RG methods at half-filling are available [12, 16, 106]. The t-J model is a model for strong electronic interactions, therefore, we consider in this section the weak-coupling Hubbard model with the interaction

$$H_{\text{int}} = U \sum_{\mathbf{r}} c^{\dagger}_{\mathbf{r}\uparrow} c^{\dagger}_{\mathbf{r}\downarrow} c_{\mathbf{r}\downarrow} c_{\mathbf{r}\uparrow}, \tag{3.28}$$

or the somewhat more general extended Hubbard interaction of Eq. (3.2). It is possible to map this weak local Coulomb repulsion on the original bisimplex lattice on an effective interaction for the underlying half-filled lattice. In this mapping the operator O_{BOW}, whose expectation value serves as an order parameter for the bond order wave instability, is mapped on a charge density wave (CDW) operator O_{CDW} on the underlying bipartite lattice.

Although we can not expect in general that the strong coupling phases are related to the physics at weak coupling, there are cases where the strong coupling phase can be understood as an instability arising at weak coupling. We will show in the following that this is the case for the one-dimensional kagomé strip, where we find in fact a CDW instability in the underlying two-leg ladder.

The Hamiltonian (3.28) does not directly drive the BOW instability on the bisimplex lattice. It turns out that also the derived effective interaction on the underlying lattice does not drive the CDW instability directly, i.e., the CDW instability can not be obtained as a mean-field instability of the effective interaction but occurs due to higher order and not due to first order terms of the interaction.

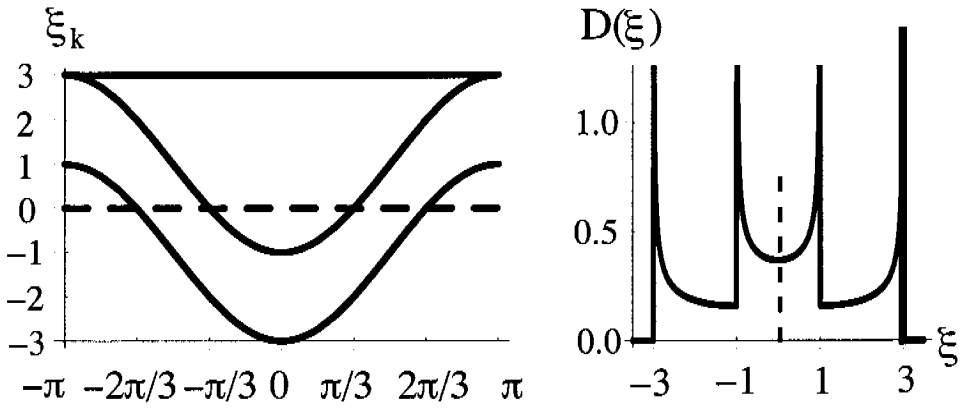

Figure 3.6: The kagomé strip bands and the density of states per unit cell and spin. The energy is measured in units of t.

In the case of the two-leg ladder the first-loop RG provides these higher order terms and the CDW instability is in fact obtained also in weak coupling with the purely local Hubbard interaction. On the other hand, the derived effective interaction for the honeycomb and the square lattice turns out to be irrelevant in the RG sense. For the checkerboard lattice, after including a nn interaction term into the Hamiltonian, both the mean-field and the RG analysis predict a CDW instability on the square lattice.

3.6.1 Kagomé strip

We consider the kagomé strip shown in Fig. 3.1 (c) as the 1D analogue of the kagomé lattice. This lattice has been introduced in Ref. [109], where it was shown to share some of the peculiar magnetic properties of the 2D kagomé lattice.

The tight-binding bands of the kagomé strip with $\mu = -t$ are shown in Fig. 3.6. The dispersing bands are the same as the bands of a two-leg ladder. The flat band originates from states that are trapped within one rhombus. The density of states has square-root singularities at $\pm t, \pm 3t$ and a delta-peak at $3t$. The Fermi surface is given by the 4 points $\pm k_{\mathrm{F}1}$ and $\pm k_{\mathrm{F}2}$, where $k_{\mathrm{F}1} = \pi/3$ and $k_{\mathrm{F}2} = 2\pi/3$. There is a finite density of states at the Fermi surface. The kagomé strip can be viewed as a kagomé lattice tube, i.e., a kagomé lattice with finite width and periodic boundary conditions. In order to see that the bands in Fig. 3.6 are in fact a cut through the kagomé dispersion shown in Fig. 3.3,

one has to shift one of the dispersing bands by π. This difference arises because our notation is chosen to emphasize the similarities of the kagomé strip to the two-leg ladder.

In contrast to the kagomé and the pyrochlore lattice, the density of states at the Fermi surface is finite for the kagomé strip and we therefore expect qualitative changes in this 1D system even for weak interactions. We perform a weak-coupling RG and bosonization analysis for the kagomé strip, and we show that the bond order wave instability is already present for arbitrary weak coupling. In this section we will only present the results of this analysis and refer to App. B.1.1 for further details.

We derive an effective interaction for the two-leg ladder, that corresponds in weak coupling to the local Coulomb repulsion on the kagomé strip (3.28). In this derivation we can drop terms that involve the high energy states of the flat band and focus on the states in the dispersing bands. We denote the annihilation operator of these states by $\gamma_{\mathbf{k}\sigma} = \gamma_{ki\sigma}$ where k is the momentum along the strip and $i = 1, 2$ is the band index. If we rewrite the Hamiltonian H_{int} of Eq. (3.28) in terms of these new operators we obtain the interaction.

$$H_{\text{int}} \to \frac{U}{L} \sum_{\mathbf{k}_1 \ldots \mathbf{k}_4}{}' g_{\mathbf{k}_1 \ldots \mathbf{k}_4} \gamma^\dagger_{\mathbf{k}_1\uparrow} \gamma^\dagger_{\mathbf{k}_2\downarrow} \gamma_{\mathbf{k}_3\downarrow} \gamma_{\mathbf{k}_4\uparrow}, \tag{3.29}$$

where the prime over the sum restricts the sum to momentum conserving $\mathbf{k}$-values. For weak interaction we can replace $\mathbf{k}_l$ in $g_{\mathbf{k}_1 \ldots \mathbf{k}_4}$ by $(k_{\text{F}i_l}, i_l)$ and we obtain the simple expression

$$g_{\mathbf{k}_1 \ldots \mathbf{k}_4} = \mathrm{e}^{-\mathrm{i}\frac{q}{2}} (\delta_{i_1 i_2} \delta_{i_3 i_4} + \delta_{i_1 i_3} \delta_{i_2 i_4} + \delta_{i_1 i_4} \delta_{i_2 i_3})/6, \tag{3.30}$$

where $q = k_1 + k_2 - k_3 - k_4$.

The effective interaction (3.29) can now be expressed in terms of left and right moving currents and in this way we find the initial values for the RG equations of the two-leg ladder. The integration of the RG equations with these initial values converges to an analytic solution that was identified by bosonization techniques as a charge density wave solution (CDW) solution [16]. This means that the operator

$$O_{\text{CDW}} = \frac{1}{L} \sum_{k\sigma} \gamma^\dagger_{k1\sigma} \gamma_{k+\pi,2\sigma} + \gamma^\dagger_{k+\pi,2\sigma} \gamma_{k1\sigma} \tag{3.31}$$

acquires a finite value. The bond order wave order-parameter on the kagomé strip is given by the expectation value of an operator O_{BOW}.

The operators O_{CDW} and O_{BOW} transform identically under all symmetries of the system and, therefore, they describe the same phase.

In addition, O_{CDW} is the effective operator on the two-leg ladder for O_{BOW}, i.e., if one does the same substitutions as we did for deriving Eq. (3.29) one sees that $O_{\mathrm{BOW}} \rightarrow O_{\mathrm{CDW}}$, if one chooses the right prefactor in the definition of O_{BOW}.

We have shown that the bond order wave instability that is expected to occur at rather strong interactions according to the arguments of the preceding sections, is in fact already present in weak coupling for the one-dimensional kagomé strip. The density matrix renormalization group (DMRG) results in Sec. 3.7 provide convincing evidence that the same symmetry breaking also occurs in the t-J model.

3.6.2 Checkerboard lattice

The tight-binding bands of the checkerboard lattice consist of an upper flat band and a lower dispersive band. The lower band is identical to the tight-binding band of the square lattice and touches the flat band at the M points. For the filling $n = 1/2$ the dispersive band is half-filled, and the Fermi surface is quadratic and perfectly nested with the nesting vector (π, π). The corners $(\pi, 0)$ and $(0, \pi)$ of the Fermi surface are saddle points and lead to a logarithmically diverging density of states.

For the checkerboard lattice we study the extended Hubbard Hamiltonian with the interaction of Eq. (3.2) including nn antiferromagnetic J exchange and nn repulsion V. We choose the chemical potential $\mu = -2t$ which corresponds to a half-filled lower band and we can write

$$H_0 = \sum_{\mathbf{k}\sigma} \xi_{\mathbf{k}} \gamma^{\dagger}_{\mathbf{k}\sigma} \gamma_{\mathbf{k}\sigma} + 4\,t N_{\mathrm{flat}} \quad \text{with} \quad \xi_{\mathbf{k}} = -2t(\cos k_1 + \cos k_2). \tag{3.32}$$

N_{flat} counts the number of electrons in the flat band at $4t$. In the weak-coupling limit these states do not affect the low-energy physics of the system and therefore they will be dropped in the following analysis.

For small couplings U, V and J we obtain an effective interaction Hamiltonian (App. B.1.2) given by

$$H_{\mathrm{int}}^{\mathrm{eff}} = \frac{1}{2N} {\sum_{\mathbf{k}_1 \ldots \mathbf{k}_4}}' g_{\mathbf{k}_1 \ldots \mathbf{k}_4} \sum_{\sigma\sigma'} \gamma^{\dagger}_{\mathbf{k}_1\sigma} \gamma^{\dagger}_{\mathbf{k}_2\sigma'} \gamma_{\mathbf{k}_3\sigma'} \gamma_{\mathbf{k}_4\sigma}, \tag{3.33}$$

with

$$\begin{aligned} g_{\mathbf{k}_1\ldots\mathbf{k}_4} &= \sum_{\nu=1}^{2}(Ue^{\nu}_{\mathbf{q}} + 2\tilde{V}e^{\nu}_{\mathbf{q}_{23}} - Je^{\nu}_{\mathbf{q}_{24}})e^{\nu}_{\mathbf{k}_1}e^{\nu}_{\mathbf{k}_2}e^{\nu}_{\mathbf{k}_3}e^{\nu}_{\mathbf{k}_4} \\ &+ \sum_{\nu=1}^{2}(4\tilde{V}f^{\nu}_{\mathbf{k}_1\mathbf{k}_4}f^{\bar{\nu}}_{\mathbf{k}_2\mathbf{k}_3} - 2Jf^{\nu}_{\mathbf{k}_1\mathbf{k}_3}f^{\bar{\nu}}_{\mathbf{k}_2\mathbf{k}_4}) \end{aligned} \tag{3.34}$$

with $e^{\nu}_{\mathbf{k}} = \cos(k_\nu/2)$, $f^{\nu}_{\mathbf{k}\mathbf{k}'} = e^{\nu}_{\mathbf{k}-\mathbf{k}'}e^{\nu}_{\mathbf{k}}e^{\nu}_{\mathbf{k}'}$, $\tilde{V} = V - J/4$, $\mathbf{q} = \mathbf{k}_1 + \mathbf{k}_2 - \mathbf{k}_3 - \mathbf{k}_4$, and $\mathbf{q}_{ij} = \mathbf{q} - 2(\mathbf{k}_i - \mathbf{k}_j)$. The two saddle points $P_1 = (0, \pi)$ and $P_2 = (\pi, 0)$ of the dispersion lead to the logarithmic divergence of the density of states. Therefore, we can characterize very weak interactions by the values of the function $g_{\mathbf{k}_1\ldots\mathbf{k}_4}$ where all four momenta $\mathbf{k}_1 \cdots \mathbf{k}_4$ lie on one of the two saddle points. Following the notation of Ref. [12] we have the following four couplings constants:

$$g_{\mathbf{k}_1\ldots\mathbf{k}_4} = \begin{cases} g_1 = -2J & \mathbf{k}_1, \mathbf{k}_3 \in P_1 \\ g_2 = +4\tilde{V} & \mathbf{k}_1, \mathbf{k}_4 \in P_1 \\ g_3 = 0 & \mathbf{k}_1, \mathbf{k}_2 \in P_1 \\ g_4 = U + 2\tilde{V} - J & \mathbf{k}_1 \ldots \mathbf{k}_4 \in P_1 \end{cases} \tag{3.35}$$

From the RG equations of Ref. [12] we see that for positive values of U, V, and J the coupling g_1 flows to $-\infty$ and the coupling g_2 flows to $+\infty$, [c] whereas the other couplings flow to 0. This shows that the charge density wave susceptibility is diverging most rapidly under the RG flow. As shown in Fig. 3.7 the CDW instability on the square lattice corresponds to the BOW instability on the checkerboard lattice, i.e., both instabilities break exactly the same symmetries. Note, that within the framework of this RG scheme, we can not determine whether a usual CDW or a so-called charge flux phase, which is a CWD with a d-wave form factor, is stabilized. In the following we will denote these two phases with s-CDW and d-CDW. (Note, that for $J = 0$ only the coupling g_2 diverges. In this case we can not even determine whether a CDW of SDW phase is stabilized.) In order to show, that the s-CDW phase is in fact favored over the d-CDW, at least in a mean-field analysis, we restrict the interaction Hamiltonian (3.33) to the CDW channel and obtain:

$$H_{\mathrm{CDW}} = \frac{1}{4N}\sum_{\mathbf{k}\mathbf{k}'} V^{\mathrm{CD}}_{\mathbf{k}\mathbf{k}'} \sum_{\sigma\sigma'} \gamma^{\dagger}_{\mathbf{k}\sigma}\gamma_{\mathbf{k}+\mathbf{Q},\sigma}\gamma^{\dagger}_{\mathbf{k}'+\mathbf{Q},\sigma'}\gamma_{\mathbf{k}'\sigma'} \tag{3.36}$$

[c] For $\tilde{V} < 0$ g_2 flows to 0, but also in this case the CDW phase is stabilized.

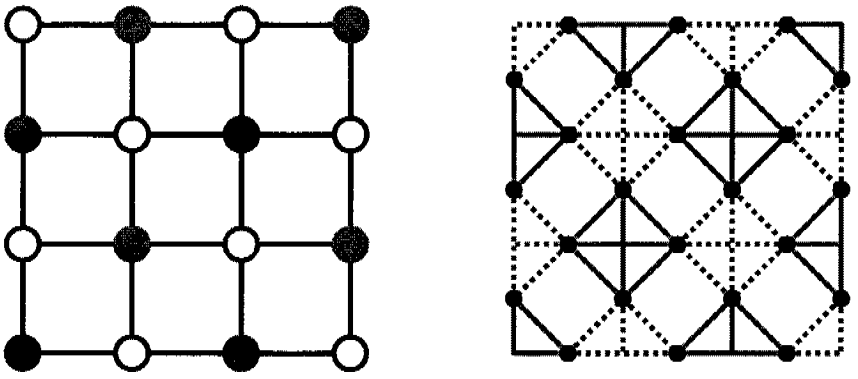

Figure 3.7: Correspondence between the s-CDW phase on the effective square lattice (left) and the plaquette phase or BOW phase on the original checkerboard lattice (right).

with

$$V^{\mathrm{CD}}_{\mathbf{k}\mathbf{k}'} = 2g_{\mathbf{k},\mathbf{k}'+\mathbf{Q},\mathbf{k}',\mathbf{k}+\mathbf{Q}} - g_{\mathbf{k},\mathbf{k}'+\mathbf{Q},\mathbf{k}+\mathbf{Q},\mathbf{k}'} \tag{3.37}$$

$$= V^{\mathrm{CD}}_{\mathbf{k}\mathbf{k}',s} + V^{\mathrm{CD}}_{\mathbf{k}\mathbf{k}',d} + V^{\mathrm{CD}}_{\mathbf{k}\mathbf{k}',d'} + V^{\mathrm{C}}_{\mathbf{k}\mathbf{k}',p} \tag{3.38}$$

$$V^{\mathrm{CD}}_{\mathbf{k}\mathbf{k}',s} = -\frac{\tilde{V}+J}{2}\left[(1-\cos k_1\cos k_2)(1-\cos k_1'\cos k_2') + (\sin^2 k_1+\sin^2 k_2)(\sin^2 k_1'+\sin^2 k_2')/2\right] \tag{3.39}$$

$$V^{\mathrm{CD}}_{\mathbf{k}\mathbf{k}',d} = -\frac{\tilde{V}+J}{2}(\cos k_1-\cos k_2)(\cos k_1'-\cos k_2') \tag{3.40}$$

$$V^{\mathrm{CD}}_{\mathbf{k}\mathbf{k}',d'} = -\frac{\tilde{V}+J}{2}\sin k_1\sin k_2\sin k_1'\sin k_2' \tag{3.41}$$

$$V^{\mathrm{CD}}_{\mathbf{k}\mathbf{k}',p} = +\frac{U}{4}(\sin k_1\sin k_1'+\sin k_2\sin k_2'). \tag{3.42}$$

In (3.40) we dropped a term proportional to $\cos k_1+\cos k_2$, as it vanishes along the FS, and in (3.42) we dropped terms proportional to V/U or J/U. With $\Delta_{\mathbf{k}} = \frac{1}{N}\sum_{\mathbf{k}'} V^{\mathrm{C}}_{\mathbf{k}\mathbf{k}'}F_{\mathbf{k}'}$ and $F_{\mathbf{k}} = \sum_\sigma\langle\gamma^\dagger_{\mathbf{k}+\mathbf{Q},\sigma}\gamma_{\mathbf{k}\sigma}\rangle$ we obtain the linearized gap equation

$$\Delta_{\mathbf{k}} = -\frac{1}{N}\sum_{\mathbf{k}'} V^{\mathrm{C}}_{\mathbf{k},\mathbf{k}'}\frac{\tanh(\xi_{\mathbf{k}'}/2T_{\mathrm{c}})}{2\xi_{\mathbf{k}'}}\Delta_{\mathbf{k}'} \tag{3.43}$$

Note, that the d'- and the p-wave instability do not open a gap at the saddle points, furthermore, the p-wave instability is strongly repulsive. For the d-CDW

state the pair potential (3.40) is separable and the linearized gap equation can be written in the simpler form

$$1 = \frac{\tilde{V}+J}{2N}\sum_{\mathbf{k}}(\cos k_1 - \cos k_2)^2 \frac{\tanh(\xi_{\mathbf{k}}/2T_c^d)}{2\xi_{\mathbf{k}}}. \tag{3.44}$$

The pair potential for the s-CDW state (3.39) is not separable. But if we neglect for a moment the second line in (3.39) we obtain an analogous expression to (3.44) for the critical temperature of the s-CDW with $\cos k_1 - \cos k_2$ replaced by $1 - \cos k_1 \cos k_2$. As on the FS we have $\cos k_2 = -\cos k_1$ and as $|2\cos k_1| \leq 1 + \cos^2 k_1$, we know that the critical temperature of the s-CDW phase is higher than the critical temperature of the d-CDW phase. Including the non-negative second term in (3.39) would only lead to a further increase of the critical temperature. Note, that the magnitude of the d- and the s-CDW potentials are identical for the momenta on the saddle points. Therefore it is not surprising that they cannot be distinguished by the two-patch RG method. However, in the mean-field we can see that the s-CDW is favored over the d-CDW state, as it opens a finite gap along the entire FS. It is possible to do such a mean-field analysis also for SDW and superconducting instabilities. For superconductivity we have the Cooper channel

$$H_{\mathrm{SC}} = \frac{1}{2N}\sum_{\mathbf{k}\mathbf{k}'} V^{\mathrm{SC}}_{\mathbf{k}\mathbf{k}'} \sum_{\sigma\sigma'} \gamma^\dagger_{\mathbf{k}\sigma}\gamma^\dagger_{-\mathbf{k}\sigma'}\gamma_{-\mathbf{k}'\sigma'}\gamma_{\mathbf{k}'\sigma} \tag{3.45}$$

that can be projected onto the different symmetry channels as follows:

$$V^{\mathrm{SC}}_{\mathbf{k}\mathbf{k}'} = g_{\mathbf{k},-\mathbf{k},-\mathbf{k}',\mathbf{k}'} = V^{\mathrm{SC}}_{\mathbf{k}\mathbf{k}',s} + V^{\mathrm{SC}}_{\mathbf{k}\mathbf{k}',d} + V^{\mathrm{SC}}_{\mathbf{k}\mathbf{k}',d'} + V^{\mathrm{SC}}_{\mathbf{k}\mathbf{k}',p} \tag{3.46}$$

$$V^{\mathrm{SC}}_{\mathbf{k}\mathbf{k}',s} = \frac{U}{4} \tag{3.47}$$

$$V^{\mathrm{SC}}_{\mathbf{k}\mathbf{k}',d} = \frac{U}{8}(\cos k_1 - \cos k_2)(\cos k_1' - \cos k_2') \tag{3.48}$$

$$V^{\mathrm{SC}}_{\mathbf{k}\mathbf{k}',d'} = \frac{\tilde{V}-J}{2}\sin k_1 \sin k_2 \sin k_1' \sin k_2' \tag{3.49}$$

$$V^{\mathrm{SC}}_{\mathbf{k}\mathbf{k}',p} = \frac{2\tilde{V}+J}{4}(2 + \cos k_1 \cos k_1' + \cos k_2 \cos k_2') (\sin k_1 \sin k_1' + \sin k_2 \sin k_2') \tag{3.50}$$

where we again set $\cos k_1 + \cos k_2 = 0$ and neglected terms proportional to J/U and V/U in the potentials containing U (3.47, 3.48). We find strong repulsion

($\propto U$) in the d- and in the s-wave channel, and only weaker ($\propto V, J$) and mainly repulsive interactions in the d'- an the p-wave channel.[d] Furthermore, the d'- an the p-wave channels do not open a gap at the saddle points. It is therefore quite clear, that the superconducting instabilities can not compete with the s-CDW instability.

For the pair SDW instabilities, we obtain the Hamiltonian

$$H_{\mathrm{SDW}} = \frac{1}{4N} \sum_{\mathbf{k}\mathbf{k}'} V^{\mathrm{SD}}_{\mathbf{k}\mathbf{k}'} \sum_{\sigma\sigma'} \sigma\sigma' \gamma^{\dagger}_{\mathbf{k}\sigma} \gamma_{\mathbf{k}+\mathbf{Q},\sigma} \gamma^{\dagger}_{\mathbf{k}'+\mathbf{Q},\sigma'} \gamma_{\mathbf{k}'\sigma'}, \tag{3.51}$$

where the SDW pair potential is given by

$$V^{\mathrm{SD}}_{\mathbf{k}\mathbf{k}'} = -g_{\mathbf{k},\mathbf{k}'+\mathbf{Q},\mathbf{k}+\mathbf{Q},\mathbf{k}'} = V^{\mathrm{SD}}_{\mathbf{k}\mathbf{k}',s} + V^{\mathrm{SD}}_{\mathbf{k}\mathbf{k}',d} + V^{\mathrm{SD}}_{\mathbf{k}\mathbf{k}',d'} + V^{\mathrm{SD}}_{\mathbf{k}\mathbf{k}',p} \tag{3.52}$$

and with the same approximation as before we have

$$\begin{aligned} V^{\mathrm{SD}}_{\mathbf{k}\mathbf{k}',s} &= -\frac{\tilde{V}}{2}[(1-\cos k_1 \cos k_2)(1-\cos k'_1 \cos k'_2) \\ &\quad +(2-\cos 2k_1 - \cos 2k_2)(2-\cos 2k'_1 - \cos 2k'_2)/8] \end{aligned} \tag{3.53}$$

$$V^{\mathrm{SD}}_{\mathbf{k}\mathbf{k}',d} = -\frac{\tilde{V}}{2}(\cos k_1 - \cos k_2)(\cos k'_1 - \cos k'_2) \tag{3.54}$$

$$V^{\mathrm{SD}}_{\mathbf{k}\mathbf{k}',d'} = -\frac{\tilde{V}}{2} \sin k_1 \sin k_2 \sin k'_1 \sin k'_2 \tag{3.55}$$

$$V^{\mathrm{SD}}_{\mathbf{k}\mathbf{k}',p} = -\frac{U}{4}(\sin k_1 \sin k'_1 + \sin k_2 \sin k'_2). \tag{3.56}$$

These SDW potentials are identical to the CDW potentials in Eqs. (3.39-3.42) if we replace only $\tilde{V}+J$ by $\tilde{V}$ and U by $-U$. For $J>0$ we have $\tilde{V}+J>\tilde{V}$ and therefore the s-, d- and d'-CDW instabilities are favored over the corresponding SDW instabilities.

The p-SDW instability is strongly attractive but has the handicap, that it does not open a gap at the saddle points, therefore for weak interactions the s-CDW state will still be favored over the p-SDW state, i.e., for interaction parameters (U,V,J) given by $(\alpha u, \alpha v, \alpha j)$ we can find for all positive values of (u,v,j) an α_0 such that for $0<\alpha<\alpha_0$ the s-CDW state is stabilized.

In conclusion, in this section we showed with two-patch RG and mean-field arguments, that for weak enough repulsive and antiferromagnetic interactions the s-CDW phase is stabilized in the effective model on the square lattice. This CDW phase corresponds to the BOW phase on the original checkerboard lattice.

[d] In the p-wave channel we would have triplet superconductivity

3.6.3 Kagomé lattice

The underlying lattice of the kagomé lattice is the bipartite honeycomb lattice. The filling considered here corresponds to a half-filled honeycomb lattice, where the Fermi surface consists of only two points. It is possible to derive an effective interaction for the honeycomb lattice that corresponds to the weak onsite Coulomb repulsion (3.28) on the kagomé lattice. The effective Hamiltonian on the honeycomb lattice contains onsite terms and nn interaction and pair hopping terms and is given by

$$H_{\text{int}} \to \frac{U}{3}\sum_i n_{i\uparrow}n_{i\downarrow} + \sum_{\langle ij\rangle}\left(Vn_in_j - J\mathbf{S}_i\cdot\mathbf{S}_j - \tilde{J}[f^\dagger_{i\uparrow}f^\dagger_{1\downarrow}f_{j\uparrow}f_{j\downarrow} + \text{h.c.}]\right), \quad (3.57)$$

where $V = U/18$, $J = 2\tilde{J} = 2U/9$. The sum $\sum_i$ ($\sum_{\langle ij\rangle}$) runs over all sites (bonds) of the honeycomb lattice. As the Hamiltonian H_{int} contains, e.g., nn repulsion terms, one could expect that the mean-field analysis of this effective interaction Hamiltonian could predict a CDW instability on the honeycomb lattice, that would correspond to the BOW instability on the kagomé lattice. Calculating all the Hartree-Fock energies using a CDW trial wave function, we find that the interaction energy does not depend on the CDW order parameter but the kinetic energy increases as the CDW order is build up. The situation does therefore not change by going to the effective Hamiltonian: In the same way as the onsite Hubbard energy does not depend on the BOW strength, the effective interaction energy on the square lattice does not depend on the CDW order parameter in the mean-field analysis. In order to see the CDW instability on the checkerboard lattice in mean-field we should also include nn interaction terms in the original Hamiltonian on the kagomé lattice. The mean-field analysis of such a Hamiltonian has already be done in Sec. 3.5.

The onsite Hubbard interaction (3.28) produces onsite and nn interaction terms in the effective interaction. As the density of states vanishes linearly at the Fermi level as seen in Fig. 3.3 such an effective short-ranged interaction is irrelevant in the RG sense [106].

In conclusion, we found for the kagomé strip that already the onsite Hubbard interaction is sufficient to produce the CDW instability in the weak-coupling RG analysis. For the checkerboard lattice, we had in addition to include nn neighbor interactions to observe the CDW instability on the square lattice both in mean-field and in the two-patch RG. For the kagomé lattice we calculated the effective Hamiltonian for the Hubbard model on the honeycomb lattice, but no CDW instability could be obtained in mean-field. In

fact, according to RG calculations on the half-filled honeycomb lattice, there is no instability in weak-coupling on the honeycomb lattice for any kind of short-ranged interactions [106].

3.7 Numerical results

In this section we compare the analytical predictions obtained in the preceding sections to various numerical results on one- and two-dimensional systems. We will first discuss some exact diagonalization results for both the kagomé lattice at $n = 2/3$ and the checkerboard lattice at $n = 1/2$. Then we move to the kagomé strip at $n = 2/3$, where we report extensive density matrix renormalization group calculations [11], both for the t-J and the Hubbard model. In essence the numerical results corroborate the analytical predictions on the presence of a bond order wave instability at a particular doping.

3.7.1 Kagomé lattice

The analytical arguments presented in Sec. 3.3, 3.4, and 3.5 predict a bond order wave instability at filling $n = 2/3$. In finite, periodic systems this instability can be detected with a correlation function of the bond strength, either of the kinetic term or the exchange term. Here we chose to work with the kinetic term, but the exchange term gives similar results. The correlation function is defined as:

$$C_{\mathrm{Kin}}[(i,j),(k,l)] = \langle \mathrm{Kin}(i,j)\ \mathrm{Kin}(k,l)\rangle - \langle \mathrm{Kin}(i,j)\rangle\langle \mathrm{Kin}(k,l)\rangle,$$

where

$$\mathrm{Kin}(i,j) = -\sum_{\sigma} c^{\dagger}_{i\sigma} c_{j\sigma} + \mathrm{h.c.}, \tag{3.58}$$

and (i,j) and (k,l) denote two different nearest-neighbor bonds of the kagomé lattice, that have no common site. This correlation function has been calculated for all distances in the ground state of a finite kagomé sample with 21 sites, containing 7 holes at $J/t = 0.4$. The result is plotted in Fig. 3.8. The reference bond uniquely belongs to a certain class of triangles (up-triangles in our case). Based on the theoretical picture one expects the correlation function to be positive for all bonds on the same type of triangles and negative on the others. This is indeed what is seen in Fig. 3.8. We have also calculated the same quantity for $J/t = 1$ and $J/t = 2$ and the bond order wave correlations

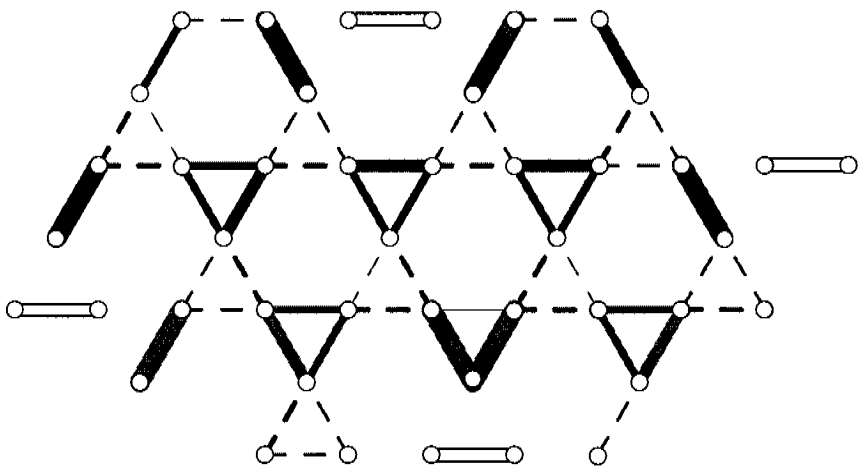

Figure 3.8: Correlation function of the kinetic energy (Eq. (3.58)) of a 21 sites kagomé sample at $n = 2/3$ and $J/t = 0.4$. The black, empty bonds denote the same reference bond, the red, full bonds negative and the blue, dashed bonds positive correlations. The line strength is proportional to the magnitude of the correlations.

(not shown) were becoming even stronger for larger J/t. In this respect the ED calculations confirm the qualitative picture developed above, that the homogeneous t-J model on the kagomé lattice at $n = 2/3$ has an intrinsic instability towards a spontaneous breaking of the inversion symmetry.

3.7.2 Checkerboard lattice

As the 3D pyrochlore lattice is out of reach of present unbiased computational methods, we chose to study a related system in 2D, the checkerboard lattice, see Fig. 3.1 (d). It is similar to the pyrochlore lattice, as it also consists of corner sharing units which are topologically equivalent to a tetrahedron. In the checkerboard lattice these units form a square lattice, compared to a diamond lattice in the true pyrochlore. This geometry still allows the inversion-breaking instability, which we therefore also expect to happen at $n = 1/2$.

The magnetic properties of the checkerboard t-J model at half-filling ($n = 1$) are somewhat better understood than for the kagomé lattice. The ground state is believed to be a valence bond solid or plaquette resonating valence bond (RVB) state where the four spins on half of the void plaquettes (i.e., *not* on the tetrahedra) form a spin singlet [110–113], yielding a two-fold degenerate ground state.

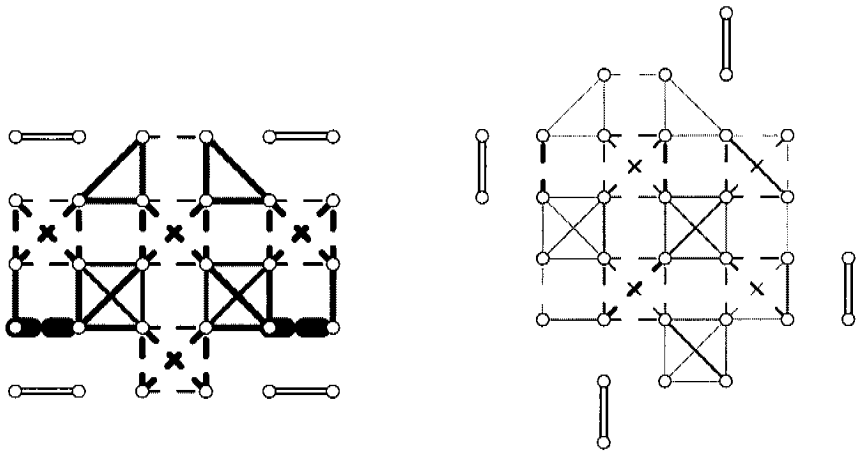

Figure 3.9: Correlation function of the kinetic energy (Eq. (3.58)) of the checkerboard lattice for a 16 sites sample (left) and a 20 sites sample (right) at $n = 1/2$ and $J/t = 1$. The colors and line styles follow the convention used in Fig. 3.8.

We have calculated the correlation function of the kinetic energy C_{Kin} (Eq. (3.58)) for the checkerboard lattice at $n = 1/2$. The results for two samples with $N = 16$ and $N = 20$ at $J/t = 1$ are shown in Fig. 3.9. The qualitative picture drawn analytically is confirmed again by the numerical calculations. Especially for the $N = 16$ sample we find pronounced bond order wave correlations, which signal inversion symmetry breaking. The $N = 20$ is in overall agreement, although the correlations are somewhat weaker. This trend is followed as well by a $N = 24$ sample which is however not shown here.

Note that the present phase at $n = 1/2$ is similar to the one discussed at half-filling. The main difference being the location of the strongly correlated units. At $n = 1$ (half-filling) these are the *uncrossed* plaquettes, while at $n = 1/2$ the strong units are the *crossed* plaquettes. Otherwise the symmetry breaking properties are the same: they both only break lattice symmetries, and the ground state is therefore two-fold degenerate, and they have a gap to all excitations. In that sense we find again a valence bond solid state at $n = 1/2$ upon doping the checkerboard lattice away from $n = 1$.

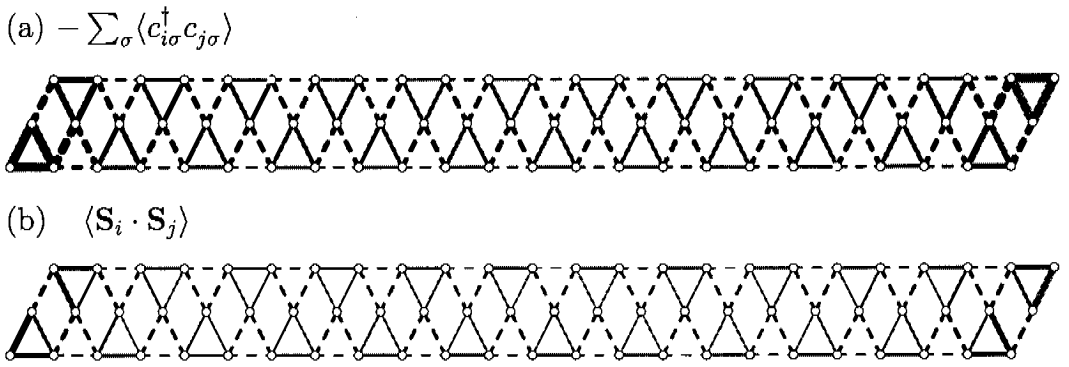

Figure 3.10: DMRG results for a $L = 24$ kagomé ladder at $J/t = 0.4$ and $n = 2/3$. (a) Local bond strength deviation of the kinetic term. Red, full bonds are stronger (lower in energy) than the average kinetic energy per bond. Blue, dashed bonds are weaker than average bonds. (b) Local bond strength deviation of the exchange term. The color pattern are the same as in the upper panel. The thickness of the bond denotes the deviation from the average value per bond. Note that the pattern of the kinetic and the exchange term are in phase.

3.7.3 Kagomé strip

The kagomé strip, being a 1D system, offers the opportunity of DMRG simulations; thus allowing a rather detailed numerical study of large systems. We first discuss the properties of the t-J model at $n = 2/3$ on this lattice, and then make a connection to the analytical weak-coupling results obtained in Sec. 3.6.1 by investigating the Hubbard model at different values of U. In both cases we report sound numerical evidence for the presence of the bond order wave instability for a large range of interactions strengths.

In contrast to the periodic systems considered above within ED, the DMRG works most efficiently for open boundary conditions. In the present context this has the additional advantage that for even length L of the strip only one of the two degenerate ground states is favored, and we can directly measure the local bond strength. For the purpose of illustration we show the local bond strengths for a system of $L = 24$ in Fig. 3.10. The upper panel shows the difference of the local kinetic energy with respect to the average, while the lower panel shows the local expectation value of the spin exchange term, using the same convention.

The calculated pattern resembles the schematic picture drawn in Fig 3.1 (c). In order to address the behavior in the thermodynamic limit we measure the

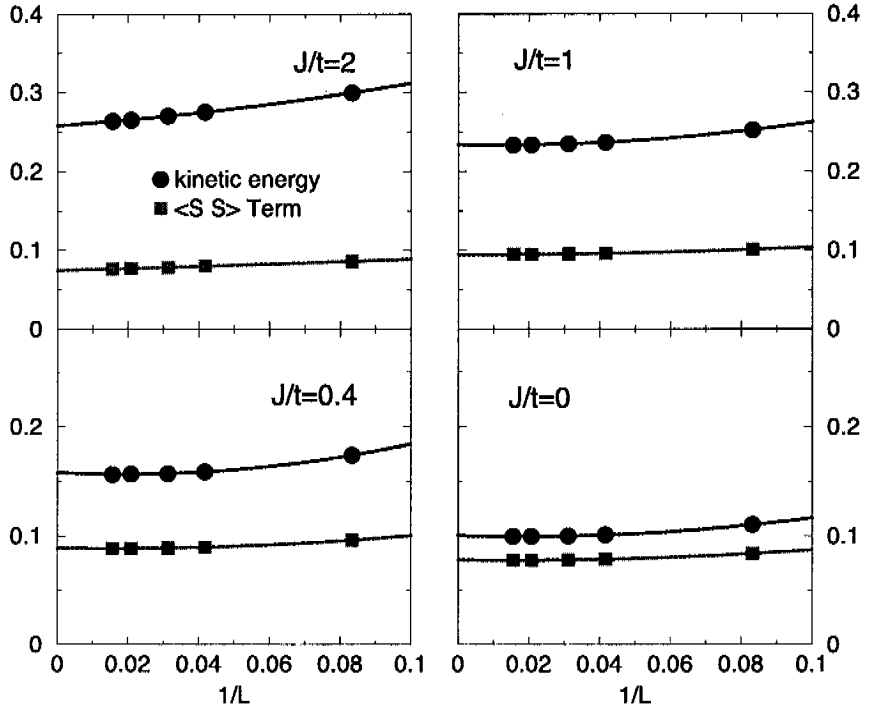

Figure 3.11: DMRG results for the alternation of the bond strength of the kinetic term and the spin exchange term as a function of inverse system size $1/L$, for different values of J/t.

bond strength alternation, i.e., the difference between the expectation values of the operators $\mathrm{Kin}(i,j)$ and $\mathbf{S}_i \cdot \mathbf{S}_j$ in the middle of the system for different lengths L and values of J/t. The scaling of these quantities is shown in Fig. 3.11. The finite size corrections are rather small and all the order parameters extrapolate to finite values, irrespective of the value of J/t. Note that even for the case $J/t = 0$ there is both a finite alternation of the kinetic energy *and* the magnetic exchange term. The alternation of the magnetic exchange energy is roughly the same for all values of J/t. The alternation of the kinetic energy however is increased with increasing J/t ratio.

Next we address the question of the excitation gaps in the symmetry broken phase. The theoretical picture predicts an insulating state with a finite gap to all excitations above the two-fold degenerate ground state. We calculate the single-particle charge gap and the spin gap defined in equations (3.6) and (3.5), respectively. The calculated gaps are shown in Fig. 3.12. The finite size gaps are extrapolated to $L = \infty$ with a simple quadratic fit. All gaps extrapolate to

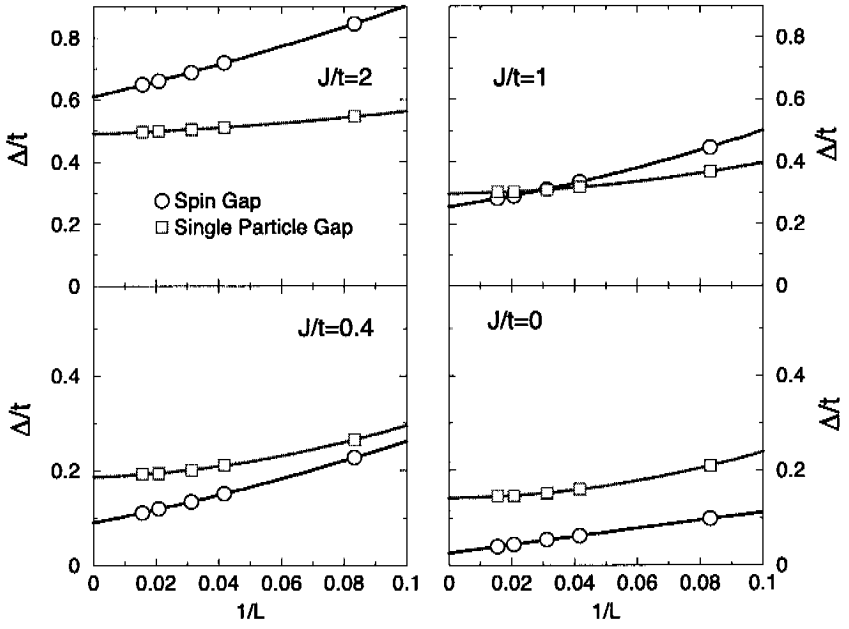

Figure 3.12: DMRG results for the spin gap and single-particle gap for $J/t = 0, 0.4, 1, 2$, as a function of inverse system size $1/L$.

a finite value, in agreement with the predictions. The charge gap more or less follows the increase of the alternation of the kinetic energy shown in Fig. 3.11, i.e., the gap is roughly multiplied by a factor three going from $J/t = 0$ to 2. The behavior of the spin gap is mainly driven by the fact that it scales with J/t. Note that even in the case $J/t = 0$ the spin gaps seem to remain finite. It will be an interesting question to characterize the precise nature of the charge and spin excitations. This will be left for a future study. The weak-coupling RG calculations in Sec. 3.6.1 have been performed for Hubbard onsite interactions. Although we expect the behavior of the t-J model and the Hubbard model at large U to be similar, we have explicitly calculated the alternation of the kinetic energy for the Hubbard model as a function of U/t. The results displayed in Fig. 3.13 show that this quantity has a maximum around $U/t \approx 10 \sim 15$, and interpolates between the exponentially small order parameter a weak U/t and the result for the t-J model at $J = 0$, which corresponds to $U = \infty$. These results therefore suggest that for the particular case of the kagomé strip the weak-coupling phase is adiabatically connected to the strong-coupling limit.

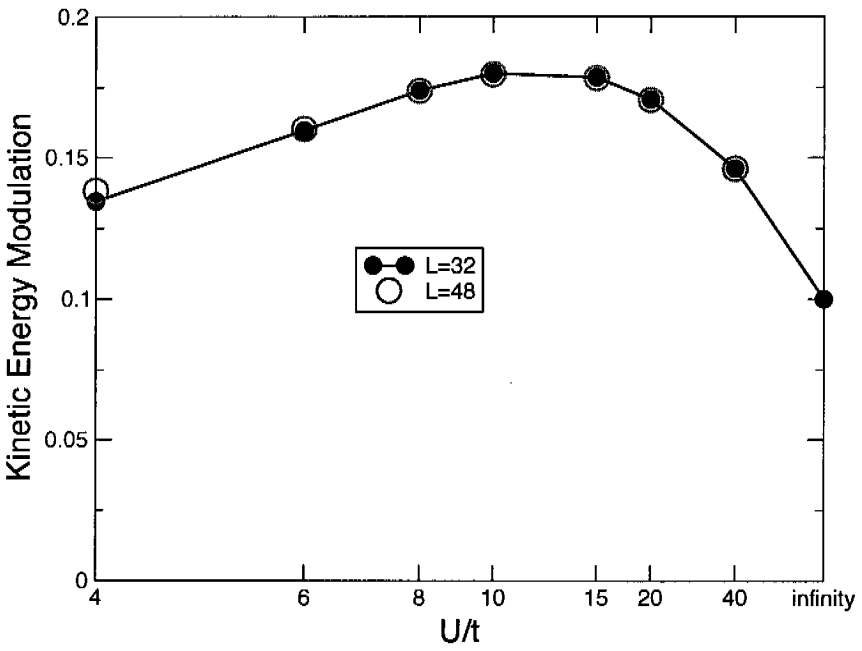

Figure 3.13: DMRG results for the kinetic energy alternation for Hubbard kagomé strips at $n = 2/3$ of length $L = 32$ and $L = 48$. The modulation is non-monotonous as a function of U/t and shows a maximum around $U/t \approx 10 \sim 15$.

3.8 The Dirac points of the kagomé lattice

So far we only considered particle-hole instabilities on the bisimplex lattices, that break lattice symmetries, i.e., the inversion symmetry or translational symmetry. In this last section we discuss the unusual properties of electrons on the kagomé lattice with broken inversion and broken time-reversal symmetry. The ideas of this section are based on previous work by Haldane [5], who presented a similar discussion for the honeycomb lattice. We will show, that the effects described by Haldane for the honeycomb lattice can also be obtained on the kagomé lattice, in fact, it turns out that it is even more natural to describe these effects on the kagomé lattice.

As can be seen from Fig. 3.3 the tight-binding dispersion of the kagomé lattice has two so-called Dirac points at the points K and K′. At such a point, two bands touch with linear dispersion and produce a double cone. At this particular filling the low-energy physics can therefore be described by two species of chiral "(2+1)-dimensional" relativistic fermions. The presence of an equal number of Weyl fermions with opposite chirality is not accidental. Apply-

ing a homotopy theory argument Nielsen and Ninomiya could prove that this kind of "fermion doubling" occurs for all quadratic fermion models on a lattice [114, 115]. These Dirac points and the related anomalous phenomena have been intensely discussed for the honeycomb lattice. Semenoff studied the effects of broken inversion symmetry on the honeycomb lattice [4], leading to a massive dispersion of the fermions, and Haldane discussed the quantum Hall phases in the system with broken time reversal and inversion symmetry [5].

In this section we will show how and to which extent the physics of the honeycomb lattice can be mapped onto the physics of the kagomé lattice. We omit the spin indices, σ, which would be only a bystander in the following discussion. The notation used on the kagomé lattice is shown in Fig. 3.14. The lattice vectors $\mathbf{a}_1 = (a, 0)$, $\mathbf{a}_2 = a(-1, \sqrt{3})/2$, and $\mathbf{a}_3 = a(-1, -\sqrt{3})/2$ satisfy $\mathbf{a}_1 + \mathbf{a}_2 + \mathbf{a}_3 = 0$. We allow for different hopping parameters t_∇ and t_Δ on the Δ and ∇ triangles. With this notation, we obtain the tight-binding Hamiltonian

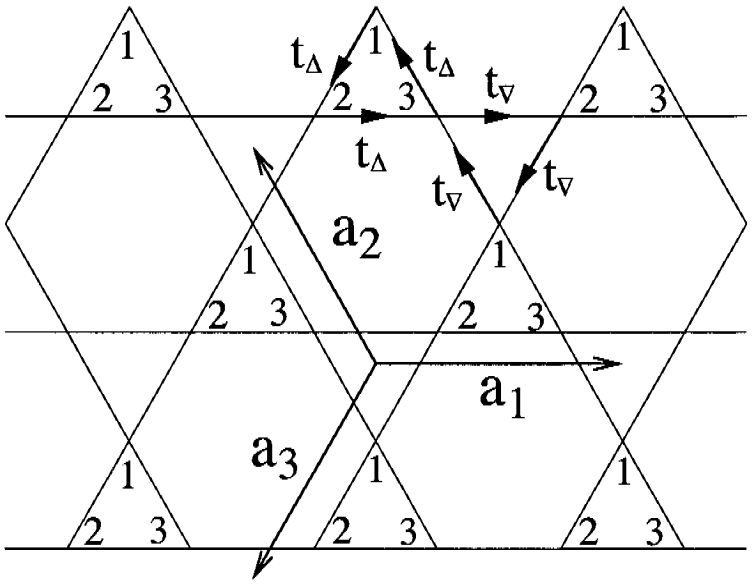

Figure 3.14: The notation on the kagomé lattice.

$$H = -\sum_{\mathbf{r}m} \left(t_\nabla c^\dagger_{\mathbf{r},m+1} c_{\mathbf{r},m-1} + t^*_\Delta c^\dagger_{\mathbf{r},m+1} c_{\mathbf{r}+\mathbf{a}_m,m-1} + \text{h.c.} \right) \tag{3.59}$$

We define the Fourier transformed operators as

$$c_{\mathbf{r}m} = \frac{1}{\sqrt{N}} \sum_{\mathbf{k}} e^{i\mathbf{k}\cdot[\mathbf{r}+(\mathbf{a}_{m-1}-\mathbf{a}_{m+1})/6]} c_{\mathbf{k}m}, \tag{3.60}$$

where N is the number of unit cells. The Hamiltonian (3.59) can be written as

$$\begin{aligned} H &= -\sum_{\mathbf{k}m}\left[\left(t_\nabla \mathrm{e}^{-\mathrm{i}\mathbf{k}\cdot\mathbf{a}_m/2} + t_\Delta^* \mathrm{e}^{\mathrm{i}\mathbf{k}\cdot\mathbf{a}_m/2}\right) c^\dagger_{\mathbf{k},m+1} c_{\mathbf{k},m-1} \;+\; \text{h.c.}\right] \qquad (3.61)\\ &= -2\sum_{\mathbf{k}m}\left\{\left[(t+\mathrm{i}\Delta'')\cos(k_m/2) - \mathrm{i}\Delta'\sin(k_m/2)\right] c^\dagger_{\mathbf{k},m+1} c_{\mathbf{k},m-1} + \text{h.c.}\right\}, \end{aligned}$$

and in the last line we have set

$$t_\nabla = t+\Delta, \qquad t_\Delta = t-\Delta, \qquad \Delta = \Delta' + \mathrm{i}\Delta'', \qquad t, \Delta', \Delta'' \in \mathbb{R}, \qquad (3.62)$$

and wrote k_m instead of $\mathbf{k}\cdot\mathbf{a}_m$. The terms proportional to Δ' break the inversion symmetry, whereas the terms proportional to Δ'' break time reversal symmetry. In the following we focus on 1/3-filling and introduce a chemical potential $\mu = -t$. For $\Delta = 0$, the electron filling is 1/3 and the Fermi surface (FS) is reduced to the two K points

$$\mathrm{K} = -\mathrm{K}' = -\frac{4\pi}{3a}\begin{pmatrix} 1 \\ 0 \end{pmatrix}. \qquad (3.63)$$

The density of states at the "Fermi points" vanishes and the dispersion is linear and cone shaped around the K points;

$$E_0^\pm(\mathbf{k}+K) = E_0^\pm(\mathbf{k}+K') = \pm\frac{\sqrt{3}}{2}|\mathbf{k}|at + \mathcal{O}((|\mathbf{k}|a)^2). \qquad (3.64)$$

We are interested, how the dispersion changes after introducing a finite Δ. At the Γ point the energies do not change for a finite value of Δ'. The degenerate states at the Γ point only split if time reversal symmetry is broken by a finite value of Δ''. At the M points the energies do not change in first order perturbation theory, as the eigenstates are real and not degenerate and the perturbation is imaginary. At the points K and K′ the Hamiltonian for $\Delta = 0$ including chemical potential is given by

$$H_0 = H_0' = t\begin{pmatrix} 1 & -1 & -1 \\ -1 & 1 & 1 \\ -1 & 1 & 1 \end{pmatrix}. \qquad (3.65)$$

This matrix is diagonalized by the unitary transformation

$$U^\dagger H_0 U = \mathrm{diag}[0,0,3\,t] \quad \text{with} \quad U = \frac{1}{\sqrt{3}}\begin{pmatrix} -1 & -1 & -1 \\ \omega & \omega^2 & 1 \\ \omega^2 & \omega & 1 \end{pmatrix} \qquad (3.66)$$

and with $\omega = e^{i2\pi/3}$. For finite Δ we have the perturbation matrices H^α_Δ ($\alpha = \pm 1$) at the points αK given by

$$H^\alpha_\Delta = \Delta^\alpha H_1 \quad \text{with} \quad H_1 = \begin{pmatrix} 0 & -i & i \\ i & 0 & i \\ -i & -i & 0 \end{pmatrix} \tag{3.67}$$

and with $\Delta^\alpha = (\Delta'' - \alpha\sqrt{3}\Delta')$.

This leads to a splitting of the degenerate states by $\pm\sqrt{3}\Delta^\alpha$ at the points αK. Note, that the splitting is symmetric if Δ is real or imaginary (fermion doubling). However, in general the splitting is asymmetric and for $\Delta'' = \pm\sqrt{3}\Delta'$ it is absent at one of the K points.

If we move a little bit away form the points K and K′ to the points $\delta\mathbf{k}^\alpha = \mathbf{k} - \alpha$K, assuming however that $|\delta\mathbf{k}^\alpha|a \ll 1$ and keeping only terms of first order in $|\delta\mathbf{k}^\alpha|$ in the Hamiltonian, we obtain an additional perturbation

$$H^\alpha_{\mathbf{k}} = \alpha\frac{\sqrt{3}\,t}{2}\begin{pmatrix} 0 & \delta k^\alpha_3 & \delta k^\alpha_2 \\ \delta k^\alpha_3 & 0 & -\delta k^\alpha_1 \\ \delta k^\alpha_2 & -\delta k^\alpha_1 & 0 \end{pmatrix}. \tag{3.68}$$

Calculating up to first order in Δ' and $|\delta\mathbf{k}^\alpha|$, we can restrict the Hilbert space to the space spanned by the first two columns of U and we obtain

$$\left[U^\dagger(H_0 + H^\alpha_\Delta + H^\alpha_{\mathbf{k}})U\right]_{2\times 2} = \begin{pmatrix} -\sqrt{3}\Delta^\alpha & -\lambda\alpha(\delta k^\alpha_x + i\delta k^\alpha_y) \\ -\lambda\alpha(\delta k^\alpha_x - i\delta k^\alpha_y) & \sqrt{3}\Delta^\alpha \end{pmatrix}, \tag{3.69}$$

where we have set $\lambda = \sqrt{3}\,ta/2$ and used that[c]

$$\delta k^\alpha_1 + \omega\delta k^\alpha_2 + \omega^2\delta k^\alpha_3 = 3a(\delta k^\alpha_x + i\delta k^\alpha_y)/2.$$

We obtain an effective Hamiltonian

$$H_{\text{eff}} = \sum_{\alpha=\pm1}\sum_{\mathbf{p}^\alpha}\begin{pmatrix} u^\dagger_{\mathbf{p}^\alpha} \\ v^\dagger_{\mathbf{p}^\alpha} \end{pmatrix}^{\mathrm{T}}\begin{pmatrix} -m_\alpha c^2 & -\alpha c(p^\alpha_x + ip^\alpha_y) \\ -\alpha c(p^\alpha_x - ip^\alpha_y) & m_\alpha c^2 \end{pmatrix}\begin{pmatrix} u_{\mathbf{p}^\alpha} \\ v_{\mathbf{p}^\alpha} \end{pmatrix}, \tag{3.70}$$

where $\mathbf{p}^\alpha = \hbar\delta\mathbf{k}^\alpha$,

$$c = \lambda/\hbar = \frac{\sqrt{3}ta}{2\hbar}, \qquad m_\alpha c^2 = \sqrt{3}\Delta^\alpha = \sqrt{3}(\Delta'' - \alpha\sqrt{3}\Delta') \tag{3.71}$$

[c] $\delta k^\alpha_x = \delta\mathbf{k}^\alpha \cdot \mathbf{e}_x$ and $\delta k^\alpha_y = \delta\mathbf{k}^\alpha \cdot \mathbf{e}_y$, where $\mathbf{e}_{x,y}$ are the unit vectors.

and

$$\begin{pmatrix} u_{\mathbf{p}^\alpha} \\ v_{\mathbf{p}^\alpha} \end{pmatrix} = \frac{1}{\sqrt{3}} \begin{pmatrix} -c_{\mathbf{k}1} + \omega^2 c_{\mathbf{k}2} + \omega\ c_{\mathbf{k}3} \\ -c_{\mathbf{k}1} + \omega\ c_{\mathbf{k}2} + \omega^2 c_{\mathbf{k}3} \end{pmatrix}. \tag{3.72}$$

Defining

$$\psi_\alpha(\mathbf{p}) = \sigma^2 \mathrm{e}^{-\mathrm{i}\alpha\frac{\pi}{4}\sigma^3} \begin{pmatrix} u_{\mathbf{p}^\alpha} \\ v_{\mathbf{p}^\alpha} \end{pmatrix}, \tag{3.73}$$

we obtain

$$\begin{aligned} H_{\text{eff}} &= \sum_{\alpha=\pm1} \sum_{\mathbf{p}^\alpha} \psi_\alpha^\dagger(\mathbf{p})(cp_x^\alpha \sigma^2 - cp_y^\alpha \sigma^1 + m_\alpha c^2 \sigma^3)\psi_\alpha(\mathbf{p}) && (3.74) \\ &= \sum_{\alpha=\pm1} \sum_{\mathbf{p}^\alpha} \psi_\alpha^\dagger(\mathbf{p})(c\gamma^0 \boldsymbol{\gamma} \cdot \mathbf{p}^\alpha + m_\alpha c^2 \gamma^0)\psi_\alpha(\mathbf{p}) && (3.75) \\ &= \sum_{\alpha=\pm1} \sum_{\mathbf{p}^\alpha} \bar{\psi}_\alpha(\mathbf{p})(c\boldsymbol{\gamma} \cdot \mathbf{p}^\alpha + m_\alpha c^2)\psi_\alpha(\mathbf{p}), && (3.76) \end{aligned}$$

where $\gamma^\mu = (\gamma^0, \boldsymbol{\gamma})$, $\gamma^0 = \sigma^3$, $\boldsymbol{\gamma} = -\mathrm{i}(\sigma^1, \sigma^2)$, and $\bar{\psi}_\alpha = \psi_\alpha^\dagger \gamma^0$. The γ^μ satisfy the Dirac anti-commutation relations $\{\gamma^\mu, \gamma^\nu\} = 2g^{\mu\nu} \times \mathbf{1}_{2\times2}$. This Hamiltonian is (2+1)-Lorentz invariant. In fact, Eq. (3.76) it is just the sum of two second quantized Hamiltonians for two different Dirac fields in (2+1) dimensions. The generators of the 2D representation of the (2+1)-Lorentz group are given by $S^{\mu\nu} = i[\gamma^\mu, \gamma^\nu]/4$. ($S^{01} = -\mathrm{i}\sigma^1/2$, $S^{02} = \mathrm{i}\sigma^3/2$, $S^{12} = \sigma^2/2$). The energy spectrum of the fermions is given by

$$E_\alpha^\pm(\mathbf{k}) = \pm\sqrt{(\hbar ck)^2 + (m_a c)^2}. \tag{3.77}$$

The situation considered by Semenoff [4] corresponds to setting $\Delta'' = 0$. We can now see the analogy of the kagomé lattice with different hopping integrals on up- and down-triangles to the model studied by Semenoff. For the honeycomb lattice with broken inversion symmetry the mass of the fermions is given by $2U/\sqrt{3}at$, where $2U$ is the difference between the potentials on the two sublattices. For the kagomé lattice with broken inversion symmetry this mass is given by $2\sqrt{3}\Delta'/at$.

Haldane extended the model of Semenoff by introducing also a next-nearest-neighbor hopping on the honeycomb lattice [5]. In addition he assumed the presence of a staggered magnetic field perpendicular to the plane. The staggering should be such that the total magnetic flux through each hexagon vanishes. Therefore the nearest-neighbor hopping integrals would not acquire a Peierls phase, but the next-nearest-neighbor hopping integrals would acquire a Peierls

phase ϕ. For the equivalent model on the kagomé lattice the staggered magnetic field is generated by a finite value of Δ'' which leads to a staggered flux phase as shown in Fig. 3.15. The magnetic field distribution corresponds to ferromagnetically ordered magnetic dipoles in the center of the hexagons.

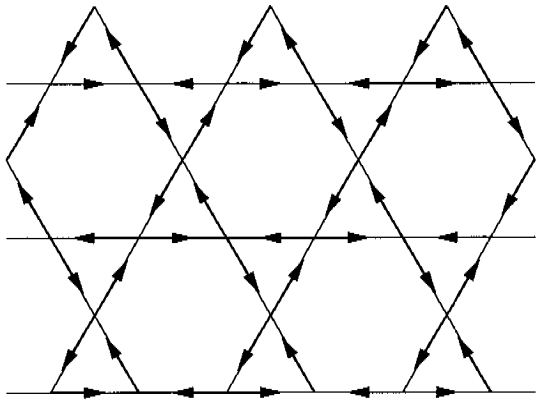

Figure 3.15: The staggered flux pattern generated by a finite value of Δ''.

In the presence of a perpendicular magnetic field we make the Landau-Peierls substitution $\mathbf{p}^\alpha \rightarrow \Pi^\alpha$, and the dynamical momentum operators satisfy the commutation relations $[\Pi_x^\alpha, \Pi_y^\alpha] = ieB_0\hbar$, where B_0 is the flux density of a uniform external magnetic field perpendicular to the plane. In this notation we have from (3.74) the two (first quantized) Hamiltonians around the points K and K′,

$$H_\alpha = c(\Pi_x^\alpha \sigma^2 - \Pi_y^\alpha \sigma^1) + m_\alpha c^2 \sigma^3. \tag{3.78}$$

This system is equivalent to the system discussed by Haldane, where the constants c and m_α are given by

$$c = \frac{3\,t_1 a}{2\hbar} \qquad m_\alpha c^2 = U - 3\sqrt{3}\,\alpha t_2 \sin\phi \tag{3.79}$$

with t_1 the nearest-neighbor and t_2 the next-nearest-neighbor hopping, $2U$ being the chemical potential difference between the sublattices, and ϕ the Peierls phase.[f]

Comparing the equations Eq. (3.71) and Eq. (3.79) we see that for the kagomé lattice the masses at the K points depend only on the complex parameter Δ. If Δ is neither real nor imaginary we have a system where time reversal and inversion symmetry are spontaneously broken. In general the two masses

[f] In the case of Haldane the commutation relations are $[\Pi_x^\alpha, \Pi_y^\alpha] = \alpha ieB_0\hbar$.

m_α are not equal and for $\Delta''/\Delta = \pm\sqrt{3}$ we have a finite gap at one K point whereas the other K point is a gapless Dirac point. It is therefore possible to avoid the fermion doubling by simultaneously breaking time reversal and inversion symmetry.[g]

The following discussion of the zero-field quantum Hall phases on the kagomé lattice follows closely the analogous discussion of Haldane for the honeycomb lattice [5]. In the presence of a uniform perpendicular magnetic field with flux density B_0 the spectra of the Hamiltonians of Eq. (3.78) change and relativistic Landau levels are obtained [116]

$$E_{\alpha n\pm} = \pm[(m_\alpha c^2)^2 + n\hbar|eB_0|c^2]^{\frac{1}{2}} \quad (n \geq 1), \tag{3.80}$$

$$E_{\alpha 0} = m_\alpha c^2 \mathrm{sign}(eB_0). \tag{3.81}$$

Note, that the spectrum of a single species of fermions is not particle-hole symmetric, as the zeroth Landau level (3.81) has no counterpart. In the time reversal symmetric case, we have $m_+ = -m_-$ and the particle hole symmetry of the total spectrum is restored. Furthermore, the spectrum is invariant under $B_0 \to -B_0$ and the quantized Hall conductance, σ^{xy}, is zero. If the masses m_α have opposite signs, there is exactly one of the two Landau level, $E_{\alpha,0}$, filled. If one of the masses m_α changes sign, an additional Landau level is filled or emptied.

In general the additional charge density in the ground state with respect to the time-reversal symmetric situation is given by[h]

$$\Delta\sigma = (e^2 B_0/h) \sum_a \mathrm{sign}(m_\alpha)/2. \tag{3.82}$$

The value of the Hall conductance can be obtained from the thermodynamic relation $\sigma^{xy} = \partial\sigma/\partial B_0|_{\mu,T}$, where σ is the 2D electric charge density. From Eq. (3.82) we get therefore the quantized Hall conductance $\sigma^{xy} = \nu e^2/h$ with $\nu = \sum_\alpha \mathrm{sign}(m_\alpha)/2$. Note, that we get a result that can be evaluated for $B_0 = 0$, i.e., we obtain an integer quantum Hall effect without applying an external magnetic field. The phase diagram depends only on the phase of Δ, ϕ and is shown in Fig. 3.16. The system posses an intrinsic chirality that leads to the non-vanishing quantized Hall conductance σ^{xy} even without applied external magnetic field.

[g] As long as only time-reversal or inversion symmetry is broken, the dispersion is still invariant under $\mathbf{k} \to -\mathbf{k}$.

[h] We choose the electronic charge $e < 0$.

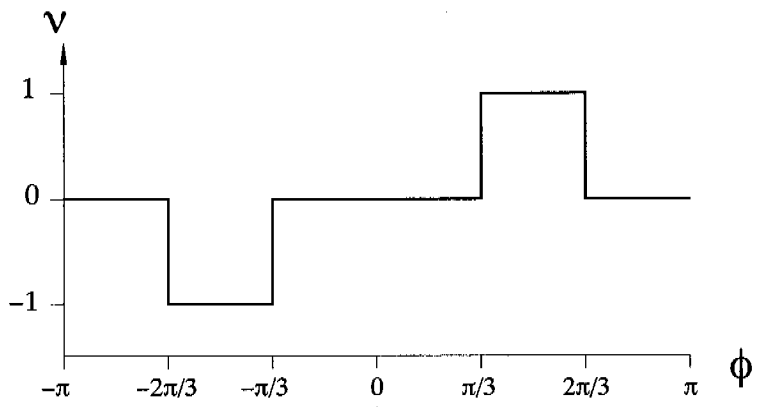

Figure 3.16: The phase diagram as a function of ϕ which is the phase of Δ. The zero-field Hall conductance at zero temperature is given by $\sigma^{xy} = \nu e^2/h$ and $\nu = \sum_\alpha \mathrm{sign}(m_\alpha)/2$.

It is interesting to look at the degenerate states at the points K and K′ in more detail. From Eq. (3.72) and Eq. (3.60) one can see that it is convenient to use the notation

$$\begin{array}{rclcrcl} u_{\mathrm{K}}^\dagger|0\rangle & = & |\nabla,\circlearrowright\rangle & & u_{\mathrm{K}'}^\dagger|0\rangle & = & |\Delta,\circlearrowright\rangle \\ v_{\mathrm{K}}^\dagger|0\rangle & = & |\Delta,\circlearrowleft\rangle & & v_{\mathrm{K}'}^\dagger|0\rangle & = & |\nabla,\circlearrowleft\rangle \end{array}, \tag{3.83}$$

where in the state $|\nabla,\circlearrowright\rangle$ the phase on each ∇ triangle increases by $2\pi/3$ along each bond in the clockwise direction, whereas the phase is constant on the Δ triangles. In the state $|\Delta,\circlearrowleft\rangle$ the phase on each Δ triangle increases by $2\pi/3$ along each bond in the anti-clockwise direction whereas the phase is constant on the ∇ triangles and analogously for the other states. For the operators

$$\begin{aligned} H_\nabla &= -\sum_{\mathbf{r}m} c_{\mathbf{r},m+1}^\dagger c_{\mathbf{r},m-1} + \mathrm{h.c.} \\ H_\Delta &= -\sum_{\mathbf{r}m} c_{\mathbf{r},m+1}^\dagger c_{\mathbf{r}+\mathbf{a}_m,m-1} + \mathrm{h.c.}, \end{aligned} \tag{3.84}$$

where H_Δ contains the hopping processes on the Δ triangles and H_∇ the processes on the ∇ triangle. For $\Delta = 0$ we have

$$\langle\Delta,\circlearrowright|H_\nabla|\Delta,\circlearrowright\rangle = -2, \qquad \langle\Delta,\circlearrowright|H_\Delta|\Delta,\circlearrowright\rangle = 1. \tag{3.85}$$

For the other states hold analog expressions. The effect of the inversion sym-

metry $\mathcal{I}$ and the time reversal symmetry $\mathcal{T}$ on these states is given by

$$\begin{array}{rclrcl} \mathcal{I}|\Delta,\circlearrowright\rangle &=& |\nabla,\circlearrowright\rangle & \mathcal{T}|\Delta,\circlearrowright\rangle &=& |\Delta,\circlearrowleft\rangle \\ \mathcal{I}|\Delta,\circlearrowleft\rangle &=& |\nabla,\circlearrowleft\rangle & \mathcal{T}|\Delta,\circlearrowleft\rangle &=& |\Delta,\circlearrowright\rangle \\ \mathcal{I}|\nabla,\circlearrowright\rangle &=& |\Delta,\circlearrowright\rangle & \mathcal{T}|\nabla,\circlearrowright\rangle &=& |\nabla,\circlearrowleft\rangle \\ \mathcal{I}|\nabla,\circlearrowleft\rangle &=& |\Delta,\circlearrowleft\rangle & \mathcal{T}|\nabla,\circlearrowleft\rangle &=& |\nabla,\circlearrowright\rangle \end{array} \tag{3.86}$$

From this follows, that if time reversal symmetry is broken, states with the same chirality are degenerate, but if the inversion symmetry is broken, states with the same triangles are degenerate. The situation where the states with the same chirality are above the gap can not be changed into the situation where the states with the same triangles are above the gap, without closing at least one gap. The closing of the gap marks the phase transition between phases with different quantum Hall conductance. In Fig. 3.17 the amplitudes of the state $|\Delta,\circlearrowright\rangle$ are drawn. For the kagomé strip we also have the four degenerate states of Eq. (3.83). Note,that in this case to outer triangles have been turned down by the periodic boundary conditions and therefore we have seemingly triangles with both chiralities in the state $|\Delta,\circlearrowright\rangle$.

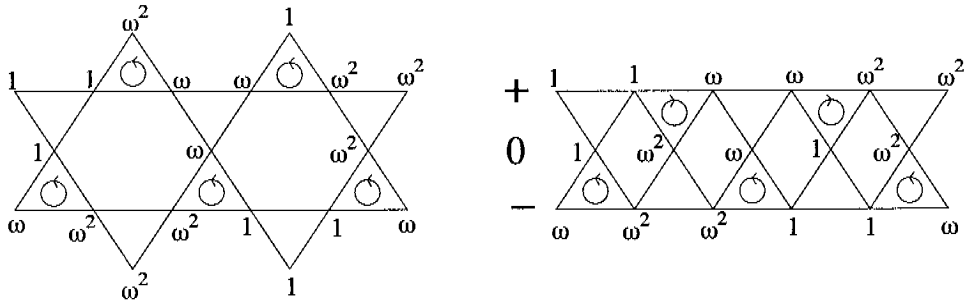

Figure 3.17: The amplitudes of the state $|\Delta,\circlearrowright\rangle$ are drawn on the kagomé lattice and on the kagomé strip where the triangles on every second rung are turned down.

3.9 Discussion and conclusion

In summary we have studied the occurrence of a bond order wave instability in the four different bisimplex lattices shown in Fig. 3.1. We provided evidence that this instability occurs quite generally in all four lattices at the fractional filling of one electron per simplex (two electrons per up-simplex),

if the correlations (i.e., nearest-neighbor repulsion and/or antiferromagnetic nearest-neighbor exchange) are strong enough.

In weak coupling the physical properties of the system are dominated by the dimensionality of the lattice, by its fermiology and by the density of states at the Fermi energy. We show that in the intermediate coupling regime, where the kinetic and the interaction energies are comparable, at the filling with two electrons per up-simplex, the physical properties of these highly frustrated lattices are dominated by local states on the simplex. The bipartite and corner-sharing arrangement of the simplices allows the creation of isolated or only weakly interacting simplices with low-energy by spontaneously breaking the inversion symmetry. This knowledge provides a good starting point for series expansions or further CORE calculations.

The magnetic interaction and the chosen sign of the dispersion leads to a tendency to form nearest-neighbor singlets and nearest-neighbor repulsion leads to a tendency to avoid configurations with more than two electrons per simplex. If the underlying lattice is bipartite the system finds a way to satisfy both tendencies simultaneously by localizing singlets on every second simplex. This localization leads only to a partial loss of the kinetic energy, because the singlets can still delocalize within the simplex. It is the cooperation between the kinetic and the interaction energy which stabilizes the bond order wave state. Note, that the bond order wave instability does not lead to an inhomogeneous charge distribution on the lattice.

The bond order wave states, which we find on the different lattices, provide a natural generalization of the well-known valence bond solid states (e.g., dimerized phases, plaquette phases) found in many frustrated spin models to situations away from half-filling where a description in terms of spin variables only breaks down. The density is still a rational fraction, but $n = 2/3$ in the kagomé and kagomé strip case while $n = 1/2$ in the pyrochlore and the checkerboard case. Approximately these states are direct products of singlets on triangles or tetrahedra, similar to the conventional picture of a dimerized phase. In contrast to the phases at $n = 1$ the present instability involves a cooperative effect of both magnetic exchange *and* kinetic energy.

An interesting task is to study the properties of a lightly doped bond order wave phase. It can be assumed that the bond order wave order parameter decreases rather quickly with doping. However, it is conceivable that away from the commensurate filling the bond order wave order parameter coexists with a small superconducting order parameter. This phase would at the same

time break lattice symmetries and the U(1) gauge symmetry and would be therefore similar to a supersolid.

In general, we conclude that the bond order wave instability in the four lattices of Fig. 3.1 occurs for physically reasonable models and interaction parameters. Our study shows that doping frustrated spin models can lead to new phases and hopefully contributes to a further understanding of the interplay of frustrated magnetic fluctuations and itinerant charge carriers, which play a role for example in the unconventional heavy Fermion material LiV_2O_4 [91, 92] or in Na_xCoO_2.

Seite Leer /
Blank leaf

Chapter 4

Inhomogeneously Doped t-J Ladder and Bilayer Systems

4.1 Introduction

Doped spin liquids have been an important subject of condensed matter research for the last two decades, mainly due to their possible relevance to the (cuprate) high-temperature superconductors (HTSC)[117, 118]. Although it is still not understood how high-temperature superconductivity emerges from an antiferromagnetic Mott-insulator upon carrier doping, there is broad consensus that an intermediate pseudogap phase plays a crucial role in understanding both the exotic normal and superconducting properties of these materials [119].

Many proposals concerning the nature of the pseudogap phase have been put forward. One candidate for the pseudogap phase is the resonating valence bond state (RVB), which describes strongly fluctuating short-ranged spin singlets [117]. While the relevance of this state to the quasi-two-dimensional HTSC is still under debate, it is realized in specially designed lattice structures [120]. Of particular interest are systems with ladder-shaped crystal structures, which are realized in various transition metal oxide compounds [1, 121].

Undoped, these ladder-systems are Mott-insulators and well described by quantum spin-1/2 Heisenberg models. For the two-leg ladder the ground state is an RVB-like state displaying short-ranged spin-singlet correlations with spin-singlet dimers on the rungs dominating over those along the legs. This constitutes a spin liquid with a finite energy gap to the lowest spin excitations. Furthermore, it was proposed that such a system would exhibit superconduc-

tivity upon hole-doping [122, 123]. Various theoretical approaches confirmed a strong tendency towards formation of Cooper pairs with phase properties reminding of the $d_{x^2-y^2}$-wave channel of the two-dimensional HTSC [124–127].

The theoretical proposals were followed by an intense material research attempting to dope holes into a variety of known insulating copper-oxide compounds displaying ladder structures [128]. Materials under consideration are $SrCu_2O_3$, $CaCu_2O_3$, $LaCuO_{2.5}$, and $Sr_{14}Cu_{24}O_{41}$. Doping these compounds is intrinsically difficult because of chemical instabilities, and carrier localization effects may inhibit the desired metallic behavior. Nevertheless, the search for superconductivity has been successful in the compound $Sr_{14-x}Ca_xCu_{24}O_{41}$ which contains layers of ladders alternating with layers of single chains [129]. In this material T_c rises up to about 12 K under high pressure, which apparently leads to a transfer of charge carriers from the chains onto the ladders. However, a detailed understanding of this system under high pressure has not been reached yet. A well-controlled and less invasive way of doping a ladder compound is thus highly desirable.

Hole and electron doping by means of field effect devices induces mobile charge carriers into the originally insulating material using a large gate voltage. This method would be ideal for doping quasi one- and two-dimensional systems, since the induced charge is confined to the outer-most layer of the compound, closest to the gate.

An alternative technique of tunable doping has been achieved using heterostructures of layered materials such as high-T_c-cuprates combined with ferroelectrics like $Pb(Zr,Ti)O_3$ [130–132].

For ladder systems the most natural choice for this type of doping control is a film in which the ladder planes lie parallel to the gate or the ferroelectric, so that the carriers enter the ladders uniformly. However, in the compound $LaCuO_{2.5}$ the ladders are not parallel to each other, but exhibit a staggering [133]. Consequently, in a field effect device the ladders would be inhomogeneously doped in the sense that the chemical potential on the two legs would be different. Similarly, a variable orientation of the dipolar moments of the ferroelectric can lead to inhomogeneous doping.

For bilayer compounds like $YBa_2Cu_3O_{7-\delta}$ the symmetry between the layers would be broken by the presence of the electric field, leading to a difference between the chemical potentials of the layers and consequently to an inhomogeneous doping concentration in the two layers.

These non-volatile techniques of tunable doping may allow for a detailed

comparison between experiment and theory in these low-dimensional structures.

In this chapter we analyze the evolution of the superconducting state under such doping circumstances. Our analytical and numerical analysis of the 1D system shows that non-uniform doping is harmful to the superconducting state of the two-leg ladder. The strong pairing correlations on the rung are suppressed by the application of the electric field. While for small $\Delta\mu$ the ladder remains superconducting, the pairing is suppressed upon increasing $\Delta\mu$, and depending on the doping level new phases with reduced, and eventually without superconductivity appear.

The mean-field analysis for the bilayer leads to similar results for the s-wave superconducting phase, which has strong inter-plane pairing correlations. In contrast to the ladder case, however, there exists also a d-wave superconducting phase for the bilayer, which is less affected by the interplane potential difference.

This chapter is organized according to the used analytical and numerical methods. In this way we study various aspects of the problem within different approximative schemes. In the following section a qualitative argument for the limited stability of the superconducting state upon inhomogeneous doping is presented. In Sec. 4.3 a discussion of numerical exact diagonalization results is given for the charge correlations of two holes in ladders with up to 22 sites. Then, in Sec. 4.4 we apply renormalization group (RG) and bosonization methods to derive the phase diagram of the weakly interacting Hubbard model in the inhomogeneously doped case. In Sec. 4.5 we consider a mean-field treatment of the t-J model based on the spinon-holon decoupling scheme. With this method we study both the inhomogeneously doped ladder and the bilayer system. Finally, we summarize and conclude in Sec. 4.7 and draw a unified picture of the behavior of inhomogeneously doped two-leg ladder and bilayer systems by combining the results from the earlier sections. The results for the two-leg ladder are published in Ref. [134]. The ED data (Sec. 4.3) were obtained from Andreas Läuchli and the RG calculations (Sec. 4.4) were performed by Stefan Wessel in the framework of a collaboration on Ref. [134].

4.2 Strong rung coupling limit

The influence of a difference in the chemical potential on the pairing state of the two-leg ladder or the bilayer can be illustrated by a simple qualitative argument for the t-J model. Consider the two-leg ladder with electrons moving

along the legs and rungs with hopping matrix elements t and t', respectively, and nearest-neighbor spin exchange with exchange constants J and J'. The Hamiltonian of the t-J model for the two-leg ladder then reads

$$\begin{aligned} H &= -t\sum_{jas}\mathcal{P}(c^\dagger_{jas}c_{j+1,as}+\text{h.c.})\mathcal{P} \\ &\quad -t'\sum_{js}\mathcal{P}(c^\dagger_{j1s}c_{j2s}+\text{h.c.})\mathcal{P} \\ &\quad +J\sum_{ja}\left(\mathbf{S}_{ja}\cdot\mathbf{S}_{j+1,a}-\frac{1}{4}n_{ja}n_{j+1,a}\right) \\ &\quad +J'\sum_{j}\left(\mathbf{S}_{j1}\cdot\mathbf{S}_{j2}-\frac{1}{4}n_{j1}n_{j2}\right) \\ &\quad -\sum_{jas}\mu_a\, n_{jas}. \end{aligned} \tag{4.1}$$

The operator $c^\dagger_{jas}$ (c_{jas}) creates (annihilates) an electron with spin s on site (j,a), where j labels the rungs and $a=1,2$ the legs. The electron number operators are defined as $n_{jas}=c^\dagger_{jas}c_{jas}$, and $n_{ja}=\sum_s n_{jas}$. The spin operators are

$$\mathbf{S}^\alpha_{ja}=\frac{1}{2}\sum_{ss'}c^\dagger_{jas}\,\boldsymbol{\sigma}^\alpha_{ss'}\,c_{jas'}, \tag{4.2}$$

where $\boldsymbol{\sigma}^\alpha$, $\alpha=1,2,3$, are the Pauli matrices. The constraint of excluded double occupancy is enforced by the projection operator

$$\mathcal{P}=\prod_{ja}(1-n_{ja\uparrow}n_{ja\downarrow}). \tag{4.3}$$

In the last line of Eq. (4.1) different chemical potentials on the two legs, μ_a, describe an inhomogeneous doping of the system. Throughout this paper we assume $\Delta\mu=\mu_1-\mu_2\geq 0$ and refer to the leg with $a=1$ ($a=2$) as the upper (lower) leg. Furthermore, the overall doping concentration $\delta=1-n$ fixes the average chemical potential $\bar{\mu}=(\mu_1+\mu_2)/2$.

The phases of the t-J model on the two-leg ladder for $\Delta\mu=0$ are well characterized [135]. At half-filling ($\delta=0$) with one electron per site the ladder is a (Mott-) insulating spin liquid. Upon removal of electrons, i.e., doping of holes, mobile carriers appear, resulting in a Luther-Emery liquid with gapless charge modes and gapped spin excitations. Furthermore, the gapless charge mode exhibits dominant superconducting correlations with a d-wave-like phase structure.

We now discuss the effect of inhomogeneous doping on this superconducting state, described by $\Delta\mu > 0$. For many aspects of ladder systems the limit of strong rung-coupling gives useful insights into their basic properties. Therefore we first consider the Hamiltonian (4.1) in the limit $J', t' \gg J, t$. Neglecting the coupling along the legs entirely the undoped system corresponds to a chain of decoupled rungs and the ground state becomes a product state of dimer spin-singlets on the rungs. Note, that this product state of singlets can also be written as a (Cooper) pair wave function in the form [118]

$$\prod_j \frac{1}{\sqrt{2}} \left(b^\dagger_{j\uparrow} b^\dagger_{j\downarrow} - a^\dagger_{j\uparrow} a^\dagger_{j\downarrow} \right) |0\rangle \tag{4.4}$$

where the operator $b^\dagger_{js}$ ($a^\dagger_{js}$) creates a bonding (antibonding) single-particle state with spin s on the rung j. The different sign for the pairs with different transverse momentum already suggests the appearance of unconventional superconductivity upon doping. In fact we will find in the mean-field calculations of Sec. 4.5 that the pairing amplitudes on the rung and on the legs (layers) do have opposite signs. If the two-leg ladder is viewed as cut of finite width through the square lattice and if the transverse momentum is denoted by k_y, the sign change between the Cooper pairs with $k_y = 0$ and $k_y = \pi$ reminds of a superconducting state with $d_{x^2-y^2}$-symmetry.

Furthermore, the lowest spin excitation corresponds to exciting one rung-singlet to a triplet, at an energy expense of J'. The superconducting state, i.e., Cooper pairing, in the doped spin liquid is inferred from the fact that two doped holes rather reside on a single rung rather than to separate onto two rungs. This is the case if the dominant energy scale is the spin exchange interaction, J'. Then the cost of breaking two spin singlets is larger than the gain of kinetic energy from separating the two holes. Namely, for two holes on a single rung the energy is

$$E_{2\mathrm{h}} = J' - 2\bar{\mu}, \tag{4.5}$$

while for a single hole

$$E_{1\mathrm{h}} = J' - \bar{\mu} - \frac{1}{2}\sqrt{4(t')^2 + \Delta\mu^2}. \tag{4.6}$$

Pairing on a rung is favored, if

$$2E_{1\mathrm{h}} - E_{2\mathrm{h}} = J' - \sqrt{4(t')^2 + \Delta\mu^2} > 0, \tag{4.7}$$

which in the uniformly doped case ($\Delta\mu = 0$) leads to the condition $J' > 2t'$ for pairing. Obviously, a finite value of $\Delta\mu$ weakens the pairing by reducing the above energy gain.

This simple observation of depairing under non-uniform doping is confirmed by more sophisticated approaches, as those considered in the following sections.

4.3 Exact diagonalization

To extend the discussion of the two-hole problem beyond the strong coupling limit we performed exact diagonalizations of finite systems, using the Lanczos algorithm. We considered the Hamiltonian (4.1) at isotropic coupling ($t = t'$, $J = J'$), and studied the half-filled system doped with two holes, using periodic boundary conditions. We studied systems of different length, L, containing 8 to 11 rungs, and furthermore considered different values of J/t.

Consistent with the strong coupling argument of the previous section the hole bound state is found to be unstable beyond a critical value of $\Delta\mu > \Delta\mu_c$. Furthermore, for the range of parameters considered here ($0.4 \leq J/t \leq 0.8$), this critical value is $\Delta\mu_c \approx J'$. This indicates that the physics of the system is quite well captured by the strong rung-coupling limit with J' being the dominant energy scale for pairing.

The behavior of the holes under non-uniform doping can be analyzed using the hole-hole correlation function. Denoting the hole number operator on rung j by $n'(j) = 2 - n_{j1} - n_{j2}$, the rung hole-hole correlation function is defined as the ground state expectation value $\langle n'(0)n'(j)\rangle$, for the rung-rung separation $j = 0, 1, \ldots, \lfloor \frac{L}{2} \rfloor$. This correlation function is shown in Fig. 4.1 for a ladder with 10 rungs for $J/t = 0.5$, and at selected values of the chemical potential difference, $\Delta\mu$. The behavior of the correlation function changes abruptly between $\Delta\mu/t = 0.5$ and $\Delta\mu/t = 0.6$. For small values of $\Delta\mu/t \leq 0.5$, we find maximal rung hole-hole correlations between neighboring rungs, and a strong decay of the correlation function at larger distances. For values of $\Delta\mu/t \geq 0.6$, the value of the correlation function is increasing with distance and has a maximum value at the maximal possible rung-rung separation. Furthermore, it almost vanishes on the same rung. This clearly indicates the destruction of the hole-hole bound state for $\Delta\mu/t \geq 0.6$, where the system consists of two holes on the lower leg which is favored by a lower chemical potential.

The sudden change in the behavior of the correlation function is due to a level crossing at $\Delta\mu_c$ in this system. While in the bound regime the ground state has

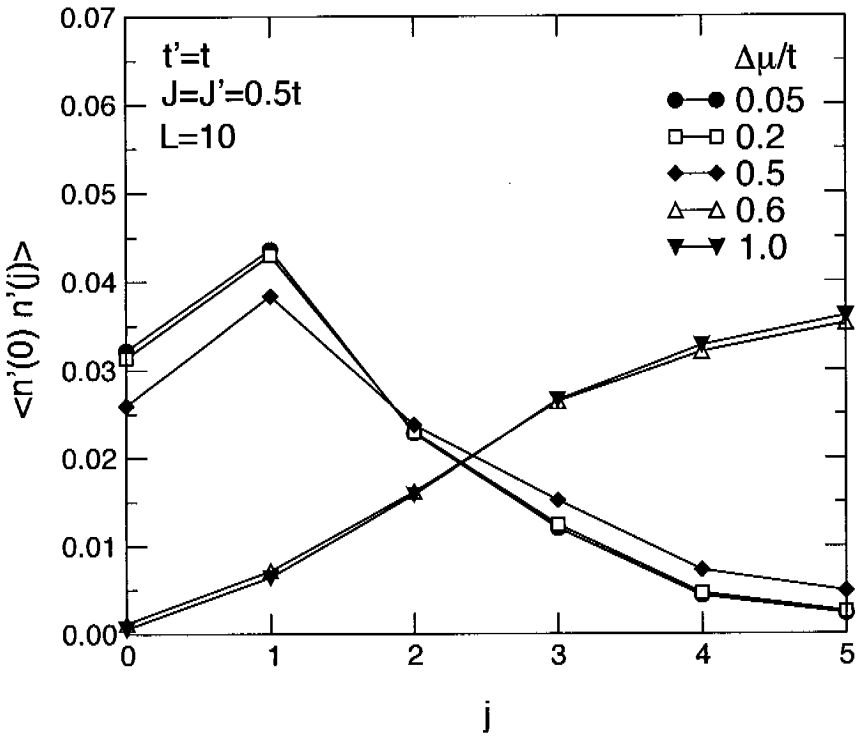

Figure 4.1: Rung hole-hole correlation-function, $\langle n'(0)n'(j)\rangle$, in the ground state of the t-J model for an inhomogeneously doped two-leg ladder at selected values of the chemical potential difference, $\Delta\mu$. The finite ladder has $L = 10$ rungs and furthermore $t = t'$ and $J = J' = 0.5t$.

zero total momentum along the legs, the lowest energy state in the unbound regime has a finite value of the total momentum. The correlation functions for $\Delta\mu/t = 0.2$ and $\Delta\mu/t = 0.05$ are almost identical, reflecting the robustness of the bound state against small doping inhomogeneities. Indeed, it can be shown that the doping asymmetry $\Delta\mu$ does not have any effect in first order perturbation theory. In the regime of unbound holes the correlation function is again insensitive to changes in $\Delta\mu$, since for large $\Delta\mu$ the holes are almost exclusively located on the lower leg, and therefore increasing $\Delta\mu$ merely results in an overall energy shift.

The drastic change in the hole-hole correlation function as a result of the transition between the bound and unbound regime is also reflected in the char-

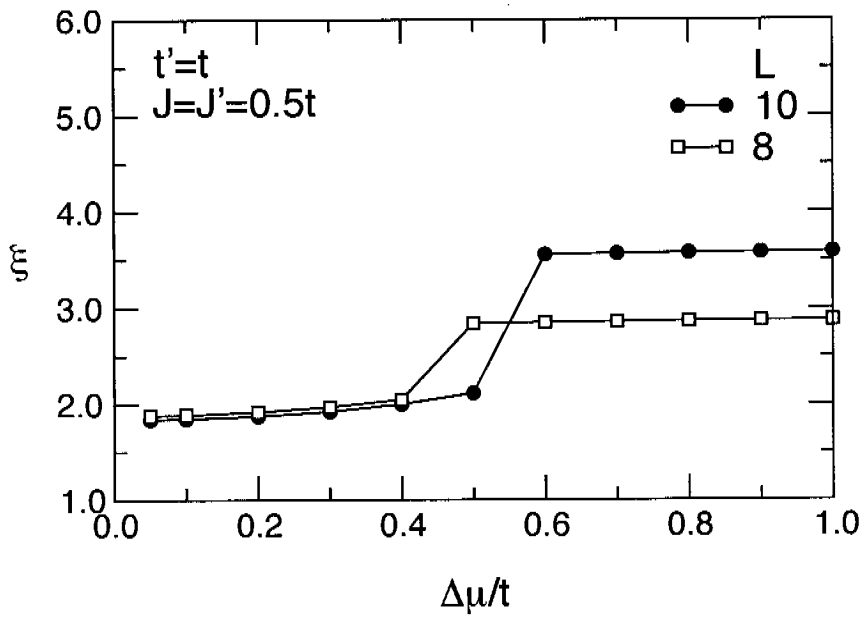

Figure 4.2: Characteristic hole-hole separation length, ξ, in the ground state of the t-J model for an inhomogeneously doped two-leg ladder as a function of the difference in the chemical potential, $\Delta\mu$, for $L = 8$ (circles), and $L = 10$ (squares). Furthermore, $t' = t$ and $J = J' = 0.5\,t$.

acteristic hole-hole separation length, ξ, defined by

$$\xi^2 = \frac{1}{N} \sum_{j=-\lfloor \frac{L}{2} \rfloor}^{\lceil \frac{L}{2} \rceil - 1} j^2 \, \langle n'(0) n'(j) \rangle, \tag{4.8}$$

where N is a normalization factor given by $N = \sum_j \langle n'(0) n'(j) \rangle$. In Fig. 4.2, this separation length is plotted as a function of $\Delta\mu$ for two different systems with an even number of rungs, $L = 8$ and $L = 10$.[a] For both systems the characteristic hole-hole separation length jumps discontinuously at a critical value of $\Delta\mu_c \approx J'$. Furthermore, in the bound regime, i.e., for $\Delta\mu \leq \Delta\mu_c$, finite size effects in this quantity are rather small already for the system sizes considered here. In this regime the holes are bound, and the rung hole-hole correlation decays

[a]The system with $L = 9$ also exhibits a clear tendency towards unbinding, however no level crossing but rather a crossover between the two regimes occurs. For $L = 11$ a level crossing is found, with the total momentum jumping from 0 to a finite value near 0, whereas in the even systems the total momentum changes from 0 to a value near π. In view of these odd-even effect, we restrict the discussion to finite ladders with an even number of rungs.

exponentially. Therefore, the bound pair wave function extends over only a few rungs. In the unbound regime, however, the two holes tend to separate onto the lower leg, and therefore ξ grows with increasing system size.

The above numerical analysis demonstrates that non-uniform doping, by confining the mobile carriers onto one of the legs, is harmful to pairing. Furthermore, the inter-leg exchange interaction plays the important role of stabilizing the bound hole pair state. While the finite ladders considered in this section may be viewed as systems with a doping concentration of roughly $\delta \sim 0.1$, different approaches are needed to analyze the finite-doping regime beyond the two-hole problem. These will be presented in the following sections.

4.4 Renormalization group

In order to complement the analysis of the t-J model, in this section we consider the weakly interacting Hubbard model on a two-leg ladder. A renormalization group (RG) treatment supplemented by Abelian bosonization allows a detailed analysis of the phase diagram in the weakly interacting limit and a characterization of the various phases in terms of the low-energy modes. We follow an approach established on standard two- and N-leg ladder systems (i.e., for $\Delta\mu = 0$) [16, 126, 136, 137].

In the current case of an inhomogeneously doped two-leg ladder we consider the weak repulsive limit, $0 < U \ll t, t'$ of the Hubbard model,

$$\begin{aligned} H &= -t\sum_{jas}(c^\dagger_{jas}c_{j+1,as} + \text{h.c.}) - t'\sum_{js}(c^\dagger_{j1s}c_{j2s} + \text{h.c.}) \\ &\quad + U\sum_{ja} c^\dagger_{ja\uparrow}c_{ja\uparrow}c^\dagger_{ja\downarrow}c_{ja\downarrow} - \sum_{jas}\mu_a\, c^\dagger_{jas}c_{jas}, \end{aligned} \tag{4.9}$$

with the same notations as is Sec. 4.2. The quadratic part of the Hamiltonian (4.9), i.e., Eq. (4.9) with $U = 0$, can be decoupled via a canonical transformation

$$d^\dagger_{j,1(2),s} = \sqrt{\frac{1 \mp \Delta\mu/D}{2}}c^\dagger_{j2s} \pm \sqrt{\frac{1 \pm \Delta\mu/D}{2}}c^\dagger_{j1s}, \tag{4.10}$$

where $D = \sqrt{4(t')^2 + \Delta\mu^2}$. These rung operators interpolate smoothly between the bonding and anti-bonding combinations at $\Delta\mu = 0$ and the original fermions for $\Delta\mu/t' \to \infty$, where $d^\dagger_{jas} \to c^\dagger_{jas}$. In momentum space two bands

corresponding to $d^\dagger_{as}(k)$ result with dispersions

$$\varepsilon_{1(2)}(k) = -2t\cos k \pm \frac{1}{2}D - \bar{\mu}, \tag{4.11}$$

and a bandwidth $4\,t$.

Consider now the effect of the Hubbard interaction term in Eq. (4.9). When both bands are completely separated in energy, only the lower band is filled, and at half-filling ($\delta = 0$) a band insulator is obtained which upon doping ($\delta > 0$) becomes an ordinary spin-1/2 Luttinger liquid (LL). For $D < 4t\cos^2(\pi\delta)$, both bands are partially filled, and inter-band interaction effects must be examined. While this proves difficult in general, progress can be made upon considering the weakly interacting limit. Since the interest is thus on the low-energy physics, the dispersions (4.11) can be linearized around the Fermi points $k_{\mathrm{F},a}$, $a = 1, 2$, determined by $\varepsilon_1(k_{\mathrm{F},1})=\varepsilon_2(k_{\mathrm{F},2})$ and $k_{\mathrm{F},1}+k_{\mathrm{F},2} = \pi(1-\delta)$. Furthermore left- and right movers, $d^\dagger_{\mathrm{R(L)},is}$, are defined with respect to the Fermi level in each band, $i = 1, 2$. For generic (i.e., incommensurate) Fermi momenta the interactions consist of intra- and inter-band forward- and Cooper- scattering. These can be organized in terms of the U(1) and SU(2) current operators

$$J_{pij} = \sum_s d^\dagger_{pis} d_{pjs}, \qquad \mathbf{J}^\alpha_{pij} = \frac{1}{2}\sum_{ss'} d^\dagger_{pis}\,\boldsymbol{\sigma}^\alpha_{ss'}\,d_{pjs'}, \tag{4.12}$$

where $p = \mathrm{R}, \mathrm{L}$, and the band indices $i, j = 1, 2$. The following non-chiral current-current interactions are allowed by symmetry,

$$\begin{aligned} H_{\mathrm{I}} &= \sum_i \int \mathrm{d}x\, (c^\rho_{ii} J_{\mathrm{R}ii} J_{\mathrm{L}ii} - c^\sigma_{ii} \mathbf{J}_{\mathrm{R}ii}\cdot\mathbf{J}_{\mathrm{L}ii}) \\ &+ \sum_{i\neq j} \int \mathrm{d}x\, (c^\rho_{ij} J_{\mathrm{R}ij} J_{\mathrm{L}ij} - c^\sigma_{ij} \mathbf{J}_{\mathrm{R}ij}\cdot\mathbf{J}_{\mathrm{L}ij}) \\ &+ \sum_{i\neq j} \int \mathrm{d}x\, (f^\rho_{ij} J_{\mathrm{R}ii} J_{\mathrm{L}jj} - f^\sigma_{ij} \mathbf{J}_{\mathrm{R}ii}\cdot\mathbf{J}_{\mathrm{L}jj}). \end{aligned} \tag{4.13}$$

In this representation f (c) denotes couplings related to forward- (Cooper-) scattering, and the symmetry of the inter-band scattering terms under the band exchange is explicitly taken into account. Using current algebra and operator product expansions, a one-loop RG flow for the various couplings can

be derived [126], which in our notation reads

$$\begin{aligned}
\frac{\mathrm{d}c^{\rho}_{ii}}{\mathrm{d}l} &= -\frac{1}{2v_{\bar{i}}}\left[(c^{\rho}_{i\bar{i}})^2+\frac{3}{16}(c^{\sigma}_{i\bar{i}})^2\right],\\
\frac{\mathrm{d}c^{\sigma}_{ii}}{\mathrm{d}l} &= -\frac{1}{2v_{\bar{i}}}\left[\frac{1}{2}(c^{\sigma}_{i\bar{i}})^2+2c^{\rho}_{i\bar{i}}c^{\sigma}_{i\bar{i}}\right]-\frac{1}{2v_i}(c^{\sigma}_{ii})^2,\\
\frac{\mathrm{d}c^{\rho}_{12}}{\mathrm{d}l} &= -\sum_i\frac{1}{2v_i}\left[c^{\rho}_{1i}c^{\rho}_{i2}+\frac{3}{16}c^{\sigma}_{1i}c^{\sigma}_{i2}\right]\\
&\quad+\frac{2}{v_1+v_2}\left[c^{\rho}_{12}f^{\rho}_{12}+\frac{3}{16}c^{\sigma}_{12}f^{\sigma}_{12}\right],\\
\frac{\mathrm{d}c^{\sigma}_{12}}{\mathrm{d}l} &= -\sum_i\frac{1}{2v_i}\left[c^{\rho}_{1i}c^{\sigma}_{i2}+c^{\sigma}_{1i}c^{\rho}_{i2}+\frac{1}{2}c^{\sigma}_{1i}c^{\sigma}_{i2}\right]\\
&\quad+\frac{2}{v_1+v_2}\left[c^{\rho}_{12}f^{\sigma}_{12}+c^{\sigma}_{12}f^{\rho}_{12}-\frac{1}{2}c^{\sigma}_{12}f^{\sigma}_{12}\right],\\
\frac{\mathrm{d}f^{\rho}_{12}}{\mathrm{d}l} &= \frac{1}{v_1+v_2}\left[(c^{\rho}_{12})^2+\frac{3}{16}(c^{\sigma}_{12})^2\right],\\
\frac{\mathrm{d}f^{\sigma}_{12}}{\mathrm{d}l} &= \frac{1}{v_1+v_2}\left[2c^{\rho}_{12}c^{\sigma}_{12}-\frac{1}{2}(c^{\sigma}_{12})^2-(f^{\sigma}_{12})^2\right],
\end{aligned} \tag{4.14}$$

where $i=1,2$, $\bar{1}=2$, $\bar{2}=1$, and $v_i=2t\sin(k_{\mathrm{F},i})$ are the Fermi velocities for the bands. The successive elimination of high frequency modes is obtained from (4.14) by integration along the logarithmic length scale l, related to an energy scale $E\sim te^{-\pi l}$. The flow equations can be integrated once the bare values of the couplings are known. For the Hubbard interaction of Eq. (4.9) they are obtained as

$$\begin{aligned}
c^{\sigma}_{11} &= c^{\sigma}_{22}=4c^{\rho}_{11}=4c^{\rho}_{22}=U\left[1+\left(\frac{\Delta\mu}{D}\right)^2\right],\\
c^{\sigma}_{12} &= 4c^{\rho}_{12}=f^{\sigma}_{12}=4f^{\rho}_{12}=U\left[1-\left(\frac{\Delta\mu}{D}\right)^2\right].
\end{aligned} \tag{4.15}$$

Increasing $\Delta\mu$ away from zero can be seen to reduce the bare inter-band scattering with respect to intra-band scattering.

Depending on the parameters, integration of the flow equations leads to different asymptotic behavior, with either a flow to a finite-valued fix point, or to instabilities characterized by universal ratios of the renormalized couplings beyond a scale l^*, where the most diverging coupling becomes of the order

the bandwidth. While the consistency of the one-loop renormalization group equations is restricted to $l < l^*$, the asymptotic ratios can be utilized to derive a description of the low-energy physics of the system within Abelian bosonization [138]. Introducing canonically conjugated bosonic fields $\Phi_{\nu i}$, and $\Pi_{\nu i}$ for the charge and spin degrees of freedom ($\nu = \rho, \sigma$) on each band $i = 1, 2$, the fermionic operators can be represented as

$$d_{\mathrm{R(L)},i,s} = \frac{\eta_{is}}{\sqrt{2\pi\alpha}} \mathrm{e}^{i\sqrt{\pi/2}[\pm(\Phi_{\rho i}+s\Phi_{\sigma i})-(\theta_{\rho i}+s\theta_{\sigma i})]}, \tag{4.16}$$

where $\theta_{\nu i}$ is the dual field of $\Phi_{\nu i}$, so that $\partial_x \theta_{\nu i} = \Pi_{\nu i}$. The η_{is} are Klein factors, ensuring anticommutation relations, and α is a short-distance cutoff. Using the above representation, the interacting fermionic Hamiltonian transforms into a bosonic Hamiltonian, $H_B = H_q + H_I$, containing quadratic terms

$$\begin{aligned} H_q &= \sum_{\nu i} \frac{1}{2} \int \mathrm{d}x \left[v_i + \frac{c^\nu_{ii}}{\beta_\nu |\beta_\nu|} \right] \partial_x \Phi^2_{\nu i} + \left[v_i - \frac{c^\nu_{ii}}{\beta_\nu |\beta_\nu|} \right] \Pi^2_{\nu i} \\ &\quad + \int \mathrm{d}x \, \frac{f^\nu_{12}}{\beta_\nu |\beta_\nu|} (\partial_x \Phi_{\nu 1} \partial_x \Phi_{\nu 2} - \Pi_{\nu 1} \Pi_{\nu 2}), \end{aligned} \tag{4.17}$$

and sine-Gordon-like interaction terms

$$\begin{aligned} H_{\mathrm{I}} &= \int \mathrm{d}x \, \{ \, c^\sigma_{11} \cos(\sqrt{2}\beta_\sigma \Phi_{\sigma 1}) + c^\sigma_{22} \cos(\sqrt{2}\beta_\sigma \Phi_{\sigma 2}) \\ &\quad - 4 c^\rho_{12} \cos(2\beta_\rho \theta_{\rho -}) [\cos(\beta_\sigma \Phi_{\sigma -}) - \cos(\beta_\sigma \theta_{\sigma -})] \\ &\quad - c^\sigma_{12} \cos(2\beta_\rho \theta_{\rho -}) [2\cos(\beta_\sigma \Phi_{\sigma +}) + \cos(\beta_\sigma \Phi_{\sigma -})] \\ &\quad - c^\sigma_{12} \cos(2\beta_\rho \theta_{\rho -}) \cos(\beta \theta_{\sigma -}) + 2 f^\sigma_{12} \cos(\beta_\sigma \theta_{\sigma -}) \cos(\beta_\sigma \Phi_{\sigma +}) \, \}, \end{aligned} \tag{4.18}$$

where $\beta_\rho = \sqrt{\pi}$, $\beta_\sigma = -\sqrt{4\pi}$, and the fields $\Phi_{\nu\pm} = (\Phi_{\nu 1} \pm \Phi_{\nu 2})/\sqrt{2}$ and $\Pi_{\nu\pm} = (\Pi_{\nu 1} \pm \Pi_{\nu 2})/\sqrt{2}$ have been introduced. Upon minimizing the energy in a semiclassical approximation, any coupling that diverges under the RG flow opens up a gap for a field that is pinned by the corresponding terms in (4.18).

Performing the above procedure, four different phases are obtained for the Hamiltonian of Eq. (4.9), shown in the (δ, $\Delta\mu$)-plane for isotropic hopping, $t' = t$, in Fig. 4.3. The various phases are labeled according to the number of gapless charge (n) and spin (m) modes by CnSm. The different asymptotic regimes of the RG flow (4.14) are related to the phases shown in Fig. 4.3 as follows:

- *(C1S1), the single band LL.* This phase with an empty upper band is labeled C1S1, reflecting the number of gapless modes. For incommensurate filling the dominant correlations are charge density waves (CDW) and spin density waves (SDW).

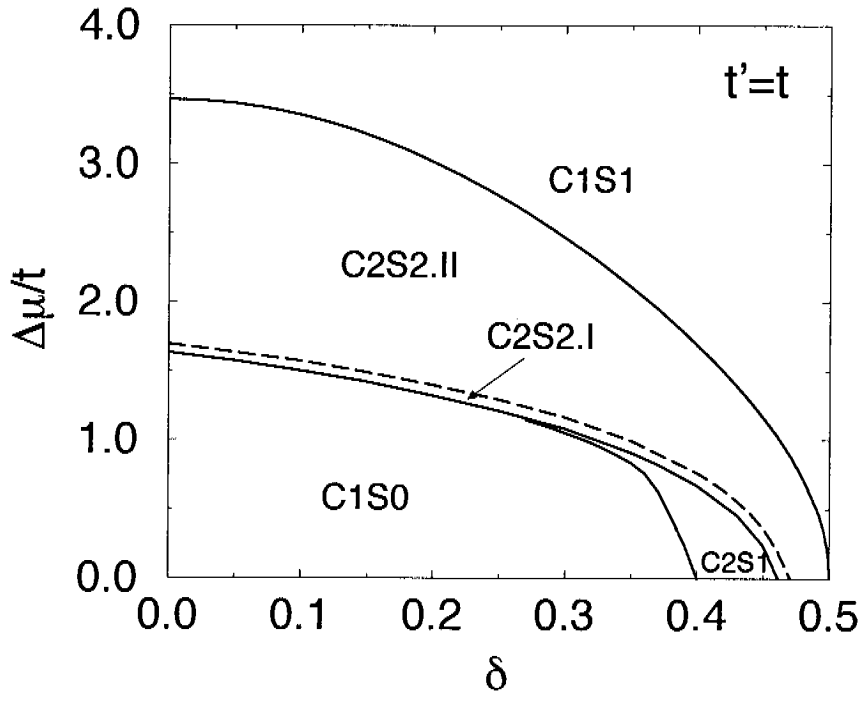

Figure 4.3: Phase diagram of the inhomogeneously doped Hubbard model on two-leg ladder in the weakly interacting limit, and for $t' = t$. The phases CnSm are labeled according to the number of gapless charge (n) and spin (m) modes. Solid lines are phase boundaries. The dashed line indicates the crossover from a region with dominant SC correlations in the lower and CDW and SDW correlations in the upper band (C2S2.I), to a region dominated by CDW and SDW correlations in both bands, for larger values of $\Delta\mu$ (C2S2.II).

- *(C2S2), the trivial fixed point.* In this regime the couplings stay of order U under the RG flow, or renormalize to zero. Therefore no gap opens in this phase, labeled C2S2. Furthermore, the two partially filled bands are decoupled in this regime. Standard LL theory [139] used to determine the dominant correlations within each band, indicates a crossover between two regions labeled C2S2.I, and C2S2.II respectively, cf. Fig. 4.3. The dominant correlations in the C2S2.II regime are CDW and SDW within both bands, whereas in the C2S2.I regime the lower band is dominated by superconducting (SC) fluctuations.

- *(C2S1), single-band superconductivity.* Here, all couplings stay of the

order of U or renormalize to zero, except for $c_{22}^{\sigma} \sim -v_2$. This results in a pinning of the spin mode of the lower band, and the number of gapless modes reduces to C2S1. SC correlations dominate the lower band, and CDW and SDW correlations the upper band. Furthermore, inter-band phase coherence is not established within this regime.

- *(C1S0), inter-band superconductivity.* In this regime the diverging couplings flow towards the asymptotic ratios

$$4c_{12}^{\rho} = 8f_{12}^{\rho} = c_{12}^{\sigma}, \quad c_{11}^{\sigma}/v_1 = c_{22}^{\sigma}/v_2. \tag{4.19}$$

From the low-energy effective bosonic Hamiltonian two finite spin gaps are obtained, and a pinning of the charge mode $\theta_{\rho-} = 0$, resulting in phase coherence between the two bands. The number of gapless modes is reduced to C1S0. The remaining total charge mode, $(\Phi_{\rho+}, \theta_{\rho+})$, is gapless and exhibits dominant superconducting pairing correlations, with a sign difference between the bands. This is usually referred to as the d-wave-like superconducting phase of the two-leg ladder [126, 136].

The phase diagram in Fig. 4.3 confirms the results obtained along the line $\Delta\mu = 0$ [126, 136]. But it also indicates a limited stability of the various phases found at $\Delta\mu = 0$ under inhomogeneously doping of the ladder. Upon increasing $\Delta\mu$, superconductivity is gradually suppressed, with intermediate phases showing residual superconducting fluctuations. Consider for example the low doping region where inter-band d-wave superconductivity occurs for vanishing $\Delta\mu$. While for small $\Delta\mu > 0$ d-wave superconductivity sustains, inter-band phase coherence is lost when $\Delta\mu$ reaches a value of approximately $1.5t'$. For larger values of $\Delta\mu$ intra-band superconductivity persists within the lower band (which predominately projects onto the lower leg of the ladder). In the upper band spin fluctuations have become gapless and SDW and CDW correlations dominate. Further increase of $\Delta\mu$ results in the suppression of all superconducting correlations, giving rise to two-band LL behavior. In the weakly interacting limit the upper band is depleted for $\Delta\mu/t > 3.5$, and a single-band LL, residing mainly on the lower leg of the ladder, dominates the large-$\Delta\mu$ regime. This progressive reduction of superconducting pairing correlations is also observed in the finite-temperature phase diagram. In Fig. 4.4 we show results for $t' = t$, and $\Delta\mu/t = 0.3$ in the (δ, T)-plane. From the renormalization of the energy scale, $E \sim te^{-\pi l}$, the logarithmic length scale of Eq. (4.14) can be related to a temperature scale $T = E = T_0 e^{-\pi l}$. While the phases of the system for $T \to 0$

are found in accordance with Fig. 4.3, the finite temperature phase diagram reveals a successive enhancement of superconducting pairing correlations with decreasing temperature. Consider again the behavior close to half-filling. At high temperatures the system is dominated by LL behavior in both bands. Upon decreasing the temperature gapless superconducting correlations develop within the lower band. At even lower temperatures, a finite spin gap opens for the lower band, then finally phase coherent inter-band d-wave superconductivity emerges, along with the opening of the second spin gap. Thus in an intermediate temperature regime, well above the onset of d-wave superconductivity, a single spin gap persists in the lower band, which is related to the bonding band at small values of $\Delta\mu$. This partial spin gap formation might be interpreted as a phenomenon similar to the pseudogap phase in the HTCS materials.

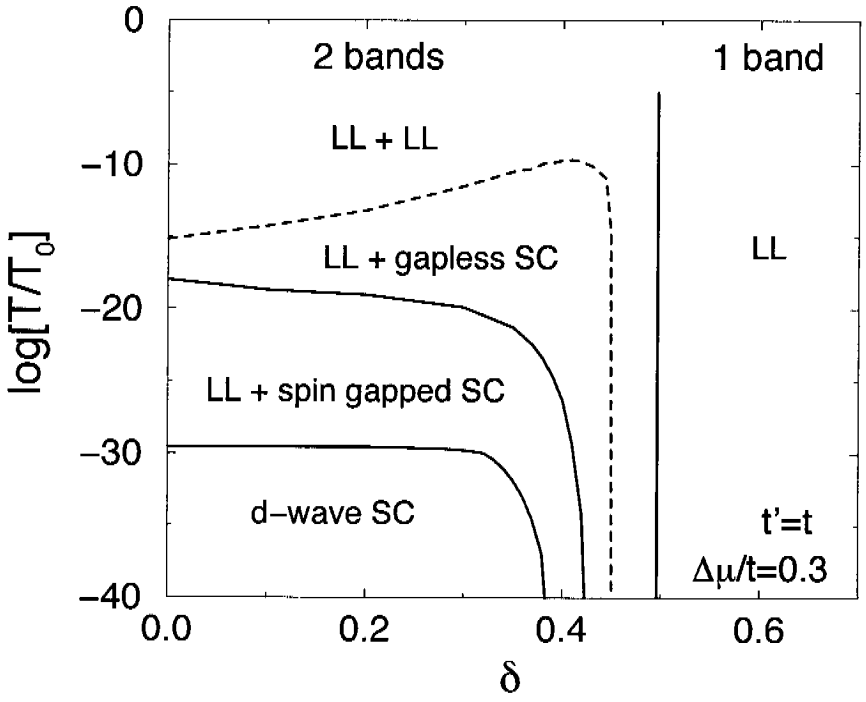

Figure 4.4: Finite temperature phase diagram of the inhomogeneously doped Hubbard model on the two-leg ladder in the weakly interacting limit for $t' = t$, and $\Delta\mu/t = 0.3$. Solid lines are phase boundaries, whereas the dashed line indicates a crossover inside the gapless regime.

4.5 Mean-field analysis for the t-J ladder

In this section we extend our analysis of the t-J model by considering a mean-field approximation based on the spinon-holon-decoupling scheme. We follow a similar approach as various previous studies on ladders as well as two-dimensional systems [135, 140–142].

4.5.1 Spinon-holon decomposition

The non holonomic local constraint $\sum_s c^\dagger_{jas} c_{jas} \leq 1$ is one of the main difficulties in treating the t-J model. The slave-boson formalism provides a possibility to take this constraint into account. Introducing fermionic spinon operators f and bosonic holon operators b, the electron creation and annihilation operators can be expressed as

$$c^\dagger_{jas} = f^\dagger_{jas} b_{ja}, \quad \text{and} \quad c_{jas} = b^\dagger_{ja} f_{j,a,s}, \tag{4.20}$$

leading to the holonomic constraint

$$\sum_s f^\dagger_{jas} f_{jas} + b^\dagger_{ja} b_{ja} = 1. \tag{4.21}$$

The Hamiltonian (4.1) can be expressed in terms of this new operators as

$$\begin{aligned} H \;=\; & -t \sum_{jas} \left(f^\dagger_{jas}\, f_{j+1,as}\, b_{ja}\, b^\dagger_{j+1,a} + \text{h.c.} \right) \\ & -t' \sum_{js} \left(f^\dagger_{j1s}\, f_{j2s}\, b_{j1}\, b^\dagger_{j2} + \text{h.c.} \right) \\ & + J \sum_{ja} \mathbf{S}^f_{ja} \cdot \mathbf{S}^f_{j+1,a} + J' \sum_{j} \mathbf{S}^f_{j1} \cdot \mathbf{S}^f_{j2} \\ & + \sum_{ja} \left[\mu_a\, b^\dagger_{ja}\, b_{ja} - \lambda_{ja} \Big(\sum_s f^\dagger_{jas} f_{jas} + b^\dagger_{ja} b_{ja} - 1 \Big) \right], \end{aligned} \tag{4.22}$$

where the Lagrange multipliers λ_{ja}, $a = 1, 2$, have been introduced to enforce the local constraint (4.21). In the interaction part, the density-density terms $n_{ja}\, n_{j'a'}$ are omitted. Within the following mean-field treatment, this term would destroy the local SU(2) gauge symmetry of the spinon representation at half-filling [20]. This symmetry corresponds to a local unitary rotation of the spinor $(f_{ia\uparrow}, f^\dagger_{ia\downarrow})$ leaving the spinon spectrum invariant [20]. This symmetry appears naturally in the large U Hubbard model [20] and is considered to be essential for various aspects of the weakly doped t-J model [141, 143]. Therefore,

we will keep only the spin exchange part of the interaction which conserves this symmetry in the mean-field approximation [141]. The last term in Eq. (4.22) takes the different chemical potentials on the two legs into account.

To proceed we decouple the terms which are not single particle terms in the Hamiltonian (4.22) by introducing the mean-fields [141]

$$\begin{aligned} \chi_{ja;j'a'} &= \frac{1}{2}\sum_s \langle f^\dagger_{jas} f_{j'a's}\rangle, \\ B_{ja;j'a'} &= \langle b_{ja}\, b^\dagger_{j'a'}\rangle, \\ \Delta_{ja;j'a'} &= \langle f_{ja\downarrow}\, f_{j'a'\uparrow}\rangle. \end{aligned} \tag{4.23}$$

In the following the mean-fields along the legs are labeled with the indices 1 and 2, and the mean-field on the rung with the index 3, e.g., for χ:

$$\begin{aligned} \chi_a &= \frac{1}{2}\sum_s \langle f^\dagger_{jas} f_{j+1,as}\rangle \qquad a = 1,2 \\ \chi_3 &= \frac{1}{2}\sum_s \langle f^\dagger_{j1s} f_{j2s}\rangle. \end{aligned} \tag{4.24}$$

This convention of labeling the bond $(ja; j'a')$ also applies to the mean-fields B, and Δ. Finally the doping level is fixed by the condition

$$1-\delta = \frac{1}{2}\sum_{as}\langle f^\dagger_{jas} f_{jas}\rangle\,. \tag{4.25}$$

The Lagrange multipliers λ_{ja} are kept uniform on each leg, i.e., $\lambda_{ja} \to \lambda_a$, so that the constraint is satisfied only on the average on each leg of the ladder. Introducing Fourier transformed operators

$$f_{kas} = \frac{1}{\sqrt{L}}\sum_j f_{jas}\, \mathrm{e}^{\mathrm{i}kj}, \qquad b_{ka} = \frac{1}{\sqrt{L}}\sum_j b_{ja}\, \mathrm{e}^{\mathrm{i}kj}, \tag{4.26}$$

the mean-field Hamiltonian reads

$$\begin{aligned} H_{\mathrm{MF}} = \sum_k \left(H^b_k + H^f_k\right) + L\Bigg[\sum_a \Big\{\frac{3}{2}J\left(\Delta_a^2 + \chi_a^2\right) + 4t\chi_a B_a\Big\} \\ + \frac{3}{2}J_3\left(\Delta_3^2 + \chi_3^2\right) + 4t'\chi_3 B_3\Bigg]. \end{aligned} \tag{4.27}$$

The quadratic terms H_k^b and H_k^f are given by

$$H_k^b = \begin{pmatrix} b_{k1}^\dagger \\ b_{k2}^\dagger \end{pmatrix}^\top \begin{bmatrix} -4t\,\chi_1 \cos k - \lambda_1 + \mu_1 & -2t'\,\chi_3 \\ -2t'\,\chi_3 & -4t\,\chi_2 \cos k - \lambda_2 + \mu_2 \end{bmatrix} \begin{pmatrix} b_{k1} \\ b_{k2} \end{pmatrix},$$

$$H_k^f = \begin{pmatrix} f_{k1\uparrow}^\dagger \\ f_{k2\uparrow}^\dagger \\ f_{-k1\downarrow} \\ f_{-k2\downarrow} \end{pmatrix}^\top \begin{bmatrix} \hat{\xi}_k & \hat{\Delta}_k \\ \hat{\Delta}_k & -\hat{\xi}_k \end{bmatrix} \begin{pmatrix} f_{k1\uparrow} \\ f_{k2\uparrow} \\ f_{-k1\downarrow}^\dagger \\ f_{-k2\downarrow}^\dagger \end{pmatrix},$$

where $\hat{\xi}_k$, and $\hat{\Delta}_k$ are the following 2×2 matrices

$$\hat{\xi}_k = \begin{bmatrix} -\lambda_1 - \left(2tB_1 + \frac{3}{2}J\chi_1\right)\cos k & -t'B_3 - \frac{3}{4}J_3\chi_3 \\ -t'B_3 - \frac{3}{4}J_3\chi_3 & -\lambda_2 - \left(2tB_2 + \frac{3}{2}J\chi_2\right)\cos k \end{bmatrix},$$

$$\hat{\Delta}_k = \begin{bmatrix} -\frac{3}{2}J\Delta_1 \cos k & -\frac{3}{4}J\Delta_3 \\ -\frac{3}{4}J\Delta_3 & -\frac{3}{2}J\Delta_2 \cos k \end{bmatrix}.$$

The mean-fields are determined by self-consistently solving the single-particle problem of H_{MF} and calculating the corresponding expectation values according to Eqs. (4.23, 4.24).

Diagonalization of the bosonic part of the Hamiltonian yields two holon bands. In the ground state of the system, the holons are assumed to Bose condense into their lowest energy state [142]. Denoting the amplitudes of the lowest holon state on the two legs by A_a, the bosonic bond mean-fields become

$$\begin{aligned} B_a &= 2\delta\, A_a^2, \qquad a = 1, 2, \\ B_3 &= 2\delta\, A_1\, A_2. \end{aligned} \tag{4.28}$$

The spinon part of the Hamiltonian can be diagonalized by a Bogoliubov transformation, from which the self-consistent equations for the mean-fields Δ and χ, and the Lagrange multipliers λ are determined numerically. Furthermore we define the BCS order parameters

$$\begin{aligned} \Delta'_{ja;j'a'} &:= \langle c_{ja\uparrow} c_{j'a'\downarrow} \rangle \\ &\approx \langle b_{ja}^\dagger b_{j'a'}^\dagger \rangle \langle f_{ja\uparrow} f_{j'a'\downarrow} \rangle = B_{ja;j'a'} \Delta_{ja;j'a'} \end{aligned} \tag{4.29}$$

in terms of the holon and spinon mean-fields [140]. For the BCS order parameters we use the same bond labeling scheme as in Eq. (4.24).

The redistribution of charge carriers due to the chemical potential difference is implemented via the holon degrees of freedom as can be seen in the mean-field Hamiltonian. In this way there is no effect at half-filling. Furthermore, the constraint and the renormalization of the coupling constants induces a non-trivial mutual feedback for the charge and spin degrees of freedom.

4.5.2 Mean-field results for the t-J ladder

Within the above mean-field description we are able to analyze the behavior of the two-leg ladder for different values of the doping concentration, δ, and chemical potential difference, $\Delta\mu$. In particular, we are interested in the BCS order parameters as the indication for Cooper paring. In the following the parameters of the t-J model are fixed to isotropic coupling with $t' = t$ and $J' = J = 0.5\,t$. Furthermore, we restrict ourselves to the low doping region $\delta < 0.25$, where the above spinon-holon decomposition is expected to be qualitatively reliable [140].

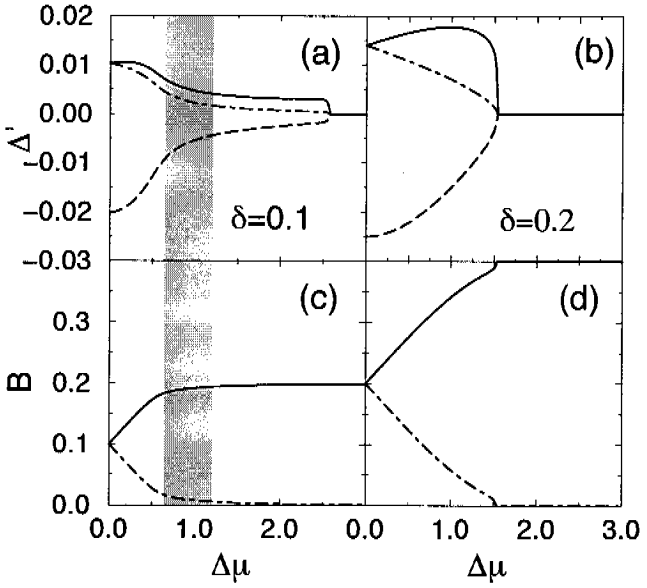

Figure 4.5: BCS mean-fields Δ', (a,b), and hole densities B, (c,d), of the t-J model on a two-leg ladder as functions of the chemical potential difference, $\Delta\mu$, at constant $\delta = 0.1$ (a,c), and $\delta = 0.2$ (b,d). $t' = t$ and $J' = J = 0.5\,t$. The values for the lower (upper) leg are plotted with solid (dotted-dashed) lines and the BCS mean-field on the rungs with dashed lines.

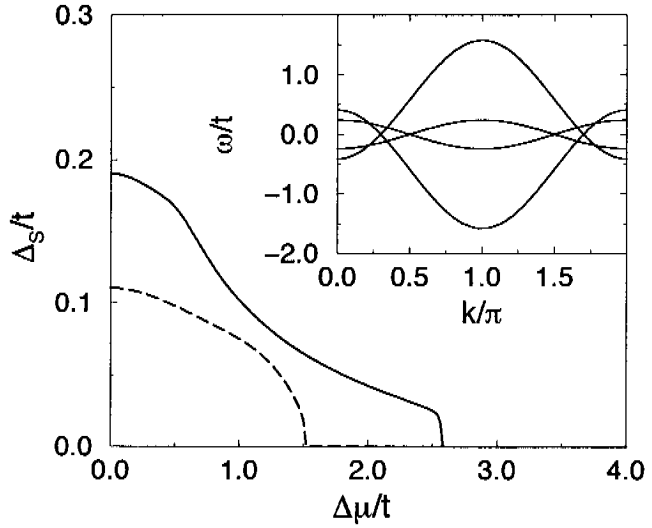

Figure 4.6: Spinon gap Δ_S of the t-J model on a two-leg ladder as a function of the chemical potential difference $\Delta\mu$ at constant hole doping $\delta = 0.1$ (solid line) and $\delta = 0.2$ (dashed line) for $t' = t$, $J' = J = 0.5t$. The inset shows the gapless spinon bands in the normal state at $\delta = 0.2$. $\Delta\mu/t = 2.0$.

For $\Delta\mu = 0$ our calculations agree well with the overall behavior obtained from similar mean-field calculations using a Gutzwiller-type renormalization method [135]. While at half-filling ($\delta = 0$) the BCS order parameters vanish, they increase monotonically with hole doping away from half-filling. Their values on the legs coincide ($\Delta'_1 = \Delta'_2$), whereas a phase shift of π exists relative to the rung order parameter Δ'_3, in analogy to the d-wave pairing symmetry on the square lattice version of the doped t-J model.

In order to analyze the influence of a chemical potential difference between the two legs on the Cooper pairing, we follow the behavior of the BCS mean-fields $\Delta'_{1,2,3}$ upon increasing $\Delta\mu > 0$ for two fixed hole concentrations, $\delta = 0.1$ and $\delta = 0.2$, shown in Fig. 4.5 (a,b). In both cases the chemical potential difference leads to the reduction and eventual destruction of the BCS mean-fields. However, there is a qualitative difference between the two doping levels. For $\delta = 0.1$ a crossover from a strong to a weak superconducting regime occurs, while no such regime change takes place for $\delta = 0.2$. The crossover at $\Delta\mu \approx 0.6\,t$ in Fig. 4.5 (a) for $\delta = 0.1$ coincides with the almost complete hole-depletion of the upper leg in Fig. 4.5 (c). This behavior can be understood by the following properties of doped two-leg ladders. These systems constitute typical

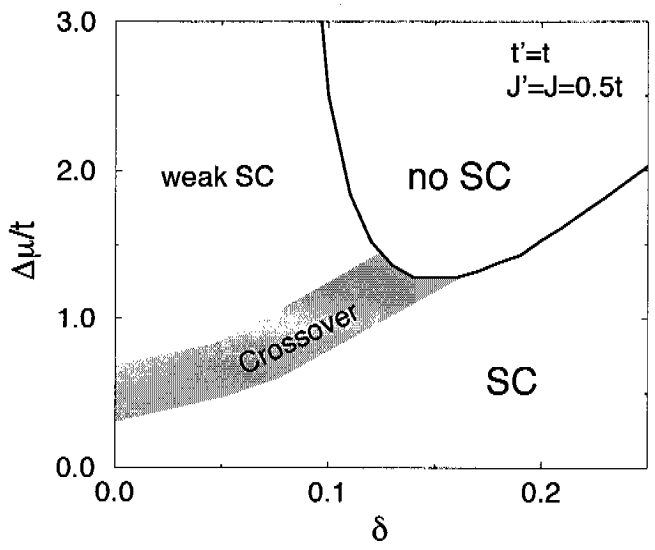

Figure 4.7: Low doping phase diagram of the inhomogeneously doped two-leg ladder in the mean-field approximation of the t-J model at $t' = t$ and $J' = J = 0.5\,t$. The BCS mean-fields vanish beyond the solid line. In the low doping region the crossover regime connecting the d-wave SC and a regime of reduced BCS mean-fields is indicated as a shaded area.

examples where superconductivity originates from a doped RVB phase, which is characterized within this mean-field approach by a finite gap in the spinon spectrum [135]. Furthermore, this spinon gap decreases upon doping holes into a half-filled two-leg ladder [135]. Within the mean-field approximation we can obtain the spinon gap at finite values of $\Delta\mu$ for the doping levels considered above. In Fig. 4.6 the development of the spinon gap upon increasing the chemical potential difference, $\Delta\mu$, is shown for both $\delta = 0.1$, and $\delta = 0.2$. In either case does the imbalance in the distribution of holes between the two legs lead to an additional reduction of the spinon gap. This behavior is expected as the RVB phase in the ladder is dominated by the formation of rung singlet pairs. Concentrating the holes onto a single leg destroys statistically more rung singlets than distributing them equally among both legs. However, at $\delta = 0.1$, a large spinon gap is found even for e.g., $\Delta\mu/t = 2$, where the upper leg is almost completely depleted, as seen in Fig. 4.5 (c). Although the holes are already strongly concentrated onto the lower leg, the spinon gap is not destroyed until $\Delta\mu$ becomes as large as $\Delta\mu_c \approx 2.6\,t$. Along with the RVB state, d-wave superconductivity thus prevails up to this critical value of $\Delta\mu_c$, as seen

in Fig. 4.5 (a). For the larger doping of $\delta = 0.2$ however, concentrating the holes onto the lower leg suppresses the spinon gap completely, thereby destroying the RVB state. This follows from a comparison of the behavior of the spinon gap in Fig. 4.6 with the corresponding behavior of the charge distribution shown in Fig. 4.5 (d). Along with the spinon gap the superconducting state disappears already at $\Delta\mu_c \approx 1.5\,t$. However, the chemical potential difference which is necessary to pull the holes onto the lower leg increases upon increasing the hole doping level.

The resulting phase diagram in Fig. 4.7 displays a peculiar structure. For low-doping concentrations $\delta < 0.15$ we observe two regimes, strong and weak superconductivity, separated by a broad crossover. The crossover region is characterized by the depletion of holes from the upper leg. For larger doping $\delta > 0.15$ only the regime of strong superconductivity remains, and the RVB state is destroyed once the holes are sufficiently unequal distributed among the two legs. The mean-field solution suggests that there exists a critical doping $\delta_c \approx 0.08$ below which the superconducting state along with the RVB spin liquid state remains stable for all $\Delta\mu$.

Within the mean-field approximation the non-superconducting phase appears to consist of two independent subsystems. This can be referred from the inset of Fig. 4.6, which displays the gapless spinon bands at $\delta = 0.2$ and $\Delta\mu/t = 2.0$, well inside the normal phase. The spectrum consists of the spinon bands of a spin-1/2 antiferromagnetic Heisenberg chain, with nodes at $k = \pm\pi/2$, and two additional bands, with nodes at $k_F = \pm\pi/2(1-2\delta)$. These nodes correspond to those of a single chain Luttinger liquid. The system in the normal state therefore appears to be separated in a t-J chain with hole doping 2δ, having the properties of a Luttinger liquid, and a spin-1/2 antiferromagnetic Heisenberg chain. Furthermore, gapless charge excitations only exist for the Luttinger liquid. This complete separation is likely an artifact of the mean-field approximation, as in the strong rung coupling limit $J' \gg J$ the system is obviously a single chain Luttinger liquid.

The mean-field description of the t-J ladder is in qualitative agreement with the numerical result of Sec. 4.3 and with the the analysis of the weak-coupling Hubbard model of the previous section. In the following section we apply the same mean-field formalism for the t-J model to an inhomogeneously doped bilayer.

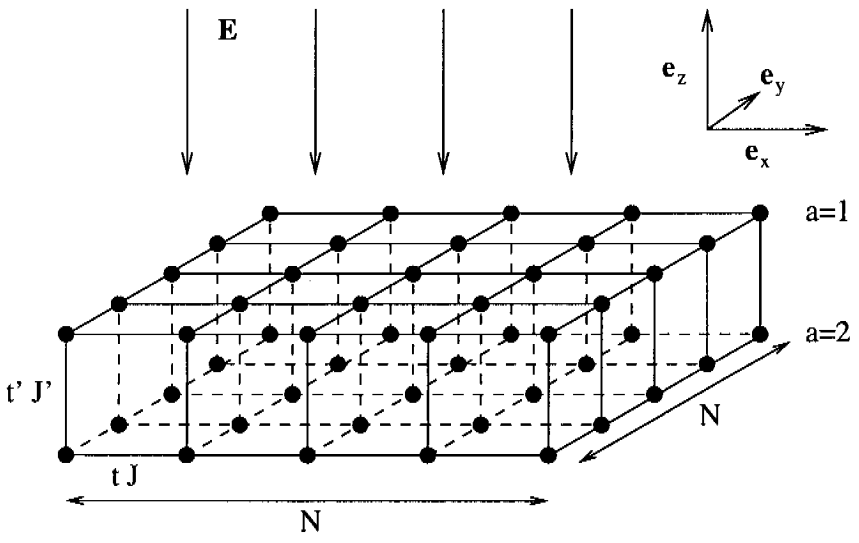

Figure 4.8: Schematic picture of the considered t-J model for the bilayer.

4.6 Mean-field analysis for the bilayer

In this section we study the bilayer system shown in Fig. 4.8 with the slave boson mean-field method. The t-J Hamiltonian for the bilayer, without the density-density terms, is given by

$$\begin{aligned} H &= -t\sum_{\mathbf{j}\mu a}\sum_{s}\mathcal{P}(c^{\dagger}_{\mathbf{j}as}c_{\mathbf{j}+\mu,as}+\text{h.c.})\mathcal{P}+J\sum_{\mathbf{j}\mu a}\mathbf{S}_{\mathbf{j}a}\cdot\mathbf{S}_{\mathbf{j}+\mu,a} \\ &\quad -t'\sum_{\mathbf{j}}\sum_{s}\mathcal{P}(c^{\dagger}_{\mathbf{j}1s}c_{\mathbf{j}2s}+\text{h.c})\mathcal{P}+J'\sum_{\mathbf{j}}\mathbf{S}_{\mathbf{j}1}\cdot\mathbf{S}_{\mathbf{j}2} \\ &\quad -\sum_{\mathbf{j}a}\sum_{s}\mu_a c^{\dagger}_{\mathbf{j}as}c_{\mathbf{j}as}, \end{aligned} \tag{4.30}$$

where $\mathbf{j}=(j_x,j_y)\in\{1\ldots N\}^2$ and $\mu=\mathbf{e}_x,\mathbf{e}_y$. The index $a=1,2$ labels the two layers and $s=\uparrow,\downarrow$ is the spin index. t and t' are the intra- and interlayer hopping matrix elements, respectively, and J and J' the corresponding spin exchange constants. The operator $\mathcal{P}=\prod_{\mathbf{j}a}(1-n_{\mathbf{j}a\uparrow}n_{\mathbf{j}a\downarrow})$ projects onto the subspace without doubly occupied sites. As in the previous section we introduce a spinon-holon decomposition $c^{\dagger}_{\mathbf{j}as}=f^{\dagger}_{\mathbf{j}as}b_{\mathbf{j}a}$. The Hamiltonian (4.30) can be rewritten with these operators which leads to the two-dimensional version of Eq. (4.22).

In order to decouple the four operator terms we introduce the "exchange" mean-fields as in Eq. (4.24) by $\chi_a=\frac{1}{2}\sum_s\langle f^{\dagger}_{\mathbf{j}as}f_{\mathbf{j}+\mu,as}\rangle$ and $\chi_3=\frac{1}{2}\sum_s\langle f^{\dagger}_{\mathbf{j}1s}f_{\mathbf{j}2s}\rangle$.

Furthermore, we have the bosonic mean-fields $B_a = \langle b_{\mathbf{j}a} b^\dagger_{\mathbf{j}+\mu,a}\rangle$ and $B_3 = \langle b_{\mathbf{j}1} b^\dagger_{\mathbf{j}2}\rangle$. With these mean-fields, the decoupling of the kinetic energy terms is straight forward. In order to decouple the exchange terms we introduce five "pairing" mean-fields

$$\begin{aligned}
\Delta_{as} &= \frac{1}{2}\langle f_{\mathbf{j}a\downarrow} f_{\mathbf{j}+\mathbf{e}_x,a\uparrow} + f_{\mathbf{j}a\downarrow} f_{\mathbf{j}+\mathbf{e}_y,a\uparrow}\rangle, \\
\Delta_{ad} &= \frac{1}{2\mathrm{i}}\langle f_{\mathbf{j}a\downarrow} f_{\mathbf{j}+\mathbf{e}_x,a\uparrow} - f_{\mathbf{j}a\downarrow} f_{\mathbf{j}+\mathbf{e}_y,a\uparrow}\rangle, \\
\Delta_3 &= \langle f_{\mathbf{j}1\downarrow} f_{\mathbf{j}2\uparrow}\rangle.
\end{aligned} \tag{4.31}$$

We assume that all mean-fields are real, in this way we fix the phase difference between the s- and the d-wave to be $\pi/2$. This allows us to work with a single complex pairing mean-field per layer, defined by $\Delta_a = \Delta_{as} + \mathrm{i}\Delta_{ad}$. This assumption is based on the following reasoning: If only one of the two order parameters is finite the phase of this order parameter can be chosen arbitrarily. If however both order parameters coexist and have a given amplitude, the combination with the relative phase $\pi/2$ opens a maximal gap without nodes. Therefore the complex combination $s + \mathrm{i}d$ can be assumed to be stabilized. With the Fourier transformed operators

$$f_{\mathbf{k}as} = \frac{1}{N}\sum_{\mathbf{j}} f_{\mathbf{j}as}\, \mathrm{e}^{\mathrm{i}\mathbf{k}\cdot\mathbf{j}}, \qquad b_{\mathbf{k}a} = \frac{1}{N}\sum_{\mathbf{j}} b_{\mathbf{j}a}\, \mathrm{e}^{\mathrm{i}\mathbf{k}\cdot\mathbf{j}}, \tag{4.32}$$

we can write the mean-field Hamiltonian as

$$H_{\mathrm{MF}} = \sum_{\mathbf{k}} \left(H^b_{\mathbf{k}} + H^f_{\mathbf{k}}\right) + N^2 E_{\mathrm{MF}} \tag{4.33}$$

$$E_{\mathrm{MF}} = \sum_a \left\{3J\left(|\Delta_a|^2 + \chi_a^2\right) + 8\,t\chi_a B_a\right\} + \frac{3}{2}J'\left(\Delta_3^2 + \chi_3^2\right) + 4\,t'\chi_3 B_3. \tag{4.34}$$

$H^b_{\mathbf{k}}$ is given by

$$H^b_{\mathbf{k}} = \begin{pmatrix} b^\dagger_{\mathbf{k}1} \\ b^\dagger_{\mathbf{k}2} \end{pmatrix}^\top \begin{bmatrix} -4\,t\,g_{\mathbf{k}}\chi_1 - \lambda_1 + \mu_1 & -2\,t'\chi_3 \\ -2\,t'\chi_3 & -4\,t\,g_{\mathbf{k}}\chi_2 - \lambda_2 + \mu_2 \end{bmatrix} \begin{pmatrix} b_{\mathbf{k}1} \\ b_{\mathbf{k}2} \end{pmatrix},$$

where $g_{\mathbf{k}} = \cos k_x + \cos k_y$ and $H^f_{\mathbf{k}}$ is given by

$$H^f_{\mathbf{k}} = \begin{pmatrix} f^\dagger_{\mathbf{k}1\uparrow} \\ f^\dagger_{\mathbf{k}2\uparrow} \\ f_{-\mathbf{k}1\downarrow} \\ f_{-\mathbf{k}2\downarrow} \end{pmatrix}^\top \begin{bmatrix} \hat{\xi}_{\mathbf{k}} & \hat{\Delta}_{\mathbf{k}} \\ \hat{\Delta}^*_{\mathbf{k}} & -\hat{\xi}_{\mathbf{k}} \end{bmatrix} \begin{pmatrix} f_{\mathbf{k}1\uparrow} \\ f_{\mathbf{k}2\uparrow} \\ f^\dagger_{-\mathbf{k}1\downarrow} \\ f^\dagger_{-\mathbf{k}2\downarrow} \end{pmatrix},$$

where $\hat{\xi}_{\mathbf{k}}$, and $\hat{\Delta}_{\mathbf{k}}$ are the following 2×2 matrices

$$\hat{\xi}_{\mathbf{k}} = \begin{bmatrix} -\lambda_1 - (2tB_1 + \frac{3}{2}J\chi_1)g_{\mathbf{k}} & -t'B_3 - \frac{3}{4}J'\chi_3 \\ -t'B_3 - \frac{3}{4}J'\chi_3 & -\lambda_2 - (2tB_2 + \frac{3}{2}J\chi_2)g_{\mathbf{k}} \end{bmatrix},$$

$$\hat{\Delta}_{\mathbf{k}} = \begin{bmatrix} -\frac{3}{2}J\{\Delta_1 \cos k_x + \Delta_1^* \cos k_y\} & -\frac{3}{4}J'\Delta_3 \\ -\frac{3}{4}J'\Delta_3 & -\frac{3}{2}J\{\Delta_2 \cos k_x + \Delta_2^* \cos k_y\} \end{bmatrix}.$$

In the following we will assume that $\Delta\mu = \mu_1 - \mu_2 \geq 0$, and we will refer to the layer with $a = 1$ ($a = 2$) as the upper (lower) layer as before. The average chemical potential $\overline{\mu} = (\mu_1 + \mu_2)/2$ is fixed by the overall hole doping concentration δ. The results, which are presented in this section, were obtained by solving numerically the self-consistency equations, obtained upon a Bogoliubov transformation of the mean-field Hamiltonian (4.33). The holons, b, are assumed to Bose condense in the lowest bosonic state.

The BCS mean-fields, that are the quantities of interest, are expressed approximatively in terms of the bosonic and the pairing mean-fields as in Eq. (4.29). We have $\Delta_3' \approx B_3\Delta_3$ and, analogously, $\Delta_{a,*}' \approx B_a\Delta_{a,*}$ for $a = 1, 2$ and $* = s, d$.

4.6.1 The symmetric bilayer

For the symmetric bilayer ($\Delta\mu = 0$), the three BCS mean-fields, Δ_s' (thicker lines), Δ_d' (thiner lines), and Δ_3' (negative values) are plotted in Fig. 4.9. The upper plot scans along the hole doping, δ, axes for three different values of J'. For $J' = J = 0.5\,t' = 0.5\,t$ we find a mixed phase where all the BCS mean-fields are finite at small doping concentrations. This phase, which breaks time reversal symmetry in addition to the U(1) symmetry, we denote by $s+id$. If we increase the doping, δ, the s-wave component vanishes in a second order phase transition and we find a superconducting phase with pure d-wave symmetry. In order to illustrate the strong sensitivity of these phases to a variation of the parameter J', we include the curves obtained for $J' = 0.45\,t$, where the s-wave component is already marginally small and confined to small doping concentrations, and the curves for $J' = 0.55\,t$ where we find two second order phase transitions. The pure s-wave phase at small doping evolves over the mixed $s + id$ phase to a pure d-wave phase, as the doping increases. In the lower plot, scans along the J' axes for three different values of the doping,

δ, are shown ($J = 0.5\,t = 0.5\,t'$). Again, we observe the two second order phase transitions mentioned above. At a first critical value, $J'_{cs}(\delta)$, the s-wave component appears and at a second critical value $J'_{cd}(\delta)$ the d-wave component vanishes. We find that always $J'_{cs} < J'_{cd}$ resulting in a mixed phase with with broken time reversal symmetry for intermediate values of J'. The difference $J'_{cd} - J'_{cs} \approx 0.1\,t$ is almost independent of δ, whereas $(J'_{cd} + J'_{cs})/2$ increases slowly but monotonically with the doping concentration. Note that the phase transitions occur relatively near to the isotropic point $J = J' = 0.5\,t = 0.5\,t'$. The obtained phase diagram is shown in the inset.

4.6.2 The inhomogeneously doped bilayer

We have seen in the previous section that applying two different chemical potentials to the legs is harmful for the superconducting phase of a t-J two-leg ladder. The d-wave-like superconducting state of a two-leg ladder has a phase difference of π between the superconducting correlations on the rung dimers and on the legs and corresponds to the s-wave phase of the bilayer. The s-wave phase occurs for strong inter-layer coupling, and it is known that for strong inter-layer coupling the undoped bilayer is a spin liquid, similar to the undoped two-leg ladder [144, 145]. We clearly expect, that two different chemical potentials on the layers repress the s-wave phase, whereas the d-wave phase might not be so strongly affected. Note, that the pairing amplitudes change sign for both the s-wave and the d-wave phase. For the s-wave phase the sign is different for the pairing on the rung and on the layer and for the d-wave phase the sign is different for the pairing on the bonds along the two different directions in the layer. The d-wave phase appears for weak or vanishing interlayer coupling where the undoped bilayer is an antiferromagnet.

In Fig. 4.10, we plot the five different BCS mean-fields Δ' as functions of the difference between the chemical potentials, $\Delta\mu$, for two different values of J' ($\delta = 0.08$). The dotted line corresponds to Δ'_3. The BCS mean-fields on the layers, $\Delta'_{a,*}$, are positive and they are plotted with different line styles. The solid (dashed) lines correspond to the lower (upper) layer and the thin (thick) line correspond to s-wave (d-wave) symmetry. For $J' = J = 0.5\,t' = 0.5\,t$ we start in a mixed $s + id$ phase. Increasing $\Delta\mu$ leads to a splitting of the degenerate BCS mean-fields $\Delta'_{a,d}$ due to the increase (depletion) of the carrier concentration on the lower (upper) leg. The BCS mean-fields $\Delta'_{a,s}$ also split slightly, but much less than the leg BCS mean-fields of Fig. 4.5. Rather

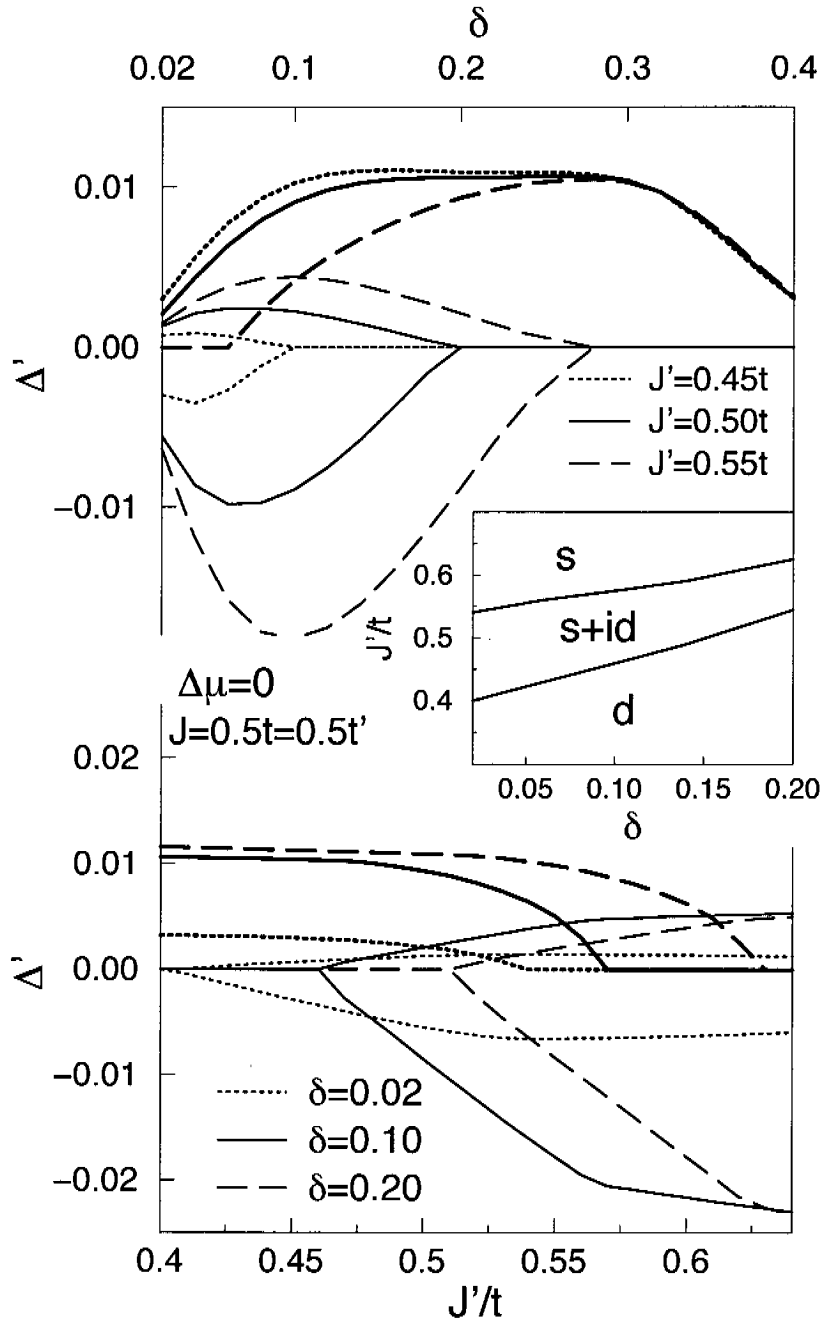

Figure 4.9: The BCS mean-fields Δ' for the symmetric bilayer ($\Delta\mu = 0$). The upper plot scans along the δ axis for fixed values of J' and the lower plot scans along the J' axis for fixed values of δ. The thicker (thiner) positive lines are Δ'_d (Δ'_s) and the negative lines correspond to Δ'_3. The inset shows the resulting phase diagram. $J = 0.5\,t = 0.5\,t'$.

than a splitting, we observe an overall decrease of the correlations with s-wave symmetry. At a critical value of the chemical potential difference, $\Delta\mu_{c,s}$, the s-wave component disappears in a second order phase transition, leading to a state with pure d-wave symmetry. In this state there are still finite pairing correlations on the upper layer, which are also enhanced due to the proximity of the lower layer. Increasing $\Delta\mu$ further we cross another critical value of $\Delta\mu$, where the pairing correlations on the upper layer vanish completely and only the lower layer stays in a superconducting state. This phase we denote by d'. Note, however, that the transition from d to d' is not a real second order phase transition, as there is no symmetry breaking associated to it. Therefore we indicate this transition by a dashed line in the phase diagram.

For $J' = 0.45\,t$, The s-wave component is already marginally small at $\Delta\mu = 0$ (for $\delta = 0.08$) and is suppressed almost immediately by increasing $\Delta\mu$. Comparing the curves of the Δ'_{ad} in the two figures, we observe that the presence of a finite s-component reduces the magnitude of the d-component, but in the d'-phase the curves are identical. Furthermore the value of Δ_{1d} in the d'-phase is considerably larger than the value of Δ_d at $\delta = 0.16$, $J' = 0.45\,t$ in Fig. 4.9. This is due to the fact that in our mean-field calculation, the d'-phase consists of a Heisenberg layer and a doped t-J layer, which are completely decoupled. In the symmetric case, however, we have two doped layers which are coupled by the non vanishing mean-field χ_3 which reduces the pairing correlations.

For larger values of inter-layer exchange coupling, $J' \approx 0.55\,t$ and for small doping, $\delta \approx 0.04$, we find a superconducting phase with pure s-wave symmetry at $\Delta\mu = 0$, as can be seen from Fig. 4.9. Applying different chemical potentials to the layers increases the hole carrier concentration in the lower layer and leads to a second order phase transition at $\Delta\mu_{cd}$, where the d-wave component appears and coexists with the s-wave component. For small doping concentrations and large values of J' the s-wave component decreases monotonically with increasing $\Delta\mu$ but fails to vanish even at very high values of $\Delta\mu$, the situation is similar to the situation illustrated in Fig. 4.5, where a crossover from a phase with strong superconductivity to a phase with weak superconductivity can be observed at low doping concentrations.

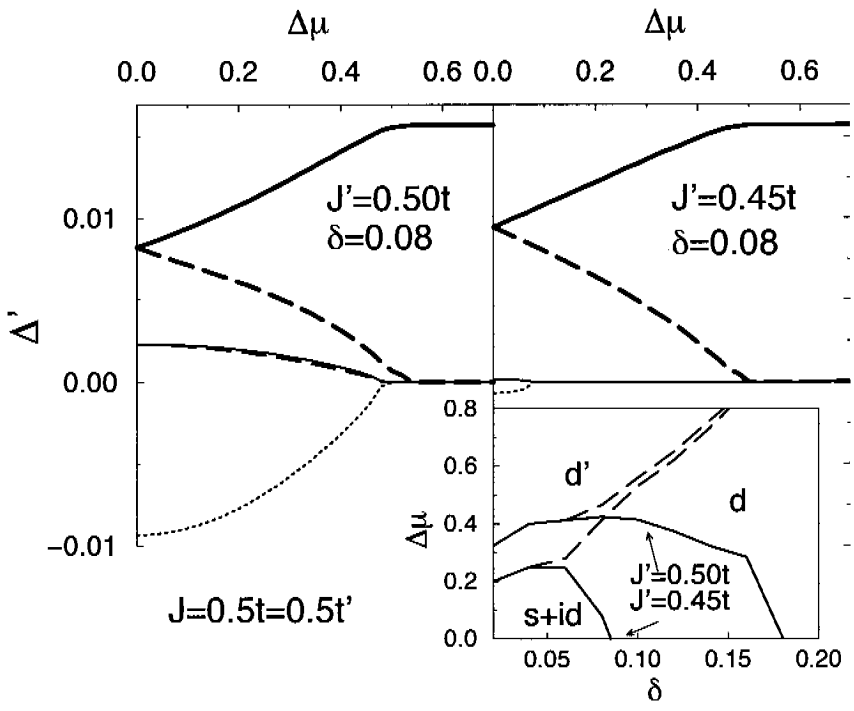

Figure 4.10: The BCS mean-fields Δ' as functions of the difference in the chemical potential, $\Delta\mu$, for $J' = 0.5\,t$ and $J' = 0.45\,t$ at a hole doping $\delta = 0.08$. The thicker (thiner) positive lines have d-wave (s-wave) symmetry and the solid (dashed) lines belong to the lower (upper) layer. The negative lines correspond to Δ'_3. The inset shows the phase diagram. $J = 0.5\,t = 0.5\,t'$.

4.7 Discussion and conclusion

We investigated the stability of the superconducting phases for inhomogeneous doping of the two-leg ladder and the bilayer t-J systems by various approaches which yield qualitatively the same picture.

As anticipated from a strong coupling point of view, where both systems can be considered as doped spin liquids, a chemical potential difference between the legs of the ladder leads to pair-breaking, as could be clearly demonstrated in numerical exact diagonalization of finite systems.

The mean-field analysis based on the spinon-holon decomposition suggests that the imbalanced carrier distribution indeed leads to the suppression of the superconducting state on the doped ladder. Nevertheless, a more differentiated picture emerges. In the low-doping region the RVB state remains stable even

for large differences in the chemical potential and supports a weakly superconducting phase. This RVB phase and the weak superconducting state do not exist for higher doping concentrations above $\delta \approx 0.15$.

The conclusions that can be drawn from the mean-field results for the bilayer are similar to the conclusions for the two-leg ladder, as far as the s-wave superconducting phase is concerned. A new aspect in 2D is the presence of another pairing state with d-wave symmetry. This state having no interlayer pairing amplitudes is only weakly affected by the charge imbalance. Starting from a strong interlayer s-wave pairing it is therefore possible to induce a transition to a d-wave pairing state by an inhomogeneous doping of the layers. Our mean-field calculations predict, that this transition occurs as two second order phase transitions with an intermediate time reversal symmetry breaking phase, where both the s-wave and the d-wave order parameters are finite.

A modified picture is observed in the renormalization group treatment of the weakly interacting Hubbard model on the two-leg ladder. Also here inhomogeneous doping leads to a suppression of the superconducting phase, a Luther-Emery-liquid characterized by one gapless charge mode (C1S0). Moreover, an intermediate phase appears which corresponds to a single channel being superconducting while a coexisting channel forms a Luttinger liquid (C2S1). In both the t-J and the Hubbard model a phase of complete destruction of superconducting fluctuations appears for large enough differences in the chemical potential. Within the renormalization group approach this normal phase is characterized as a single Luttinger liquid state (C1S1). While this identifies the true low-energy properties of this regime, the change in the spinon spectrum discussed in Sec. 4.5 rather reflects a short-coming of the mean-field solution.

In conclusion we emphasize that inhomogeneous doping is harmful for the formation of the superconducting state in the two-leg ladder and for the s-wave superconducting state on the bilayer. Furthermore, inhomogeneous doping of the legs of the ladder or of the layers can be an interesting tool to access new phases for this type of systems.

Chapter 5

Existence of Long Range Magnetic Order in the Ground State of Two-Dimensional Spin-1/2 Heisenberg Antiferromagnets

5.1 Introduction

The first mathematical proof on the existence of long range order (LRO) at low temperature and therefore the existence of a finite temperature phase transition for classical systems with a continuous symmetry group was given by Fröhlich *et al.* in Ref. [146, 147] The central part of their proof lies in the derivation of an upper bound for the continuous part of the two-point function. Soon afterwards, Dyson, Lieb, and Simon (DLS) [148] extended the proof to quantum spin systems, including the antiferromagnetic Heisenberg model with spin larger than 1/2 and dimension larger than 2.

For two-dimensional quantum spin systems with complete spin rotation symmetry there is no LRO at finite temperature based on the Mermin-Wagner-Hohenberg theorem. However, the question whether the ground state has LRO or whether it is disordered by quantum fluctuations is a question which has not been resolved rigorously for all cases.

Nevez and Perez [149, 150] extended the method of DLS to zero-temperature

and proved the existence of LRO for the two-dimensional antiferromagnetic Heisenberg model in the ground state for spin larger than 1/2. Improving the method of DLS further, Kennedy, Lieb, and Shastry (KLS) [151] succeeded in proving the existence of LRO in the ground state of the three-dimensional antiferromagnetic Heisenberg model with spin-1/2. Further, they approached the two-dimensional spin-1/2 case by decreasing the antiferromagnetic coupling in the third dimension. Kubo *et al.* [152] and Ozeki *et al.* [153] studied the spin-1/2 antiferromagnetic XXZ model on the square lattice and showed, that for a large enough as well as for a small enough anisotropy parameter, $\Delta = J_z/J_x$, LRO in the ground state exists. Until now, however, there is no mathematical proof for the existence of LRO in the ground state of the two-dimensional SU(2) symmetric antiferromagnetic Heisenberg model for spin-1/2 on the square lattice. Parreira *et al.* [154] demonstrated that for an antiferromagnet that consists of 8 layers, that are coupled antiferromagnetically and with periodic boundary conditions along the third dimension, LRO exists.

A very interesting and physically very relevant system is the spin-1/2 antiferromagnetic Heisenberg bilayer. A small antiferromagnetic inter-layer coupling tends to stabilize the antiferromagnetic LRO and to reduce the effect of the quantum fluctuations. On the other hand the inter-layer coupling must not be too strong, as in this case local singlets are formed which destroy the antiferromagnetic order and lead to a quantum disordered ground state [144, 145]. Although the rigorous proof of the existence of antiferromagnetic LRO should be easier for the bilayer than for the single layer, it still remains an open problem.

In this chapter, extending the methods introduced by Kennedy *et al.* [151], we will show that already for 4 weakly coupled layers LRO exists in the ground state. Further, we will study two different Heisenberg models on the bilayer lattice. The first one contains in addition to the nearest-neighbor antiferromagnetic couplings also ferromagnetic next-nearest-neighbor (nnn) inter-plane couplings. If these additional couplings are strong enough, we can prove the existence of LRO in the ground state. Finally we will study two antiferromagnetic spin-1/2 layers that are coupled by antiferromagnetic nnn couplings. If the inter-layer and the intra-layer couplings are of about the same strength, the existence of LRO in the ground state can be proven.

5.2 N layers with nearest-neighbor couplings

We study an antiferromagnetic Heisenberg model with nearest-neighbor interactions on the following hypercubic lattice

$$\Lambda = \{\mathbf{a} \in \mathbb{Z}^3 | 1 \leq \alpha_1 \leq L, 1 \leq \alpha_2 \leq L, 1 \leq \alpha_3 \leq N\}, \tag{5.1}$$

where L and N are even numbers, and $|\Lambda| = NL^2$. The Hamiltonian is given by

$$H = \sum_{\mathbf{a}\in\Lambda} (\mathbf{S}_\mathbf{a} \cdot \mathbf{S}_{\mathbf{a}+\delta_1} + \mathbf{S}_\mathbf{a} \cdot \mathbf{S}_{\mathbf{a}+\delta_2} + r\, \mathbf{S}_\mathbf{a} \cdot \mathbf{S}_{\mathbf{a}+\delta_3}) \,. \tag{5.2}$$

The coupling along the third direction can be tuned by the parameter r and periodic boundary conditions are implied in all directions. For every $\mathbf{q} = 2\pi(n_1/L, n_2/L, n_3/N)$ we define the Fourier transformed spin operators

$$S_\mathbf{q} = \frac{1}{\sqrt{|\Lambda|}} \sum_{\mathbf{a}\in\Lambda} \mathrm{e}^{-\mathrm{i}\mathbf{q}\cdot\mathbf{a}} S^z_\mathbf{a}, \qquad S^\pm_\mathbf{q} = \frac{1}{\sqrt{|\Lambda|}} \sum_{\mathbf{a}\in\Lambda} \mathrm{e}^{-\mathrm{i}\mathbf{q}\cdot\mathbf{a}} \left(S^x_\mathbf{a} \pm i S^y_\mathbf{a}\right), \tag{5.3}$$

and write the Hamiltonian as

$$H = \sum_\mathbf{q} E_\mathbf{q} \left[S_{-\mathbf{q}} S_\mathbf{q} + \frac{1}{2} \left(S^+_{-\mathbf{q}} S^-_\mathbf{q} + S^-_{-\mathbf{q}} S^+_\mathbf{q} \right) \right] \tag{5.4}$$

with $E_\mathbf{q} = \cos q_1 + \cos q_2 + r \cos q_3$. The ground state of H is non-degenerate [155] and we denote with $\langle\cdot\rangle$ the expectation value of an operator in this ground state. For the two-point function

$$g_\mathbf{q} = \langle S_{-\mathbf{q}} S_\mathbf{q} \rangle \geq 0 \tag{5.5}$$

the following sum rules hold,

$$\frac{1}{|\Lambda|} \sum_\mathbf{q} g_\mathbf{q} = \frac{S(S+1)}{3} = \frac{1}{4}, \tag{5.6a}$$

$$\frac{1}{|\Lambda|} \sum_\mathbf{q} E_\mathbf{q}\, g_\mathbf{q} = \frac{\langle H \rangle}{3|\Lambda|} = -\frac{e}{3}, \tag{5.6b}$$

where $-e$ is the ground state energy per lattice site. The usual strategy to prove the existence of long-range order in the ground state is to find an upper bound for $g_\mathbf{q}$ for almost all values of $\mathbf{q}$ and then to show that in the thermodynamic limit a finite contribution to the integrals of the sum rules (5.6) must come from the single $\mathbf{q}$ points, where the bound of $g_\mathbf{q}$ is divergent.

The two-point function, $g_{\mathbf{q}}$, can be expressed as an integral over the spectral weight function $R(\omega) = \frac{1}{2}\sum_n (|\langle n|S_{\mathbf{q}}|0\rangle|^2 + |\langle n|S_{-\mathbf{q}}|0\rangle|^2)\,\delta(\omega - E_n + E_0)$, where $|n\rangle$ are eigenstates of H with energy E_n and 0 denotes the ground state. From the Cauchy-Schwarz inequality we obtain

$$g_{\mathbf{q}}^2 = \left[\int_0^\infty \mathrm{d}\omega R(\omega)\right]^2 \leq \underbrace{\left(\int_0^\infty \mathrm{d}\omega R(\omega)\omega\right)}_{\frac{1}{2}\langle[[S_{\mathbf{q}},H],S_{-\mathbf{q}}]\rangle} \underbrace{\left(\int_0^\infty \mathrm{d}\omega R(\omega)\omega^{-1}\right)}_{\chi_{\mathbf{q}}}. \tag{5.7}$$

where $\chi_{\mathbf{q}}$ is the magnetic susceptibility. Using the commutation relations

$$[S_{\mathbf{q}}\,, S^{\pm}_{\mathbf{q}'}] = \pm\frac{1}{\sqrt{|\Lambda|}} S^{\pm}_{\mathbf{q}+\mathbf{q}'} \qquad [S^{+}_{\mathbf{q}}, S^{-}_{\mathbf{q}'}] = \frac{1}{\sqrt{|\Lambda|}} 2S_{\mathbf{q}+\mathbf{q}'} \tag{5.8}$$

we can calculate the double commutator

$$[[S_{\mathbf{q}}, H], S_{-\mathbf{q}}] = \frac{1}{|\Lambda|}\sum_{\mathbf{q}'} (E_{\mathbf{q}-\mathbf{q}'} + E_{\mathbf{q}+\mathbf{q}'} - 2E_{\mathbf{q}'})\,\frac{1}{2}\left(S^{+}_{\mathbf{q}'}S^{-}_{-\mathbf{q}'} + S^{-}_{\mathbf{q}'}S^{+}_{-\mathbf{q}'}\right). \tag{5.9}$$

We introduce now the quantities

$$\rho_l = -\langle \mathbf{S}_{\mathbf{a}} \cdot \mathbf{S}_{\mathbf{a}+\boldsymbol{\delta}_l}\rangle = -\frac{3}{|\Lambda|}\sum_{\mathbf{q}} g_{\mathbf{q}} \cos q_l \qquad l = 1, 3, \tag{5.10}$$

for which the relation

$$e = 2\rho_1 + r\rho_3 \tag{5.11}$$

holds. For the expectation value of the double commutator (5.9) one obtains

$$\frac{1}{2}\langle[[S_{\mathbf{q}}, H], S_{-\mathbf{q}}]\rangle = \frac{2}{3}\left[e - \rho_1(\cos q_1 + \cos q_2) - r\rho_3 \cos q_3\right]. \tag{5.12}$$

Using the reflection positivity of the system, KLS [a] showed that the susceptibility is bounded by

$$\chi_{\mathbf{q}} \leq \frac{1}{4(2 + r + E_{\mathbf{q}})}. \tag{5.13}$$

With (5.7), (5.12), and (5.13) we obtain the upper bound

$$g_{\mathbf{q}} \leq \bar{g}_{\mathbf{q}} = \frac{1}{\sqrt{6}}\left(\frac{e - \rho_1(\cos q_1 + \cos q_2) - r\rho_3 \cos q_3}{2 + r + E_{\mathbf{q}}}\right)^{\frac{1}{2}}. \tag{5.14}$$

[a] Note, that $E^{\tau}_{\mathbf{q}}$ in the notation of KLS corresponds to $2 + r - E_{\mathbf{q}}$ in our notation.

The exact values of the ρ_l are not known. It is possible to derive an upper bound that is bigger than (5.14) but only depends on the energy e [151, 154]. It turns out, however, that the integrals depend quite strongly on the upper bound and therefore we will work directly with the upper bound of Eq. (5.14), which is the best possible bound within this method. Therefore, in order to prove the existence of LRO in the ground state, we must show that for the whole range of possible values of e, ρ_1, and ρ_3 the continuous part of the two-point function $g_{\mathbf{q}}$ cannot be sufficient to fulfill the sum rules (5.6).

The following (Anderson) bound for ρ_l holds (Theorem C.2 of DLS [148]):

$$\rho_l \leq \rho_l^{\max} = \frac{n_l + 2}{4n_l}, \tag{5.15}$$

where n_l is the number of equivalent neighbors. In our case $n_1 = 4$ and n_3 equals 1 for the bilayer and 2 for 4 or more layers in the 3-direction. The absolute value of the energy per site, e, is bounded by

$$e_{\mathrm{N}} \leq e \leq e_{\mathrm{A}} \tag{5.16}$$

where $e_{\mathrm{N}} = (2 + r)/4$ is the Néel bound and e_{A} is the Anderson bound for the ground state energy given by (App. C.1)

$$e_{\mathrm{A}} = \begin{cases} \frac{1}{8}\left(1 + 2r + \sqrt{25 - 8r + 16r^2}\right) & \text{if } N = 2, \\ \frac{1}{8}\left(1 + r + \sqrt{25 + 2r + 9r^2}\right) & \text{if } N > 2. \end{cases} \tag{5.17}$$

With Eq. (5.11), (5.15), and (5.16) we have therefore restricted the possible values of e, ρ_1, and ρ_3 to a finite, two-dimensional parameter space A. To show the existence of LRO in the ground state, we first define the functions

$$a(\alpha) = \lim_{L\to\infty} \frac{1}{|\Lambda|} \sum_{\mathbf{q}\neq\mathbf{Q}} \bar{g}_{\mathbf{q}}\, \theta(\alpha - E_{\mathbf{q}}) - \frac{1}{4} \tag{5.18a}$$

$$b(\alpha) = \lim_{L\to\infty} \frac{1}{|\Lambda|} \sum_{\mathbf{q}\neq\mathbf{Q}} \bar{g}_{\mathbf{q}}\, E_{\mathbf{q}}\, \theta(\alpha - E_{\mathbf{q}}) + \frac{e}{3}, \tag{5.18b}$$

where $\mathbf{Q} = (\pi, \pi, \pi)$ is the antiferromagnetic ordering vector. The system has LRO in the ground state, if for all $(\rho_1, \rho_3) \in A$ either $a(\infty) < 0$, which states the impossibility to fulfill sum rule (5.6a) with the continuous part of $g_{\mathbf{q}}$, or $b(0) > 0$, which states the impossibility to fulfill sum rule (5.6b). If there

are however points in A, where both sum rules can be fulfilled separately, we can still check, for the case where $b(0) < 0 < b(\infty)$, whether it is possible to fulfill both sum rules simultaneously. If there is an $\alpha_0 > 0$ with $b(\alpha_0) = 0$ and $a(\alpha_0) < 0$, it is not possible to fulfill both sum rules simultaneously, because of all functions $g_{\mathbf{q}}$ with $0 \leq g_{\mathbf{q}} \leq \bar{g}_{\mathbf{q}}$ that satisfy (5.6b), the function $g_{\mathbf{q}} = \bar{g}_{\mathbf{q}}\theta(\alpha_0 - E_{\mathbf{q}})$ maximizes the r.h.s. of (5.6a). For further details we refer to KLS [151]. In summary, we can prove the existence of LRO if the condition

$$a(\infty) < 0 \ \vee \ b(0) > 0 \ \vee \ (b(\alpha_0) = 0 \wedge a(\alpha_0) < 0) \qquad \forall(\rho_1, \rho_3) \in A \quad (5.19)$$

is fulfilled. For a given value of r and of N we scanned the entire parameter space A, and we can prove with this method the existence of long-range order for the three-dimensional case if $r \geq 0.14$. If we reduce the number of layers in order to approach the 2-dimensional case, we can rigorously show that for 4 layers with $r \geq 0.16$ we have long-range order. If r is large the 4-layer system consists of weakly coupled square plaquets which in the limit of infinite r form a plaquet singlet state without LRO in the ground state. However, we can show that for 4 (or more) layers and $0.16 \leq r \leq 2.1$ LRO in the ground state exists. For the bilayer system, we were not able to prove the existence of magnetic order for any value of r. This rather abrupt change from 4 to 2 layers is due to the fact that the number of neighboring spins is reduced from 6 to 5 in the bilayer. Attempts to split the sum rule (5.6b) into two separate sum rules for ρ_1 and ρ_3 and to request that all three sum rules should be satisfied simultaneously were still insufficient to prove LRO for the bilayer system. This is somewhat unfortunate, because the bilayer would be a physically more relevant system than the four layer system with periodic boundary conditions. In the next section, however, we show the existence of LRO for a modified bilayer system.

5.3 Antiferromagnetic bilayer with ferromagnetic next-nearest-neighbor coupling

The simplest way to reduce the effects of the quantum fluctuations and to stabilize the antiferromagnetic ground state is to introduce next-nearest-neighbor (nnn) ferromagnetic couplings. It is not possible to apply the methods of reflection positivity to quantum mechanical Heisenberg models with ferromagnetic nearest-neighbor exchange couplings. For example, there is still no rigorous proof, that the ferromagnetic spin-1/2 Heisenberg model on the cubic lattice

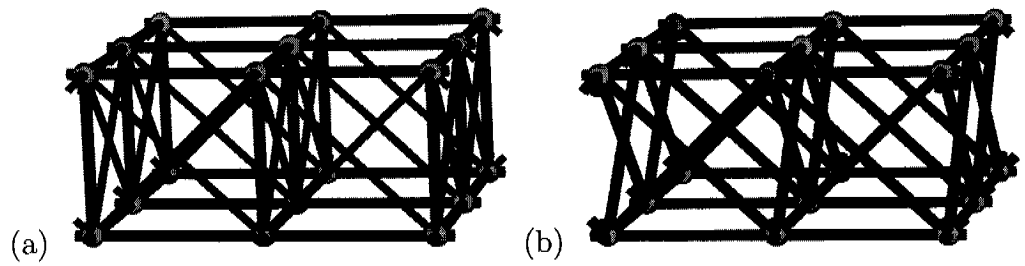

Figure 5.1: (a) The bilayer lattice with antiferromagnetic nearest-neighbor couplings (blue) and ferromagnetic nnn inter-plane couplings (red). (b) The bilayer lattice with antiferromagnetic inplane nearest-neighbor couplings and antiferromagnetic nnn inter-plane couplings.

has a finite temperature phase transition. However, in this section we will show that the method of reflection positivity can be applied on hypercubic lattices with ferromagnetic nnn Heisenberg couplings, if strong enough antiferromagnetic nearest-neighbor couplings are present. It is for example possible to apply the method of reflection positivity to the famous J_1-J_2 model on the square lattice with $0 \leq -J_2 \leq J_1/2$. However, it turns out, that also the addition of the diagonal ferromagnetic couplings does not allow to prove LRO in the ground state.

In the following we study a spin-1/2 antiferromagnetic Heisenberg model on the bilayer with ferromagnetic next-nearest-neighbor inter-layer couplings as shown in Fig. 5.1 (a) with the Hamiltonian

$$H = \sum_{\mathbf{a}\in\Lambda} \left[\frac{1}{2}\, \mathbf{S}_{\mathbf{a}} \cdot \mathbf{S}_{\mathbf{a}+\boldsymbol{\delta}_3} + \sum_{j=1}^{2} \mathbf{S}_{\mathbf{a}} \cdot \left(\mathbf{S}_{\mathbf{a}+\boldsymbol{\delta}_j} - r\, \mathbf{S}_{\mathbf{a}+\boldsymbol{\delta}_j+\boldsymbol{\delta}_3} \right) \right]. \tag{5.20}$$

Note that the sum over $\mathbf{a}$ runs over all lattice sites. We use periodic boundary conditions and therefore the coupling along $\boldsymbol{\delta}_3$ is also 1. Further, we assume $0 \leq r \leq 1/4$ for the ferromagnetic coupling between the layers. With the definition (5.3) we can write H in the form (5.4) with $E_{\mathbf{q}}$ given by

$$E_{\mathbf{q}} = (1 - r\cos q_3)(\cos q_1 + \cos q_2) + \frac{1}{2}\cos q_3. \tag{5.21}$$

For the expectation value of the double commutator (5.9) one obtains

$$D_{\mathbf{q}} := \frac{1}{2}\langle[[S_{\mathbf{q}}, H], S_{-\mathbf{q}}]\rangle = \frac{\rho_3}{3}(1-\cos q_3) + \frac{2}{3}\sum_{j=1}^{2}\rho_1(1-\cos q_j) \quad (5.22)$$
$$+\frac{2}{3}\sum_{j=1}^{2} r\rho_{\mathrm{d}}(1-\cos q_j \cos q_3),$$

with ρ_l defined as in (5.10) and with

$$\rho_{\mathrm{d}} = \langle \mathbf{S_a} \cdot \mathbf{S_{a+\delta_j+\delta_3}}\rangle = \frac{3}{|\Lambda|}\sum_{\mathbf{q}} g_{\mathbf{q}} \cos q_j \cos q_3. \quad (5.23)$$

Further, we have the relation

$$e = \frac{1}{2}(4\rho_1 + \rho_3 + 4r\rho_{\mathrm{d}}), \quad (5.24)$$

and $-e$ is the ground state energy per lattice site.

We derive now an upper bound for the susceptibility. The first step is to apply the unitary transformation, that rotates all the spins on a sublattice by π around the y axes, i.e., we obtain new spin operators $\mathbf{T_a}$ that are related to the original spin operators $\mathbf{S_a}$ by

$$T^x_{\mathbf{a}} = e^{i\mathbf{Q}\cdot\mathbf{a}} S^x_{\mathbf{a}}, \qquad T^y_{\mathbf{a}} = S^y_{\mathbf{a}}, \qquad T^z_{\mathbf{a}} = e^{i\mathbf{Q}\cdot\mathbf{a}} S^z_{\mathbf{a}}, \quad (5.25)$$

where $\mathbf{Q} = (\pi, \pi, \pi)$ as before.

We want to use the reflection symmetries of the lattice in order to derive an upper bound for the susceptibility. For every pair of parallel planes that separate the lattice Λ into two equal subsystems the Hilbert space is the direct product of the two Hilbert spaces associated with the two subsystem, $\mathcal{H} = \mathcal{H}_1 \otimes \mathcal{H}_1$. The reflection at the two planes allows to associate to each operator $A \otimes 1 := \mathcal{A}$ an operator $1 \otimes A := \tilde{\mathcal{A}}$. The Lemma 6.1 of DLS [148], in the zero-temperature limit, states that the ground state energy of the Hamiltonian

$$H(h_i) = \mathcal{A} + \tilde{\mathcal{B}} + \sum_i (\mathcal{C}_i - \tilde{\mathcal{C}}_i - h_i)^2 - \sum_j (\mathcal{D}_j - \tilde{\mathcal{D}}_j)^2 \quad (5.26)$$

is bigger than the averaged ground state energy of the Hamiltonians

$$H_{\mathcal{A}} = \mathcal{A} + \tilde{\mathcal{A}} + \sum_i (\mathcal{C}_i - \tilde{\mathcal{C}}_i)^2 - \sum_j (\mathcal{D}_j - \tilde{\mathcal{D}}_j)^2 \quad (5.27a)$$

$$H_{\mathcal{B}} = \mathcal{B} + \tilde{\mathcal{B}} + \sum_i (\mathcal{C}_i - \tilde{\mathcal{C}}_i)^2 - \sum_j (\mathcal{D}_j - \tilde{\mathcal{D}}_j)^2, \quad (5.27b)$$

i.e.,

$$E[H(h_i)] \geq (E[H_{\mathcal{A}}] + E[H_{\mathcal{B}}])/2, \tag{5.28}$$

where $E[H]$ denotes the ground state energy of the Hamiltonian H. In (5.26) and (5.27) $\mathcal{A}$, $\tilde{\mathcal{B}}$ are self-adjoint operators, $\mathcal{C}_i$ are *real* self-adjoint operators and $\mathcal{D}_j$ are *imaginary* self-adjoint operators. Further, h_i are real numbers. We decompose the Hamiltonian (5.20) into the three terms $H = H_x + H_y + H_z$. The Hamiltonian H_y can up to constant terms be written as

$$\begin{aligned} H_y \;=\; \sum_{\mathbf{a}\in\Lambda} \Bigg[& -\frac{1-4r}{4}\left(T^y_{\mathbf{a}} - T^y_{\mathbf{a}+\boldsymbol{\delta}_3}\right)^2 - \frac{1-r}{2}\sum_{j=1}^{2}\left(T^y_{\mathbf{a}} - T^y_{\mathbf{a}+\boldsymbol{\delta}_j}\right)^2 \\ & - \frac{r}{4}\sum_{j=1}^{2}\left(T^y_{\mathbf{a}} - T^y_{\mathbf{a}+\boldsymbol{\delta}_j} - T^y_{\mathbf{a}+\boldsymbol{\delta}_3} + T^y_{\mathbf{a}+\boldsymbol{\delta}_j+\boldsymbol{\delta}_3}\right)^2 \Bigg], \end{aligned} \tag{5.29}$$

which is of the form (5.26) for all symmetry planes of the bilayer that contain no lattice sites. Note, that in our notation $T^y_{\mathbf{a}}$ are imaginary operators. The terms H^x and H^z, containing the real operators $T^x_{\mathbf{a}}$ and $T^z_{\mathbf{a}}$, can not be written in the form required by (5.26) for all symmetry planes of the bilayer. However, we can define the Hamiltonians

$$\begin{aligned} H^\nu_z(h_{\mathbf{a}}) \;=\; \sum_{\mathbf{a}\in\Lambda} \Bigg[& +\frac{1-4\nu r}{4}\left(T^z_{\mathbf{a}} - T^z_{\mathbf{a}+\boldsymbol{\delta}_3} - \delta_{\nu,+}h_{\mathbf{a},3}\right)^2 \\ & + \frac{1+\nu r}{2}\sum_{j=1}^{2}\left(T^z_{\mathbf{a}} - T^z_{\mathbf{a}+\boldsymbol{\delta}_j} - \delta_{\nu,-}h_{\mathbf{a},j}\right)^2 \\ & + \frac{r}{4}\sum_{j=1}^{2}\left(T^z_{\mathbf{a}} + \nu T^z_{\mathbf{a}+\boldsymbol{\delta}_j} - \nu T^z_{\mathbf{a}+\boldsymbol{\delta}_3} - T^z_{\mathbf{a}+\boldsymbol{\delta}_j+\boldsymbol{\delta}_3} - d^\nu_{\mathbf{a},j}\right)^2 \Bigg], \end{aligned} \tag{5.30}$$

with $\nu = \pm 1$, δ is the Kronecker symbol, and

$$h_{\mathbf{a},l} \;=\; h_{\mathbf{a}} - h_{\mathbf{a}+\boldsymbol{\delta}_l} \qquad l = 1,2,3, \tag{5.31a}$$

$$d^\nu_{\mathbf{a},j} \;=\; h_{\mathbf{a}} + \nu h_{\mathbf{a}+\boldsymbol{\delta}_j} - \nu h_{\mathbf{a}+\boldsymbol{\delta}_3} - h_{\mathbf{a}+\boldsymbol{\delta}_j+\boldsymbol{\delta}_3}, \tag{5.31b}$$

where $h_{\mathbf{a}}$ is a real valued function on the lattice. Note that that H^+_ν is of the form (5.26) for the symmetry planes perpendicular to $\boldsymbol{\delta}_3$, whereas H^-_ν is of the form (5.26) for all symmetry planes parallel to $\boldsymbol{\delta}_3$. In an analogous way we define H^ν_x by replacing z with x and and setting $h_{\mathbf{a}} = 0$ in (5.30) and finally, we define

$$H^\nu(h_{\mathbf{a}}) = H^\nu_x + H_y + H^\nu_z(h_{\mathbf{a}}) \qquad \nu = \pm. \tag{5.32}$$

For $h_{\mathbf{a}} = 0$ both Hamiltonians $H^{\pm}(0)$ are up to constant terms equal to the original Hamiltonian H. From (5.28) it follows that (App. C.2)

$$E[H^{\nu}(h_{\mathbf{a}})] \geq E[H^{\nu}(0)] \quad \text{for} \quad \nu = \pm. \tag{5.33}$$

The next step is to calculate $E[H^{\nu}(h_{\mathbf{a}})]$ in second order perturbation theory in $h_{\mathbf{a}}$. The linear terms in $H^{\nu}(h_{\mathbf{a}})$ are given by

$$\begin{aligned} V^{\nu}(h_{\mathbf{a}}) \;=\; \sum_{\mathbf{a}\in\Lambda} T^z_{\mathbf{a}} \Big[& \frac{\delta_{\nu,+}}{2}\Big(h_{\mathbf{a}-\boldsymbol{\delta}_3,3} - h_{\mathbf{a},3}\Big) + \delta_{\nu,-} \sum_{j=1}^{2} \Big(h_{\mathbf{a}-\boldsymbol{\delta}_j,j} - h_{\mathbf{a},j}\Big) \\ & -2r\delta_{\nu,-}\Big(h_{\mathbf{a}+\boldsymbol{\delta}_3} + h_{\mathbf{a}-\boldsymbol{\delta}_3}\Big) - r\delta_{\nu,+} \sum_{j=1}^{2} \Big(h_{\mathbf{a}+\boldsymbol{\delta}_j} + h_{\mathbf{a}+\boldsymbol{\delta}_j}\Big) \\ & + \sum_{j=1}^{2} \frac{r}{2}\Big(h_{\mathbf{a}+\boldsymbol{\delta}_j+\boldsymbol{\delta}_3} + h_{\mathbf{a}+\boldsymbol{\delta}_j-\boldsymbol{\delta}_3} + h_{\mathbf{a}-\boldsymbol{\delta}_j+\boldsymbol{\delta}_3} + h_{\mathbf{a}-\boldsymbol{\delta}_j-\boldsymbol{\delta}_3}\Big)\Big]. \end{aligned} \tag{5.34}$$

Choosing $h_{\mathbf{a}}$ as

$$c_{\mathbf{a}} = \cos(\mathbf{q}\cdot\mathbf{a})/\sqrt{|\Lambda|} \qquad s_{\mathbf{a}} = \sin(\mathbf{q}\cdot\mathbf{a})/\sqrt{|\Lambda|} \tag{5.35}$$

we obtain with (5.3)

$$V^{\nu}(c_{\mathbf{a}}) = -(T_{\mathbf{q}} + T_{-\mathbf{q}})f^{\nu}_{\mathbf{q}}, \qquad V^{\nu}(s_{\mathbf{a}}) = -i(T_{\mathbf{q}} - T_{-\mathbf{q}})f^{\nu}_{\mathbf{q}}, \tag{5.36}$$

with $T_{\mathbf{q}} = S_{\mathbf{q}+\mathbf{Q}}$ and

$$f^{+}_{\mathbf{q}} = (1-\cos q_3)(1/2 + r\cos q_1 + r\cos q_2), \tag{5.37a}$$

$$f^{-}_{\mathbf{q}} = (2-\cos q_1 - \cos q_2)(1 + r\cos q_3). \tag{5.37b}$$

The quadratic terms in the Hamiltonian (5.30) are given by

$$q^{\nu}(h_{\mathbf{a}}) = \frac{1-4r}{4}\delta_{\nu,+}\, h^2_{\mathbf{a},3} + \sum_{j=1}^{2}\Big(\frac{1-r}{2}\delta_{\nu,-}\, h^2_{\mathbf{a},j} + \frac{r}{4}(d^{\nu}_{\mathbf{a},j})^2\Big), \tag{5.38}$$

and for the fields $c_{\mathbf{a}}$ and $s_{\mathbf{a}}$ we find the relation

$$q^{\nu}(c_{\mathbf{a}}) + q^{\nu}(s_{\mathbf{a}}) = f^{\nu}_{\mathbf{q}} \quad \text{for} \quad \nu = \pm. \tag{5.39}$$

Applying second order perturbation theory in $s_{\mathbf{a}}$ and $c_{\mathbf{a}}$ and summing up all second order terms, we obtain from (5.33) the inequality

$$0 \leq f^{\nu}_{\mathbf{q}} + 4(f^{\nu}_{\mathbf{q}})^2 \underbrace{\frac{1}{2}\sum_{n\neq 0} \frac{|\langle n|T_{\mathbf{q}}|0\rangle|^2 + |\langle n|T_{-\mathbf{q}}|0\rangle|^2}{E_0 - E_n}}_{-\chi_{\mathbf{q}+\mathbf{Q}}} \tag{5.40}$$

which yields the following upper bound for the susceptibility

$$\chi_{\mathbf{q}} \leq \bar{\chi}_{\mathbf{q}} = \min_{\nu} \frac{1}{4f^{\nu}_{\mathbf{q}+\mathbf{Q}}}. \tag{5.41}$$

With (5.7), (5.22) and (5.41) we obtain an upper bound for $g_{\mathbf{q}}$

$$g_{\mathbf{q}} \leq \bar{g}_{\mathbf{q}} = \sqrt{D_{\mathbf{q}}\bar{\chi}_{\mathbf{q}}}. \tag{5.42}$$

In order to use this upper bound we need bounds for the expectation values ρ_1, ρ_3, ρ_{d} and for the energy e. We find the following bounds:

$$\begin{aligned}
(5+4r)/8 \;\leq\; & e & \leq\; (7+4r)/8 & \quad (5.43a)\\
1/8 \;\leq\; & \rho_1 & \leq\; 3/8 & \quad (5.43b)\\
0 \;\leq\; & \rho_3 & \leq\; 3/4 & \quad (5.43c)\\
0 \;\leq\; & \rho_{\mathrm{d}} & \leq\; 1/4 & \quad (5.43d)
\end{aligned}$$

Note, that all the ground state expectation values of ρ_1, ρ_3, and ρ_{d} (cf. (5.10) and (5.23)) must be positive, because all off-diagonal matrix elements in the eigenbasis of the $T^z_{\mathbf{a}}$ operators are negative. From $\langle \mathbf{S}_i \cdot \mathbf{S}_j \rangle \leq 1/4$ follows the r.h.s. of (5.43d). From $-\langle \mathbf{S}_i \cdot \mathbf{S}_j \rangle \leq 3/4$ follows the r.h.s. of (5.43c). From (5.15) with $n_l = 4$ follows the r.h.s. of (5.43b) and the r.h.s. of (5.43a) follows from (5.24), from the Anderson bound (5.15) with $n_l = 5$ and from the r.h.s. of (5.43d). The l.h.s. of (5.43a) comes from the Néel state. The l.h.s. of (5.43b) follows from (5.24), the l.h.s. of (5.43a), and the r.h.s. of (5.43c) and (5.43d). Now, we can again define the functions (5.18) and use the condition (5.19) to prove LRO. In fact for $0.21 \leq r \leq 0.25$ we can prove LRO by scanning the whole three-dimensional parameter space $A \ni (\rho_1, \rho_3, \rho_{\mathrm{d}})$ defined by the equations (5.43). Note, that our method requires $r < 0.25$. It is however easy to prove the existence of LRO for $r = \infty$,[b] where the systems consists of two antiferromagnetically coupled classical spins. This gives us good reasons to believe, that the systems will have LRO in the ground state for all values of $r \geq 0.21$.

[b] Denoting by S^z_{A} (S^z_{B}) the z-component of the total spin operator on sublattice A (B), we have $\langle g_{\mathbf{Q}} \rangle = \langle \frac{1}{|\Lambda|}(S^z_{\mathrm{A}} - S^z_{\mathrm{B}})^2 \rangle = (2\langle (S^z_{\mathrm{A}})^2 \rangle + 2\langle (S^z_{\mathrm{B}})^2 \rangle - \langle S^z_{\mathrm{tot}} \rangle)/|\Lambda|$. As in the ground state $S^z_{\mathrm{tot}} = 0$, and for large r we have $\lim_{r\to\infty}\langle (S^z_{\mathrm{A}})^2 \rangle = \lim_{r\to\infty}\langle \mathbf{S}^2_{\mathrm{A}} \rangle/3 = (|\Lambda|/4)[(|\Lambda|/4)+1]/3$ and the same for $\langle (S^z_{\mathrm{B}})^2 \rangle$, we find therefore $\lim_{r\to\infty}\langle g_{\mathbf{Q}} \rangle = |\Lambda|/12 + \mathcal{O}(1)$.

5.4 Diagonal bilayer

In Sec. 5.2 we saw, that it is difficult to prove LRO on the bilayer for antiferromagnetic rung coupling. On the other hand we know, that for infinitely strong ferromagnetic rung coupling, the bilayer reduces to a square lattice of spin-1 moments, for which the existence of LRO in the ground state has been rigorously established [151]. Therefore, an alternative way to approach the spin-1/2 square lattice would be to reduce the ferromagnetic rung couplings to finite values. But it is not possible to apply the ideas of reflection positivity to quantum Heisenberg models with ferromagnetic nearest-neighbor couplings.[c] It is possible to mimic the ferromagnetic rung coupling by nnn antiferromagnetic couplings and Kishi and Kubo found a way to prove LRO in frustrated systems with antiferromagnetic nearest- and next-nearest-neighbor couplings [156].

Motivated by these ideas we consider in this section the spin-1/2 bilayer with the following antiferromagnetic Hamiltonian

$$H = \sum_{\mathbf{a}\in\Lambda} \sum_{j=1}^{2} \left(\mathbf{S}_{\mathbf{a}} \cdot \mathbf{S}_{\mathbf{a}+\delta_j} + r\, \mathbf{S}_{\mathbf{a}} \cdot \mathbf{S}_{\mathbf{a}+\delta_j+\delta_3} \right). \tag{5.44}$$

The two layers are connected in a diagonal way by antiferromagnetic couplings as shown in Fig. 5.1 (b) but they are not connected by perpendicular couplings. For $r = 1$ this Hamiltonian depends only on the operators $\mathbf{S}_{\mathbf{a},+} = \mathbf{S}_{\mathbf{a}} + \mathbf{S}_{\mathbf{a}+\delta_3}$. Therefore the operators $\mathbf{S}^2_{\mathbf{a},+}$ commute with the Hamiltonian H and therefore the eigenstates of H can be chosen to be eigenstates of $\mathbf{S}^2_{\mathbf{a},+}$, too. Alternatively, one can consider the unitary transformations $\mathcal{S}_{\mathbf{a}}$, that exchange the sites on the rung $\mathbf{a}$. For $r = 1$ these are symmetries of the Hamiltonian and the parity of this local reflection is related to the eigenvalues of $\mathbf{S}^2_{\mathbf{a},+}$.

It is easy to see that in the ground state the eigenvalue of each $\mathbf{S}^2_{\mathbf{a},+}$ must be 2, i.e., the two spins must form a spin-1 moment.[d] We can reduce therefore the

[c] In order to apply the methods of reflection positivity, we should write the Hamiltonian in the form (5.26). For the antiferromagnet we can apply local unitary transformations which change the sign of S^x and S^z. There is however no unitary transformation on $\mathbb{C}^2$, which only changes the sign of S^y, and such a transformation would be needed in the ferromagnetic case.

[d] Let us assume that the ground state is in the sector with $S^2_{\mathbf{a},+} = 0$. In this case we can write the wave function in the form $|\psi_0\rangle = |s_{\mathbf{a}}\rangle \otimes |\psi'\rangle$, where $s_{\mathbf{a}}$ stands for a singlet at site $\mathbf{a}$. However, the wave function $|\psi_1\rangle = |t^0_{\mathbf{a}}\rangle \otimes |\psi'\rangle$ has the same expectation value of the Hamiltonian and lies in a different sector of the Hilbert space. We know that the ground state is not degenerate [155] and therefore $|\psi_0\rangle$ can not be the ground state.

Hilbert space to the subspace where $\mathbf{S}^2_{\mathbf{a},+} = 2$ for all $\mathbf{a}$. Within this subspace, the problem is equivalent to a $S = 1$ Heisenberg model on the square lattice, which is known to have long range order [151].

For $r = 1$ the Hamiltonian H is effectively a spin-1 and not a spin-1/2 Hamiltonian, but we will now show that also for $r < 1$ LRO exists, and that the existence of LRO is not restricted to the case where effective spin-1 moments are present. For $r = 0$ our model describes two independent spin-1/2 square lattices. In this sense, we can interpolate with our model between the spin-1 and the spin-1/2 case.

The strategy of the proof is again to derive an upper bound for $g_{\mathbf{q}}$ for almost all values of $\mathbf{q}$ using the inequality (5.7). The double commutator is straightforward to calculate and is given by

$$\frac{1}{2}\langle[[S_{\mathbf{q}}, H], S_{-\mathbf{q}}]\rangle = \frac{2}{3}\left[e - (\rho_1 + r\rho_{\mathrm{d}}\cos q_3)(\cos q_1 + \cos q_2)\right], \tag{5.45}$$

where $\rho_{\mathrm{d}} = -\langle \mathbf{S}_{\mathbf{a}} \cdot \mathbf{S}_{\mathbf{a}+\boldsymbol{\delta}_1+\boldsymbol{\delta}_3}\rangle$ and $e = 2(\rho_1 + r\rho_{\mathrm{d}})$. To find an upper bound for the susceptibility we rotate all the spins on one sublattice by π around the y-axis. With this unitary transformation the local spin operators $(S^x_{\mathbf{a}}, S^y_{\mathbf{a}}, S^z_{\mathbf{a}})$ transform to the new spin operators $(T^x_{\mathbf{a}}, iT^y_{\mathbf{a}}, T^z_{\mathbf{a}})$, given by

$$T^x_{\mathbf{a}} = e^{i\mathbf{Q}\cdot\mathbf{a}}S^x_{\mathbf{a}} \qquad iT^y_{\mathbf{a}} = S^y_{\mathbf{a}} \qquad T^z_{\mathbf{a}} = e^{i\mathbf{Q}\cdot\mathbf{a}}S^z_{\mathbf{a}}, \tag{5.46}$$

where $\mathbf{Q} = (\pi, \pi, 0)$. We define the Hamiltonian

$$\begin{aligned} H(h_{\mathbf{a}}) \;=\; & \frac{1}{2}\sum_{\mathbf{a}}\sum_{j=1}^{2}\Big[(1-r)\Big(\mathbf{T}_{\mathbf{a}} - \mathbf{T}_{\mathbf{a}+\boldsymbol{\delta}_j} - \mathbf{h}^{(1)}_{\mathbf{a},j}\Big)^2 + r\Big(\mathbf{T}_{\mathbf{a}} - \mathbf{T}_{\mathbf{a}+\boldsymbol{\delta}_3}\Big)^2 \\ & + \frac{r}{2}\Big(\mathbf{T}_{\mathbf{a}} + \mathbf{T}_{\mathbf{a}+\boldsymbol{\delta}_3} - \mathbf{T}_{\mathbf{a}+\boldsymbol{\delta}_j} - \mathbf{T}_{\mathbf{a}+\boldsymbol{\delta}_3+\boldsymbol{\delta}_j} - \mathbf{h}^{(2)}_{\mathbf{a},j}\Big)^2\Big] \end{aligned} \tag{5.47}$$

with $\mathbf{h}^{(l)}_{\mathbf{a},j} = (0, 0, h^{(l)}_{\mathbf{a},j})$. This Hamiltonian is of the form (5.26) for all pairs of symmetry planes parallel to $\boldsymbol{\delta}_3$. Using (5.28) and the same arguments as in Appendix C.2, we can show that

$$E[H(h_{\mathbf{a}})] \geq E[H(0)], \tag{5.48}$$

where $E[H(h_{\mathbf{a}})]$ denotes the ground state energy of the Hamiltonian $H(h_{\mathbf{a}})$. Note that the Hamiltonian $H(0)$, i.e., the Hamiltonian (5.47) with all $h^{(l)}_{\mathbf{a},j} = 0$, is up to a constant term equal to the Hamiltonian H in (5.44).

We now calculate the terms in $E[H(h_{\mathbf{a}})]$ that are quadratic in the fields for the following specific choice of the fields

$$h^{(1)}_{\mathbf{a},j} = h_{\mathbf{a}} - h_{\mathbf{a}+\boldsymbol{\delta}_j} \qquad h^{(2)}_{\mathbf{a},j} = h_{\mathbf{a}} + h_{\mathbf{a}+\boldsymbol{\delta}_3} - h_{\mathbf{a}+\boldsymbol{\delta}_j} - h_{\mathbf{a}+\boldsymbol{\delta}_3+\boldsymbol{\delta}_j}.$$

The linear terms in $H(h_{\mathbf{a}})$ are given by

$$\begin{aligned} V(h_{\mathbf{a}}) \;=\; \sum_{\mathbf{a},j} T^z_{\mathbf{a}} \Big[& (h_{\mathbf{a}+\boldsymbol{\delta}_j} + h_{\mathbf{a}-\boldsymbol{\delta}_j} - 2h_{\mathbf{a}}) - r(h_{\mathbf{a}+\boldsymbol{\delta}_3} + h_{\mathbf{a}-\boldsymbol{\delta}_3}) \\ & + \frac{r}{2}(h_{\mathbf{a}+\boldsymbol{\delta}_3+\boldsymbol{\delta}_j} + h_{\mathbf{a}+\boldsymbol{\delta}_3-\boldsymbol{\delta}_j} + h_{\mathbf{a}-\boldsymbol{\delta}_3+\boldsymbol{\delta}_j} + h_{\mathbf{a}-\boldsymbol{\delta}_3-\boldsymbol{\delta}_j}) \Big], \end{aligned} \tag{5.49}$$

and choosing $c_{\mathbf{a}}$ and $s_{\mathbf{a}}$ as in (5.35) we obtain $V(c_{\mathbf{a}}) = -(T_{\mathbf{q}} + T_{-\mathbf{q}})f_{\mathbf{q}}$ and $V(s_{\mathbf{a}}) = -\mathrm{i}(T_{\mathbf{q}} - T_{-\mathbf{q}})f_{\mathbf{q}}$ with $T_{\mathbf{q}} = S_{\mathbf{q}+\mathbf{Q}}$ and with

$$f_{\mathbf{q}} = \sum_{j=1}^{2} (1 - \cos q_j)(1 + r\cos q_3). \tag{5.50}$$

The quadratic part of $H(h_{\mathbf{a}})$ is given by

$$q(h_{\mathbf{a}}) = \frac{1}{2}\sum_{\mathbf{a},j} (1-r)\left(h_{\mathbf{a}} - h_{\mathbf{a}+\boldsymbol{\delta}_j}\right)^2 + \frac{r}{2}\left(h_{\mathbf{a}} + h_{\mathbf{a}+\boldsymbol{\delta}_3} - h_{\mathbf{a}+\boldsymbol{\delta}_j} - h_{\mathbf{a}+\boldsymbol{\delta}_3+\boldsymbol{\delta}_j}\right)^2, \tag{5.51}$$

and we have the relation $q(s_{\mathbf{a}}) + q(c_{\mathbf{a}}) = f_{\mathbf{q}}$. Applying second order perturbation theory in $s_{\mathbf{a}}$ and $c_{\mathbf{a}}$ and summing up all second order terms, we find again the inequality (5.40) (without the ν index) which is equivalent to $\chi_{\mathbf{q}} \leq 1/(4f_{\mathbf{q}+\mathbf{Q}})$. Finally, we obtain with Eq. (5.7) and Eq. (5.45) the upper bound

$$g_{\mathbf{q}} \leq \sqrt{e}\, b^{\lambda}_{\mathbf{q}} = \sqrt{e}\left(\frac{2 + 2\lambda r - (1 + \lambda r\cos q_3)(\cos q_1 + \cos q_2)}{12(1+\lambda r) f_{\mathbf{q}+\mathbf{Q}}}\right)^{\frac{1}{2}} \tag{5.52}$$

with $\rho_{\mathrm{d}} = \lambda\rho_1$. Note, that this upper bound diverges at the two $\mathbf{q}$ values $\mathbf{Q} = (\pi, \pi, 0)$ and $\mathbf{Q}' = (\pi, \pi, \pi)$. The divergence of the magnetic susceptibility at the point $\mathbf{Q}$ is expected for our system. That the bound for the magnetic susceptibility is also divergent at $\mathbf{Q}'$ is due to the fact, that in the derivation of Eq. (5.52) only reflection planes parallel to $\boldsymbol{\delta}_3$ but not the plane perpendicular to $\boldsymbol{\delta}_3$ could be used.

From the sum rule (5.6b) we can deduce, that the diagonal bilayer has LRO in the ground state, if for all possible values of λ we have

$$\lim_{L\to\infty} \frac{1}{|\Lambda|} \sum_{\mathbf{q}\neq\mathbf{Q},\mathbf{Q}'} b^{\lambda}_{\mathbf{q}} (-E_{\mathbf{q}})_+ < \frac{\sqrt{e_N}}{3} = \frac{\sqrt{1+r}}{3\sqrt{2}}, \tag{5.53}$$

with $E_{\mathbf{q}} = (\cos q_1 + \cos q_2)(1 + r \cos q_3)$. It is clear that for $r \leq 1$ we must have $0 \leq \lambda \leq 1$.[e] But in addition we have the inequality $e_N < 2(1 + \lambda r)\rho_1^{\max}$ which gives us with $\rho_1^{\max}$ from (5.15) the following range of possible values of λ

$$\max(0, (2r - 1)/3r) \leq \lambda \leq 1. \tag{5.54}$$

The numerical evaluation of the integral (5.53) for the whole range of possible values of λ shows that we have LRO for $r \geq 0.85$. Note, that for $r = 1$ we have $\lambda = 1$ and a flat band with $E_{\mathbf{q}} = 0$. In this case the condition (5.53) for LRO reduces to the condition for a spin-1 system on the square lattice.

5.5 Discussion and conclusion

We extended the method of DLS and KLS for proving the existence of antiferromagnetic LRO, by scanning not only the whole possible energy range (e), like in the work of KLS, but also scanning all possible ratios between the Heisenberg terms (ρ_l) on non-equivalent bonds. In this way we could show antiferromagnetic LRO for various two-dimensional spin-1/2 Heisenberg models.

We approached the two-dimensional Heisenberg model on the square lattice in two different ways:

First, we started from the three-dimensional spin-1/2 antiferromagnet and then reduced both the number of layers in the third dimension and the coupling along this direction. For 4 layers, only a weak inter-layer coupling ($r = 0.16$) is required for proving LRO, but for the bilayer, where the number of nearest-neighbors is reduced to 5, the current method fails to show the existence of LRO.

Further, we could show that the antiferromagnetic bilayer with small ferromagnetic diagonal couplings ($r \geq 0.21$) between the layers has LRO in the ground state. One can view this as approaching the quantum mechanical two-dimensional case from the classical zero-dimensional case, as for very large ferromagnetic couplings the system reduces to two antiferromagnetically coupled classical spins.

Finally, we approached the single layer spin-1/2 antiferromagnetic Heisenberg model on the square lattice by starting from an effective spin-1 antiferro-

[e] This follows from the operation $\mathcal{S} = \prod_{e^{\mathbf{Q}\cdot\mathbf{a}}=1} \mathcal{S}_{\mathbf{a}}$ that exchanges the two sites for every rung with $e^{\mathbf{Q}\cdot\mathbf{a}} = 1$. With this operation the bonds with coupling r are mapped on bonds with coupling 1 and vice versa. For $r < 1$, we must have $\lambda \leq 1$ in the ground state, because otherwise we could apply $\mathcal{S}$ to the ground state and obtain a state with lower energy.

magnetic Heisenberg model on the square lattice, that consists of two diagonally coupled layers. Here, the inter-layer coupling strength $r \in [0, 1]$ interpolates continuously between spin-1/2 and spin-1 square lattice Heisenberg models. We showed that for $r \geq 0.85$ there exists LRO in the ground state.

We believe that there is space for improvement of the present ranges of validity by further extensions of the method of "Gaussian domination". Indeed our analysis shows that the bilayer system does only marginally not satisfy the conditions within the present scheme. Moreover the range of validity of the proven long range order in the diagonal bilayer system could be considerably extended, if the mock divergence at (π, π, π) of the upper bound for the susceptibility could be eliminated. The rigorous proof of long range order in the two-dimensional spin-1/2 Heisenberg model on a square lattice with nearest-neighbor coupling remains, however, still a formidable task and essentially new techniques might be required.

A

Appendix to Chapter 2

A.1 Definitions of the pocket operators

The equivalence of the two definitions for the pocket-operators made in Eq. (2.9) and in Eq. (2.8) follows from

$$\begin{aligned} b^{\dagger j}_{\mathbf{K}m\sigma} &= \frac{1}{2}\sum_{l} \mathrm{e}^{\mathrm{i}\mathbf{B}_j\cdot\mathbf{a}_l} a^{\dagger l}_{\mathbf{K}m\sigma} \\ &= \frac{1}{2}\sum_{l} \mathrm{e}^{\mathrm{i}\mathbf{B}_j\cdot\mathbf{a}_l} \frac{2}{\sqrt{N}} \sum_{\mathbf{R}} \mathrm{e}^{\mathrm{i}\mathbf{K}\cdot(\mathbf{R}+\mathbf{a}_l+\mathbf{a}_m)} a^{\dagger l}_{\mathbf{R}m\sigma} \\ &= \mathrm{e}^{-\mathrm{i}\mathbf{B}_j\cdot\mathbf{a}_m} \frac{1}{\sqrt{N}} \sum_{l\mathbf{R}} \mathrm{e}^{\mathrm{i}(\mathbf{K}+\mathbf{B}_j)\cdot(\mathbf{R}+\mathbf{a}_l+\mathbf{a}_m)} c^{\dagger}_{\mathbf{R}+\mathbf{a}_l+\mathbf{a}_m m\sigma} \\ &= \mathrm{e}^{-\mathrm{i}\mathbf{B}_j\cdot\mathbf{a}_m} c^{\dagger}_{\mathbf{K}+\mathbf{B}_j m\sigma}. \end{aligned} \tag{A.1}$$

The diagonal form of the tight-binding Hamiltonian in Eq. (2.11) follows directly from the relation

$$\epsilon^{mm'}_{\mathbf{K}+\mathbf{B}_j} = \mathrm{e}^{-\mathrm{i}\mathbf{B}_j\cdot(\mathbf{a}_m-\mathbf{a}_{m'})} \epsilon^{mm'}_{\mathbf{K}}. \tag{A.2}$$

A.2 Derivation of the effective Hamiltonian

Here, we provide some details concerning the derivation of the effective Hamiltonian in Eq. (2.19). It is convenient to treat each term in Eq. (2.15) separately.

Let us start with the Hund's coupling.

$$\frac{J_{\mathrm{H}}}{2}\sum_{\mathrm{r}}\sum_{m\neq m'} c^{\dagger}_{\mathbf{r}m\sigma}c^{\dagger}_{\mathbf{r}m'\sigma'}c_{\mathbf{r}m\sigma'}c_{\mathbf{r}m'\sigma} \tag{A.3}$$

$$= \frac{J_{\mathrm{H}}}{2N}\sum_{\mathbf{kqk'q'}}{}^{\mathrm{r}}\sum_{m\neq m'} c^{\dagger}_{\mathbf{k}m\sigma}c^{\dagger}_{\mathbf{k'}m'\sigma'}c_{\mathbf{q}m\sigma'}c_{\mathbf{q'}m'\sigma} \tag{A.4}$$

$$= \frac{J_{\mathrm{H}}}{2N}\sum_{\mathbf{KK'Q}}\sum_{ijkl}{}^{\mathrm{r}}\sum_{m\neq m'} \mathrm{e}^{\mathrm{i}(\mathbf{B}_i-\mathbf{B}_k)\cdot\mathbf{a}_m}\mathrm{e}^{\mathrm{i}(\mathbf{B}_l-\mathbf{B}_j)\cdot\mathbf{a}_{m'}} \cdot \tag{A.5}$$
$$\cdot\, b^{\dagger i}_{\mathbf{K}m\sigma}b^{\dagger l}_{-\mathbf{K}+\mathbf{Q}\,m'\sigma'}b^{k}_{-\mathbf{K'}+\mathbf{Q}\,m\sigma'}b^{j}_{\mathbf{K'}m'\sigma}.$$

The sum over the momenta in (A.4) is restricted such that $\mathbf{k}+\mathbf{k'}-\mathbf{q}-\mathbf{q'}$ equals a reciprocal lattice vector. (A.5) follows from (A.4) by using the definition of the pocket operators in Eq. (2.8). The sum over the pocket indices is again restricted such that $\mathbf{B}_i+\mathbf{B}_j+\mathbf{B}_k+\mathbf{B}_l$ equals a reciprocal lattice vector, whereas the sum over the momenta in the reduced BZ is simplified to an unrestricted sum over three momenta. Note that this is a good approximation for small pockets, because all the processes at the Fermi energy are kept. [a]

The next step is to go from orbital operators to the band operators. Restricting ourselves to the top band and taking into account Eq. (2.16) we can simply substitute $b^{\dagger j}_{\mathbf{K}m\sigma} \rightarrow \frac{1}{\sqrt{3}}b^{\dagger j}_{\mathbf{K}\sigma}$. Now we can sum over the orbital indices in Eq. (A.5) and taking into account that the sum over the pocket indices is restricted we obtain the sum

$$\sum_{m\neq m'} \mathrm{e}^{\mathrm{i}(\mathbf{B}_i-\mathbf{B}_k)\cdot(\mathbf{a}_m-\mathbf{a}_{m'})} = 2(4\,\delta_{ik}-1), \tag{A.6}$$

and for the Hund's coupling term

$$\frac{J_{\mathrm{H}}}{9N}\sum_{\mathbf{KK'Q}}\sum_{ijkl}{}^{\mathrm{r}}\, b^{\dagger i}_{\mathbf{K}\sigma}\, b^{\dagger l}_{-\mathbf{K}+\mathbf{Q}\,\sigma'}\, b^{k}_{-\mathbf{K'}+\mathbf{Q}\,\sigma'}\, b^{j}_{\mathbf{K'}\sigma}(4\delta_{ik}-1). \tag{A.7}$$

The restriction of the sum can be dropped, if we replace $(4\delta_{ik}-1)$ with $(2\delta_{ijkl}-\epsilon^2_{ijkl}-\delta_{il}\delta_{jk}-\delta_{ij}\delta_{kl}+3\delta_{ik}\delta_{jl})$. The terms proportional to J_{H} in the interaction of Eq. (2.19) are now obtained by dividing Eq. (A.7) into two equal parts, rewrite one directly in terms of density-density operators, and rewrite the other in terms of density-density and spin-density spin-density operators using the SU(2) relation $2\delta_{\alpha\delta}\delta_{\beta\gamma} = \delta_{\alpha\gamma}\delta_{\beta\delta}+\boldsymbol{\sigma}_{\alpha\gamma}\cdot\boldsymbol{\sigma}_{\beta\delta}$. Terms which renormalize the chemical potential are dropped. All the other terms in Eq. (2.15) are treated in the same way.

[a] Small pockets means here $4\mathbf{K}_{\mathrm{F}} < |\mathbf{B}_1|$, this corresponds to a doping with $x > 0.55$

A.3 The symmetry group G

The symmetry group G of H_{eff} (2.29) is a finite subgroup of U(4) that is generated by t the permutation matrices $\mathcal{P} \in \mathcal{S}_4$ and the diagonal orthogonal matrices $\mathcal{D} \in (Z_2)^4$. G is a semi-direct product of $\mathcal{S}_4$ and the normal subgroup $(Z_2)^4$. This allows us to find the irreducible representations of G, cf. Ref. [157]. The elements can be written in a unique way as $(\mathcal{P}, \mathcal{D})$ with $\mathcal{P} \in \mathcal{S}_4$ and $\mathcal{D} \in (Z_2)^4$. The product of two elements $(\mathcal{P}, \mathcal{D}) \circ (\mathcal{P}', \mathcal{D}')$ is given by $(\mathcal{P} \circ \mathcal{P}', \mathcal{D}'')$. From this follows that if $(\mathcal{P}, \mathcal{D})$ is conjugate to $(\mathcal{P}', \mathcal{D}')$, $\mathcal{P}$ is conjugate to $\mathcal{P}'$, and the class of $(\mathcal{P}, \mathcal{D}) \in G$ can be labeled by the class of $\mathcal{P} \in \mathcal{S}^4$. The elements of $\mathcal{S}_4$ can be classified by writing them as disjunct cyclic permutations. We label the five classes as follows: e=1, f=(ab), g=$(ab)(cd)$, h=(abc), i=$(abcd)$. In total there are twenty 20 classes in G. The character table is shown in Table A.1. The character corresponding to the natural representation of G by orthogonal 4×4 matrices is χ_{11}. The representation on the 16 dimensional space V spanned by Q^{0-15}, that was defined in Sec. 2.4, acts irreducibly on the subspaces V^0, V^{1-3}, V^{4-9}, and V^{10-15} with the characters χ_0, χ_7, χ_{15}, and χ_{16}, respectively.

With help of Schur's Lemma, it is now easy to show that the interaction H_{eff} in the Basis Q^{0-15} is diagonal, i.e.,

$$\sum_{ijkl} Q^r_{ji} A^{\text{c/s}}_{ijkl} Q^{r'}_{kl} = \delta_{rr'} \Lambda^{\text{c/s}}_r, \tag{A.8}$$

and that the coupling constant $\Lambda^{\text{c/s}}_r$ depend only on the irreducible subspace.

As discussed in Sec. 2.5, the subgroup $(Z_2)^4$ describes gauge symmetries, that are broken in the real system whereas the subgroup $\mathcal{S}_4$ describes the space-group symmetries. The subgroup $\mathcal{S}_4$ consists of the classes e_1, f_1, g_1, h_1, and i_1. The irreducible representations of G are in general reducible for the subgroup $\mathcal{S}_4$. For example we have $\chi_7 = \Gamma_5$, $\chi_{15} = \Gamma_1 \oplus \Gamma_3 \oplus \Gamma_5$, and $\chi_{16} = \Gamma_4 \oplus \Gamma_5$.

Table A.1: The character table for the symmetry group G of the effective Hamiltonian H_{eff}. The first line labels the classes and gives the number of elements in each class. The letters of the classes indicate classes of the subgroup $\mathcal{S}_4$: e=1, f=(ab), g=$(ab)(cd)$, h=(abc), i=$(abcd)$. The characters appearing in our effective Hamiltonian are χ_1 for Q^0, χ_7 for Q^{1-3}, χ_{15} for Q^{4-9} (real matrices) and χ_{16} for Q^{10-15} (imaginary matrices). χ_{11} is the natural representation of G defined in Sec. 2.4. The last column gives the reduction of the representations into irreducible representations of the subgroup $\mathcal{S}_4$, that consists of the classes e_1, f_1, g_1, h_1, and i_1.

	e_1	e_2	e_3	e_4	e_5	f_1	f_2	f_3	f_4	f_5	f_6	g_1	g_2	g_3	h_1	h_2	h_3	h_4	i_1	i_2	reduction
#	1	4	6	4	1	12	12	24	24	12	12	12	24	12	32	32	32	32	48	48	to $\mathcal{S}_4$
χ_1	1	1	1	1	1	1	1	1	1	1	1	1	1	1	1	1	1	1	1	1	Γ_1
χ_2	1	1	1	1	1	$\bar{1}$	$\bar{1}$	$\bar{1}$	$\bar{1}$	$\bar{1}$	$\bar{1}$	1	1	1	1	1	1	1	$\bar{1}$	$\bar{1}$	Γ_2
χ_3	1	$\bar{1}$	1	$\bar{1}$	1	1	$\bar{1}$	$\bar{1}$	1	1	$\bar{1}$	1	$\bar{1}$	1	1	$\bar{1}$	$\bar{1}$	1	1	$\bar{1}$	Γ_1
χ_4	1	$\bar{1}$	1	$\bar{1}$	1	$\bar{1}$	1	1	$\bar{1}$	$\bar{1}$	1	1	$\bar{1}$	1	1	$\bar{1}$	$\bar{1}$	1	$\bar{1}$	1	Γ_2
χ_5	2	2	2	2	2	0	0	0	0	0	0	2	2	2	$\bar{1}$	$\bar{1}$	$\bar{1}$	$\bar{1}$	0	0	Γ_3
χ_6	2	$\bar{2}$	2	$\bar{2}$	2	0	0	0	0	0	0	2	$\bar{2}$	2	$\bar{1}$	1	1	$\bar{1}$	0	0	Γ_3
χ_7	3	3	3	3	3	1	1	1	1	1	1	$\bar{1}$	$\bar{1}$	$\bar{1}$	0	0	0	0	$\bar{1}$	$\bar{1}$	Γ_5
χ_8	3	3	3	3	3	$\bar{1}$	$\bar{1}$	$\bar{1}$	$\bar{1}$	$\bar{1}$	$\bar{1}$	$\bar{1}$	$\bar{1}$	$\bar{1}$	0	0	0	0	1	1	Γ_4
χ_9	3	$\bar{3}$	3	$\bar{3}$	3	1	$\bar{1}$	$\bar{1}$	1	1	$\bar{1}$	$\bar{1}$	1	$\bar{1}$	0	0	0	0	$\bar{1}$	1	Γ_5
χ_{10}	3	$\bar{3}$	3	$\bar{3}$	3	$\bar{1}$	1	1	$\bar{1}$	$\bar{1}$	1	$\bar{1}$	1	$\bar{1}$	0	0	0	0	1	$\bar{1}$	Γ_4
χ_{11}	4	2	0	$\bar{2}$	$\bar{4}$	2	2	0	0	$\bar{2}$	$\bar{2}$	0	0	0	1	$\bar{1}$	1	$\bar{1}$	0	0	$\Gamma_1 \oplus \Gamma_5$
χ_{12}	4	2	0	$\bar{2}$	$\bar{4}$	$\bar{2}$	$\bar{2}$	0	0	2	2	0	0	0	1	$\bar{1}$	1	$\bar{1}$	0	0	$\Gamma_2 \oplus \Gamma_4$
χ_{13}	4	$\bar{2}$	0	2	$\bar{4}$	2	$\bar{2}$	0	0	$\bar{2}$	2	0	0	0	1	1	$\bar{1}$	$\bar{1}$	0	0	$\Gamma_1 \oplus \Gamma_5$
χ_{14}	4	$\bar{2}$	0	2	$\bar{4}$	$\bar{2}$	2	0	0	2	$\bar{2}$	0	0	0	1	1	$\bar{1}$	$\bar{1}$	0	0	$\Gamma_2 \oplus \Gamma_4$
χ_{15}	6	0	$\bar{2}$	0	6	2	0	0	$\bar{2}$	2	0	2	0	$\bar{2}$	0	0	0	0	0	0	$\Gamma_1 \oplus \Gamma_3 \oplus \Gamma_5$
χ_{16}	6	0	$\bar{2}$	0	6	0	2	$\bar{2}$	0	0	2	$\bar{2}$	0	2	0	0	0	0	0	0	$\Gamma_4 \oplus \Gamma_5$
χ_{17}	6	0	$\bar{2}$	0	6	0	$\bar{2}$	2	0	0	$\bar{2}$	$\bar{2}$	0	2	0	0	0	0	0	0	$\Gamma_4 \oplus \Gamma_5$
χ_{18}	6	0	$\bar{2}$	0	6	$\bar{2}$	0	0	2	$\bar{2}$	0	2	0	$\bar{2}$	0	0	0	0	0	0	$\Gamma_1 \oplus \Gamma_3 \oplus \Gamma_5$
χ_{19}	8	4	0	$\bar{4}$	$\bar{8}$	0	0	0	0	0	0	0	0	0	$\bar{1}$	1	$\bar{1}$	1	0	0	$\Gamma_3 \oplus \Gamma_4 \oplus \Gamma_5$
χ_{20}	8	$\bar{4}$	0	4	$\bar{8}$	0	0	0	0	0	0	0	0	0	$\bar{1}$	$\bar{1}$	1	1	0	0	$\Gamma_3 \oplus \Gamma_4 \oplus \Gamma_5$

B

Appendix to Chapter 3

B.1 RG analysis

B.1.1 Kagomé strip

The tight-binding Hamiltonian for the kagomé strip with periodic boundary conditions is given by

$$\begin{aligned} H_0 &= -t\sum_{r=1}^{L}\sum_{\nu=\pm1}\sum_{\sigma}\left[c^{\dagger}_{r\nu\sigma}c_{r+\nu,\nu\sigma} + \right. \\ &\quad \left. + c^{\dagger}_{r0\sigma}(c_{r\nu\sigma} + c_{r+\nu,\nu\sigma}) + \text{h.c.}\right] - \mu\hat{N}, \end{aligned} \tag{B.1}$$

where $\sigma = \uparrow, \downarrow$ are the spin indices and $\hat{N}$ is the number operator. The chemical potential, μ, will be fixed to $-t = -1$ in the following. It is convenient to introduce Fourier transformed operators

$$c_{rx\sigma} = \frac{1}{\sqrt{L}}\sum_{k} \mathrm{e}^{\mathrm{i}k(r-\frac{x}{2})}\, c_{kx\sigma} \quad \text{with} \quad x = \pm1, 0, \tag{B.2}$$

where the k-sum runs over the L k-values in $[-\pi, \pi)$. We can write this Hamiltonian in a diagonal form

$$H_0 = \sum_{k\sigma}\sum_{l=1}^{3} \xi_{kl}\, \gamma^{\dagger}_{kl\sigma}\gamma_{kl\sigma}, \tag{B.3}$$

and obtain the energies

$$\xi_{k1} = 1 - 2\cos k, \qquad \xi_{k2} = -1 - 2\cos k, \qquad \xi_{k3} = 3, \tag{B.4}$$

and the operators

$$\begin{pmatrix} \gamma_{k1\sigma} \\ \gamma_{k2\sigma} \\ \gamma_{k3\sigma} \end{pmatrix} = \frac{1}{\sqrt{2}\beta_k} \begin{pmatrix} \beta_k & 0 & -\beta_k \\ \alpha_k & \sqrt{2} & \alpha_k \\ 1 & -\sqrt{2}\alpha_k & 1 \end{pmatrix} \begin{pmatrix} c_{k,-1} \\ c_{k,0} \\ c_{k,+1} \end{pmatrix} \tag{B.5}$$

with $\alpha_k = \sqrt{2}\cos(k/2)$ and $\beta_k = \sqrt{1+\alpha_k^2}$ and $k \in [-\pi, \pi)$.

The local Coulomb interaction introduced in Eq. (3.28) can be written as

$$H_{\text{Int}} = \frac{U}{L} \sum_{k_1 \ldots k_4}{}' \sum_{x=-1}^{1} \mathrm{e}^{-\mathrm{i}\frac{xq}{2}} c^\dagger_{k_1 x\uparrow} c^\dagger_{k_2 x\downarrow} c_{k_3 x\downarrow} c_{k_4 x\uparrow}. \tag{B.6}$$

The sum over the momenta $k_1 \ldots k_4$ is restricted, such that $q = k_1 + k_2 - k_3 - k_4$ is a multiple of 2π. Note, that the appearing phase factor is important to determine the sign of the Umklapp scattering processes correctly. We obtain the effective low-energy Hamiltonian (3.29) from Eq. (B.6) by doing the substitutions

$$\begin{aligned} c_{k,\pm,\sigma} &\rightarrow \mp\frac{1}{\sqrt{2}}\gamma_{k1\sigma} + \frac{1}{\sqrt{6}}\gamma_{k2\sigma} \\ c_{k,0,\sigma} &\rightarrow \sqrt{\frac{2}{3}}\gamma_{k2\sigma}. \end{aligned} \tag{B.7}$$

These substitutions rules are obtained from Eq. (B.5) if we set $k = k_{\text{F}1}$ in the first row and $k = k_{\text{F}2}$ in the second row and drop the third row in the matrix of the transformation.

In this way we can map the weak coupling Hubbard model on the kagomé strip on an effective weak coupling model on the two-leg ladder. The problem of a weak coupling two-leg ladder has been extensively studied by renormalization-group and bosonization techniques [16, 158, 159]. We will adopt here the notation of Lin *et al.* in Ref. [16]. A general weak interaction can be conveniently expressed in terms of left and right moving currents. Dropping purely chiral terms the momentum-conserving four fermion interactions can be written as

$$\begin{aligned} \mathcal{H}^{(1)} &= b^\rho_{ij}\, J_{\text{R}ij}\, J_{\text{L}ij} - b^\sigma_{ij}\, \mathbf{J}_{\text{R}ij} \cdot \mathbf{J}_{\text{L}ij} \\ &+ f^\rho_{ij}\, J_{\text{R}ii}\, J_{\text{L}jj} - f^\sigma_{ij}\, \mathbf{J}_{\text{R}ii} \cdot \mathbf{J}_{\text{L}jj}. \end{aligned} \tag{B.8}$$

To avoid double counting we set $f_{ii} = 0$. Furthermore, the symmetry relations $f_{12} = f_{21}$ (parity), $b_{12} = b_{21}$ (hermicity), and $b_{11} = b_{22}$ (only at half filling)

hold. We have therefore six independent coefficients. For our interaction we find the values

$$4b_{11}^{\rho} = b_{11}^{\sigma} = U, \quad 4b_{12}^{\rho} = b_{12}^{\sigma} = \frac{U}{3}, \quad 4f_{12}^{\rho} = f_{12}^{\sigma} = \frac{U}{3}. \tag{B.9}$$

In addition we have Umklapp terms given by

$$\mathcal{H}^{(2)} = u_{ij}^{\rho} I_{\mathrm{R}ij}^{\dagger} I_{\mathrm{L}\bar{i}\bar{j}} - u_{ij}^{\sigma} \mathbf{I}_{\mathrm{R}ij}^{\dagger} \cdot \mathbf{I}_{\mathrm{L}\bar{i}\bar{j}} + \mathrm{h.c.} \tag{B.10}$$

with $u_{ii}^{\sigma} = 0$, $u_{11}^{\rho} = u_{22}^{\sigma}$, $u_{12}^{\rho} = u_{21}^{\rho}$ and $u_{12}^{\sigma} = u_{21}^{\sigma}$. Here we have the values

$$u_{12}^{\sigma} = 0, \quad u_{12}^{\rho} = -\frac{U}{12}, \quad u_{11}^{\rho} = -\frac{U}{24}. \tag{B.11}$$

Integrating the RG equations with these initial values shows that the solution converges to the analytic solution of the RG equation where all coupling constants except for b_{11}^{σ} and b_{11}^{ρ} diverge with fixed ratios given by

$$\begin{aligned} f_{12}^{\rho} &= -\frac{1}{4} f_{12}^{\sigma} = b_{12}^{\rho} = -\frac{1}{4} b_{12}^{\sigma} \\ &= \frac{1}{2} u_{12}^{\sigma} = -2u_{12}^{\rho} = -2u_{11}^{\rho} = g > 0. \end{aligned} \tag{B.12}$$

This solution was identified by bosonization techniques as a charge density wave solution solution.

B.1.2 Checkerboard lattice

The checkerboard lattice is shown in Fig. 3.1 (d). The elementary unit cell contains two lattice sites situated $\mathbf{x}_{\nu}/2$ ($\nu = 1, 2$) where the vectors $\mathbf{x}_{\nu}$ are two primitive lattice vectors. With this convention we choose the origin of the lattice at the center of a crossed plaquette, where there is no lattice site. The tight-binding Hamiltonian for this system is given by

$$\begin{aligned} H_0 = -t \sum_{\mathbf{r}\nu\sigma} \Big[& c_{\mathbf{r}\nu\sigma}^{\dagger} (c_{\mathbf{r}+\mathbf{x}_{\nu},\nu\sigma} + c_{\mathbf{r}-\mathbf{x}_{\bar{\nu}},\bar{\nu}\sigma} \\ & + c_{\mathbf{r}-\mathbf{x}_1+\mathbf{x}_{\nu},\bar{\nu}\sigma}) + \mathrm{h.c.} \Big] - \mu \hat{N}, \end{aligned} \tag{B.13}$$

where $\bar{\nu} = 2, 1$ if $\nu = 1, 2$ and $\mu = -2t$ in the following. The operator $\hat{N}$ is the number operator. We introduce Fourier transformed operators as

$$c_{\mathbf{r}\nu\sigma} = \frac{1}{\sqrt{N}} \sum_{\mathbf{k}} \mathrm{e}^{\mathrm{i}\mathbf{k}\cdot(\mathbf{r}+\mathbf{x}_{\nu}/2)} c_{\mathbf{k}\nu\sigma}, \tag{B.14}$$

where N is the number of unit cells. With these operators the tight-binding Hamiltonian reads

$$H_0 = 4t \sum_{\mathbf{k}\mu\nu\sigma} \left[\delta_{\mu\nu} - \cos\left(\frac{k_\mu}{2}\right)\cos\left(\frac{k_\nu}{2}\right)\right] c^\dagger_{\mathbf{k}\mu\sigma} c_{\mathbf{k}\nu\sigma}, \tag{B.15}$$

where $k_\nu = \mathbf{k}\cdot\mathbf{x}_\nu$. Diagonalizing this Hamiltonian leads to a flat band at $4t$ and to a band with the dispersion $\xi_\mathbf{k} = -2t\sum_\nu \cos k_\nu$ which is nothing but the nearest-neighbor tight-binding dispersion of the square lattice. The operators of this dispersive band are expressed in terms of the original operators by

$$\gamma_{\mathbf{k}\sigma} = \frac{1}{\sqrt{r_\mathbf{k}}} \sum_\nu \cos\left(\frac{k_\nu}{2}\right) c_{\mathbf{k}\nu\sigma} \tag{B.16}$$

with $r_\mathbf{k} = \sum_\nu \cos^2(k_\nu/2)$. In weak coupling we can restrict our attention to the states close the Fermi surface where $r_\mathbf{k} = 1$ and for every operator on the checkerboard lattice we can obtain an effective operator on the square lattice by the substitution $c_{\mathbf{k}\nu\sigma} \to \cos(k_\nu/2)\gamma_{\mathbf{k}\sigma}$.

B.1.3 Weak-coupling on the honeycomb lattice

If we associate with each triangle of the kagomé lattice a site, we obtain the honeycomb lattice. Suppressing the spin indices, the tight-binding Hamiltonian on the honeycomb lattice can be written as

$$H = -t \sum_\mathbf{r} \left(f^\dagger_{\mathbf{r}1} f_{\mathbf{r}2} + f^\dagger_{\mathbf{r}1} f_{\mathbf{r}+\mathbf{a}_2,2} + f^\dagger_{\mathbf{r}1} f_{\mathbf{r}+\mathbf{a}_2+\mathbf{a}_1,2} + \text{h.c.} \right), \tag{B.17}$$

where the vectors $\mathbf{a}_i$ are defined as in Fig. 3.14. With the Fourier transformed operators[a]

$$f_{\mathbf{r}1} = \frac{1}{\sqrt{N}} \sum_\mathbf{k} \mathrm{e}^{\mathrm{i}\mathbf{k}\cdot\mathbf{r}} f_{\mathbf{k}1} \qquad f_{\mathbf{r}2} = \frac{1}{\sqrt{N}} \sum_\mathbf{k} \mathrm{e}^{\mathrm{i}\mathbf{k}\cdot[\mathbf{r}+(\mathbf{a}_3-\mathbf{a}_2)/3]} f_{\mathbf{k}2}, \tag{B.18}$$

this reads

$$H = -t \sum_\mathbf{k} \Big[\underbrace{\left(\mathrm{e}^{\mathrm{i}(k_1-k_3)/3} + \mathrm{e}^{\mathrm{i}(k_2-k_1)/3} + \mathrm{e}^{\mathrm{i}(k_3-k_2)/3}\right)}_{x_\mathbf{k}} f^\dagger_{\mathbf{k}1} f_{\mathbf{k}2} + \text{h.c.} \Big]. \tag{B.19}$$

[a] N is the number of lattice sites.

This Hamiltonian can be diagonalized as

$$H = t \sum_{\mathbf{k}} \sum_{p=\pm 1} p|x_{\mathbf{k}}| \gamma^{\dagger}_{\mathbf{k}p} \gamma_{\mathbf{k}p} \tag{B.20}$$

with

$$\gamma_{\mathbf{k}p} = \frac{1}{\sqrt{2}} \left(f_{\mathbf{k}1} - p \mathrm{e}^{\mathrm{i}\varphi_{\mathbf{k}}} f_{\mathbf{k}2} \right) \qquad x_{\mathbf{k}} = |x_{\mathbf{k}}| \mathrm{e}^{\mathrm{i}\varphi_{\mathbf{k}}}. \tag{B.21}$$

At half-filling, the Fermi surface reduces to the to points $\mathrm{K} = -\mathrm{K}' = -4\pi(1,0)/3a$. We have the relation

$$x_{\mathrm{K}+\mathbf{k}} = \omega^2 \mathrm{e}^{\mathrm{i}(k_1 - k_3)/3} + \omega \mathrm{e}^{\mathrm{i}(k_2 - k_1)/3} + \mathrm{e}^{\mathrm{i}(k_3 - k_2)/3} \approx \frac{\sqrt{3}a}{2} (k_x - \mathrm{i}k_y) \tag{B.22}$$

where the last approximation is the first non-vanishing order of $\mathbf{k}$. We obtain for the eigenstates close to K and K'

$$\gamma_{\mathrm{K}+\mathbf{k},p} \approx \frac{1}{\sqrt{2}} \left(f_{\mathrm{K}+\mathbf{k},1} - p k_{\mathrm{c}}^* f_{\mathrm{K}+\mathbf{k},2} \right) \tag{B.23}$$

$$\gamma_{\mathrm{K}'+\mathbf{k},p} \approx \frac{1}{\sqrt{2}} \left(f_{\mathrm{K}'+\mathbf{k},1} + p k_{\mathrm{c}} f_{\mathrm{K}'+\mathbf{k},2} \right)$$

with $k_{\mathrm{c}} = (k_x + \mathrm{i}k_y)/k$.

Let us now return again to the kagomé lattice and let us work with a new BZ consisting of the two subzones Z and Z' around the points K and K' as shown in Fig. B.1. We introduce the operators ($\omega = \mathrm{e}^{\mathrm{i}2\pi/3}$)

$$\begin{pmatrix} f_{\mathbf{k}1} \\ f_{\mathbf{k}2} \\ f_{\mathbf{k}3} \end{pmatrix} = \frac{1}{\sqrt{3}} \begin{pmatrix} \omega & -\omega^2 & -1 \\ -1 & \omega^2 & \omega \\ -1 & 1 & 1 \end{pmatrix} \begin{pmatrix} c_{\mathbf{k}1} \\ c_{\mathbf{k}2} \\ c_{\mathbf{k}3} \end{pmatrix} \qquad \mathbf{k} \in \mathrm{Z} \tag{B.24}$$

$$\begin{pmatrix} f_{\mathbf{k}1} \\ f_{\mathbf{k}2} \\ f_{\mathbf{k}3} \end{pmatrix} = \frac{1}{\sqrt{3}} \begin{pmatrix} \omega^2 & -\omega & -1 \\ -1 & \omega & \omega^2 \\ -1 & 1 & 1 \end{pmatrix} \begin{pmatrix} c_{\mathbf{k}1} \\ c_{\mathbf{k}2} \\ c_{\mathbf{k}3} \end{pmatrix} \qquad \mathbf{k} \in \mathrm{Z}' \tag{B.25}$$

where the operators $c_{\mathbf{k}i}$ are defined as in Eq. (3.60). This is just a transformation to an orthonormal basis in which the kinetic energy is diagonal at the points K and K'. The operators $f^{\dagger}_{\mathrm{K}+\mathbf{k},3}$ and $f^{\dagger}_{\mathrm{K}'+\mathbf{k},3}$ create states in the top flat band. Using exactly the same formulas as in Eq. (B.23) we can now define the states $\gamma_{\mathrm{K}+\mathbf{k},p}$ and $\gamma_{\mathrm{K}'+\mathbf{k},p}$ for $p = \pm 1$ that are approximate eigenstates of the kinetic energy close to K and K'. Therefore, the weakly interacting kagomé lattice at 1/3-filling can be mapped to a weakly interacting honeycomb lattice.

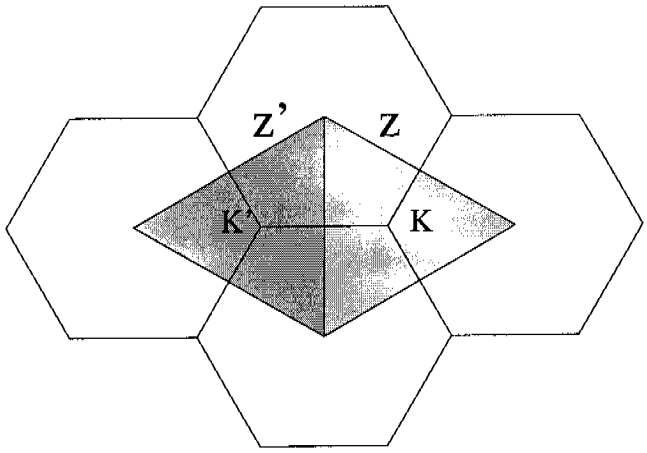

Figure B.1: The zones Z and Z' are triangles around the points K and K'. They form together a Brillouin zone.

Let us now look, to what kind of interaction a weak Coulomb repulsion on the kagomé lattice corresponds on the honeycomb lattice. First of all we note that for sufficiently small U, we can neglect Umklapp processes.[b] We obtain

$$\begin{aligned} H_{\text{int}} &= U \sum_{\mathbf{r}} \sum_{m} n_{\mathbf{r}m\uparrow} n_{\mathbf{r}m\downarrow} \\ &= U \sum_{\mathbf{k}\mathbf{k}'\mathbf{q}} \sum_{m} c^{\dagger}_{\mathbf{k}+\mathbf{q},m\uparrow} c^{\dagger}_{\mathbf{k}'-\mathbf{q},m\downarrow} c_{\mathbf{k}'m\downarrow} c_{\mathbf{k}m\uparrow} \\ &= U \sum_{ABCD\in\{\mathrm{K},\mathrm{K}'\}} \overset{A+B=C+D}{\overset{\triangle}{\sum_{\mathbf{k}\mathbf{k}'\mathbf{q}}}} \sum_{m} c^{\dagger}_{A+\mathbf{k}+\mathbf{q},m\uparrow} c^{\dagger}_{B+\mathbf{k}'-\mathbf{q},m\downarrow} c_{C+\mathbf{k}',m\downarrow} c_{D+\mathbf{k},m\uparrow}, \end{aligned} \tag{B.26}$$

where in the last expression the sum over the momenta is restricted to the triangle of the corresponding zone. With help of Eq. (B.24, B.25) we can rewrite this expression in terms of the f operators and dropping the terms involving the top band this amounts to doing the substitutions.

$$\begin{array}{lcll} c_{\mathbf{k}1} & \to & \frac{1}{\sqrt{3}}(\omega^2 f_{\mathbf{k}1} - f_{\mathbf{k}2}) & \\ c_{\mathbf{k}2} & \to & \frac{\omega}{\sqrt{3}}(f_{\mathbf{k}2} - f_{\mathbf{k}1}) & \mathbf{k}\in \mathrm{Z} \\ c_{\mathbf{k}2} & \to & \frac{1}{\sqrt{3}}(\omega^2 f_{\mathbf{k}2} - f_{\mathbf{k}1}) & \end{array} \qquad \begin{array}{lcll} c_{\mathbf{k}1} & \to & \frac{1}{\sqrt{3}}(\omega f_{\mathbf{k}1} - f_{\mathbf{k}2}) & \\ c_{\mathbf{k}2} & \to & \frac{\omega^2}{\sqrt{3}}(f_{\mathbf{k}2} - f_{\mathbf{k}1}) & \mathbf{k}\in \mathrm{Z}' \\ c_{\mathbf{k}2} & \to & \frac{1}{\sqrt{3}}(\omega f_{\mathbf{k}2} - f_{\mathbf{k}1}) & \end{array} \tag{B.27}$$

[b]For the kagomé strip the Umklapp processes were very important, but in that case the Fermi points were connected by half of the reciprocal lattice vector, which is here not the case.

a little algebra shows, that this leads to two different terms: The first term is just a renormalized Coulomb repulsion on the honeycomb lattice, given by[c]

$$\frac{U}{3}\sum_{\mathbf{k}\mathbf{k}'\mathbf{q}}\sum_{l=1}^{2} f^{\dagger}_{\mathbf{k}+\mathbf{q},l\uparrow} f^{\dagger}_{\mathbf{k}'-\mathbf{q},l\downarrow} f_{\mathbf{k}'l\downarrow} f_{\mathbf{k}l\uparrow}. \tag{B.28}$$

The second term is of the form

$$\frac{U}{9}\sum_{\mathbf{k}\mathbf{k}'\mathbf{q}}^{\triangle}\sum_{l=1}^{2}\left(x_{A+B} f^{\dagger}_{al\uparrow} f^{\dagger}_{bl\downarrow} f_{c\bar{l}\downarrow} f_{d\bar{l}\uparrow} + x_{A-C} f^{\dagger}_{al\uparrow} f^{\dagger}_{b\bar{l}\downarrow} f_{cl\downarrow} f_{d\bar{l}\uparrow} + x_{A-D} f^{\dagger}_{al\uparrow} f^{\dagger}_{b\bar{l}\downarrow} f_{c\bar{l}\downarrow} f_{dl\uparrow}\right), \tag{B.29}$$

where $\bar{1}=2, \bar{2}=1$, and the same sum over A, B, C, D is performed as in the last line of Eq. (B.26). Furthermore, we abbreviated $a = A+\mathbf{k}+\mathbf{q}$, $b = B+\mathbf{k}'-\mathbf{q}$, $c = C+\mathbf{k}'$, and $d = D+\mathbf{k}$. Note, that $x_0 = 3$ and $x_{\pm\mathrm{K}} = x_{\pm 2\mathrm{K}} = 0$, where $x_{\mathbf{k}}$ is the function defined in Eq. (B.19). On the other hand, consider now the following Hamiltonian on the honeycomb lattice

$$\sum_{\langle ij\rangle}\left(U'\sum_{\sigma\sigma'} f^{\dagger}_{i\sigma} f_{i\sigma} f^{\dagger}_{j\sigma'} f_{j\sigma'} - \tilde{J}\sum_{\sigma\sigma'} f^{\dagger}_{i\sigma} f_{i\sigma'} f^{\dagger}_{j\sigma'} f_{j\sigma} - \tilde{J}[f^{\dagger}_{i\uparrow} f^{\dagger}_{i\downarrow} f_{j\uparrow} f_{j\downarrow} + \mathrm{h.c.}]\right). \tag{B.30}$$

with $U' = \tilde{J} = U/9$.[d] If we Fourier transform this Hamiltonian using Eq. (B.18) we obtain, e.g., for the first term in Eq. (B.30)

$$\frac{U'}{2}\sum_{\mathbf{k}\mathbf{k}'\mathbf{q}}^{\triangle}\sum_{l=1}^{2}\sum_{\sigma,\sigma'} x_{A-D}\, f^{\dagger}_{A+\mathbf{k}+\mathbf{q},l\sigma} f^{\dagger}_{B+\mathbf{k}'-\mathbf{q},\bar{l}\sigma'} f_{C+\mathbf{k}',\bar{l}\sigma'} f_{D+\mathbf{k},l\sigma} \tag{B.31}$$

where we also suppressed the sum over A, B, C, D and approximated $x_{A-D+\mathbf{q}}$ with x_{A-D}, which is correct up to second order in $\mathbf{q}$. Note, that terms with anti-parallel spins in Eq. (B.31) yield exactly the third term in Eq. (B.29). Note, that all terms with parallel spins in Eq. (B.30) cancel. In this way it is straightforward to check, that in the weak-coupling limit Eq. (B.29) and Eq. (B.30) are identical. Using the SU(2) relation $2\delta_{\alpha\delta}\delta_{\beta\gamma} = \delta_{\alpha\gamma}\delta_{\beta\delta} + \boldsymbol{\sigma}_{\alpha\gamma}\cdot\boldsymbol{\sigma}_{\beta\delta}$ the interaction (B.30) together with (B.28) can also be written as in Eq. (3.57) where $V = U'/2 = U/18$ and $J = 2\tilde{J} = 2U/9$.

[c]The sum over $\mathbf{k}$, $\mathbf{k}'$, and $\mathbf{q}$ runs here over the entire Brillouin zone.

[d]Note, that the relation $U' + 2\tilde{J} = \tilde{U}$ holds.

Seite Leer /
Blank leaf

C

Appendix to Chapter 5

C.1 Anderson bound for the energy

We consider the antiferromagnetic Heisenberg Hamiltonian

$$H = \boldsymbol{S}_0 \cdot \boldsymbol{S}_1 + \lambda \boldsymbol{S} \cdot \boldsymbol{S}_2 \tag{C.1}$$

with $\lambda > 0$, $\boldsymbol{S}_1 = \boldsymbol{S}_{1,1} + \cdots + \boldsymbol{S}_{1,n_1}$ and $\boldsymbol{S}_2 = \boldsymbol{S}_{2,1} + \cdots + \boldsymbol{S}_{2,n_2}$. Here, $\boldsymbol{S}_0$ and all $\boldsymbol{S}_{i,j}$ are spin-1/2 operators. The Hamiltonian H commutes with $\boldsymbol{S}_0^2$, $\boldsymbol{S}_1^2$, $\boldsymbol{S}_2^2$, $\boldsymbol{S}_{\rm tot}^2 = (\boldsymbol{S}_0 + \boldsymbol{S}_1 + \boldsymbol{S}_2)^2$, and with $S_{\rm tot}^z$. We can therefore assume that the ground state lies in a sector of the Hilbert space, where $\boldsymbol{S}_1^2 = S_1(S_1+1)$, $\boldsymbol{S}_2^2 = S_2(S_2+1)$, $\boldsymbol{S}_{\rm tot} = S_{\rm tot}(S_{\rm tot}+1)$, and $S_{\rm tot}^z = S_{\rm tot}$. Further, we know that $S_{\rm tot} = (n_1 + n_2 - 1)/2$ [155]. This leaves us with the following three possibilities: $S_1 = n_1/2 - 1$, $S_2 = n_2/2$, or $S_1 = n_1/2$, $S_2 = n_2/2 - 1$, or $S_1 = n_1/2$, $S_2 = n_2/2$. In the first two cases the three spins $\boldsymbol{S}_0$, $\boldsymbol{S}_1$, and $\boldsymbol{S}_2$ must be parallel in order to produce $S_{\rm tot}$. This leads to a ferromagnetic state which has positive energy. In the ground state we must therefore have the third possibility, $S_1 = n_1/2$ and $S_2 = n_2/2$. In the $2(2n_1+1)(2n_2+1)$ dimensional Hilbert space, given by the tensor product of the three spin representations, we have only a three-dimensional subspace with $S_{\rm tot}^z = (n_1 + n_2 - 1)/2$. It is straightforward to diagonalize the Hamiltonian in this subspace and the lowest eigenvalue is given by:

$$E_0 = -\frac{1}{4}\,(1 + \lambda + R) \tag{C.2}$$

with

$$R = \sqrt{(1-\lambda^2)(1+n_1)^2 - 2\lambda(1-\lambda)(1+n_1+n_2-n_1n_2) + \lambda^2(n_1+n_2)^2}.$$

The Hamiltonian (5.2) is the sum of Hamiltonians of the form (C.1). As the sum of the minima can not be larger than the minimum of the sum, it is clear that we obtain an upper bound by minimizing every Hamiltonian separately. The equations (5.17) are now obtained from (C.2) with $n_1 = 4$, $n_2 = 2$ and $\lambda = r$ if $N > 2$, or with $n_1 = 4$, $n_2 = 1$ and $\lambda = 2r$ if $N = 2$. Note, that energy per site is $-e = E_0/2$.

C.2 Proof of Gaussian domination

For the Hamiltonian $H^+(h_{\mathbf{a}})$ of (5.32) we can choose the planes perpendicular to $\boldsymbol{\delta}_3$ to separate the Hilbert space into two equal Hilbert spaces corresponding to the two layers. With respect to these planes the Hamiltonian $H^+(h_{\mathbf{a}})$ takes the form $\mathcal{A}+\tilde{\mathcal{A}}+\sum_i(\mathcal{C}_i-\tilde{\mathcal{C}}_i-h_i)^2-\sum_j(\mathcal{D}_j-\tilde{\mathcal{D}}_j)^2$ and (5.33) follows therefore directly from (5.28). To prove (5.33) for the Hamiltonian $H^-(h_{\mathbf{a}})$ we define the more general Hamiltonian $H^-(h^{(l)}_{\mathbf{a},j})$, which is given by (5.32) and (5.30) for $\nu = -$, $h_{\mathbf{a},j} = h^{(1)}_{\mathbf{a},j}$, and $d^-_{\mathbf{a},j} = h^{(2)}_{\mathbf{a},j}$. It depends on four fields and not only on one and is therefore more general than $H^-(h_{\mathbf{a}})$. We will show that

$$E[H^-(h^{(l)}_{\mathbf{a},j})] \geq E[H^-(0)] \tag{C.3}$$

from which (5.33) for the Hamiltonian $H^-(h_{\mathbf{a}})$ follows as a special case. We denote by $\{h^{(l)}_{\mathbf{a},j}\}$ a configuration of the $4|\Lambda|$ real fields and we will assume that of all configurations that minimize $E[H^-(h^{(l)}_{\mathbf{a},j})]$ the configuration $\{\bar{h}^{(l)}_{\mathbf{a},j}\}$ has the largest number of vanishing fields. If the configuration $\{\bar{h}^{(l)}_{\mathbf{a},j}\}$ had a non-vanishing field $\bar{h}^{(l)}_{\mathbf{a},j} \neq 0$, we could choose a pair of planes parallel to $\boldsymbol{\delta}_3$, that separate the lattice Λ into two equal subsystems in such a way that the term containing $\bar{h}^{(l)}_{\mathbf{a},j}$ in (5.30) connects the two subsystems. With respect to these planes the Hamiltonian $H^-(\bar{h}^{(l)}_{\mathbf{a},j})$ can be written in the form of (5.26) and we can apply (5.28). The Hamiltonians $H_{\mathcal{A}}$ and $H_{\mathcal{B}}$ can be written in the form $H^-(a^{(l)}_{\mathbf{a},j})$ and $H^-(b^{(l)}_{\mathbf{a},j})$ and therefore, due to our assumption, we must have $E[H^-(\bar{h}^{(l)})] \leq E[H^-(a^{(l)}_{\mathbf{a},j})]$ and $E[H^-(\bar{h}^{(l)}_{\mathbf{a},j})] \leq E[H^-(b^{(l)}_{\mathbf{a},j})]$. From (5.28) follows now that $E[H^-(\bar{h}^{(l)}_{\mathbf{a},j})] = E[H^-(a^{(l)}_{\mathbf{a},j})] = E[H^-(b^{(l)}_{\mathbf{a},j})]$. The number of vanishing fields is at least in one of the two configurations $\{a^{(l)}_{\mathbf{a},j}\}$ and $\{b^{(l)}_{\mathbf{a},j}\}$ strictly larger than in $\{\bar{h}^{(l)}_{\mathbf{a},j}\}$, which contradicts the assumption that the number of vanishing fields in $\{\bar{h}^{(l)}_{\mathbf{a},j}\}$ is maximal. This shows that all the fields in $\{\bar{h}^{(l)}_{\mathbf{a},j}\}$ must be zero and proves the inequality (C.3).

Bibliography

[1] E. Dagotto and T. M. Rice, Science **271**, 618 (1996).

[2] K. S. Novoselov *et al.*, Science **306**, 666 (2004).

[3] M. I. Katsnelson, K. S. Novoselov, and A. K. Geim, Nature Physics (2006).

[4] G. W. Semenoff, Phys. Rev. Lett. **53**, 2449 (1984).

[5] F. D. M. Haldane, Phys. Rev. Lett. **61**, 2015 (1988).

[6] K. Takada *et al.*, Nature **422**, 53 (2003).

[7] B. Pedrini *et al.*, Phys. Rev. B **72**, 214407 (2005).

[8] M. E. Brühwiler, *Groundstate Properties of Electrons on the Triangular Lattice*, PhD thesis, ETH Zürich, 2006.

[9] G. Misguich and C. Lhuillier, *Frustrated spin systems*, H. T. Diep editor, World-Scientific, 2005, (cond-mat/0310405).

[10] J. Solyom, Adv. Phys. **28**, 201 (1979).

[11] S. R. White, Phys. Rev. Lett. **69**, 2863 (1992).

[12] B. Binz, D. Baeriswyl, and B. Doucot, Eur. Phys. J. B **25**, 69 (2002).

[13] J. Gonzalez, F. Guinea, and M. A. H. Vozmediano, Nucl. Phys. B **424**, 595 (1994).

[14] R. Shankar, Rev. Mod. Phys. **66**, 129 (1994).

[15] M. Salmhofer, C. Honerkamp, W. Metzner, and O. Lauscher, Prog. Theor. Phys. **112**, 943 (2004).

[16] H. H. Lin, L. Balents, and M. P. A. Fisher, Phys. Rev. B **58**, 1794 (1998).

[17] B. Frischmuth, PhD thesis, ETH Zürich, 1998.

[18] P. Coleman, Phys. Rev. B **29**, 3035 (1984).

[19] F. C. Zhang and T. M. Rice, Phys. Rev. B **37**, 3759 (1988).

[20] I. Affleck, Z. Zou, T. Hsu, and P. W. Anderson, Phys. Rev. B **38**, 745 (1988).

[21] P. A. Lee and N. Nagaosa, Phys. Rev. B **46**, 5621 (1992).

[22] T. Tanaka, S. Nakamura, and S. Iida, Japn. J. Appl. Phys. **33**, L581 (1994).

[23] I. Terasaki, Y. Sasago, and K. Uchinokura, Phys. Rev. B **56**, R12685 (1997).

[24] Y. Wang, N. S. Rogado, R. J. Cava, and N. P. Ong, Nature **423**, 425 (2003).

[25] T. Valla *et al.*, Nature **417**, 627 (2002).

[26] R. E. Schaak, T. Klimczuk, M. L. Foo, and R. J. Cava, Nature **424**, 527 (2003).

[27] M. L. Foo *et al.*, Phys. Rev. Lett. **92**, 247001 (2004).

[28] Q. Huang *et al.*, J. Phys.: Condens. Matter **16**, 5803 (2004).

[29] H. W. Zandbergen *et al.*, Phys. Rev. B **70**, 024101 (2004).

[30] Y. G. Shi, H. C. Yu, C. J. Nie, and J. Q. Li, cond-mat/0401052 (2004).

[31] X. Z. Chen *et al.*, cond-mat/0412299 (2004).

[32] Q. Huang *et al.*, Phys. Rev. B **70**, 184110 (2004).

[33] N. L. Wang *et al.*, Phys. Rev. Lett. **93**, 237007 (2004).

[34] R. Ray, A. Ghoshray, and K. Ghoshray, Phys. Rev. B **59**, 9454 (1999).

[35] J. L. Gavilano *et al.*, Phys. Rev. B **69**, 100404 (2004).

[36] P. Carretta *et al.*, Phys. Rev. B **70**, 024409 (2004).

[37] M. Brühwiler, B. Batlogg, S. M. Kazakov, C. Niedermayer, and J. Karpinski, Physica B: Condensed Matter **378-80**, 630 (2006).

[38] C. Bernhard *et al.*, Phys. Rev. Lett. **93**, 167003 (2004).

[39] S. Lupi, M. Ortolani, and P. Calvani, Phys. Rev. B **69**, 180506 (2004).

[40] L. Balicas, M. Abdel-Jawad, N. E. Hussey, F. C. Chou, and P. A. Lee, Phys. Rev. Lett. **94**, 236402 (2005).

[41] C. H. Wang *et al.*, Solid State Commun. **138**, 169 (2006).

[42] S. Lupi *et al.*, Phys. Rev. B **72**, 024550 (2005).

[43] I. R. Mukhamedshin, H. Alloul, G. Collin, and N. Blanchard, Phys. Rev. Lett. **93**, 167601 (2004).

[44] A. T. Boothroyd *et al.*, Phys. Rev. Lett. **92**, 197201 (2004).

[45] L. M. Helme *et al.*, Phys. Rev. Lett. **94**, 157206 (2005).

[46] Y. Ihara *et al.*, J. Phys. Soc. Jpn. **73**, 2963 (2004).

[47] T. Motohashi *et al.*, Phys. Rev. B **67**, 064406 (2003).

[48] B. C. Sales *et al.*, Phys. Rev. B **70**, 174419 (2004).

[49] J. Sugiyama *et al.*, Phys. Rev. B **67**, 214420 (2003).

[50] J. Sugiyama *et al.*, Phys. Rev. Lett. **92**, 017602 (2004).

[51] J. Wooldridge, D. M. Paul, G. Balakrishnan, and M. R. Lees, J. Phys.: Condens. Matter **17**, 707 (2005).

[52] F. C. Chou, J. H. Cho, and Y. S. Lee, Phys. Rev. B **70**, 144526 (2004).

[53] G. Caimi *et al.*, Eur. Phys. J. B **40**, 231 (2004).

[54] J. L. Luo *et al.*, Phys. Rev. Lett. **93**, 187203 (2004).

[55] Y. J. Uemura *et al.*, cond-mat/0403031 (2004).

[56] P. Mendels *et al.*, Phys. Rev. Lett. **94**, 136403 (2005).

[57] D. J. Singh, Phys. Rev. B **61**, 13397 (2000).

[58] G. Gasparovic *et al.*, cond-mat/0508158 (2005).

[59] M. Yokoi *et al.*, J. Phys. Soc. Jpn. **74**, 3046 (2005).

[60] Y. Yanase, M. Mochizuki, and M. Ogata, J. Phys. Soc. Jpn. **74**, 430 (2005).

[61] K. Miyoshi, E. Morikuni, K. Fujiwara, J. Takeuchi, and T. Hamasaki, Phys. Rev. B **69**, 132412 (2004).

[62] G. Baskaran, Phys. Rev. Lett. **91**, 097003 (2003).

[63] B. Kumar and B. S. Shastry, Phys. Rev. B **68**, 104508 (2003).

[64] A. Tanaka and X. Hu, Phys. Rev. Lett. **91**, 257006 (2003).

[65] M. Ogata, J. Phys. Soc. Jpn. **72**, 1893 (2003).

[66] Q.-H. W. D.-H. Lee and P. A. Lee, Phys. Rev. B **69**, 092504 (2004).

[67] C. Honerkamp, Phys. Rev. B **68**, 104510 (2003).

[68] A. Ferraz, E. Kochetov, and M. Mierzejewski, Phys. Rev. B **73**, 064516 (2006).

[69] W. Koshibae and S. Maekawa, Phys. Rev. Lett. **91**, 257003 (2003).

[70] M. Mochizuki, Y. Yanase, and M. Ogata, Phys. Rev. Lett. **94**, 147005 (2005).

[71] D. J. Singh, Phys. Rev. B **68**, 020503 (2003).

[72] M. D. Johannes, I. I. Mazin, D. J. Singh, and D. A. Papaconstantopoulos, Phys. Rev. Lett. **93**, 097005 (2004).

[73] K.-W. Lee, J. Kunes, and W. E. Pickett, Phys. Rev. B **70**, 045104 (2004).

[74] Z. Li, J. Yang, J. G. Hou, and Q. Zhu, Phys. Rev. B **71**, 024502 (2005).

[75] P. Zhang, W. Luo, V. H. Crespi, M. L. Cohen, and S. G. Louie, Phys. Rev. B **70**, 085108 (2004).

[76] P. Zhang, R. B. Capaz, M. L. Cohen, and S. G. Louie, Phys. Rev. B **71**, 153102 (2005).

[77] M. D. Johannes, I. I. Mazin, and D. J. Singh, Phys. Rev. B **71**, 205103 (2005).

[78] M. Z. Hasan *et al.*, Phys. Rev. Lett. **92**, 246402 (2004).

[79] H.-B. Yang *et al.*, Phys. Rev. Lett. **92**, 246403 (2004).

[80] H.-B. Yang *et al.*, cond-mat/0501403 (2005).

[81] D. Qian *et al.*, Phys. Rev. Lett. **96**, 046407 (2006).

[82] D. Qian *et al.*, Phys. Rev. Lett. **96**, 216405 (2006).

[83] W. B. Wu *et al.*, cond-mat/0408467 (2004).

[84] M. Indergand, Y. Yamashita, H. Kusunose, and M. Sigrist, Phys. Rev. B **71**, 214414 (2005).

[85] M. Indergand and M. Sigrist, Phys. B: Condens. Matter **359-361**, 1357 (2005).

[86] Y. Imai, N. Kawakami, and H. Tsunetsugu, Phys. Rev. B **68**, 195103 (2003).

[87] A. Läuchli and D. Poilblanc, Phys. Rev. Lett. **92**, 236404 (2004).

[88] D. Poilblanc, Phys. Rev. Lett. **93**, 197204 (2004).

[89] N. Bulut, W. Koshibae, and S. Maekawa, Phys. Rev. Lett. **95**, 037001 (2005).

[90] E. Runge and P. Fulde, Phys. Rev. B **70**, 245113 (2004).

[91] S. Kondo *et al.*, Phys. Rev. Lett. **78**, 3729 (1997).

[92] S. H. Lee, Y. Qiu, C. Broholm, Y. Ueda, and J. J. Rush, Phys. Rev. Lett. **86**, 5554 (2001).

[93] L. Santos *et al.*, Phys. Rev. Lett. **93**, 030601 (2004).

[94] B. Damski *et al.*, Phys. Rev. Lett. **95**, 060403 (2005).

[95] C. L. Henley, Can. J. Phys. **79**, 1307 (2001).

[96] M. Indergand, A. Läuchli, S. Capponi, and M. Sigrist, Phys. Rev. B **74**, 064429 (2006).

[97] M. Indergand, C. Honerkamp, A. Läuchli, D. Poilblanc, and M. Sigrist, cond-mat/0609129 (2006).

[98] T. Koretsune and M. Ogata, J. Phys. Soc. Jpn. **72**, 2437 (2003).

[99] C. J. Morningstar and M. Weinstein, Phys. Rev. D **54**, 4131 (1996).

[100] S. Capponi, A. Läuchli, and M. Mambrini, Phys. Rev. B **70**, 104424 (2004).

[101] E. Berg, E. Altman, and A. Auerbach, Phys. Rev. Lett. **90**, 147204 (2003).

[102] R. Budnik and A. Auerbach, Phys. Rev. Lett. **93**, 187205 (2004).

[103] R. Moessner, S. L. Sondhi, and M. O. Goerbig, Phys. Rev. B **73**, 094430 (2006).

[104] S. Sorella and E. Tosatti, Europhys. Lett. **19**, 699 (1992).

[105] L. M. Martelo, M. Dzierzawa, L. Siffert, and D. Baeriswyl, Z. Phys. B Condens. Matter **103**, 335 (1997).

[106] J. Gonzalez, F. Guinea, and M. A. H. Vozmediano, Phys. Rev. B **6313**, 134421 (2001).

[107] F. C. Zhang, C. Gros, T. M. Rice, and H. Shiba, Supercond. Sci. Technol. **1**, 36 (1988).

[108] V. Yushankhai, P. Fulde, and P. Thalmeier, Phys. Rev. B **71**, 245108 (2005).

[109] C. Waldtmann, H. Kreutzmann, U. Schollwock, K. Maisinger, and H. U. Everts, Phys. Rev. B **62**, 9472 (2000).

[110] R. Moessner, O. Tchernyshyov, and S. Sondhi, J. Stat. Phys. **116**, 755 (2004).

[111] B. Canals, Phys. Rev. B **65**, 184408 (2002).

[112] J.-B. Fouet, M. Mambrini, P. Sindzingre, and C. Lhuillier, Phys. Rev. B **67**, 054411 (2003).

[113] W. Brenig and A. Honecker, Phys. Rev. B **65**, 140407 (2002).

[114] H. B. Nielsen and M. Ninomiya, Nucl. Phys. B **193**, 173 (1981).

[115] H. B. Nielsen and M. Ninomiya, Nucl. Phys. B **185**, 20 (1981).

[116] R. Jackiw, Phys. Rev. D **29**, 2375 (1984).

[117] P. W. Anderson, Science **235**, 1196 (1987).

[118] M. P. A. Fisher, *Topological Aspects of Low Dimensional Systems*, Session LXIX, EDP Sciences, 1998.

[119] T. Timusk and B. Statt, Rep. Prog. Phys. **62**, 61 (1999).

[120] R. Coldea, D. A. Tennant, A. M. Tsvelik, and Z. Tylczynski, Phys. Rev. Lett. **86**, 1335 (2001).

[121] M. Azuma, Z. Hiroi, M. Takano, K. Ishida, and Y. Kitaoka, Phys. Rev. Lett. **73**, 3463 (1994).

[122] E. Dagotto, J. Riera, and D. Scalapino, Phys. Rev. B **45**, 5744 (1992).

[123] T. M. Rice, S. Goplan, and M. Sigrist, Europhys. Lett. **23**, 445 (1993).

[124] C. A. Hayward, D. Poilblanc, R. M. Noack, D. J. Scalapino, and W. Hanke, Phys. Rev. Lett. **75**, 926 (1995).

[125] M. Troyer, H. Tsunetsugu, and T. M. Rice, Phys. Rev. B **53**, 251 (1996).

[126] L. Balents and M. P. A. Fisher, Phys. Rev. B **53**, 12133 (1996).

[127] K. L. Hur, Phys. Rev. B **64**, 060502 (2001).

[128] E. Dagotto, Rep. Prog. Phys. **62**, 1525 (1999).

[129] M. Uehara *et al.*, J. Phys. Soc. Jpn. **65**, 2764 (1996).

[130] C. H. Ahn *et al.*, Science **276**, 1100 (1997).

[131] C. H. Ahn *et al.*, Science **284**, 1152 (1999).

[132] S. Gariglio, C. H. Ahn, D. Matthey, and J. M. Triscone, Phys. Rev. Lett. **88**, 067002 (2002).

[133] Z. Hiroi and M. Takano, Nature **377**, 41 (1995).

[134] S. Wessel, M. Indergand, A. Läuchli, U. Ledermann, and M. Sigrist, Phys. Rev. B **67**, 184517 (2003).

[135] M. Sigrist, T. M. Rice, and F. C. Zhang, Phys. Rev. B **49**, 12058 (1994).

[136] H. H. Lin, L. Balents, and M. P. A. Fisher, Phys. Rev. B **56**, 6569 (1997).

[137] U. Ledermann, K. L. Hur, and T. M. Rice, Phys. Rev. B **62**, 16383 (2000).

[138] F. D. M. Haldane, J. Phys. C: Solid State Phys. **14**, 2585 (1981).

[139] H. J. Schulz, *Proceedings of Les Houches Summer School LXI*, Elsevier Amsterdam, 1995.

[140] T. M. Rice, S. Haas, M. Sigrist, and F. C. Zhang, Phys. Rev. B **56**, 14655 (1997).

[141] M. U. Ubbens and P. A. Lee, Phys. Rev. B **46**, 8434 (1992).

[142] G. Kotliar and J. L. Liu, Phys. Rev. B **38**, 5142 (1988).

[143] C. Honerkamp and P. A. Lee, Phys. Rev. Lett. **90**, 246402 (2003).

[144] T. Matsuda and K. Hida, J. Phys. Soc. Jpn. **59**, 2223 (1990).

[145] K. Hida, J. Phys. Soc. Jpn. **61**, 1013 (1992).

[146] J. Fröhlich, B. Simon, and T. Spencer, Comm. Math. Phys. **50**, 79 (1976).

[147] J. Fröhlich, B. Simon, and T. Spencer, Phys. Rev. Lett. **36**, 804 (1976).

[148] F. J. Dyson, E. H. Lieb, and B. Simon, J. Stat. Phys. **18**, 335 (1978).

[149] I. Affleck, T. Kennedy, E. H. Lieb, and H. Tasaki, Comm. Math. Phys. **115**, 477 (1988).

[150] E. J. Neves and J. F. Perez, Phys. Lett. A **114**, 331 (1986).

[151] T. Kennedy, E. H. Lieb, and B. S. Shastry, J. Stat. Phys. **53**, 1019 (1988).

[152] K. Kubo and T. Kishi, Phys. Rev. Lett. **61**, 2585 (1988).

[153] Y. Ozeki, H. Nishimori, and Y. Tomita, J. Phys. Soc. Jpn. **58**, 82 (1988).

[154] J. R. Parreira, O. Bolina, and J. F. Perez, J. Stat. Phys. **86**, 1367 (1997).

[155] E. H. Lieb and D. Mattis, J. Math. Phys. **3**, 749 (1962).

[156] T. Kishi and K. Kubo, J. Phys. Soc. Jpn. **58**, 2547 (1989).

[157] J. P. Serre, *Linear Representations of Finite Groups*, Springer-Verlag, New York, 1977.

[158] J. O. Fjaerestad and J. B. Marston, Phys. Rev. B **65**, 125106 (2002).

[159] M. Tsuchiizu and A. Furusaki, Phys. Rev. B **66**, 245106 (2002).

Seite Leer /
Blank leaf

Acknowledgments

First of all I would like to express my gratitude to my supervisor Manfred Sigrist for accepting me as a student. During the numerous discussions with him I could profit enormously from his deep insights and his broad overview on solid state physics. His friendly and humorous personality provided an enjoyable working atmosphere that I appreciated a lot. I am also deeply indepted to my co-examiner Andreas Läuchli. Already during my diploma thesis he supported me with his advice and also during my PhD time we continued to collaborate in a fruitful and enjoyable way. Apart from work I could also count on Andreas as a reliable table-soccer or mountaineering partner. Many thanks also go to Carsten Honerkamp who as a young father found time to read my thesis and agreed to be my co-examiner.

I enjoyed to share the office with two dynasties of postdocs. On one hand there was the Japanese dynasty with Hiro, Yasu, Waka, and Hirono and on the other hand the Spanish-German dynasty with Klaus, Leni, Sebastian, and Christian. I could profit a lot from their experience and I would probably even have learned Japanese, if I had stayed much longer in this office. But also outside of the office I could discuss with experienced people like Beni, Benedikt, Christian, Dima, Matthias, Masa, Stefan, Urs, and Youichi. Particularly interesting where the discussions with the experimentalists Markus Brühwiler, Betram Batlogg, Bill Pedrini and Jorge Gavilano about the cobaltates.

I believe that it is sufficient to thank my friends who did their PhD together with me only with a few words, as they surely know how grateful I am for the beautiful time we spent together. In particular my thanks go to: Jérôme and Kathi, whose friendship already dates back to an ERASMUS exchange in Spain and survived several years of flatsharing. Samuel, Barbara, and Martin with whom I climbed steep walls and skied white powder-slopes. Igor i Renata, koji su me pozvali na Hvar i koji su pričali srpsko-hrvatski sa mnom. Alvise, Chiara, and Paolo who embellished our lives with delicious food or simply with their

Italianità.

Towards the end of my thesis I got to know more and more PhD students of the younger generation like Andreas Schnyder, Sebastian, Fabian, Andreas Rüegg, Alexander, and Mark who seem to be quite cool as well. With Andreas and Mark I had the pleasure to collaborate while they were writing their diploma thesis in the group of Manfred Sigrist. Of course, special thanks belong to Fabian, who as my new flatmate was a worthy successor of Jérôme.

Before finishing, I want to express my thanks to Dirk Manske for Badminton and Berlin, to all members of the VAK for the cool ski-tours and to Serge and Eugénie for all the funny weekend trips around Karlsruhe.

Last but not least I am very grateful to my parents who supported me during the whole time of my studies. I always could find a beautiful warm home in Andermatt if I wanted to escape the busy life of Zurich. Finally, I thank my Marijana for everything she did for me.

Curriculum Vitae

Persönliche Daten

Name:	Martin Franz Indergand
Geburtsdatum:	21. Februar 1975
Nationalität:	Schweizer

Ausbildung

1982–1988	Primarschule Andermatt
1988–1995	Gymnasium an der Klosterschule Disentis
1996–2001	Physikstudium an der ETH Zürich
1998–1999	Erasmus–Studienjahr in Granada, Spanien
2001	Diplomarbeit an der ETH Zürich bei Prof. Manfred Sigrist
2002–2006	Dissertation am Institut für Theoretische Physik der ETH Zürich bei Prof. Manfred Sigrist